Doctoral Dissertation

High-Speed Si Photonic Crystal Optical Modulator and Its Applications

(高速 Si フォトニック結晶光変調器とその応用)

Yosuke Hinakura

(雛倉陽介)

Yokohama National University

Department of Electrical and Computer Engineering

September 2020

論文主旨

近年，データセンタの大規模化と大容量化が進行するとともに，機器間の電気配線を光配線に置き換える，光インターコネクションの導入が始まっている．データセンタでは大量のサーバーやイーサネットスイッチが相互接続されるため，安価な光トランシーバが大量に必要になる．そのための光集積技術として期待されているのがシリコン (Si) フォトニクスである．Si フォトニクスは Si on insulator (SOI) 基板上に相補型金属酸化膜半導体 (CMOS) プロセスで微細な光回路製作する技術で，低コスト大規模生産が可能であるという大きな利点がある．データセンタ向け光トランシーバへの要求性能は，イーサネット規格によって定められている．次世代のデータセンタに適用されることが見込まれる IEEE802.3bs では，400 Gbps イーサネットの光トランシーバの仕様を，例えば，2 シンボル×50 Gbaud×4 レーン，伝送距離 500 m として規定している．しかし，現在の主要技術である垂直共振器面発光レーザの直接変調とマルチモードファイバを用いた方式では，このような高いビットレートと比較的長い距離での伝送は困難である．一方で，外部光変調器とシングルモードファイバを備えた Si フォトニクストランシーバはより有望な解決策であり，Si 光変調器がそのキーデバイスある．光インターコネクト向けの光トランシーバとそこに用いられる Si 光変調器には，小型化，低動作電圧，低消費電力，低光損失，高速化といった多くの性能が同時に要求される．しかし Si は変調の動作原理となるキャリアプラズマ分散が小さいため，そのサイズと性能のトレードオフ関係は厳しく制約される．例えば，マッハツェンダー型変調器 (MZM) はキャリアプラズマ分散による十分な位相変化$\Delta\phi$を得るために数 mm の長い移相器を必要とするが，一方で，共振を利用した小型なマイクロリング変調器は動作波長帯域が極端に狭く，環境温度変化に対して不安定であるという課題がある．

この制約を破る一つのアプローチがスローライトの利用である．小さな群速度 v_g（または大きな群屈折率 $n_g \equiv c/v_g$）を持つスローライトは光-物質感相互作用を増大する．これは微細な周期構造体であるフォトニック結晶 (PhC) を用いた，フォトニック結晶導波路 (PCW) で容易に生成が可能である．MZM の移相器にスローライトを利用した場合，単位長さ当たりの$\Delta\phi$が増大されるため，移相器の小型化に寄与する．また PCW の特定の円孔列の位置をシフトさせた LSPCW は広い波長範囲~20 nm で一定の n_g をもつ低分散 (LD) スローライトを生成するため，広い動作波長帯域も同時に確保することができる．本研究室では移相器長 $L = 50$–200 μm の小型 Si PCW/LSCPW MZM 変調器を研究しており，これまでに，LD スローライトを利用した 19～124℃の範囲でのアサーマル動作や，波長範囲$\Delta\lambda = 16.9$ nm での一定のアイ開口が観測されているが，明瞭なアイ開口が得られたビットレートは 32 Gbps にとどまっている．そのため 400G イーサネットやさらに次世代の規格で求められる 50 Gbps 以上の高いビットレートでの動作が可能になるように，周波数応答の改善が必要である．

本研究は，Si LSPCW MZM の周波数応答を改善し，ビットレート 50 Gbps 以上での高速動作を実証することを大きな目標とする．このデバイスの周波数応答は電気光学 (EO) 位相不整合によって制限されている．この対策としてメアンダライン電極を導入し，その効果を理論と実験の両面から示す．またスローライト効果による$\Delta\phi$増大や，広い波長範囲の動作についてさらに詳細に検証し，MZM へのスローライトを適用する利点をより明確に示す．さらに新たな応用先として，周波数変調連続波 (FMCW) 方式光レーダーで必要となる周波数掃引変調についても検討する．

第 2 章ではマルチプロジェクトウェハサービスを用いたデバイス作製と，そこで用いられる CMOS 互換プロセスの概要について述べる．このプロセスに含まれるフォトリソグラフィに使用するフォトマスクは，デバイスレイアウトの CAD データから GDSII ストリーム形式で作成した．また Si LSPCW MZM の基本的な構成要素である Si 導波路，スポットサイズ変換器 (SSC)，多モード干渉 (MMI) カプラ，LSPCW，移相器の p-n 接合の設計についてもここで説明する．Si ワイヤ導波路，SSC，MMI カプラには本研究室で最適化された基本設計を採用した．一方，LSPCW と p-n 接合は本研究の目的に合わせて設計し，シミュレーションによりその基本的な特性を確認した．LSPCW のフォトニックバンドと n_g スペクトルは時間領域有限差分 (FDTD) 法を用いたシミュレーションにより計算され，これをもとに LSPCW の構造パラメータを決定した. p-n 接合に関しては, そのキャリア分布や電圧に対するその挙動, キャリア空乏領域とスローライトモードの重なり具合を確認した．製作したデバイスの基本的な光学特性である光透過スペクトルと n_g スペクトルを評価するための測定系についてもここで述べる．

第 3 章ではスローライト効果による変調効率の向上について実験を通して議論する．波長に対して n_g が 20–80 の範囲で緩やかに変化する高分散デバイスを設計，作製し，これを用いて n_g を変化させながら 25 Gbps 変調実験を行った．駆動電圧 V_{pp} = 1.75 V，バイアス電圧 V_{DC} = –0.9 V に対して観測されたアイパターンの消光比 (*ER*) は，n_g の増加に伴って増大した．*ER* から推定された$\Delta\phi$は理論的な予測の通り，n_g とほぼ比例関係にあることを確認した．つまり n_g が増大してもスローライトモードと屈折率変化領域との重なり効率は低下せず，スローライト効果の有効性が維持されることが示された．さらに設計が異なる 5 つの LSPCW デバイス (L = 90 μm) で LD スローライトによる変調効率の増大を確認した．5 つのデバイスは n_g = 22, 26, 31, 33, 38 を示し，ここでも n_g にほぼ比例して$\Delta\phi$が増大した．特に n_g = 33 のデバイスで小さな半波長電圧-移相器長積 $V_\pi L$ = 0.22 V·cm が得られた．

第 4 章では Si LSPCW MZM の広い波長範囲での周波数応答, *ER*, *BER* の測定と調査について議論する．設計，作製した 3 列目シフト LSPCW デバイスは，広い LD 帯域 21 nm を示した．周波数応答測定では，V_{DC} = –1.1 V 印可時に波長範囲λ = 1550–1556 nm で遮断周波数 f_{3dB} = 18 GHz を観測した．この値は p-n 接合の RC 時定数や EO 位相不整合だけでなく，望まれない RF 反射の影響も受けたものである．また$\Delta\lambda$ = 16 nm でアイパターンを観測したところ，消光比 *ER* は 1 dB の幅をもって変動した．*BER* 測定では受光パワーP_r = –4 dBm のときすべての測定波長でエラーフリーな伝送が観測されたものの，それより小さい P_r では *ER* の変動に対応してエラーフリーとなる P_r も約 1 dB 変動した．つまり P_r か *ER* に対して 1 dB のマージンを与えれば広い$\Delta\lambda$ = 16 nm で安定したエラーフリー動作が可能であることが分かった．

第 5 章では周波数応答の改善と高速動作の実証に取り組んだ．はじめに高分散デバイスを用いて n_g に対する周波数応答スペクトルを測定したところ，n_g が大きくなるほど周波数応答が劣化し，その f_{3dB} も低下することが観測された．これはスローライトと変調に用いる RF 信号の間の EO 位相不整合によるものである．そこで RF 信号を迂回，遅延させ，EO 位相不整合を軽減するメアンダライン電極を導入した．その設計のために，進行波電極モデルと分布定数回路モデルを構築し，理論的な解析を行ったところ，メアンダライン長 L_d に加えて RF 反射の位相を制御するΓ_L も重要な要素であることがわかった．また L_d = 425 μm, Γ_L = –0.5 のとき非常に高い f_{3dB} = 56 GHz が得られると予測された．この製作と実証実験の前に，第 4 章で測定した周波数応答に現れたディップとピークを除去することを試みた．これらの望まれないディップとピークはコプレーナ伝送路内の 2 つのグランド (G) 電極間の電位非平衡に

より励起される結合スロットラインモードに起因するものである．そこで 2 つの G 電極を共通化した構造を導入することで，その励振を抑制し，ディップとピークを除去した．このような G 共通化構造を取り入れた上で，$L = 200$ μm のメアンダライン電極デバイスを製作，周波数特性を測定した．実際のデバイスにおいてΓ_L は電極端に負荷する終端電極によって決定される．50 Ωの抵抗で終端した通常電極デバイスは $V_{DC} = -2$ V 印可時に $f_{3dB} = 19$ GHz を示した一方で，メアンダライン電極デバイスでは $f_{3dB} > 30$ GHz 程度が観測された．さらに 20 Ω終端したメアンダライン電極デバイスでは，より高い $f_{3dB} = 38$ GHz が得られた．DC 変調実験ではその $V_\pi L$ は 0.44 V·cm と評価された．一方，高速変調実験においては，50 Ω終端メアンダライン電極素子に対して $V_{pp} = 1, 2$ V を印可したとき，それぞれ，25, 32 Gbps で非常に明瞭なアイパターンが観測された．また 20 Ω終端メアンダラインデバイスでは $V_{pp} = 3.5$ V 印可時に 50 Gbps と 56 Gbps の明瞭なアイ開口が得られ、V_{pp} を 5.2 V に増加させた場合はさらに高速な 64 Gbps での明瞭なアイ開口が得られた．さらに 1 シンボル当たり 2 bit の情報をエンコードする 4 値パルス振幅変調 (PAM4) 実験も行った．シンボルレート 20, 25, 28 Gbaud では PAM-4 変調としては小さな $V_{pp} = 3.5$ V に対してアイ開口が観測されより高いシンボルレート 32, 40, 50 Gbaud ではノイズが増加したものの，アイの形状は維持された．これらの変調を発展させ, 追加の光マルチプレクサチップを用いて波長分割多重 (WDM) 伝送を試みたところ, 50 Gbps/ch の伝送速度で明瞭なアイパターンが観測された．ただしこの実験用いた変調器は WDM 用に設計されたものではないため，波長チャネルが 4 チャネルに制限された．WDM 専用の設計に変更すれば, 8 チャネルに拡張可能, つまり合計ビットレート 400 Gbps の WDM 伝送が可能になると期待される．

第 6 章では FMCW LiDAR 向け周波数掃引変調に関する検討を行った．はじめに周波数掃引変調の基礎となる単一周波数変調を行い，光電変換された信号の周波数スペクトルを観測した．単一周波数成分を持つスペクトルピークの線幅は 1.2 kHz と狭く，十分なコヒーレント長が確保できることを確認した．さらに任意波形発生器を用いてノコギリ歯形もしくは三角形に周波数が時間的に変化する，掃引幅 3 GHz の周波数掃引信号を生成し，Si LSPCW MZM で変調を行った．変調された信号の周波数スペクトルは生成された信号に対応したことから，周波数掃引変調が行われたことを確認した．同様の信号を用いて光ファイバ系での初期的な測距実験を試みた．測距対象との距離を模擬した遅延用ファイバ長 $L_{delay} = 1002 \pm 10$ cm に対して，理論値と一致するビート周波数 $f_{beat} = 25.0$ MHz が得られた．また異なる $L_{delay} = 556.8$, 2009 cm に対しても対応する f_{beat} も観測されたことから，初期的な測距動作が実証された．

本研究では 64 Gbps 動作可能な $L = 200$ μm の Si PCW 変調器を実証した．同時にこのデバイスに 3 列目 LSPCW を採用することで容易に広い$\Delta\lambda = 16$ nm を持つことになる．また $V_\pi L$ は 0.44 V·cm と評価された．以上のことから 400G イーサネットやさらに次世代の規格で使用される小さなフットプリント，低い製作コスト，広い動作波長を持つ高速変調器として，Si LSPCW MZM の可能性を示した．また FMCW LiDAR に使用される周波数掃引光源の実現可能性も示した．

Contents

Chapter1 Introduction 1

1. 1 Silicon Photonics 1
1. 1. 1 Overview 1
1. 1. 2 Applications 2
1. 2 Optical Modulator 6
1. 2. 1 Modulation Formats 6
1. 2. 2 Direct Modulation 7
1. 2. 3 External Modulators 7
1. 2. 4 Si Optical Modulators 8
1. 3 Photonic Crystal Waveguide (PCW) 13
1. 3. 1 Overview 13
1. 3. 2 Slow Light in PCW 14
1. 4 Slow Light Optical Modulators 15
1. 4. 1 Principle 15
1. 4. 2 Variety of Slow Light Modulators 15
1. 4. 3 CPD Based Si PCW MZM 16
1. 4. 4 Comparison and Remaining Problems 17
1. 5 Objective of this Study 17
1. 5. 1 Observation of Modulation Efficiency Enhancement 18
1. 5. 2 Wide Wavelength Range Operation 18
1. 5. 3 Investigation of Limiting Factor of Frequency Response and its Improvement 18
1. 5. 4 Application to FMCW LiDAR Transmitter 18
1. 6 Outline of this Dissertation 20

Chapter2 Fabrication and Components 28

2. 1 Fabrication 28
2. 1. 1 Si Photonics Foundry Service 28
2. 1. 2 Outline of the Fabrication Process 29
2. 1. 1 CAD Data Production 30
2. 2 Fundamental Components 31
2. 2. 1 Si Wire Waveguide 31
2. 2. 2 Spot Size Converter 32
2. 2. 3 Multi-Mode Interference Coupler 34
2. 2. 4 LSPCW 35
2. 2. 5 P-N Junction 38
2. 3 Evaluation Methods for Fundamental Optical Characteristics 39
2. 3. 1 Optical Transmission Measurement System 39
2. 3. 2 Group Index Measurement System 40
2. 4 Summary 40

References 41

Chapter3 Modulation Efficiency Enhancement via the Slow-Light Effect 42

3. 1 Overview 42
3. 2 Observation of Modulation Efficiency Enhancement 42
3. 2. 1 Dispersive Device 42
3. 2. 2 Fundamental Characteristics 44
3. 2. 3 Modulation Characteristics 45
3. 3 Sub-100-μm Si LSPCW MZM using a High Group Index 47
3. 3. 1 LD Devices 47
3. 3. 2 Fundamental Characteristics 49
3. 3. 3 Modulation Characteristics 50
3. 4 Summary 50
References 52

Chapter4 Wide-Wavelength-Range Operation 53

4. 1 Overview 53
4. 2 Device 53
4. 2. 1 Design and Fabrication 53
4. 2. 2 Fundamental Characteristics 55
4. 3 Frequency Response Measurement 56
4. 3. 1 Measurement Setup 56
4. 3. 2 Results 57
4. 4 Modulation Characteristics 59
4. 4. 1 Measurement Setup 59
4. 4. 2 Results 59
4. 4. 3 Discussion 60
4. 5 Summary 61
References 62

Chapter5 High-speed Operation by Electrooptic (EO) Phase Matching 63

5. 1 Experimental Observation of EO Phase Mismatch 63
5. 2 Meanderline Electrode 64
5. 3 Theoretical Analysis 65
5. 3. 1 Traveling-Wave Electrode Design 65
5. 3. 2 Distributed Constant Circuit 67
5. 3. 3 *S* Parameter 70
5. 3. 4 Calculation Results 71
5. 4 Suppression of the Coupled Slotline Mode 75
5. 4. 1 Design and Fabrication of Meanderline Electrode Device 78
5. 5 Frequency Response Measurement 84
5. 5. 1 Measurement Setup 84

5. 5. 2 Results 85
5. 6 High-speed Modulation Experiments 85
5. 6. 1 OOK Modulation 85
5. 6. 2 PAM4 Modulation 91
5. 6. 3 50 Gbps/ch WDM Transmission 95
5. 7 Summary 98
References 98

Chapter6 Frequency-Swept Modulation for a FMCW LiDAR System 100

6. 1 Overview 100
6. 2 Evaluation of Single-Tone Modulation 100
6. 3 Beat Signal Generation between Two Single-Tone Signals 102
6. 4 Frequency-Swept Modulation 105
6. 4. 1 Frequency-Swept Signal Generation 105
6. 4. 2 Modulation Experiment 107
6. 5 Ranging Experiment in Optical Fiber System 108
6. 5. 1 Measurement Setup 108
6. 5. 2 Results 110
6. 6 Summary 111
References 112

Chapter7 Conclusion 113

7. 1 Modulation Efficiency Enhancement via Slow Light Effect 113
7. 2 Wide-Wavelength-Range Operation 113
7. 3 High-Speed Operation via Electrooptic (EO) Phase Matching 114
7. 4 Frequency-Swept Modulation for a FMCW LiDAR System 114
7. 5 Comprehensive Conclusion 115
References 116

Acknowledgements 113
Publications 119

Journal Papers 119
International Conferences 119
Domestic Conferences 120

Chapter1
Introduction

1. 1 Silicon Photonics

1. 1. 1 Overview

Silicon (Si) photonics involves fabrication of photonics components in a thin Si slab via mature complementary metal oxide semiconductor (CMOS) technology [1-1]–[1-4]. Si has been intensively used as a material for integrated circuits (IC) because it is a stable, safe, and easily obtainable semiconductor. In addition, the band gap energy of Si is 1.12 eV, corresponding to the band gap wavelength λ_g of 1.1 μm; thus, Si is transparent at the optical communication wavelengths, e.g., 1.3 μm (O band) and 1.55 μm (C band) [1-1-4]. Si photonics has the following attractive advantages: (1) strong light confinement in a small volume, (2) low-cost mass production, and (3) monolithic integration with electronic IC. Therefore, Si photonics is expected to be applied to various fields involving optical interconnects [1-5]–[1-7], as a densely integrated photonics platform with complex functionalities. Figure 1.1 shows an example of a Si photonics chip fabricated on a silicon-on-insulator (SOI) wafer via a CMOS fabrication process. This several-mm^2-size chip can contain various compact optical components including optical waveguides [1-8]–[1-10], optical couplers and splitter [1-11]–[1-14], multiplexers/demultiplexers for wavelength division multiplexing [1-15]–[1-18], Germanium (Ge) photodetectors (PDs) [1-19]–[1-21], and optical modulators [1-22]–[1-25]. The Si photonics can utilize CMOS fabrication facilities and produce integrated photonics chips at large scale. This capability allows for photoelecrical fusion on chip scale as well as low-cost mass production.

The strong light confinement in Si waveguides enables waveguide bending at small radius. This capability is advantageous for high-density optical integration because the bending radius usually limits the device footprint. The degree of light confinement depends on the refractive indices of the waveguide core and the cladding materials and is characterized by the relative refractive index difference Δ [1-26]:

$$\Delta = \frac{n_1^{\,2} - n_2^{\,2}}{2n_1^{\,2}} \tag{1.1}$$

where n_1 and n_2 are the refractive indices of the core and cladding materials, respectively. Δ of the waveguides consisting of a Si core (refractive index $n \sim 3.45$) and SiO_2 ($n \sim 1.45$) cladding is as high as ~40%. This high Δ enables sharp bends at a small radius of ~5 μm [1-27] and dense photonic integration on a small chip as small as several mm^2. In contrast, Δ of SiO_2 planar waveguides is typically lower than 1%, resulting in a large bending radius of over 5 mm [1-28].

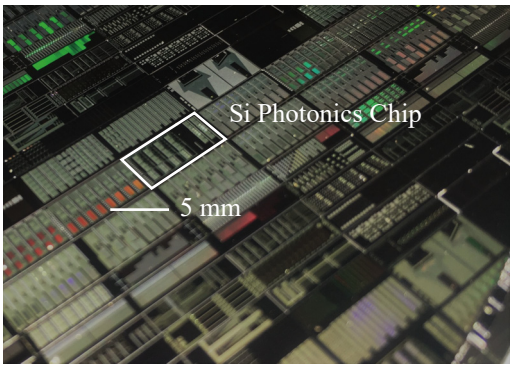

Figure 1.1 Si photonics chip fabricated on a SOI wafer.

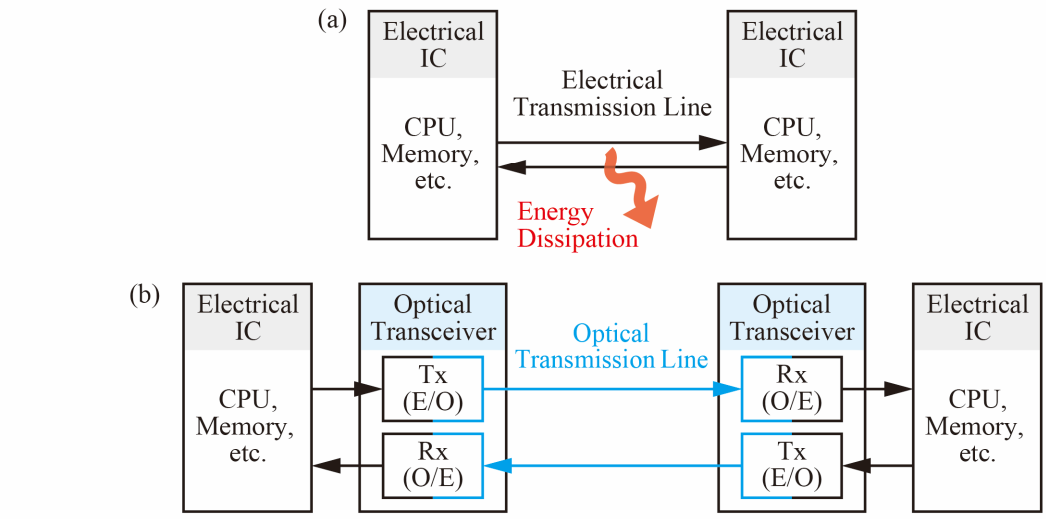

Figure 1.2 Concept of interconnection schemes. (a) electrical interconnects. (b) optical interconnects.

1. 1. 2 Applications

(a) Optical Interconnects in Data Centers

Data centers are facilities that aggregate information technology (IT) instruments, such as server computers and Ethernet switches. Data centers have become the new infrastructure of IT services, for example, cloud storage, social networking, and video streaming. However, with the growth of data centers, three problems are becoming more serious. The first problem is the huge amount of power consumption; the power consumption of a data center has reached up to several megawatts [1-29]. The second problem is the rapidly increasing enormous data traffic; Cisco estimated that data traffic in global data centers will reach 19.5 Zbytes/year by the end of 2021, up from 6.0 Zbytes/year in 2016 [1-30]. The third problem is physical upscaling of the data centers; the number of “hyperscale datacenters,” defined as any data center with at least 5000 servers and 10000 square feet [1-31], is increasing to support the huge amount of data traffic.

Optical interconnects, i.e., relatively short-distance optical data communications between electrical circuits constituting a network, is the key technology to solve these problems. Figures 1.1(a) and (b) are illustrations of traditional electrical interconnects and optical interconnects. In electrical interconnects,

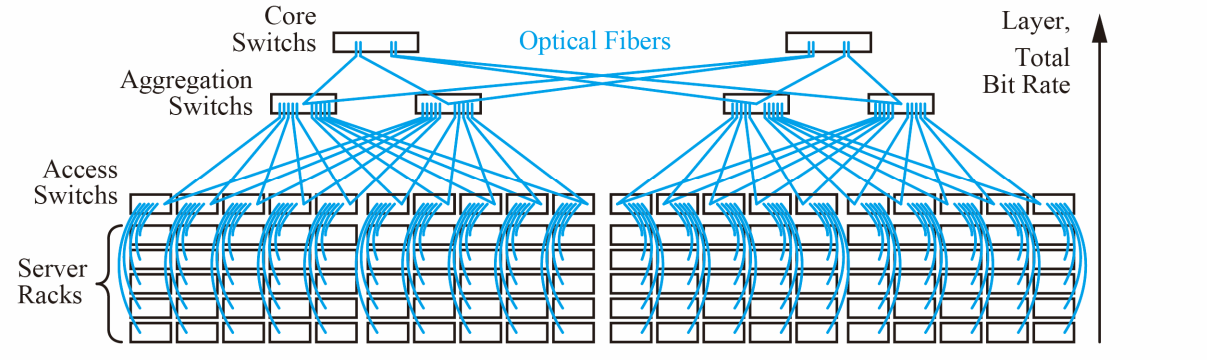

Figure 1.3 Network architecture in a data center.

Table 1.1 Spesification of Ethernet Standards

Standards	Interface	Optical Fiber	Distance	Baud Rate	Bits per symbol	Number of Lanes or Wavelengths
IEEE 802.3ba	100GBASE-SR10	MMF	0.1 km	10 Gbaud/lane	1 bit/symbol (NRZ)	16 lanes
	100GBASE-LR4	SMF	10 km	25 Gbaud/λ	1 bit/symbol (NRZ)	4λ
	100GBASE-ER4	SMF	40 km	25 Gbaud/λ	1 bit/symbol (NRZ)	4λ
IEEE 802.3bm	100GBASE-SR4	MMF	0.1 km	25 Gbaud/lane	1 bit/symbol (NRZ)	4 lanes
IEEE 802.3bs	400GBASE-SR16	MMF	0.1 km	25 Gbaud/lane	1 bit/symbol (NRZ)	16 lanes
	400GBASE-DR4	SMF	0.5 km	50 Gbaud/lane	2 bit/symbol (PAM4)	4 lanes
	400GBASE-FR8	SMF	2 km	25 Gbaud/λ	2 bit/symbol (PAM4)	8λ
	400GBASE-LR8	SMF	10 km	25 Gbaud/λ	2 bit/symbol (PAM4)	8λ

electrical circuits are connected to each other via electrical transmission lines. These lines dissipate a part of the signal energy, particularly at high signal frequency. Therefore, this energy dissipation can be the bottleneck of the bit rate and reduction of the power consumption. In contrast, in optical interconnects, the electrical data sequences are converted into the optical data sequences using optical transceivers to transmit signals over low-loss and broad-bandwidth optical transmission lines, such as optical fibers.

Figure 1.3 shows an illustration of the network architecture in a data center. The network is connected layer by layer with Ethernet switches, such as access switches, aggregation switches, and core switches, and it requires a significant number of optical transceivers. Therefore, Si photonics is a suitable optical platform for use in optical interconnects because of its high productivity and low cost. In addition, Si photonics can merge electrical ICs and optical ICs onto a small chip; this allows the reduction of the transceiver module size and assembly process as well as introduction to a smaller region of the network, e.g., memory-to-core, core-to-core, and ultimately intra-core.

To maximize the benefits of optical interconnects of high-speed and low power consumption, optical transceivers are necessary. Here, an optical modulator in the transmitter side is one of the key devices required to develop an optical transceiver. A comparison with the existing electrical interconnects indicated that total power consumption of the optical transceiver module cannot exceed ~1 pJ, and the power consumption of the individual optical component, including the optical modulators, in the transceiver should be much less than 1 pJ [1-5]. Moreover, the bit rates in actual data centers are determined by Ethernet standards, which define network protocols in wide area networks and metropolitan networks. 100G Ethernet was approved as IEEE 802.3ba in 2010 [1-32] and IEEE 802.3bm,

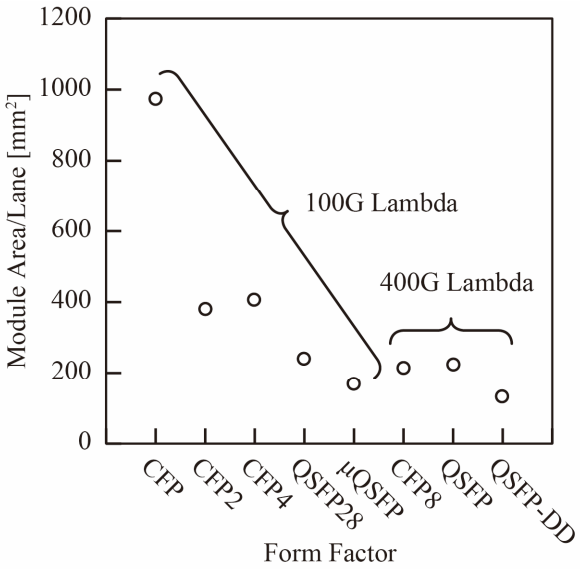

Figure 1.4 Configuration of the optical transceiver.

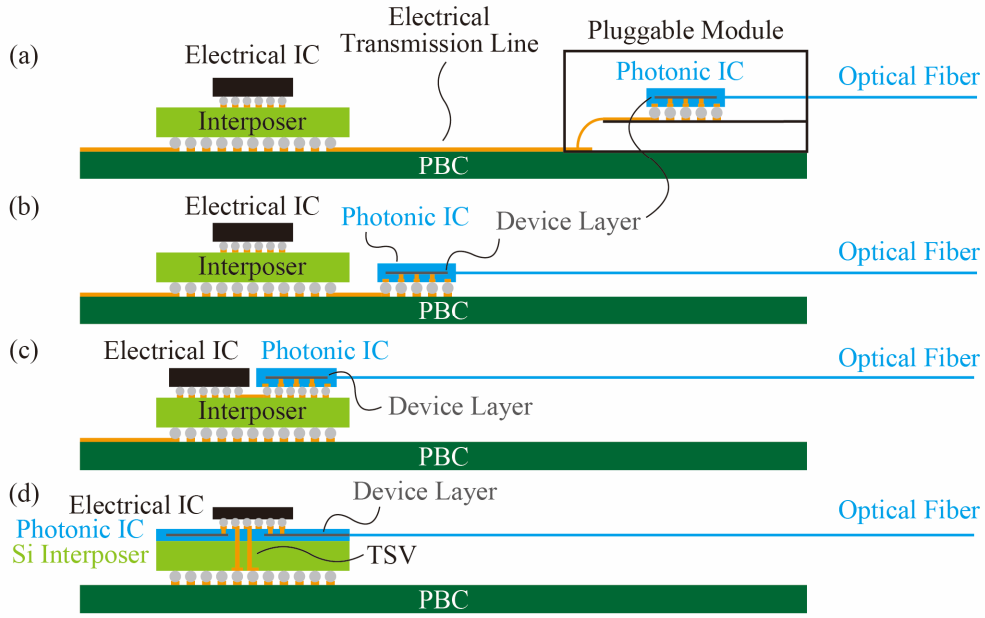

Figure 1.5 Configurations of photonics implementation on an Ethernet linecard. (a) Pluggable module implementation. (b) Mid-board implementation. (c) MCM implementation. (d) TSV implementation.

which was approved in 2015 [1-33], is expected to be widely used by 2020. A new standard, 400G Ethernet, was approved as IEEE 802.3bs in 2017 [1-34]. This standard is expected to spread to the high-layer interconnects in the next few years. Thus, the development of 400G-Ethernet-capable optical transceivers is urgently required. Table 1.1 summarizes the specification of the 100G and 400G standards. The bit rates of the 400G standards per channel (baud rate/lane × bit per symbol) have reached up to 50 Gbps or 100 Gbps. In addition, the middle-reach and long-reach standards are expected to be frequently used because of the upscaling of each data center. This higher-speed and longer-distance communication environment requires low-dispersion single-mode fibers (SMFs) and external modulators, which are described in Section 1. 2. 4. Furthermore, it is expected that 800-Gbps and 1.6-

Table 1.2 Comparison of EA and EO effects.

Effects		Material
EA Effects	FK Effect	Bulk Semiconductors
	QCSE	Semiconductor QWs
EO Effects	Pockels Effect	Non-Centrosymmetric Crystals (III-V Semiconductors, $LiNbO_3$, $LiTaO_3$, etc.)
	CPD	Semiconductors

Tbps standards will emerge as future standards. Moreover, the multi-source agreement (MSA) group standardized the form factor of the pluggable transceiver modules into the equipment [1-35]. Figure 1.4 shows the module area per lane of the form factors. The form factors of 400G lambda MSA can have a module area per lane of less 225 mm^2. It is estimated that the form factor becomes smaller and the transceivers transfer to mid-board optics (Figure 1.5(b)) from the current pluggable modules (Figure 1.5(b)) in the future standards, because of the denser connection and shorter electrical transmission lines as well as the lower implementation cost. Furthermore, it will be advanced to on-board optics using a multiple chip module (MCM) or through silicon vias (TSVs) [1-36], [1-37], shown in Figure 1.5(c) and (d), respectively. Therefore, the Si photonics platform, which offers dense photonic integration, is an attractive candidate for being the platform of the next-era optical interconnects.

(b) Light detection and ranging (LiDAR)

An emerging field of Si photonics is on-chip LiDAR [1-38], [1-39] for use in advanced driver-assistance systems (ADAS), 3D mapping, drones, and robotics. Although mechanical beam steering LiDARs, which are the currently dominant beam steering devices, are in the practical stage, these devices are still bulky and expensive. In contrast, Si photonic deflectors, such as optical phased arrays [1-40]–[1-43], can change the angle of the light beam based on electro-optic (EO) or thermo-optic (TO) effects, i.e., without any moving mechanical components. As a result, Si photonics has the potential to integrate a LiDAR system on a chip and significantly reduce the size and cost of such systems.

The simplest ranging method is time of flight (ToF), which involves measurement of the time from an irradiation of an optical pulse to the reception of the reflected light, as shown in Figure 1.6(a). This method requires a high-power pulse laser to achieve an adequate signal-to-noise ratio (SNR). However, high-power pulse lasers have not been developed for the O band or C band in which Si photonics components operate. Therefore, Si frequency-modulated continuous wave (FMCW) LiDAR chips, which are robust to exogenous noise (even at relatively low optical power), are being developed [1-36], [1-37]. A FMCW LiDAR chip ranges the distance to a target based on the beat frequency between a frequency-swept transmitted light beam and the received light beam. Such a system may consist of an frequency modulation (FM) transmitter, deflectors, and interferometer for the comparison of the reference light and the received light, as shown in Figure 1.6(b). Although the FMCW LiDAR system is much more complex compared with the ToF LiDAR system, Si photonics can integrate this system into a small chip. The ranging accuracy of the FMCW LiDAR system depends on the temporal linearity of the frequency sweep. The simple scheme ensures high linearity via the combination of the FM driver and the modulator because it can utilize the mature electrical signal generation technology. To increase

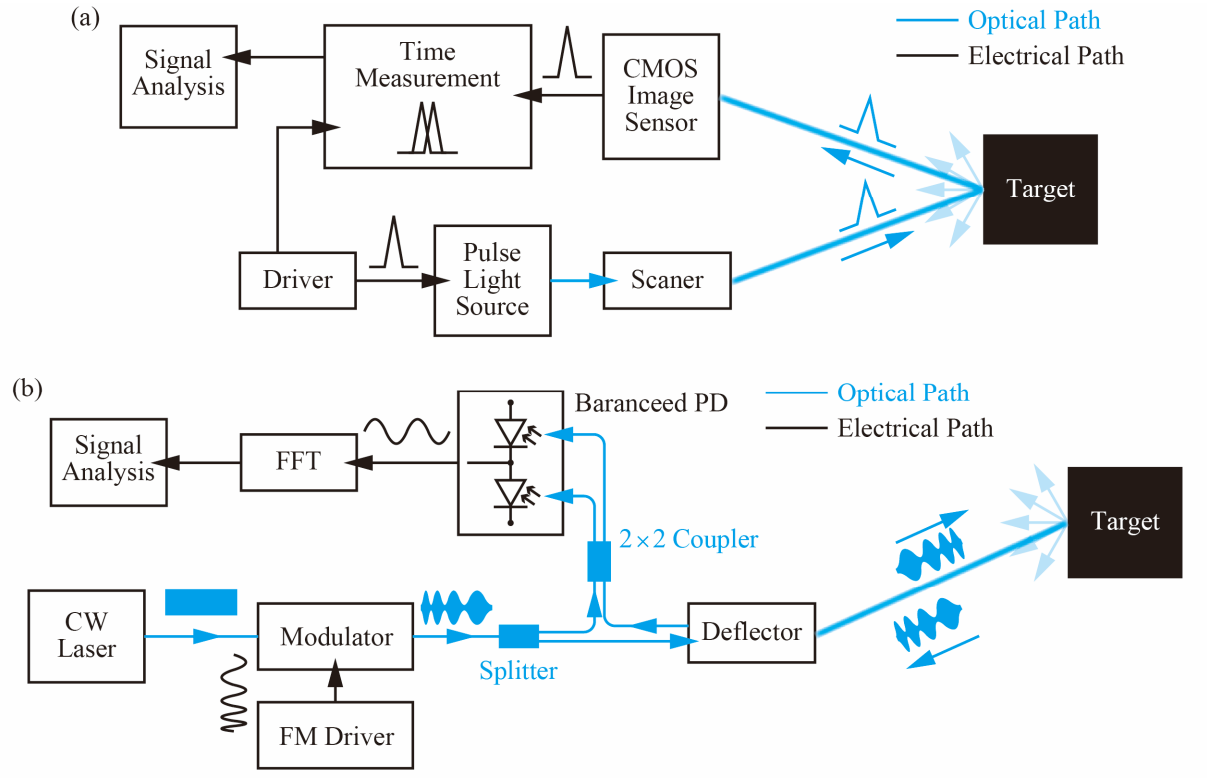

Figure 1.6 Configurations of LiDARs. (a) ToF LiDAR. (b) FMCW LiDAR.

the degree of the layout freedom in such a complex system, a small modulator is desired.

1. 2 Optical Modulator

An optical modulator is a device that dynamically controls light via external signals, e.g., electricity or heat; it acts as a converter from the domain of the external signal to the optical domain. In this section, after introduction of the various modulation formats, I describe EO modulators, which can convert radio frequency (RF) electrical signals to optical signals.

1. 2. 1 Modulation Formats

There are several modulation formats, classified according to which domain the light is modulated and how the modulation is achieved. For example, amplitude modulation (AM), a.k.a. intensity modulation (IM), FM, and phase modulation (PM) are commonly used analog modulation formats; these formats correspond to amplitude shift keying (ASK), frequency shift keying, and phase shift keying (PSK), respectively, in digital modulations. ASK, which requires only direct detection, is the simplest receiver configuration, whereas FM and PM require more complex coherent detection schemes. Therefore, ASK is intensively used in systems requiring simplicity and low cost, such as short-reach optical interconnects. In particular, ASK that is digitized into only two levels (“1” and “0” or “on” and “off”) is called on-off keying (OOK). In contrast, digital coherent technology [1-44], which realizes high spectral efficiency using the complex vector space (i.e., the amplitude and phase), has been used in metro networks and long-haul networks, which require high transmission capacity. Recently, multilevel pulse amplitude modulation (PAM) has also been considered as a path toward the 400G Ethernet, as shown in Table 1.1.

This scheme encodes multilevel information only in the amplitude of light, allowing simple direct detection while increasing the bits per symbol.

1. 2. 2 Direct Modulation

The variety of types of optical modulators that have been studied and developed are classified according to the material used, the effect used, and the configuration used. The largest classes are direct modulation and external modulation. The direct modulation is the method that involves directly driving an optical source, such as a laser diode. For example, if the output amplitude is changed by its injection current, then AM modulation is realized, and if the output frequency is changed with cavity length, then FM modulation is realized. This method can reduce cost because it is the simplest method of modulation. The most widely used devices for the direct modulation in optical interconnects are vertical cavity surface emitting lasers (VCSELs) because they have the following attractive advantages: (1) longitudinal single-mode operation, (2) low power consumption due to the low driving current, (3) wafer-scale testing, (4) ease of two-dimensional arrangement, (5) high-speed modulation due to the small cavity volume, and (6) high-efficiency optical coupling with multimode fibers (MMF). Some research groups have reported high-speed direct modulation of the VCSEL that exceed 50 Gbps. For example, P. Westbergh et al. reported error-free 57-Gbps OOK modulation without frequency response equalization [1-45], and D. M. Kuchta et al. reported error-free 71-Gbps OOK modulation with feed-forward equalization (FFE) [1-46]. However, the error-free transmission links in these papers consisting of OM4 MMF and OM3 MMF standardized in ISO/IEC 1180 [1-47], and the lengths considered back-to-back and 7 m, respectively. These distances were limited by the strong mode dispersion in the MMFs, and the transmission bandwidths are 2000 MHz·km for the OM3 and 4700 MHz·km for the OM4 [1-47], [1-48]. This dispersion makes it difficult to use these lasers in interconnects of relatively long distances of several kilometers. Another choice of a single-longitudinal-mode laser for direct modulation is a distributed feedback (DFB) laser [1-49]–[1-53]. This type of laser has the advantages of high power, high temperature stability, and integration with waveguides. K. Nakahara et al. reported 56-Gbps direct modulation of a ridge-shaped-buried heterostructure DFB laser and its transmission over a 10-km single-mode fiber at 1.3-μm at the O band [1-51]. However, DFB lasers are costly for short-reach interconnection, which requires a large amount of laser sources. In addition, wavelength chirping of lasers under direct modulation [1-54] produces a power penalty for long-distance transmission at high bit rates. Furthermore, as direct modulation is intrinsically AM modulation, external modulators, which are described in detail below, is prevalent at these distances.

1. 2. 3 External Modulators

A method that uses an external modulator in addition to a light source is called external modulation. This method has the following advantages: (1) the light source and the modulator can be optimized separately, (2) high speed operation, (3) small wavelength chirping (or no chirping), and (4) advanced modulation methods (such as the digital coherent technique) are available. High-speed external modulators are classified into electro absorption (EA) modulators based on EA effects and EO modulators based on EO effects. The available effects differ according to the material used. Table 1.1 summarizes the material and EA and EO effects used for optical modulators. At the optical

communication wavelengths, EA effects occur in III-V compound semiconductors, such as Gallium Arsenide (GaAs) and Indium Phosphide (InP), and group-IV semiconductors. In bulk semiconductors, λ_g shifts toward longer wavelengths via applied electric fields. This phenomenon is called the Franz–Keldysh (FK) effect. In a quantum well (QW) structure, the quantum confined Stark effect (QCSE) occurs. The QCSE also shifts λ_g toward longer wavelength via electric fields perpendicularly applied to the QW. The EA effects respond at very high frequency. W. Kobayashi et al. reported equalization-free 100-Gbps PAM4 transmission over a 2-km SMF via an optical transmitter module consisting of an EA modulator integrated with a DFB laser and an RF driver circuit [1-50]. Moreover, the authors also reported 214-Gbps PAM4 transmission over a 10-km SMF at the O band utilizing FFE [1-53]. The FK effect occurs in group-IV semiconductors as well. On a Si photonics platform, the FK effect is available in Silicon-Germanium (SiGe). The band gap energy of SiGe is tunable according to the composition. However, because EA modulators are intrinsically intensity modulators, the modulation method is limited. In addition, the EA effects induce frequency chirping according to the Kramers–Kronig relations. The Pockels Effect occurs in non-centrosymmetric crystals, represented by $LiNbO_3$ (LN). The LN modulators have the attractive properties of high operation speed and high linearity. These properties support the high capacity, high spectral efficiency, and complex digital coherent technology used in core networks. Using nested LN modulators and digital coherent technology, very high capacity transmission of 10 Tbps or more has been achieved [1-55]–[1-57]. However, the large size of several centimeters [1-58]–[1-61] is not suitable for the high-density integration required for the data center application.

1. 2. 4 Si Optical Modulators

(a) Carrier Plasma Dispersion (CPD) Based Phase shifter

The EA effect and the Pockels Effect cannot be used in a pure Si crystal because it is a centrosymmetric and widegap material. As a result, CPD, which involves changes to the refractive index via the free-carrier density, is used for PM modulation. If necessary, PM can be converted into AM and IM modulation via an interferometer. The refractive index change Δn via CPD in crystalline Si is empirically given by Equation (1.2) [1-62]:

$$\Delta n = -5.40\times10^{-22}\Delta N_e^{1.011} - 1.53\times10^{-18}\Delta N_h^{0.838} \tag{1.2}$$

where ΔN_e and ΔN_h are the free electron density and the free electron density, respectively, in units of cm^{-3}. Simultaneously, absorption coefficient α corresponding to the imaginary part of the refractive index changes is given as follows:

$$\Delta\alpha = 8.88\times10^{-21}\Delta N_e^{1.167} + 5.84\times10^{-20}\Delta N_h^{1.109} \tag{1.3}$$

This effect is called free-carrier absorption (FCA). FCA can induce excess optical loss in Si optical modulators. Therefore, Δn and α are in a tradeoff relationship. To control Δn, the impurities of Boron (B) and Phosphorus (P) are implanted into intrinsic (i) Si to make p-type and n-type regions, respectively. A Si phase shifter is classified into three schemes: carrier injection mode, carrier depletion mode, and carrier accumulation mode.

A carrier-injection phase shifter consists of a p-i-n junction. Figure 1.7 shows an illustration of the cross section and the energy band of a carrier-injection phase shifter. The light is confined in a rib waveguide

of two different thickness slabs. This waveguide ensures the light remains far from the absorptive metal electrodes used for carrier concentration control. As shown in Figure 1.6(a), the side ribs (thinner slabs) are doped to have high electrical conductivity, whereas undoped i-type Si are placed at the center of the waveguide to avoid FCA. The carriers are prevented from moving across the i-type region by the built-in potential voltage V_{bi}. When the bias voltage V_{bias} is higher than the V_{bi} applied to the p-i-n junction, the potential barrier disappears, and the carriers are able to move. As a result, current begins to flow, thereby inducing a refractive index change; thus, Δn in the i-type region largely changes. The dynamic response of this scheme is limited by the carrier recombination rate, resulting in the low cutoff frequency f_{3dB} of several GHz [1-63], and the limited operation data rate of approximately 10 Gbps [1-64], [1-65].

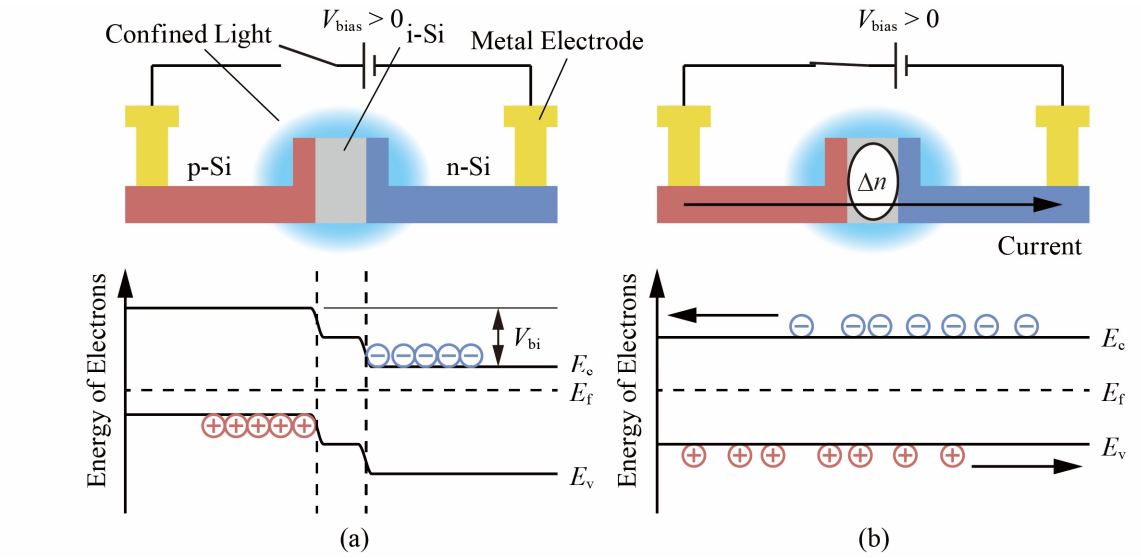

Figure 1.7 Cross section and the energy band of a carrier injection phase shifter. (a) Equilibrium state. (b) Flat band state under forward bias voltage.

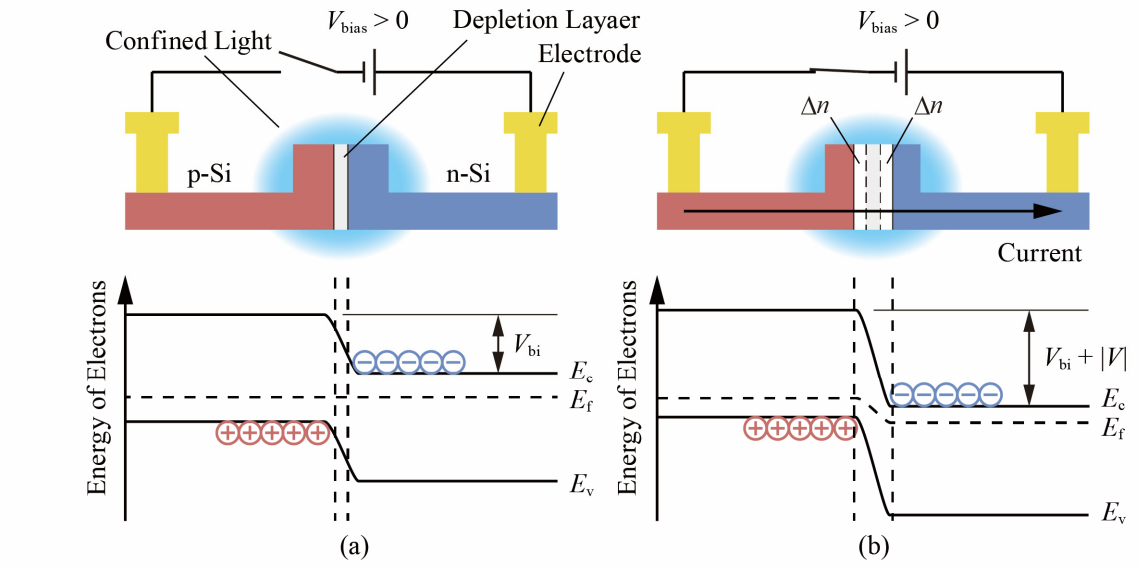

Figure 1.8 Cross section and the energy band of a carrier depletion phase shifter. (a) Equilibrium state. (b) Energy band under reversed bias voltage.

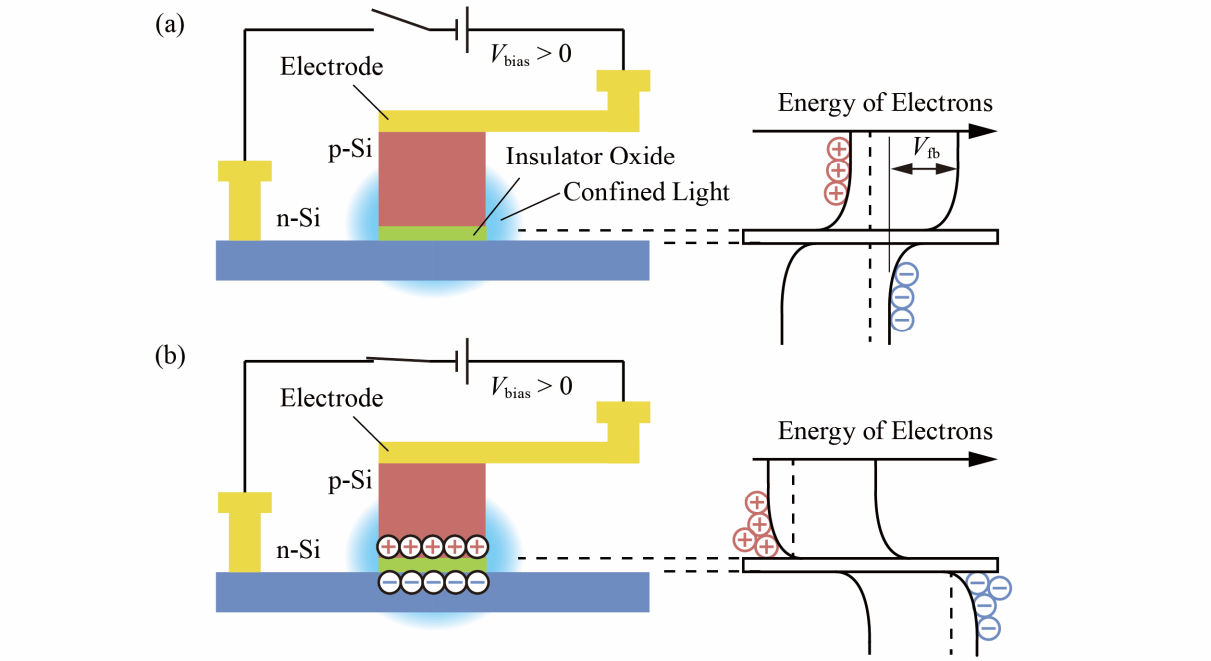

Figure 1.9 Cross section and the energy band of a carrier accumulation phase shifter. (a) Equilibrium state. (b) State under forward bias voltage larger than V_{fb}.

A carrier depletion phase shifter consists of a p-n junction. Figure 1.7 shows an illustration of the cross section and energy band of the carrier-depletion-type phase shifter. As in a p-i-n junction, the carrier depletion region appears at the junction. When negative V_{bias} is applied, the carrier depletion region is expanded, thereby inducing the refractive index change at the both edges of the depletion region. Therefore, the area of the refractive-index-changed region is much smaller than that of the carrier-injection phase shifter. To improve the modulation efficiency, an interleaved p-n junction has been proposed [1-23], [1-66], [1-67]. This junction increases the overlap between the modal field and the refractive-index-changed region. The dynamic response of the carrier depletion mode phase shifter is much faster than that of the carrier injection mode phase shifter because the carriers are controlled by strong electric fields applied to the depletion region. The response is limited by the charging time of the depletion region, which behaves as a capacitor. The response time of the interleaved p-n junction is determined by the *RC* time constant (*R* is a series resistance, and *C* is a capacitance of the depletion region); thus, f_{3dB} is much higher than that of the carrier-injection phase shifter [1-22], [1-68]–[1-74]. The *RC* time constant of the interleaved p-n junction is longer than that of simple lateral junctions because it has longer junction length, which contributes to high *C*.

A carrier accumulation phase shifter has a similar structure as that of a MOS capacitor: p-type Si and n-type Si vertically sandwich an insulator oxide, as shown in Figure 1.8. The carriers begin to be accumulated when V_{bias} is greater than flat band potential voltage V_{fb}. As a result, the refractive index changes at the vicinity of the insulator oxide. This type of phase shifters tends to have high capacity because of the large area of the insulator oxide, resulting in higher Δn and lower f_{3dB} than the carrier depletion phase shifter. In addition, because crystalline Si cannot be fabricated on an insulator oxide using a standard CMOS compatible process, polycrystalline Si is used for this structure. The poly-Si film quality affects the optical loss and the carrier mobility.

Si IM modulators are configured as interferometers or resonators to convert from PM modulation to

IM modulation. Here, I describe two widely used schemes: (a) micro ring resonator (MRR) and (b) Mach-Zehnder interferometer (MZI).

(b) Microring Modulator

A microring modulator (MRM) based on the MRR is a compact modulator scheme based on resonance [1-24], [1-73], [1-75]–[1-79]. Figure 1.9 shows an illustration of the MRM and its transmission spectrum. The MRR is in the resonant condition when the incident wavelength meats the resonant wavelength λ_{res}, resulting in the appearance of notches in the spectrum [1-80]:

$$\lambda_{res} = \frac{n_{eff} L_{cir}}{m} \quad (m = 1, 2, 3, \ldots) \tag{1.4}$$

where n_{eff} is the effective refractive index of the waveguide, and L_{cir} is the circumference of the MRR. The sharpness of this resonance is evaluated by the Q factor, with a high Q factor corresponding to a sharp resonance. When the wavelength λ_1 of the incident light propagating in the bus waveguide is equal to the resonant wavelength λ_{res}, the light is coupled to the MRR and the output is extinct. In contrast, at the wavelength of λ_2 (which is out the resonance), the light cannot remain in the MRR. Hence, the light is output to the bus waveguide. PM modulation in MRR changes this resonant condition, i.e., λ_{res} shifts to a different wavelength λ_{res}', thus changing the output power P_{out} simultaneously and switching between the on state and the off state. This on-off power contrast is evaluated by the extinction ratio ER:

$$ER = P_{on}/P_{off} \tag{1.5}$$

where P_{on} is the output power of the on state, and P_{off} is the output power of the off state. The ER depends on the amount of the resonant frequency shift $\Delta\lambda$ due to the $\Delta\phi$ in the phase shifter, and the $\Delta\phi$ depends

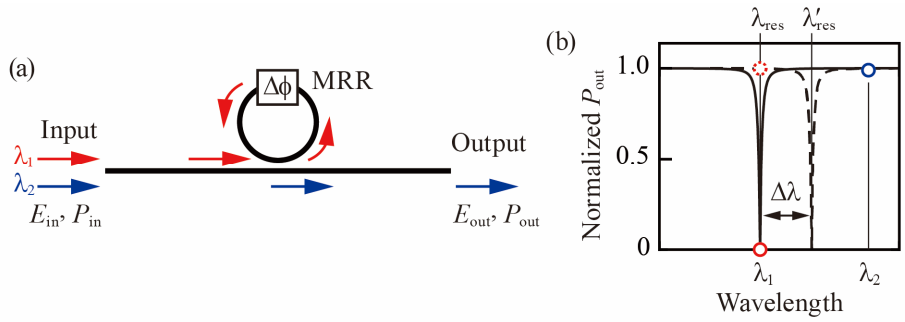

Figure 1.10 Operation principle of an MRM. (a) Scheme. (b) Transmission spectrum.

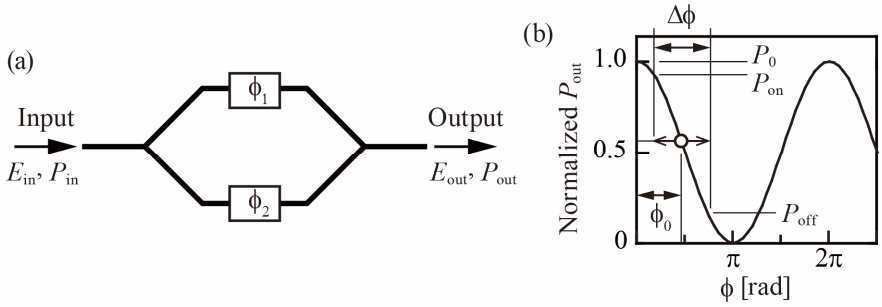

Figure 1.11 Operation principle of an MZM. (a) Scheme. (b) ϕ dependence of the transmission.

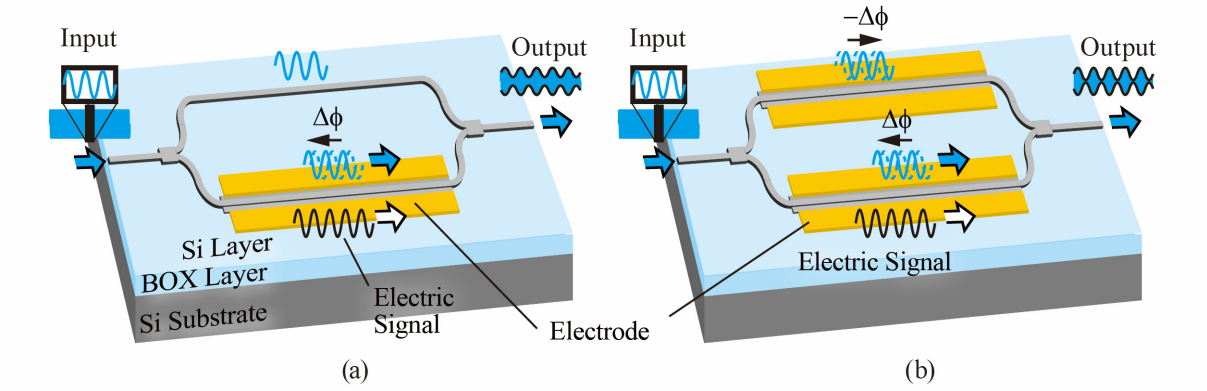

Figure 1.12 Driving schemes of an MZM. (a) Single-ended drive. (b) Push-pull drive.

on the peak-to-peak driving voltage V_{pp}. A high Q factor enhances the *ER* for the V_{pp} limited by a system requirement, resulting in low power consumption. However, the frequency response of the MRM is limited by the Q factor as well as the *RC* time constant of the phase shifter. Therefore, the *ER* and the f_{3dB} of the frequency response are in a tradeoff relationship. Some groups have reported high-speed MRMs beyond 50 Gbps [1-73], [1-75]–[1-79]. The radiuses *r* of the high-speed MRMs were set to be approximately 5 μm to have enough low Q factors for the beyond-50-Gbps operation. However, MRMs still strongly depend on the temperature fluctuation of the environment because of the effect of temperature on the resonance. Therefore, a resonance stabilization system is necessary to maintain stable operation. This requirement results in system complexity and high total energy consumption [1-77], [1-81], [1-82].

(c) Mach-Zehnder Modulator (MZM)

Figure 1.9(a) shows a configuration of an MZI modulator (MZM). The incident light is branched into two optical paths: path 1 (upside path) and path 2 (downside path). The phase of light in each path is shifted depending on the optical path length. Here, I define ϕ_1 and ϕ_2 as the phase shifts in the path 1 and path 2, respectively. The output electric field E_{out} and power P_{out} continuously change according to the phase difference $\phi = \phi_2 - \phi_1$.

$$E_{out} = E_{in}\frac{e^{i\phi_1} + e^{i\phi_2}}{2} = E_{in}\frac{1 + e^{i(\phi_2 - \phi_1)}}{2}e^{i\phi_1} = E_{in}\frac{1 + e^{i\phi}}{2}e^{i\phi_1} \tag{1.6}$$

$$P_{out} = P_{in}\frac{1 + \cos\phi}{2} \tag{1.7}$$

where E_{in} and P_{in} are the electric field and the power of the incident light, respectively. Figure 1.9(b) shows the normalized P_{out} versus ϕ. The normalized P_{out} becomes unity when ϕ is equal to $2m\pi$ (*m* is an integer), and it becomes 0 when ϕ is equal to $(2m - 1)\pi$. Therefore, one can switch between the "on state" and the "off state". The switching ability is evaluated by the *ER* and the modulation loss *ML* in this dissertation, which is expressed by:

$$ML = P_0 / P_{on} \tag{1.8}$$

When ϕ includes static initial phase difference ϕ_0 as well as dynamic phase shift $\Delta\phi$, *ER* and *ML* can be tuned by ϕ_0. This characteristic is applied by EO effects or the TO effect in actual devices. One of the

most important advantages of MZMs is stability to environmental temperature fluctuation. Even if the environmental temperature changes, the operating condition does not change because it depends on the temperature difference change between the two arms, in other words, the fluctuation of ϕ_0 rather than the absolute temperature change. This feature is beneficial for short-reach communication systems requiring system simplicity.

Figure 1.12(a) shows a single-ended driving scheme, which applies the RF signal to only one arm. In contrast, Figure 1.12(b) shows a push-pull driving scheme. When the MZM has two phase shifters that are driven by inversed-phase RF signals, Equation (1.6) is expressed as follows:

$$E_{\text{out}} = E_{\text{in}} \frac{e^{-i\Delta\phi} + e^{i(\Delta\phi+\phi_0)}}{2} \tag{1.9}$$

This balanced driving scheme eliminates wavelength chirping, which prevents long-reach transmission, while increasing the equivalent phase shift to $2\Delta\phi$.

The MZMs tend to be a large size of several millimeters to obtain enough $\Delta\phi$. This size is relatively large compared with the wavelength of the RF signal of several ten GHz. Therefore, the phase of the RF signal must be considered to obtain high $f_{3\text{dB}}$. Traveling-wave electrodes and distributed-element circuit design, which is described in Section 5. 3, is effective for such high-speed operation. The high-speed MZMs beyond 50 Gbps have been reported in this decade [1-22], [1-68], [1-69], [1-72]–[1-74], [1-83]–[1-85]. I will describe those papers in Section 1. 4. 4 in detail. However, a several-millimeter length L might prevent large-number integration in a small form factor module or mid-board integration in next-era optical interconnects. The area per lane of QSFP-DD (including a laser, a detector, and ICs), which is the smallest form factor in 400G lambda, is only 134 mm^2. An on-board transceiver should be even smaller. Therefore, the millimeter length is no longer adequate for the next-era optical interconnection systems. In addition, as the dynamic power consumption is proportional to L, a long L is intrinsically disadvantageous for the development of energy-efficient transceivers.

1. 3 Photonic Crystal Waveguide (PCW)

1. 3. 1 Overview

A photonic crystal (PhC) is a structure in which the refractive index is periodically modulated at the scale of the wavelength of light. Usually, it is composed of two dielectric materials: low-refractive-index and high-refractive-index materials. Figure 1.13(a) shows a two-dimensional (2D) Si PhCas an example of a PhC structure. In this structure, Si is the high-refractive-index part, and silica holes are the low-refractive index part. These parts are periodically placed and the unit cell is the triangular lattices highlighted by the yellow line. Figure 1.13(b) shows the photonic band of the PhC, which shows the relationship between the frequency f and the wavenumber k. The most remarkable difference from the usual dispersion relations is that the PhC prohibits the existence of light in a particular wavelength range, and this range is called the photonic bandgap (PBG). Therefore, the PhC behaves as an optical insulator, which is unavailable in normal materials. This characteristic allows localization of light in introduced defects. If a point defect is introduced, then the propagation to all directions is forbidden, i.e., it acts as a cavity. Furthermore, if a line defect is introduced, it allows light to propagate along the defect,as shown in Figure 1.14(a); this is called a PCW.

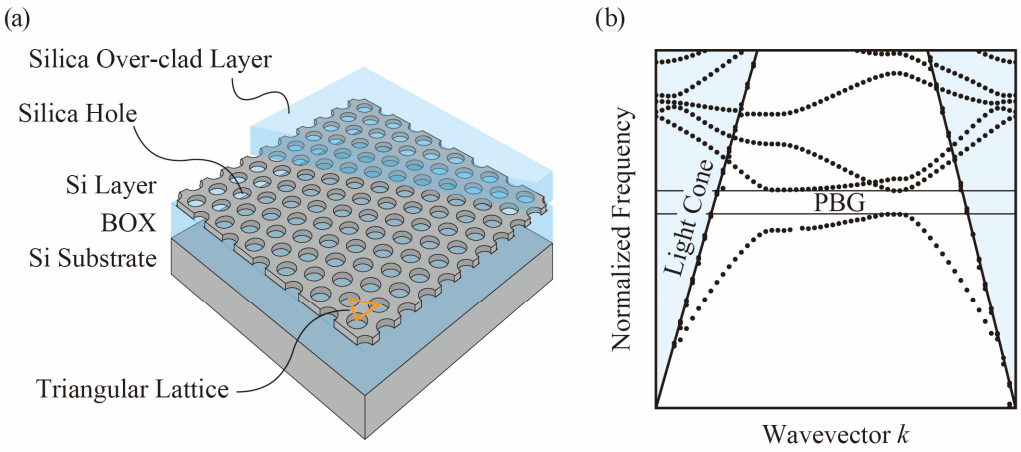

Figure 1.13 (a) Structure of the 2D Si PhC. (b) Photonic band of the Si PhC.

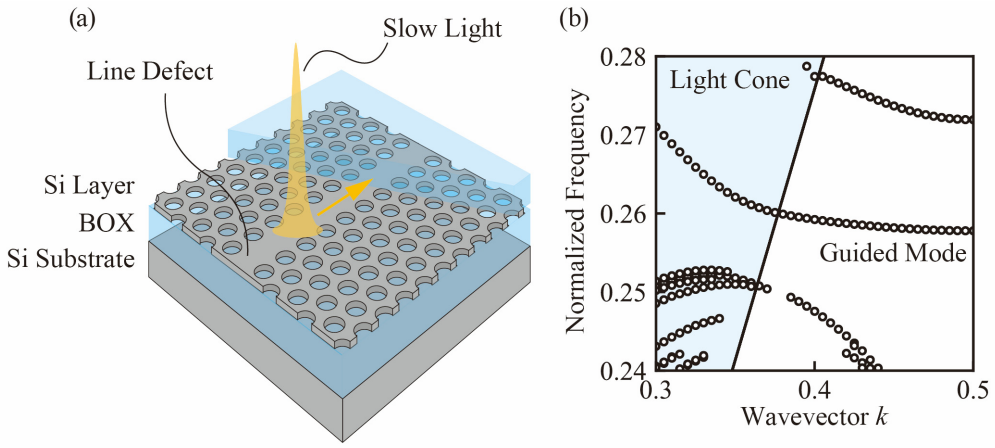

Figure 1.14 (a) Structure of the 2D Si PCW. (b) Photonic band of the Si PCW.

1. 3. 2 Slow Light in PCW

The PCW generates slow light, whose group velocity v_g is much smaller than that of normal waveguides, i.e., a pulse in the PCW propagates slowly compared with a pulse in normal media, resulting in the slow transport of the pulse energy. Figure 1.14(b) shows the photonic band of the PCW. A slow-light guided mode in the line defect appears between the bulk bands of the PhC, and it becomes flatter towards the photonic band edge, i.e., n_g becomes larger as the wavelength of the light is closer to the band edge.n_g is given as follow:

$$n_g = c\left(\frac{\partial \omega}{\partial k}\right)^{-1} \tag{1.10}$$

where $\omega = 2\pi f$ is the angular frequency. In the Si PCW, n_g is increased to a value typically larger than 20, which corresponds to 5-times that of a Si wire waveguide. The slow light enhances the light-matter interaction per propagation length; this characteristic is advantageous for size reduction of an optical device and thus contributes to the low power consumption.

Although the silica-cladded PCW shown in Figure 1.14(a) is mechanically durable, n_g varies depending on the wavelength, as described in Section 3. 2. 2. This variability is not desired for applications that

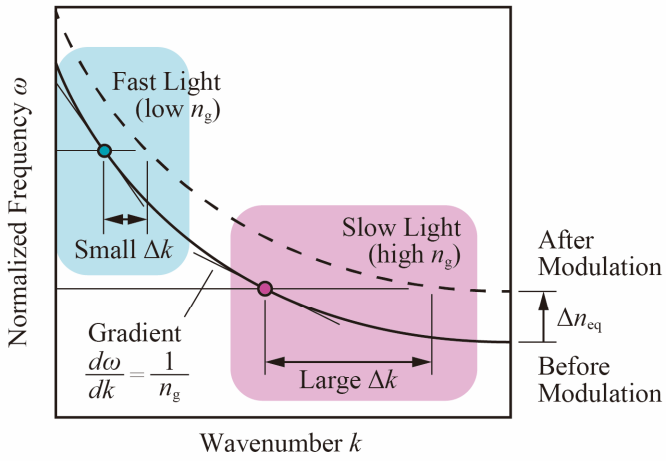

Figure 1.15 Principle of modulation enhancement by slow light.

require constant n_g in the wide wavelength range. However, this wavelength dependence of n_g can be flattened via structural tuning.

I used *x*th row lattice-shifted PCWs (LSPCWs), in which holes on a *x*th row are slightly shifted along the line defect, in this dissertation. The slow-light guided mode in this waveguide can have a flat band caused by the change in the photonic band. This flat band allows wide wavelength range operation. The photonic band varies according to not only the amount of the shift but also the shifted row. For example, a third-row shifted LSPCW exhibit n_g of ~20 within the wavelength range $\Delta\lambda$ of ~15 nm [1-86]. This feature allows the wide wavelength range operation of devices, including a slow light EO modulator.

1. 4 Slow Light Optical Modulators

1. 4. 1 Principle

The slow light effect is attractive for optical modulators because it enhances $\Delta\phi$, which corresponds to the modulation efficiency per length. $\Delta\phi$ in a phase shifter is proportional to n_g, as shown in following equation:

$$\Delta\phi = \Delta kL = k_0 n_g \frac{\Delta n_{eq}}{n_{eq}} \zeta L, \quad \zeta \equiv \frac{n_{eq}}{\omega_b} \frac{d\omega_b}{dn_{eq}} \tag{1.11}$$

where Δk is the wavenumber shift, k_0 is the wavenumber in vacuum, n_{eq} is the modal equivalent index, and Δn_{eq} is the change of n_{eq} by the modulation. Figure 1.15 provides an explanation of this equation. Δn_{eq} shifts the photonic band and thus changes wavenumber k. When n_g is low, the gradient of the photonic band $d\omega/dk = 1/n_g$ is also low, resulting in the small Δk. In contrast, Δk is large when n_g is high because of the small gradient of the photonic band. This results in a small device size, with the corresponding small footprint and low power consumption. However, the overlap between the guided mode and the index-changed region also affects $\Delta\phi$.

1. 4. 2 Variety of Slow Light Modulators

The slow light is used in combination with some types of the phase shifters, e.g., the CPD, TO effect,

and Pockels Effect types. In this section, I describe experimentally demonstrated slow light modulators based on two effects other than the CPD, which is described in Section 1. 4. 3.

A dispersion-engineered Si PCW MZM and a Si PCW directional coupler modulator using the TO effect have been reported [1-87], [1-88]. The slow light effect reduced the TO-effect-based phase shifter lengths in the Si PCW MZM and a Si PCW directional coupler modulator to 80 μm and 5 μm, respectively, in contrast to the typical several hundred microns. However, the modulation speed is limited to ~50 kHz because of slow thermal diffusion. Furthermore, theoretically fast EO-polymer-based PhC modulators have been reported [1-89]–[1-92]. A high in-device Pockels coefficient r_{33} of 1190 pm/V, which corresponds to a considerably small $V_\pi L$ of ~0.03 V·cm, was demonstrated in an EO-polymer-refilled Si PCW MZM [1-1-56]. However, only 100-kHz triangular shape modulation was performed as the dynamic operation in this device. In addition, achieving the fabrication approach that maximizes the material's advantage remains a challenge, although the Pockels coefficient is improved by the optimization of the polling process.

1. 4. 3 CPD Based Si PCW MZM

Several groups have reported CPD-based Si PCW MZMs [1-93]–[1-101] and the reduction of $V_\pi L$ due to the slow light effect. Y. Jiang et al experimentally demonstrated the first CPD-based Si PCW MZM [1-91]. 80-μm-length p-i-p junctions were used as the carrier-injection phase shifters. The value of V_π was extremely small, as low as 7.5 mV; however, the operation speed was only 300 kHz. The same group also reported capacitor-embedded Si PCW MZMs [1-94]. They used slotted Si PCWs as the carrier-accumulated phase shifters and demonstrated 0.18 V·cm at a bit rate of 1.6 Gbps. Moreover, the group reported p-i-n carrier-injection Si PCW MZM. $V_\pi L$ of ~0.005 V·cm at 2 GHz using this scheme [1-95]. In such a situation, our group reported 10-Gbps and 40-Gbps high-speed modulation using a Si LSPCW MZM shown in with 90-μm-length p-n incorporated phase shifters operating in the

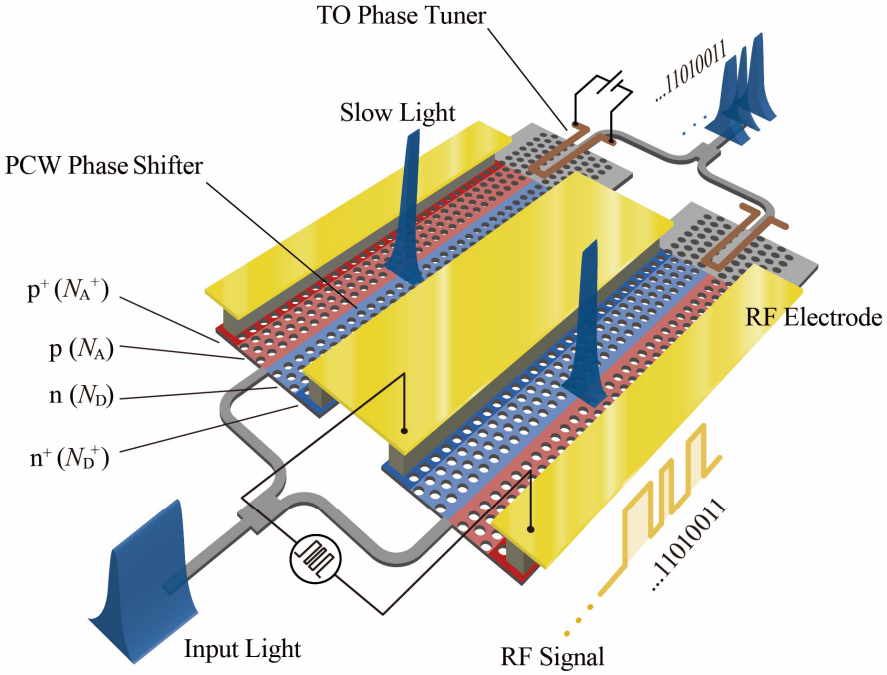

Figure 1.16 Schematic of the Si PCW/LSPCW MZM.

carrier-depletion mode in 2012 [1-96], [1-97]. Figure 1.16 shows one example of the schematic of the device. In this paper, the authors also reported the operation in the wide wavelength range $\Delta\lambda$ of 16.9 nm and athermal operation in the wide temperature range of 19°C–124°C utilizing a dispersion-engineered LSPCW. Furthermore, the optimization of periodical p-n incorporated modulators, including an interleaved p-n junction and wavy p-n junction, enabled 32 Gbps operation at low voltage of V_{pp} = 1.75 V and V_{DC} = −0.9 V [1-100] and quadrature PSK (QPSK) modulation at 64 Gbps was also reported [1-99].

1. 4. 4 Comparison and Remaining Problems

As mentioned in Section 1. 2. 4, MRMs and MZMs each have drawbacks and attractive characteristics. To solve these problems, some research groups have reported different material/ Si hybrid modulators, such as III-V/Si hybrid [1-102], Si organic hybrid (SOH) [1-103], [1-104], and LN/Si hybrid modulators [1-105]. These modulators have the features of a significant reduction of $V_\pi L$ and improvement of the operation speed because of the superior material properties. In fact, III-V/Si MOS modulators were demonstrated to obtain a small $V_\pi L$ of 0.1 V·cm [1-102], and are theoretically expected to achieve extremely small $V_\pi L$ of 0.047 V·cm [1-106]. The SOH modulator has been reported to demonstrate 100-Gbps OOK modulation without any pre-emphasis compensation [1-103]. However, such a modulator requires additional complicated fabrication processes and further confirmation of the reliability. The former causes difficulty for cost-effective production, and the latter requires additional development time before practical use of such modulators is possible. From these perspectives, the Si LSPCW MZM is a strong candidate for use in practice because it has well-balanced properties: (1) small $V_\pi L$, (2) relatively wide operating wavelength range corresponding to the wide temperature operation, (3) tunable balance between properties (1) and (2), and (4) fabrication by standard CMOS compatible process without additional process. Table 1.3 summarizes the specifications of 50-Gbps capable Si MZMs, cutting-edge hybrid modulators, and Si LSPCW MZMs. The Si LSPCW MZM reported in Ref. [1-100] exhibited $V_\pi L$ as small as 0.34 V·cm, and Si rib-waveguide MZMs exhibited $V_\pi L$ of 1.4–3.2 V·cm. Note that a group of Huazhong University of Science and Technology reported a 90-Gbps capable Si MZM with small $V_\pi L$ of 1.4 V·cm; however, it required the removal of the substrate to realize the accurate traveling wave electrode design [1-74]. The Si LSPCW has been reported to achieve a much smaller $V_\pi L$ than the cutting-edge Si MZMs, although the high-quality operation bit rate was limited to 32 Gbps. If this moderate operation speed is improved, the compactness, high-speed operation, stability to thermal fluctuation, and easy fabrication can be simultaneously achieved in a Si LSPCW MZM.

1. 5 **Objective of this Study**

The main goal of this work is to develop a Si LSPCW MZM with well-balanced performance. However, because only a few research groups have studied such devices, the number of demonstrations is very limited. Therefore, the characteristics, including modulation enhancement and broad-wavelength operation, must first be evaluated in detail. Next, I investigate the frequency response of the Si LSPCW MZM that allows for the improvement of f_{3dB} and demonstrate high-speed operation. Furthermore, I demonstrate frequency-swept modulation for FMCW LiDAR using the Si LSPCW MZM that provides extended application range.

1. 5. 1 Observation of Modulation Efficiency Enhancement

To date, the modulation efficiency enhancement via the slow light effect has only been qualitatively evaluated as the short $V_\pi L$ compared with Si MZMs. In contrast, a quantitative relationship between n_g and $\Delta\phi$ has not been evaluated in experiments, although it can be expected to agree with Equation (1.11). I perform modulation experiments for different n_gs to confirm the relationship and show the advantage of using slow light for Si MZMs. Through these investigations, I show the effectiveness of the use of slow light to develop compact modulators.

1. 5. 2 Wide Wavelength Range Operation

I show the wide wavelength range operation and characterize it in the more general evaluation indices, such as the *ER*, bit error rate (*BER*), and frequency response. Although the ideal operation wavelength range is over the entire C band, it has been confirmed that $\Delta\lambda$ of ~16.9 nm corresponds to 19°C–124°C [1-95]. This range is considered to be sufficient for stable operation without any temperature control in a data center. Therefore, I design and fabricate a Si LSPCW MZM of similar design and investigate the behaviors in oscillating transmission and n_g spectra of the Si LSPCW MZM in more detail.

1. 5. 3 Investigation of Limiting Factor of Frequency Response and its Improvement

The improvement of the frequency response of the Si LSPCW is necessary for high-speed operation beyond 50-Gbps, which is required in 400G Ethernet. However, the effect of slow light to the frequency response has not been investigated to date. Here, I show the importance of EO phase matching (velocity matching in other wards) in Si PCW MZMs using the slow-light effect. This slow-light effect can occur in an EO system in which light and RF signal are copropagating, such as traveling-wave modulators. This configuration is particularly important in modulators using slow light because of its very small v_g. I propose novel driving RF electrodes that reduce the large EO phase mismatch in a Si LSPCW MZM for beyond 50-Gbps capable Si LSPCW MZM. Figure 1.17 shows the bench marking from the perspective of $V_\pi L$ and the operation baud rate. The upper left region corresponds to the high-performance region. The Si MZMs are placed at $V_\pi L$ of 1.39–3.2 V·cm and operated at the baud rate of 50–70 Gbaud. In contrast, the Si LSPCW MZM shows a baud rate of 32 Gbaud with $V_\pi L$ of 0.2 V·cm. In other words, there are no reports in the range where $V_\pi L$ is less than 1.4 V·cm and the baud rate is higher than 50 Gbaud. This range is the target of this study. In order to realize the high system bit rate, I consider the use of PAM4 modulation and WDM transmission.

1. 5. 4 Application to FMCW LiDAR Transmitter

To expand the application field of the Si PCW MZM, I consider using it in a transmitter of a FMCW LiDAR. The high productivity of Si photonics is particularly advantageous for applications demanding low-cost mass production, such as ADAS. First, I must confirm the linewidth δf of the modulated spectra, which determines the coherence length L_c. For example, δf of 1 MHz is necessary to ensure the 150-m distant ranging (300 m in round trip) required for the ADAS application. Considering that the

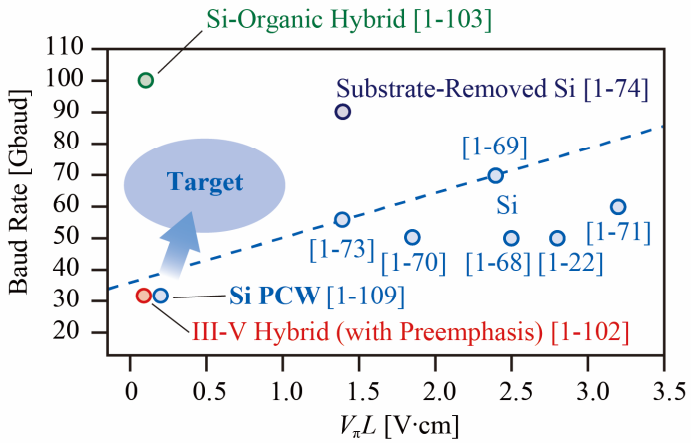

Figure 1.17 Benchmarking of reported MZMs on SOI.

Table 1.3 Comparison of reported MZMs fabricated on SOI.

Ref.	Group	Year	Material	Structure	L [mm]	f_{3dB} [GHz]	Baud Rate [Gbaud]	V_{pp} [V]	V_{DC} [V]	ER [dB]	On-chip IL (under Operation) [dB]	$V_\pi L$ [V·cm]	E_{bit} [pJ/bit]
[1-22]	Univ. Surrey	2012	Si	Rib MZM	1	>40 @–4V	50	6.5	–6	2.22	4.2 (7.4)	2.8 @–4 V	4.2
[1-68]	A*STAR	2013	Si	Rib MZM	3	30 @0 V	50	1.5	0	3.4	5.5 (7.1)	~2.5 @0 V	0.45
[1-70]	A*STAR	2014	Si	Rib MZM	3	37 @–5 V	50.5	3.5	–5	7.08	~9 (NA)	1.85 @–6 V	NA
[1-69]	CAS	2014	Si	Rib MZM	0.75	55 @–3 V	70	5.3	–1.5	6.1	3.3 (NA)	2.4 @–3 V	NA
[1-71]	McGill Univ.	2015	Si	Rib MZM	4.25	41 @–4 V	60	4.8	–4	3.8	3.8 (NA)	3.2 @–4 V	NA
[1-73]	IMEC	2017	Si	Rib MZM	1.5	27 @–1 V	56	2.5	–0.75	2.3	2.2 (NA)	1.39 @ NA	0.75
[1-74]	HUST	2018	Substrate-Removed Si	Rib MZM	2	>60 @-8 V	90	5	–6	3.3	5.4 (NA)	1.4 @–4 V	NA
[1-103]	KIT	2018	SOH	MZM	1.1	25	100	1.4	NA	NA	~11 (NA)	0.1 @–2 V	0.098
[1-102]	NTT	2017	III-V/Si Hybrid	MOS MZM	0.25	2.2	32	0.9	0.9	3.1	~1 (NA)	0.09	NA
[1-97]	YNU	2012	Si	LSPCW MZM	0.09	NA	40	5.3	–0.5	NA	6.2 (NA)	NA	NA
[1-109]	YNU	2017	Si	LSPCW MZM	0.2	22 (Calc.)	32	1.75	–0.9	3	>2 (>3)	0.2 @0 V	0.17

margin must be provided, δf of less than 100 kHz is desired. The next step is the demonstration of the frequency-swept modulation and the ranging action using the device. I attempt these demonstrations using an arbitrary waveform generator and a fiber optic system.

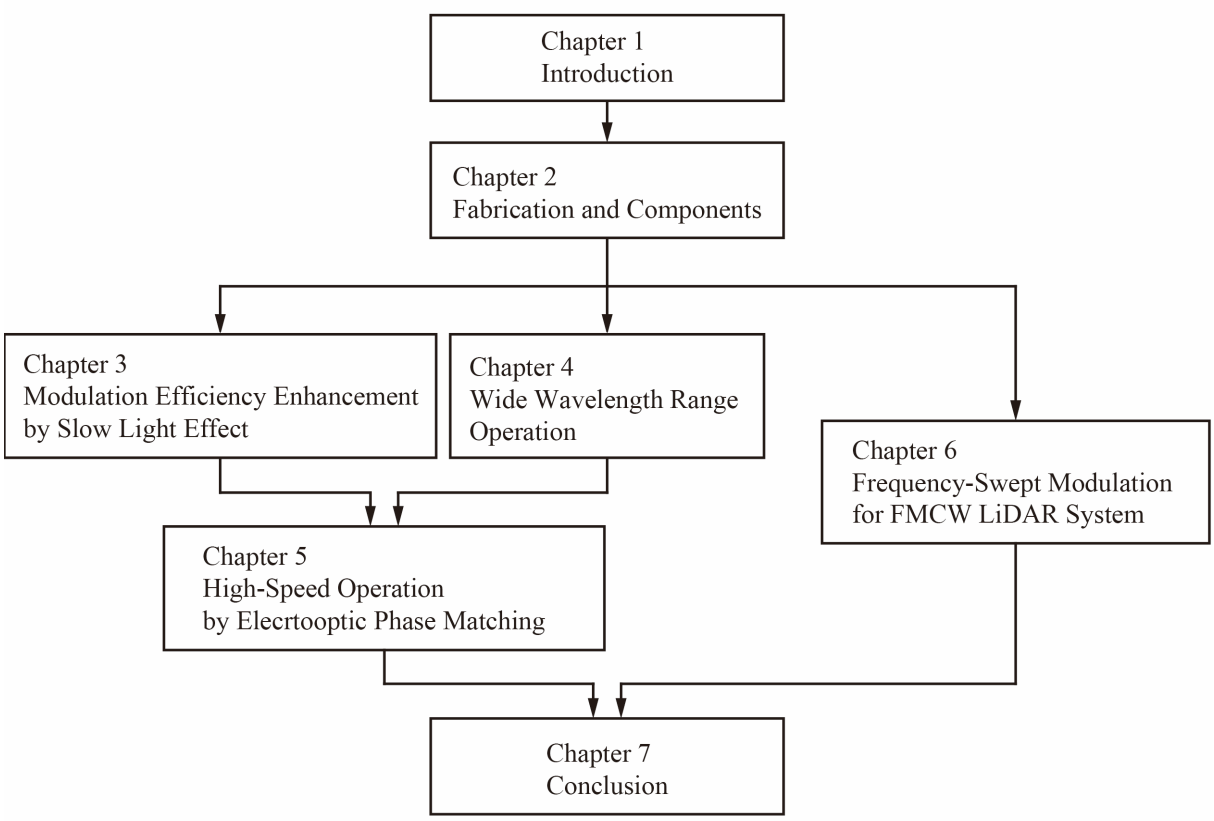

Figure 1.18 Flowchart of this dissertation.

1. 6 Outline of this Dissertation

Figure 1.18 shows the flowchart of this dissertation. This dissertation consists of seven chapters, including this introduction. In Chapter2, I describe the fabrication methods and fundamental structures of the relevant devices. Furthermore, I explain the fundamental components used in Si photonics chips. I present an investigation of the modulation efficiency enhancement by slow light in Chapter3, and I present an investigation of the wide wavelength range operation in a low-dispersion slow light band in Chapter4 to highlight the advantages of LSPCWs. Next, I present an investigation of the limiting factor of the frequency response and a method to address it in Chapter5. In Chapter6, I demonstrate frequency-swept modulation for FMCW LiDARs and its primitive ranging action in a fiber optic system. Finally, I conclude this study in Chapter7.

References

[1-1] B. Jalali and S. Fathpour, “Silicon photonics,” *J. Light. Technol.*, vol. 24, no. 12, pp. 4600–4615, Dec. 2006, doi: 10.1109/JLT.2006.885782.

[1-2] R. Soref, “The past, present, and future of silicon photonics,” *IEEE Journal of Selected Topics in Quantum Electronics*, vol. 12, no. 6, 2. IEEE-INST ELECTRICAL ELECTRONICS ENGINEERS INC, 445 HOES LANE, PISCATAWAY, NJ 08855-4141 USA, pp. 1678–1687, Dec. 2006, doi: 10.1109/JSTQE.2006.883151.

[1-3] D. Thomson *et al.*, “Roadmap on silicon photonics,” *J. Opt.*, vol. 18, no. 7, p. 073003, Jul. 2016, doi: 10.1088/2040-8978/18/7/073003.

[1-4] R. A. Soref and J. P. Lorenzo, “Single-crystal silicon: a new material for 1.3 and 1.6 μm integrated-optical components,” *Electron. Lett.*, vol. 21, no. 21, pp. 953–954, Oct. 1985, doi: 10.1049/el:19850673.

[1-5] D. Miller, “Device Requirements for Optical Interconnects to Silicon Chips,” *Proc. IEEE*, vol. 97, no. 7, pp. 1166–1185, Jul. 2009, doi: 10.1109/JPROC.2009.2014298.

[1-6] A. Benner, M. Ignatowski, J. Kash, D. Kuchta, and M. Ritter, “Exploitation of optical interconnects in future server architectures,” *IBM J. Res. Dev.*, vol. 49, no. 4–5, pp. 755–775, Sep. 2005, doi: 10.1147/rd.494.0755.

[1-7] D. Miller, “Rationale and challenges for optical interconnects to electronic chips,” *Proc. IEEE*, vol. 88, no. 6, pp. 728–749, Jun. 2000, doi: 10.1109/5.867687.

[1-8] K. Lee, D. Lim, L. Kimerling, J. Shin, and F. Cerrina, “Fabrication of ultralow-loss Si/SiO2 waveguides by roughness reduction,” *Optics Letters*, vol. 26, no. 23. OPTICAL SOC AMER, 2010 MASSACHUSETTS AVE NW, WASHINGTON, DC 20036 USA, pp. 1888–1890, Dec. 2001, doi: 10.1364/OL.26.001888.

[1-9] T. Lipka, O. Horn, J. Amthor, and J. Mueller, “Low-loss multilayer compatible a-Si:H optical thin films for photonic applications,” *Journal of The European Optical Society-Rapid Publications*, vol. 7. SPRINGEROPEN, CAMPUS, 4 CRINAN ST, LONDON, N1 9XW, ENGLAND, 2012, doi: 10.2971/jeos.2012.12033.

[1-10] R. A. Soref, S. J. Emelett, and A. R. Buchwald, “Silicon waveguided components for the long-wave infrared region,” *Journal of Optics A-Pure and Applied Optics*, vol. 8, no. 10. IOP PUBLISHING LTD, TEMPLE CIRCUS, TEMPLE WAY, BRISTOL BS1 6BE, ENGLAND, pp. 840–848, Oct. 2006, doi: 10.1088/1464-4258/8/10/004.

[1-11] D. Dai and S. He, “Design of an ultrashort Si-nanowaveguide-based multimode interference coupler of arbitrary shape,” *Applied Optics*, vol. 47, no. 1. OPTICAL SOC AMER, 2010 MASSACHUSETTS AVE NW, WASHINGTON, DC 20036 USA, pp. 38–44, Jan. 2008, doi: 10.1364/AO.47.000038.

[1-12] Q. Lai, M. Bachmann, and H. Melchior, “Low-loss 1xN multimode interference couplers with homogeneous output power distributions realised in silica on Si material,” *Electronics Letters*, vol. 33, no. 20. IEE-INST ELEC ENG, MICHAEL FARADAY HOUSE SIX HILLS WAY STEVENAGE, HERTFORD SG1 2AY, ENGLAND, pp. 1699–1700, Sep. 1997, doi: 10.1049/el:19971142.

[1-13] J. David Domenech, J. S. Fandino, B. Gargallo, and P. Munoz, “Arbitrary Coupling Ratio Multimode Interference Couplers in Silicon-on-Insulator,” *Journal of Lightwave Technology*, vol. 32, no. 14. IEEE-INST ELECTRICAL ELECTRONICS ENGINEERS INC, 445 HOES LANE, PISCATAWAY, NJ 08855-4141 USA, Jul. 2014, doi: 10.1109/JLT.2014.2329994.

[1-14] A. Hosseini, D. Kwong, C.-Y. Lin, B. S. Lee, and R. T. Chen, “Output Formulation for Symmetrically Excited One-to-N Multimode Interference Coupler,” *IEEE Journal of Selected Topics in Quantum Electronics*, vol. 16, no. 1. IEEE-INST ELECTRICAL ELECTRONICS ENGINEERS INC, 445 HOES LANE, PISCATAWAY, NJ 08855-4141 USA, pp. 61–69, Feb. 2010, doi: 10.1109/JSTQE.2009.2032669.

[1-15] B. Little *et al.*, “Ultra-compact Si-SiO2 microring resonator optical channel dropping filters,” *IEEE Photonics Technol. Lett.*, vol. 10, no. 4, pp. 549–551, Apr. 1998, doi: 10.1109/68.662590.

[1-16] M. Greenberg and M. Orenstein, “Multimode Add-Drop multiplexing by adiabatic linearly tapered coupling,” *Opt. Express*, vol. 13, no. 23, pp. 9381–9387, Nov. 2005, doi: 10.1364/OPEX.13.009381.

[1-17] T. Fukazawa, F. Ohno, and T. Baba, “Very compact arrayed-waveguide-grating demultiplexer using Si photonic wire waveguides,” *Jpn. J. Appl. Phys. Part 2-Lett. Express Lett.*, vol. 43, no. 5B, pp. L673–L675, May 2004, doi: 10.1143/JJAP.43.L673.

[1-18] K. Sasaki, F. Ohno, A. Motegi, and T. Baba, “Arrayed waveguide grating of 70x60 mu m(2) size based on Si photonic wire waveguides,” *Electron. Lett.*, vol. 41, no. 14, pp. 801–802, Jul.

2005, doi: 10.1049/el:20051541.

[1-19] D. Ahn *et al.*, "High performance, waveguide integrated Ge photodetectors," *Optics Express*, vol. 15, no. 7. OPTICAL SOC AMER, 2010 MASSACHUSETTS AVE NW, WASHINGTON, DC 20036 USA, pp. 3916–3921, Apr. 2007, doi: 10.1364/OE.15.003916.

[1-20] L. Vivien *et al.*, "High speed and high responsivity germanium photodetector integrated in a Silicon-on-insulator microwaveguide," *Opt. Express*, vol. 15, no. 15, pp. 9843–9848, Jul. 2007, doi: 10.1364/OE.15.009843.

[1-21] T. Yin *et al.*, "31GHz Ge n-i-p waveguide photodetectors on Silicon-on-Insulator substrate," *Optics Express*, vol. 15, no. 21. OPTICAL SOC AMER, 2010 MASSACHUSETTS AVE NW, WASHINGTON, DC 20036 USA, pp. 13965–13971, Oct. 2007, doi: 10.1364/OE.15.013965.

[1-22] D. J. Thomson *et al.*, "50-Gb/s Silicon Optical Modulator," *IEEE Photonics Technol. Lett.*, vol. 24, no. 4, pp. 234–236, Feb. 2012, doi: 10.1109/LPT.2011.2177081.

[1-23] H. Xu *et al.*, "High speed silicon Mach-Zehnder modulator based on interleaved PN junctions," *Opt. Express*, vol. 20, no. 14, p. 15093, Jul. 2012, doi: 10.1364/OE.20.015093.

[1-24] Q. Xu, B. Schmidt, S. Pradhan, and M. Lipson, "Micrometre-scale silicon electro-optic modulator," *Nature*, vol. 435, no. 7040, pp. 325–327, May 2005, doi: 10.1038/nature03569.

[1-25] F. Y. Gardes *et al.*, "High-speed modulation of a compact silicon ring resonator based on a reverse-biased pn diode," *Opt. Express*, vol. 17, no. 24, p. 21986, Nov. 2009, doi: 10.1364/OE.17.021986.

[1-26] A. W. Snyder and J. Love, *Optical waveguide theory*. Springer Science & Business Media, 2012.

[1-27] A. Sakai, G. Hara, and T. Baba, "Propagation Characteristics of Ultrahigh-Δ Optical Waveguide on Silicon-on-Insulator Substrate," vol. 40, no. 4, p. 3, 2001.

[1-28] A. Himeno, K. Kato, and T. Miya, "Silica-based planar lightwave circuits," *IEEE J. Sel. Top. Quantum Electron.*, vol. 4, no. 6, pp. 913–924, Dec. 1998, doi: 10.1109/2944.736076.

[1-29] K. Kant, "Data center evolution," *Comput. Netw.*, vol. 53, no. 17, pp. 2939–2965, Dec. 2009, doi: 10.1016/j.comnet.2009.10.004.

[1-30] "Cisco Annual Internet Report," *Cisco Annual Internet Report - Cisco*. https://www.cisco.com/c/en/us/solutions/executive-perspectives/annual-internet-report/index.html#cloud-forecast (accessed Apr. 20, 2020).

[1-31] "Understanding Different Types of Data Center," *AFL Hyperscale*. https://www.aflhyperscale.com/understanding-different-types-of-data-center (accessed Aug. 05, 2020).

[1-32] "IEEE Standard for Information technology– Local and metropolitan area networks– Specific requirements– Part 3: CSMA/CD Access Method and Physical Layer Specifications Amendment 4: Media Access Control Parameters, Physical Layers, and Management Parameters for 40 Gb/s and 100 Gb/s Operation," *IEEE Std 8023ba-2010 Amend. IEEE Stand. 8023-2008*, pp. 1–457, Jun. 2010, doi: 10.1109/IEEESTD.2010.5501740.

[1-33] "IEEE Standard for Ethernet - Amendment 3: Physical Layer Specifications and Management Parameters for 40 Gb/s and 100 Gb/s Operation over Fiber Optic Cables," *IEEE Stand. Ethernet Amend. 3 Phys. Layer Specif. Manag. Parameters 40 Gbs 100 Gbs Oper. Fiber Opt. Cables*, pp. 1–172, 2015.

[1-34] "IEEE Standard for Ethernet - Amendment 10: Media Access Control Parameters, Physical Layers, and Management Parameters for 200 Gb/s and 400 Gb/s Operation," *IEEE Std 8023bs-2017 Amend. IEEE 8023-2015 Amend. IEEEs 8023bw-2015 8023by-2016 8023bq-2016 8023bp-2016 8023br-2016 8023bn-2016 8023bz-2016 8023bu-2016 8023bv-2017 IEEE 8023-2015Cor1-2017*, pp. 1–372, Dec. 2017, doi: 10.1109/IEEESTD.2017.8207825.

[1-35] "100G Lambda MSA." https://100glambda.com/ (accessed Apr. 20, 2020).

[1-36] Q. Cheng, M. Bahadori, M. Glick, S. Rumley, and K. Bergman, "Recent advances in optical technologies for data centers: a review," *Optica*, vol. 5, no. 11, p. 1354, Nov. 2018, doi: 10.1364/OPTICA.5.001354.

[1-37] X. Ma, Z. Zhang, and S. Su, "Cost-Aware Multi-Domain Virtual Data Center Embedding," *CHINA Commun.*, vol. 15, no. 12, pp. 190–207, Dec. 2018.

[1-38] F. Aflatouni, B. Abiri, A. Rekhi, and A. Hajimiri, "Nanophotonic coherent imager," *Opt. Express*, vol. 23, no. 4, p. 5117, Feb. 2015, doi: 10.1364/OE.23.005117.

[1-39] C. V. Poulton *et al.*, "Coherent solid-state LIDAR with silicon photonic optical phased arrays," *Opt. Lett.*, vol. 42, no. 20, p. 4091, Oct. 2017, doi: 10.1364/OL.42.004091.

[1-40] J. Dieckroger, R. Marz, P. C. Clemens, G. Heise, and H. W. Schneider, "Thermooptically Tunable Optical Phased Array in SiO –Si," *IEEE Photonics Technol. Lett.*, vol. 11, no. 2, p. 3, 1999.

[1-41] C. T. DeRose *et al.*, "Electronically controlled optical beam-steering by an active phased array of metallic nanoantennas," *Opt. Express*, vol. 21, no. 4, p. 5198, Feb. 2013, doi: 10.1364/OE.21.005198.

[1-42] Jie Sun *et al.*, "Large-Scale Silicon Photonic Circuits for Optical Phased Arrays," *IEEE J. Sel. Top. Quantum Electron.*, vol. 20, no. 4, pp. 264–278, Jul. 2014, doi: 10.1109/JSTQE.2013.2293316.

[1-43] K. Wang *et al.*, "Si Integrated Optical Phased Array for Efficient Beam Steering in Optical Wireless Communications," in *2014 GLOBECOM WORKSHOPS (GC WKSHPS)*, 2014, pp. 541–546.

[1-44] K. Kikuchi, "Digital coherent optical communication systems: fundamentals and future prospects," *IEICE Electron. Express*, vol. 8, no. 20, pp. 1642–1662, 2011, doi: 10.1587/elex.8.1642.

[1-45] R. Safaisini, E. Haglund, A. Larsson, J. S. Gustavsson, E. P. Haglund, and P. Westbergh, "High-speed 850 nm VCSELs operating error free up to 57 Gbit/s," *Electron. Lett.*, vol. 49, no. 16, pp. 1021–1023, Aug. 2013, doi: 10.1049/el.2013.2042.

[1-46] D. M. Kuchta *et al.*, "A 71-Gb/s NRZ Modulated 850-nm VCSEL-Based Optical Link," *IEEE Photonics Technol. Lett.*, vol. 27, no. 6, pp. 577–580, Mar. 2015, doi: 10.1109/LPT.2014.2385671.

[1-47] "ISO/IEC 11801-1:2017(en), Information technology — Generic cabling for customer premises — Part 1: General requirements." https://www.iso.org/obp/ui/#iso:std:iso-iec:11801:-1:ed-1:v1:en (accessed Apr. 21, 2020).

[1-48] Y. Sun *et al.*, "Advanced multimode fiber for high-speed short-read interconnect," Hangzhou, China, Nov. 2008, p. 71341L, doi: 10.1117/12.803721.

[1-49] S. Paul *et al.*, "10-Gb/s Direct Modulation of Widely Tunable 1550-nm MEMS VCSEL," *IEEE J. Sel. Top. Quantum Electron.*, vol. 21, no. 6, pp. 436–443, Nov. 2015, doi: 10.1109/JSTQE.2015.2418218.

[1-50] W. Kobayashi *et al.*, "50-Gb/s Direct Modulation of a 1.3-μm InGaAlAs-Based DFB Laser With a Ridge Waveguide Structure," *IEEE J. Sel. Top. Quantum Electron.*, vol. 19, no. 4, pp. 1500908–1500908, Jul. 2013, doi: 10.1109/JSTQE.2013.2238509.

[1-51] K. Nakahara *et al.*, "Direct Modulation at 56 and 50 Gb/s of 1.3- $¥mu $ m InGaAlAs Ridge-Shaped-BH DFB Lasers," *IEEE Photonics Technol. Lett.*, vol. 27, no. 5, pp. 534–536, Mar. 2015, doi: 10.1109/LPT.2014.2384520.

[1-52] A. Abbasi *et al.*, "43 Gb/s NRZ-OOK Direct Modulation of a Heterogeneously Integrated InP/Si DFB Laser," *J. Light. Technol.*, vol. 35, no. 6, pp. 1235–1240, Mar. 2017, doi: 10.1109/JLT.2016.2638619.

[1-53] S. Kanazawa *et al.*, "214-Gb/s 4-PAM Operation of Flip-Chip Interconnection EADFB Laser

Module," *J. Light. Technol.*, vol. 35, no. 3, pp. 418–422, Feb. 2017, doi: 10.1109/JLT.2016.2632164.

[1-54] J. C. Cartledge and G. S. Burley, "The effect of laser chirping on lightwave system performance," *J. Light. Technol.*, vol. 7, no. 3, pp. 568–573, Mar. 1989, doi: 10.1109/50.16895.

[1-55] H. Masuda *et al.*, "13.5-Tb/s (135 × 111-Gb/s/ch) No-Guard-Interval Coherent OFDM Transmission over 6,248 km using SNR Maximized Second-order DRA in the Extended L-band," in *Optical Fiber Communication Conference and National Fiber Optic Engineers Conference*, 2009, p. PDPB5, doi: 10.1364/NFOEC.2009.PDPB5.

[1-56] Y. Miyamoto, "Digital modulation challenges for high-capacity Optical Transport Network with 100Gbps channels and beyond," p. 4, 2009.

[1-57] X. Zhou *et al.*, "32Tb/s (320×114Gb/s) PDM-RZ-8QAM transmission over 580km of SMF-28 ultra-low-loss fiber," in *Optical Fiber Communication Conference and National Fiber Optic Engineers Conference*, 2009, p. PDPB4, doi: 10.1364/OFC.2009.PDPB4.

[1-58] M. Izutsu, Y. Yamane, and T. Sueta, "Broad-band traveling-wave modulator using a LiNbO3 optical waveguide," *IEEE J. Quantum Electron.*, vol. 13, no. 4, pp. 287–290, Apr. 1977, doi: 10.1109/JQE.1977.1069310.

[1-59] K. Kawano, T. Kitoh, O. Mitomi, T. Nozawa, and H. Jumonji, "A wide-band and low-driving-power phase modulator employing a Ti:LiNbO/sub 3/ optical waveguide at 1.5 mu m," *IEEE Photonics Technol. Lett.*, vol. 1, no. 2, pp. 33–34, Feb. 1989, doi: 10.1109/68.91000.

[1-60] M. Howerton, R. Moeller, A. Greenblatt, and R. Krahenbuhl, "Fully packaged, broad-band LiNbO3 modulator with low drive voltage," *IEEE Photonics Technol. Lett.*, vol. 12, no. 7, pp. 792–794, Jul. 2000, doi: 10.1109/68.853502.

[1-61] K. Higuma, S. Oikawa, Y. Hashimoto, H. Nagata, and M. Izutsu, "X-cut lithium niobate optical single-sideband modulator," *Electron. Lett.*, vol. 37, no. 8, pp. 515–516, Apr. 2001, doi: 10.1049/el:20010342.

[1-62] M. Nedeljkovic, R. Soref, and G. Z. Mashanovich, "Free-Carrier Electrorefraction and Electroabsorption Modulation Predictions for Silicon Over the 1–14-$¥mu¥hbox{m}$ Infrared Wavelength Range," *IEEE Photonics J.*, vol. 3, no. 6, pp. 1171–1180, Dec. 2011, doi: 10.1109/JPHOT.2011.2171930.

[1-63] G. Zhou *et al.*, "Effect of carrier lifetime on forward-biased silicon Mach-Zehnder modulators," *Opt. Express*, vol. 16, no. 8, p. 5218, Apr. 2008, doi: 10.1364/OE.16.005218.

[1-64] W. M. Green, M. J. Rooks, L. Sekaric, and Y. A. Vlasov, "Ultra-compact, low RF power, 10 Gb/s silicon Mach-Zehnder modulator," *Opt. Express*, vol. 15, no. 25, p. 17106, 2007, doi: 10.1364/OE.15.017106.

[1-65] Q. Xu, S. Manipatruni, B. Schmidt, J. Shakya, and M. Lipson, "12.5 Gbit/s carrier-injection-based silicon micro-ring silicon modulators," *Opt. Express*, vol. 15, no. 2, p. 430, Jan. 2007, doi: 10.1364/OE.15.000430.

[1-66] Z.-Y. Li *et al.*, "Silicon waveguide modulator based on carrier depletion in periodically interleaved PN junctions," *Opt. Express*, vol. 17, no. 18, p. 15947, Aug. 2009, doi: 10.1364/OE.17.015947.

[1-67] X. Xiao *et al.*, "25 Gbit/s silicon microring modulator based on misalignment-tolerant interleaved PN junctions," *Opt. Express*, vol. 20, no. 3, p. 2507, Jan. 2012, doi: 10.1364/OE.20.002507.

[1-68] M. Streshinsky *et al.*, "Low power 50 Gb/s silicon traveling wave Mach-Zehnder modulator near 1300 nm," *Opt. Express*, vol. 21, no. 25, pp. 30350–30357, Dec. 2013, doi: 10.1364/OE.21.030350.

[1-69] H. Xu *et al.*, "High-speed silicon modulator with band equalization," *Opt. Lett.*, vol. 39, no. 16, pp. 4839–4842, Aug. 2014, doi: 10.1364/OL.39.004839.

[1-70] Y. Yang, Q. Fang, M. Yu, X. Tu, R. Rusli, and G.-Q. Lo, "High-efficiency Si optical modulator using Cu travelling-wave electrode," *Opt. Express*, vol. 22, no. 24, p. 29978, Dec. 2014, doi: 10.1364/OE.22.029978.

[1-71] D. Patel *et al.*, "Design, analysis, and transmission system performance of a 41 GHz silicon photonic modulator," *Opt. Express*, vol. 23, no. 11, p. 14263, Jun. 2015, doi: 10.1364/OE.23.014263.

[1-72] C. Xiong, D. M. Gill, J. E. Proesel, J. S. Orcutt, W. Haensch, and W. M. Green, "Monolithic 56 Gb/s silicon photonic pulse-amplitude modulation transmitter," *Optica*, vol. 3, no. 10, pp. 1060–1065, 2016.

[1-73] M. Pantouvaki *et al.*, "Active Components for 50 Gb/s NRZ-OOK Optical Interconnects in a Silicon Photonics Platform," *J. Light. Technol.*, vol. 35, no. 4, pp. 631–638, Feb. 2017, doi: 10.1109/JLT.2016.2604839.

[1-74] M. Li, L. Wang, X. Li, X. Xiao, and S. Yu, "Silicon intensity Mach–Zehnder modulator for single lane 100 Gb/s applications," *Photonics Res.*, vol. 6, no. 2, p. 109, Feb. 2018, doi: 10.1364/PRJ.6.000109.

[1-75] X. Wu, C. Huang, K. Xu, C. Shu, and H. K. Tsang, "128-Gb/s Line Rate OFDM Signal Modulation Using an Integrated Silicon Microring Modulator," *IEEE Photonics Technol. Lett.*, vol. 28, no. 19, pp. 2058–2061, Oct. 2016, doi: 10.1109/LPT.2016.2575042.

[1-76] H. Ramon *et al.*, "Low-Power 56Gb/s NRZ Microring Modulator Driver in 28nm FDSOI CMOS," *IEEE Photonics Technol. Lett.*, vol. 30, no. 5, pp. 467–470, Mar. 2018, doi: 10.1109/LPT.2018.2799004.

[1-77] J. Sun, R. Kumar, M. Sakib, J. Driscoll, H. Jayatilleka, and H. Rong, "A 128 Gb/s PAM4 Silicon Microring Modulator with Integrated Thermo-optic Resonance Tuning," *J. Light. Technol.*, 2018.

[1-78] M. Moralis-Pegios *et al.*, "52 km-Long Transmission Link Using a 50 Gb/s *O* -Band Silicon Microring Modulator Co-Packaged With a 1V-CMOS Driver," *IEEE Photonics J.*, vol. 11, no. 4, pp. 1–7, Aug. 2019, doi: 10.1109/JPHOT.2019.2921730.

[1-79] H. Li *et al.*, "A 112 Gb/s PAM4 Silicon Photonics Transmitter With Microring Modulator and CMOS Driver," *J. Light. Technol.*, vol. 38, no. 1, pp. 131–138, Jan. 2020, doi: 10.1109/JLT.2019.2938731.

[1-80] K. Okamoto, *Fundamentals of optical waveguides*, 2nd ed. Amsterdam ; Boston: Elsevier, 2006.

[1-81] K. Padmaraju, J. Chan, L. Chen, M. Lipson, and K. Bergman, "Thermal stabilization of a microring modulator using feedback control," *Opt. Express*, vol. 20, no. 27, p. 27999, Dec. 2012, doi: 10.1364/OE.20.027999.

[1-82] H. Jayatilleka *et al.*, "Wavelength tuning and stabilization of microring-based filters using silicon in-resonator photoconductive heaters," *Opt. Express*, vol. 23, no. 19, p. 25084, Sep. 2015, doi: 10.1364/OE.23.025084.

[1-83] H. Zhu *et al.*, "Optimized Silicon QPSK Modulator With 64-Gb/s Modulation Speed," *IEEE Photonics J.*, vol. 7, no. 3, pp. 1–6, Jun. 2015, doi: 10.1109/JPHOT.2015.2425875.

[1-84] K. Bédard, A. D. Simard, B. Filion, Y. Painchaud, L. A. Rusch, and S. LaRochelle, "Dual phase-shift Bragg grating silicon photonic modulator operating up to 60 Gb/s," *Opt. Express*, vol. 24, no. 3, p. 2413, Feb. 2016, doi: 10.1364/OE.24.002413.

[1-85] S. Pitris *et al.*, "O-Band Silicon Photonic Transmitters for Datacom and Computercom Interconnects," *J. Light. Technol.*, vol. 37, no. 19, pp. 5140–5148, Oct. 2019, doi: 10.1109/JLT.2019.2929593.

[1-86] T. Tamura, K. Kondo, Y. Terada, Y. Hinakura, N. Ishikura, and T. Baba, "Silica-Clad Silicon Photonic Crystal Waveguides for Wideband Dispersion-Free Slow Light," *J. Light. Technol.*, vol. 33, no. 14, pp. 3034–3040, Jul. 2015, doi: 10.1109/JLT.2015.2420685.

[1-87] D. M. Beggs, T. P. White, L. Cairns, L. O'Faolain, and T. F. Krauss, "Ultrashort Photonic Crystal Optical Switch Actuated by a Microheater," *IEEE Photonics Technol. Lett.*, vol. 21, no. 1, pp. 24–26, Jan. 2009, doi: 10.1109/LPT.2008.2008104.

[1-88] L. O'Faolain, D. M. Beggs, T. P. White, T. Kampfrath, K. Kuipers, and T. F. Krauss, "Compact Optical Switches and Modulators Based on Dispersion Engineered Photonic Crystals," *IEEE Photonics J.*, vol. 2, no. 3, pp. 404–414, Jun. 2010, doi: 10.1109/JPHOT.2010.2047918.

[1-89] J. H. Wuelbern, A. Petrov, and M. Eich, "Electro-optical modulator in a polymer-infiltrated silicon slotted photonic crystal waveguide heterostructure resonator," *Opt. Express*, vol. 17, no. 1, pp. 304–313, Jan. 2009, doi: 10.1364/OE.17.000304.

[1-90] C.-Y. Lin *et al.*, "Electro-optic polymer infiltrated silicon photonic crystal slot waveguide modulator with 23 dB slow light enhancement," *Appl. Phys. Lett.*, vol. 97, no. 9, p. 093304, Aug. 2010, doi: 10.1063/1.3486225.

[1-91] X. Wang, C.-Y. Lin, S. Chakravarty, J. Luo, A. K.-Y. Jen, and R. T. Chen, "Effective in-device r_33 of 735 pm/V on electro-optic polymer infiltrated silicon photonic crystal slot waveguides," *Opt. Lett.*, vol. 36, no. 6, p. 882, Mar. 2011, doi: 10.1364/OL.36.000882.

[1-92] X. Zhang, A. Hosseini, S. Chakravarty, J. Luo, A. K.-Y. Jen, and R. T. Chen, "Wide optical spectrum range, subvolt, compact modulator based on an electro-optic polymer refilled silicon slot photonic crystal waveguide," *Opt. Lett.*, vol. 38, no. 22, pp. 4931–4934, Nov. 2013, doi: 10.1364/OL.38.004931.

[1-93] Y. Jiang, W. Jiang, L. Gu, X. Chen, and R. T. Chen, "80-micron interaction length silicon photonic crystal waveguide modulator," *Appl. Phys. Lett.*, vol. 87, no. 22, p. 221105, Nov. 2005, doi: 10.1063/1.2138367.

[1-94] X. Chen, Y.-S. Chen, Y. Zhao, W. Jiang, and R. T. Chen, "Capacitor-embedded 0.54 pJ/bit silicon-slot photonic crystal waveguide modulator," *Opt. Lett.*, vol. 34, no. 5, pp. 602–604, Mar. 2009, doi: 10.1364/OL.34.000602.

[1-95] A. Hosseini, X. Xu, H. Subbaraman, C.-Y. Lin, S. Rahimi, and R. T. Chen, "Large optical spectral range dispersion engineered silicon-based photonic crystal waveguide modulator," *Opt. Express*, vol. 20, no. 11, pp. 12318–12325, May 2012, doi: 10.1364/OE.20.012318.

[1-96] H. C. Nguyen, S. Hashimoto, M. Shinkawa, and T. Baba, "Compact and fast photonic crystal silicon optical modulators," *Opt. Express*, vol. 20, no. 20, p. 22465, Sep. 2012, doi: 10.1364/OE.20.022465.

[1-97] H. C. Nguyen, N. Yazawa, S. Hashimoto, S. Otsuka, and T. Baba, "Sub-100 μm Photonic Crystal Si Optical Modulators: Spectral, Athermal, and High-Speed Performance," *IEEE J. Sel. Top. Quantum Electron.*, vol. 19, no. 6, pp. 127–137, Nov. 2013, doi: 10.1109/JSTQE.2013.2265193.

[1-98] Y. Terada, H. Ito, H. C. Nguyen, and T. Baba, "Theoretical and experimental investigation of low-volgage and low-loss 25-Gbps Si photonic crystal slow light Machâ€"Zehnder modulators with interleaved p/n junction," *Front. Phys.*, vol. 2, Nov. 2014, doi: 10.3389/fphy.2014.00061.

[1-99] K. Hojo, Y. Terada, N. Yazawa, T. Watanabe, and T. Baba, "Compact QPSK and PAM Modulators With Si Photonic Crystal Slow-Light Phase Shifters," *IEEE Photonics Technol. Lett.*, vol. 28, no. 13, pp. 1438–1441, Jul. 2016, doi: 10.1109/LPT.2016.2544848.

[1-100] Y. Terada, T. Tatebe, Y. Hinakura, and T. Baba, "Si Photonic Crystal Slow-Light Modulators with Periodic p–n Junctions," *J. Light. Technol.*, vol. 35, no. 9, pp. 1684–1692, May 2017, doi: 10.1109/JLT.2017.2658668.

[1-101] Y. Terada, K. Kondo, R. Abe, and T. Baba, "Full C-band Si photonic crystal waveguide modulator," *Opt. Lett.*, vol. 42, no. 24, p. 5110, Dec. 2017, doi: 10.1364/OL.42.005110.

[1-102] T. Hiraki *et al.*, "Heterogeneously integrated III-V/Si MOS capacitor Mach-Zehnder modulator," *Nature Photonics*, vol. 11, no. 8. NATURE PUBLISHING GROUP,

MACMILLAN BUILDING, 4 CRINAN ST, LONDON N1 9XW, ENGLAND, p. 482+, Aug. 2017, doi: 10.1038/NPHOTON.2017.120.

[1-103] S. Wolf *et al.*, “Silicon-Organic Hybrid (SOH) Mach-Zehnder Modulators for 100 Gbit/s on-off Keying,” *Sci. Rep.*, vol. 8, no. 1, p. 2598, Dec. 2018, doi: 10.1038/s41598-017-19061-8.

[1-104] C. Haffner *et al.*, “Low-loss plasmon-assisted electro-optic modulator,” *Nature*, vol. 556, no. 7702, pp. 483–486, Apr. 2018, doi: 10.1038/s41586-018-0031-4.

[1-105] C. Wang, M. Zhang, B. Stern, M. Lipson, and M. Lončar, “Nanophotonic lithium niobate electro-optic modulators,” *Opt. Express*, vol. 26, no. 2, p. 1547, Jan. 2018, doi: 10.1364/OE.26.001547.

[1-106] M. Takenaka *et al.*, “III–V/Si Hybrid MOS Optical Phase Shifter for Si Photonic Integrated Circuits,” *J. Light. Technol.*, vol. 37, no. 5, pp. 1474–1483, Mar. 2019, doi: 10.1109/JLT.2019.2892752.

[1-107] K. Kondo, “Co-propagating slow-light systems in photonic crystal waveguides,” Doctral Dissertation, Yokohama National University, 2016.

[1-108] H. Ito, “Wavelength division multiplexing in Si photonics and its applications,” Doctral Dissertation, Yokohama National University, 2019.

[1-109] Y. Terada, K. Miyasaka, K. Kondo, N. Ishikura, T. Tamura, and T. Baba, “Optimized optical coupling to silica-clad photonic crystal waveguides,” *Opt. Lett.*, vol. 42, no. 22, p. 4695, Nov. 2017, doi: 10.1364/OL.42.004695.

Chapter2
Fabrication and Components

2. 1 Fabrication

2. 1. 1 Si Photonics Foundry Service

A CMOS-compatible Si photonics fabrication process [2-1], [2-2] requires very large scale and extremely expensive facilities, such as semiconductor manufacturing equipment and a clean room. Therefore, it is difficult for a single group to own such facilities and fabricate Si photonics chips in laboratory scale. However, some foundries with such large facilities (e.g., the Interuniversity Microelectronics Centre and Advanced Micro Foundry) are offering multi-project wafer (MPW) services [2-3], [2-4]. Many different users share a reticle space and integrate devices designed by each of them on the wafer. This approach enables the laboratory-scale fabrication without acquiring and managing the fabrication equipment. The fabrication processes are conducted by the serving specialized

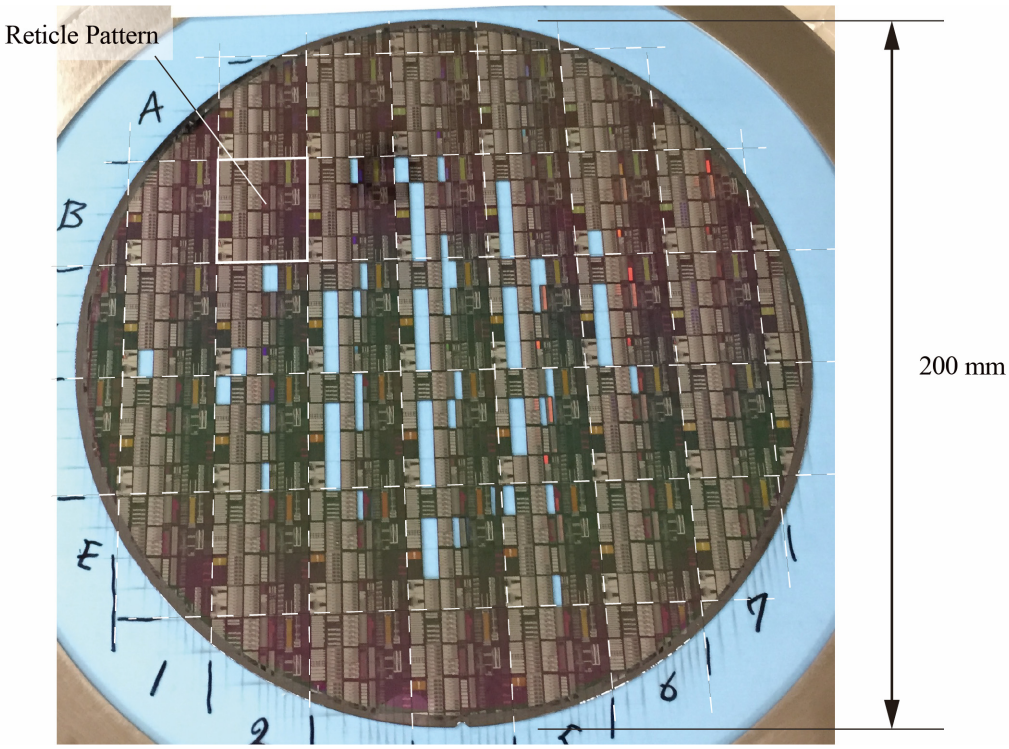

Figure 2.1 Si photonics MPW fabricated by a foundry service.

foundry staff. Therefore, the effort required for users to set the process condition is reduced. In addition, some foundries are allowing users access to their basic device library. I used the MPW services to fabricate the Si devices used in this study. Figure 2.1 shows a fabricated 200-mm-diameter Si photonics wafer that includes several-cm-square periodic reticle patterns and is diced into several-mm-square chips. I fabricated devices on five different lots and selected some chips from the fabricated wafers for testing.

2. 1. 2 Outline of the Fabrication Process

The devices used in this study were fabricated via a CMOS compatible process using KrF excimer laser lithography at λ = 248 nm on a 200-mm-diameter SOI wafer with a Si slab thickness t_{Si} of 205 or 210 nm. Table 2.1 shows the layer information. Of the 32 layers prepared for this process, I used necessary fourteen layers. Photomasks for the photolithography were produced from these layers. These photomasks were primarily binary masks; however, phase shift masks are particularly used for the Si layer and the PhC layer to enhance the resolution to approximately 100 nm. Figure 2.2 shows the structure of the wafer after the device fabrication. Optical components were formed in the Si slab on the buried-oxide (BOX) layer. After the processes on the Si layer, PhC holes were also formed on the Si layer. Next, the holes were buried via silica deposition for over cladding. Acceptors (B) and donors (P) were implanted on the Si slab to form p-type and n-type Si regions, respectively, for p–n incorporated phase shifters. I set the different accepter concentrations N_A and donor concentrations N_D in the five lots I used in this study. I used high-concentration p^+-type and n^+-type Si regions, of which the concentrations are $N_A{}^+ = N_D{}^+ = 1.9 \times 10^{20}$ cm^{-3}, for the ohmic contact with metal electrodes. The TiN layer, which was for resistors and heaters, was formed after the silica deposition and flattening via chemical mechanical polishing (CMP). The TiN layer and the Si layer were placed at adequate distance apart to avoid optical absorption. Subsequently, the aluminum (Al) layer was formed after an additional silica deposition step and the CMP step. This layer was connected with the Si layer and the TiN layer via the contact holes. To maximize the efficiency of the TiN heaters and avoid thermal crosstalk, thermal isolation trenches were formed by etching thorough the silica layer. The facet deep trenches were also formed at the edge of each chip to eliminate the sidewall roughness caused by the blade dicing process.

Table 2.1 Layer information. Grayed-out layers are unused in this study.

Layer No.	Layer Name	Layer No.	Layer Name
1	Si	13	Contact Hole to p-n dope/Ge
2	Rib Structure	14	n-type implant on Si
3	PhC	15	p-type implant on Si
4	Trench for SSC	16	n+-type implant on Si
5	Crad Window at PCW	17	p+-type implant on Si
6	Crad Window at Si	18	n-type implant on Ge
7	Facet Deep Trench	19	p-type implant on Si for PD
8	Thermal Isolation Trench	20	Ge
9	Al	21	Pad Window
10	Contact Hole to Heater	22	Si_3N_4
11	Upper Heater	32	Grating
12	Lower Heater		

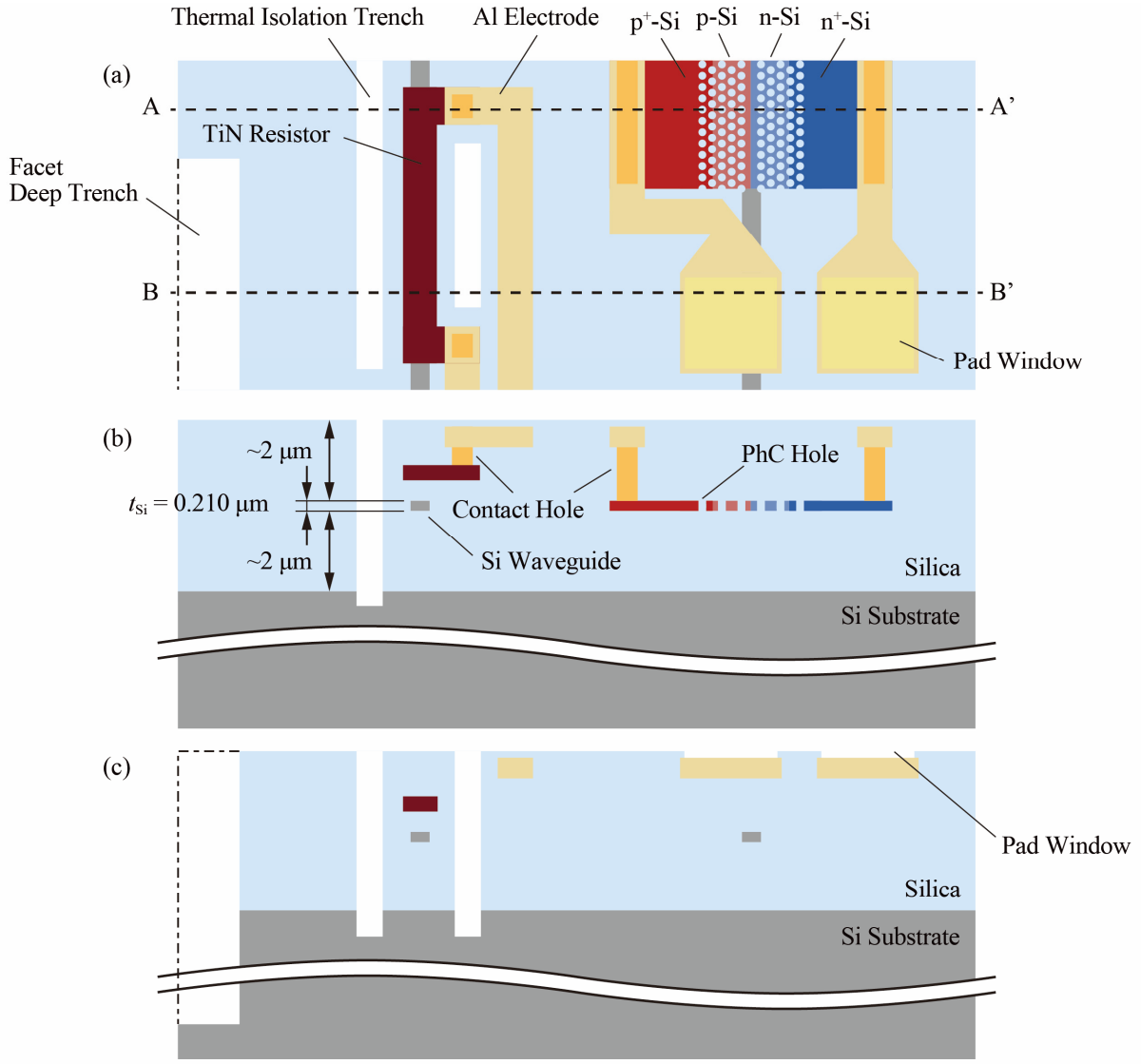

Figure 2.2 Structure of a SOI wafer after device fabrication. (a) Top view. (b) Cross-section at A-A' line. (c) Cross section at B-B' line.

2. 1. 1 CAD Data Production

The photomasks for the lithography were produced from the CAD data of the designed device layouts. Figure 2.3 shows the data production procedure. The CAD data of the device layout was submitted to the foundry in GDSII stream format, which is a standard data format in the semiconductor industry. The GDSII stream format includes position and layer information of the device patterns. I produced the GDSII-format data via conversion from DXF-format data, which is a basic data format used in the software distributed by Autodesk Inc., such as AutoCAD. Si photonics devices, particularly PCWs, include many geometrical figures placed repeatedly and requires precise positions and precisely defined shapes. Therefore, I used a program written in C programming language to produce the DXF-format data. The DXF-format data was converted to GDS II-formal data using Dvogue PC, which is a conversion software that sets the conversion rules.

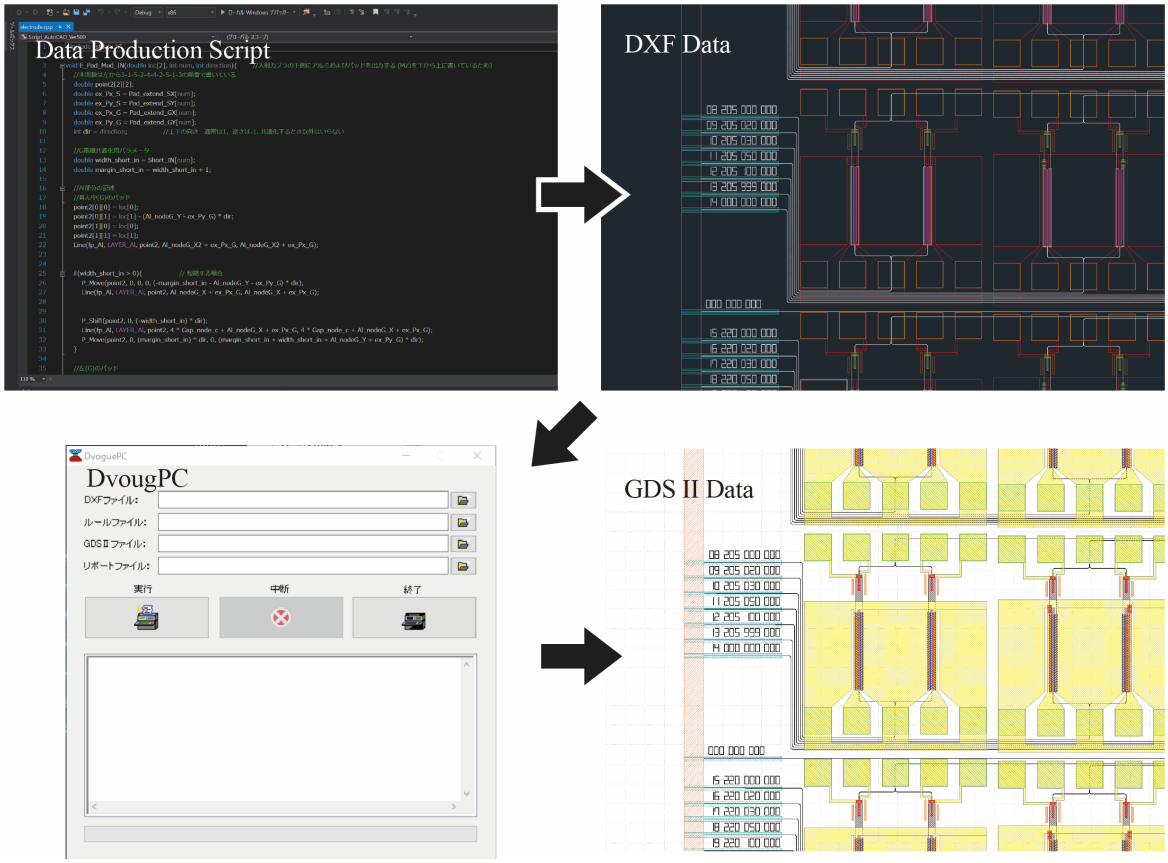

Figure 2.3 Procedure of CAD data production.

2. 2 Fundamental Components

A Si PCW MZM consists of Si wire waveguides, spot size converters (SSC), multimode interference (MMI) couplers, LSPCWs, and p–n junctions. I describe the structures and fundamental characteristics of these components in the sections below. I adopted the basic designs used in our laboratory to the Si wire waveguide, SSC, and MMI coupler, and I designed the LSPCW and p–n junction used in this study.

2. 2. 1 Si Wire Waveguide

The Si wire waveguide is the most basic component in Si photonics. Single-mode propagation is desired in a Si LSPCW MZM. Therefore, the Si waveguide was designed to have a single eigenmode. Figure 2.4(a) shows the cross section of the Si wire waveguide. The 210-nm thick Si slab was formed in the 400-nm width wire. This structure satisfies the single-mode condition. I confirmed the fundamental mode distribution in the waveguide using an eigenmode solver of *MODE* distributed by Lumerical Inc. I built the calculated model shown in Figure 2.5(a) and set the parameters presented in Table 2.2. The geometry of the solver is set to be a 4-μm square per side. Figure 2.5(b) shows the calculated electric field of the fundamental TE-like mode. Because the only one TE-like eigenmodes was found, it was confirmed that this waveguide satisfies the single-mode condition. The equivalent index n_{eq} was calculated to be 2.21, and the modal area was as small as 0.21 μm^2. The realistic propagation loss could not be estimated because the scattering loss due to the sidewall roughness is dominant in a fabricated Si waveguide. The loss was evaluated to be 2–3 dB/cm in a previous study of our group [2-5], [2-6]. n_g of

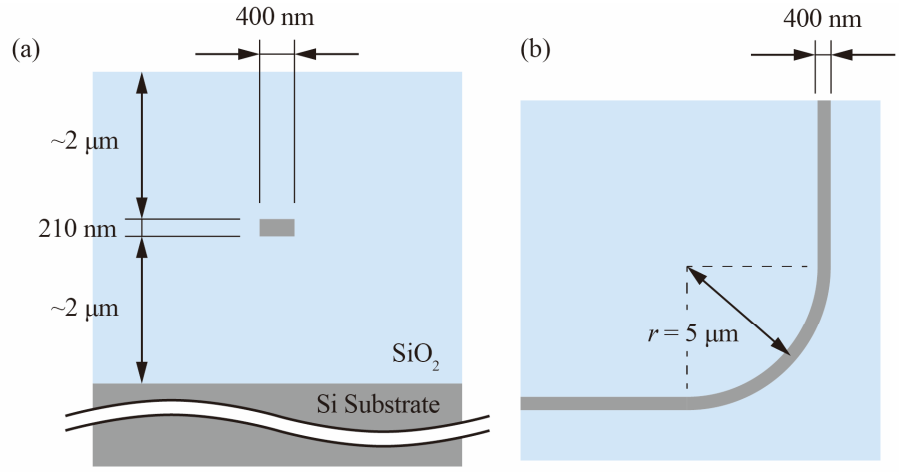

Figure 2.4 Structure of a Si wire waveguide and bend. (a) Cross section. (b) Top view.

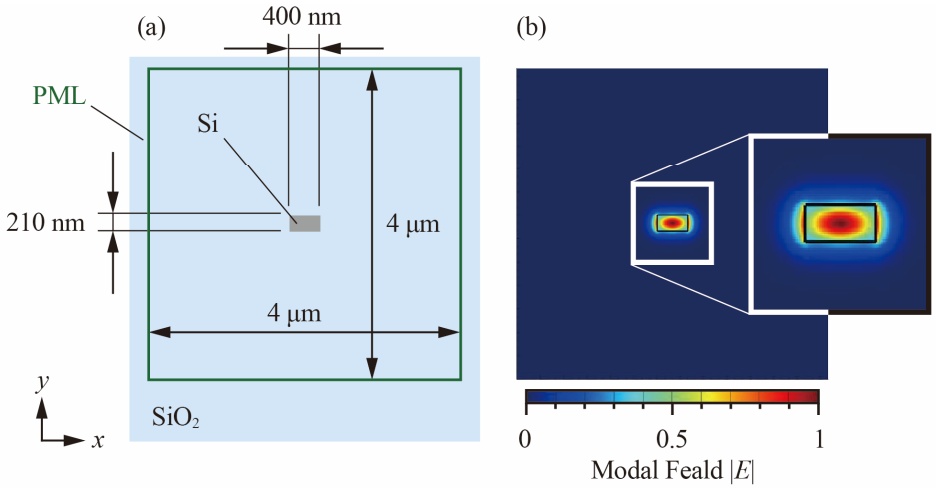

Figure 2.5 Eigenmode simulation of the Si wire waveguide. (a) Model. (b) Simulated fundamental TE mode.

Table 2.2 Simulation condition of the Si wire waveguide.

Parameter		Value
Refractive Index	Si	3.47638
	SiO_2	1.45
Number of mesh cells	x	413
	y	265
Solver Algorithm		TE

this waveguide was evaluated to be 4.385 [2-5]. This waveguide can be bent at a small radius of 5 μm, as shown in Figure 2.4(b). The 90-degree bending loss of the fabricated waveguide was evaluated to be as small as 0.06–0.07 dB/bend [2-5].

2. 2. 2 Spot Size Converter

I used the SSCs for optical coupling with an external optical circuit via SMFs with lenses. As mentioned

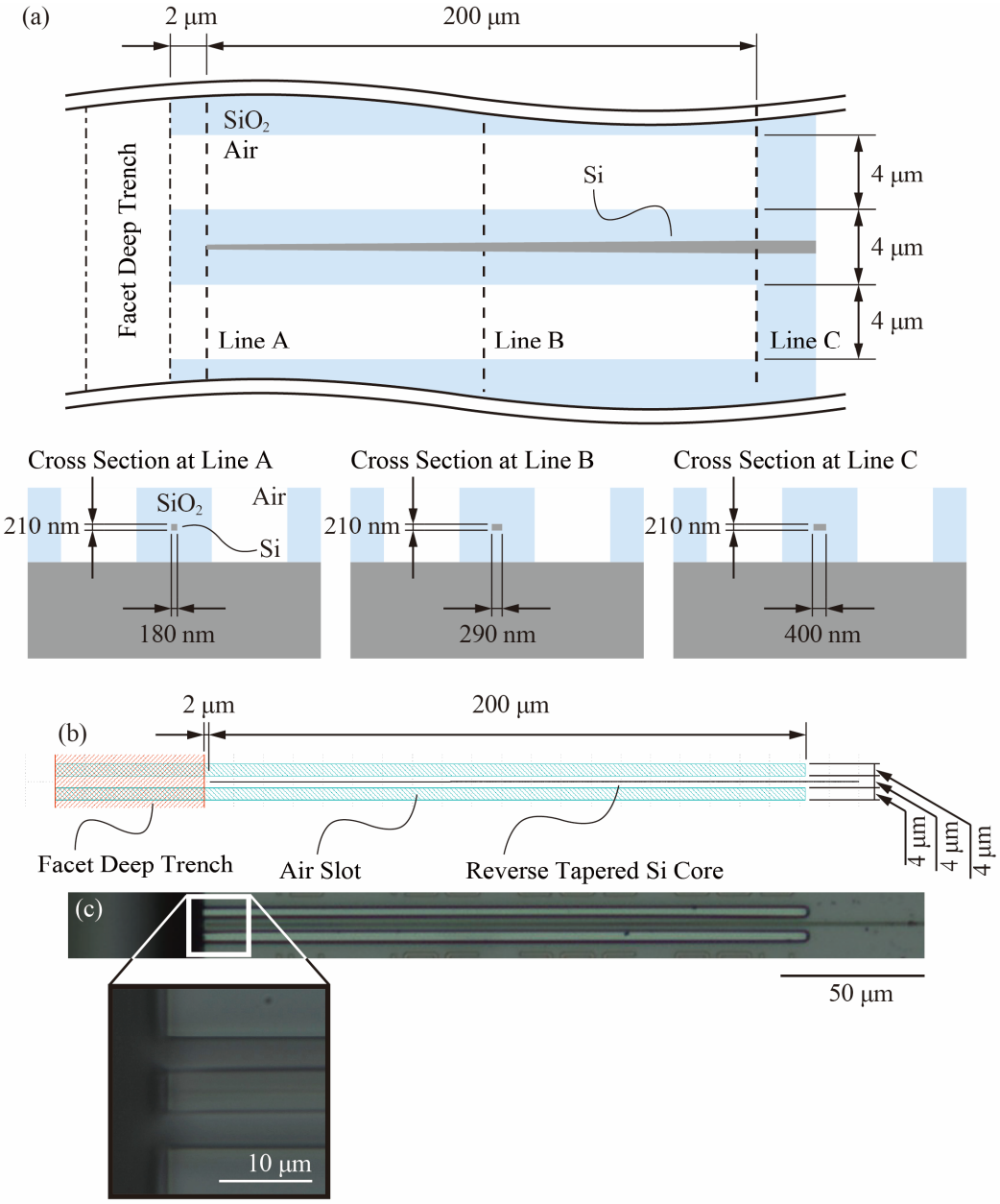

Figure 2.6 Structure of the SSC. (a) Illustration. (b) CAD pattern. (c) Fabricated device.

in the previous section, the modal size of the Si wire waveguides is as small as 0.21 μm^2, which is much smaller than that of the SMFs. Therefore, spot size conversion is necessary to achieve high-efficiency optical coupling. Figure 2.6(a) shows the structure of the SSC. The SSC has a reverse-tapered Si core with the tip width of 180 nm and is surrounded by a silica second core. The 4-μm width side slots serve as air cladding. The width of the Si core is gradually broadened in the 200-μm length and then is connected with a 400-nm wide Si wire waveguide. In contrast, the modal distribution becomes narrower during the propagation and eventually is confined in the Si wire waveguide. The deep trench layer is placed at the edge of the chip to obtain a smooth side wall and minimize the scattering loss. Figure 2.6(b) and Figure 2.6(c) show the generated CAD layout and a fabricated device, respectively. Smooth side walls were observed in the fabricated device. The coupling loss was evaluated to be 2–3 dB in our laboratory.

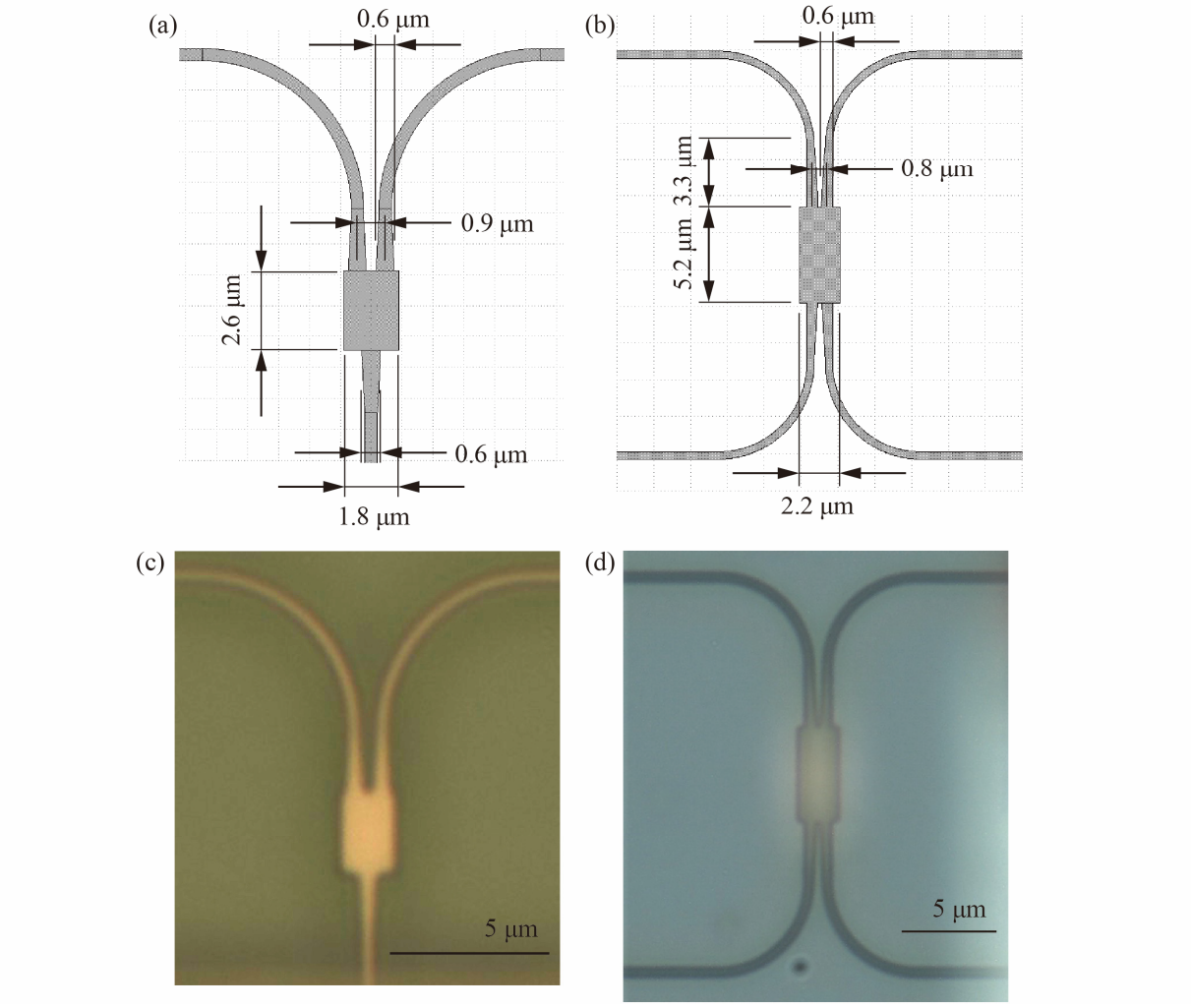

Figure 2.7 Structure of the MMI couplers. (a) CAD pattern of the 2 × 1 coupler. (b) Fabricated 2 × 1 coupler. (c) CAD pattern of the 2 × 2 coupler. (d) Fabricated 2 × 2 coupler.

2. 2. 3 Multi-Mode Interference Coupler

I used compact multimode interference (MMI) couplers and splitters to construct the MZIs. Note that the couplers and splitters have the same structure and that only the propagation direction of light is different; thus, I refer to each of them as “coupler” in this dissertation. Figure 2.7(a) and Figure 2.7(b) show a CAD patterns of the 2 × 1 and 2 × 2 MMI couplers, respectively. A center broad area is coupled with Si waveguides via moderately tapered waveguides. The incident light from the Si wire waveguides drastically diffracts at the coupling, with several eigenmodes excited. The plural eigenmodes interfere with each other, resulting in the appearance of a regular interference pattern in the broad area. One can obtain the desired branching ratio and number of branches by determining the length of the broad area that corresponds to the interference length. The dimensions employed in this study were optimized to obtain an accurate 3-dB branching ratio, high tolerance to the fabrication error, and small excess optical loss. Figure 2.7(c) and Figure 2.7(d) show the fabricated 2 × 1 and 2 × 2 MMI couplers. The optical loss of these devices were evaluated to be approximately 0.2 dB and 0.4 dB, respectively, in previous studies of our laboratory [2-6].

2. 2. 4 LSPCW

Figure 2.8 shows an overall structure of the LSPCW used in the phase shifters. A pair of ten rows of holes sandwiches the line defect. This number of rows was determined to not produce excess propagation loss. I employed the lattice constant a = 400 nm and designed the hole diameter $2r$ = 190-220 nm, the amount of the xth lattice shift s_x = 0-110 nm, and the line defect width of $3^{-1/2}a + \Delta w$. $2r$ indicates the target diameter on the fabricated device; the hole diameter drawn in CAD patterns was slightly tuned to obtain an accurate $2r$ considering the fabrication condition. Δw denotes the additional shift of the line defect width I used to tune n_g and the transmission wavelength of the 1st-row shifted and 2nd-row shifted LSPCWs. The above parameters were determined to obtain slow light transmission in the C-band according to the simulations using finite-difference time-domain (FDTD) method presented below. I used *FDTD solutions*, which is a commercial electromagnetic simulator developed by Lumerical Inc., for such simulations. The LSPCW was coupled with Si wire waveguides via tapered line defect junctions. These junctions remarkably reduce the coupling loss to approximately 0.5 dB [2-7].

Figure 2.9 shows the simulation model of the LSPCW. The y-direction length of the simulation region

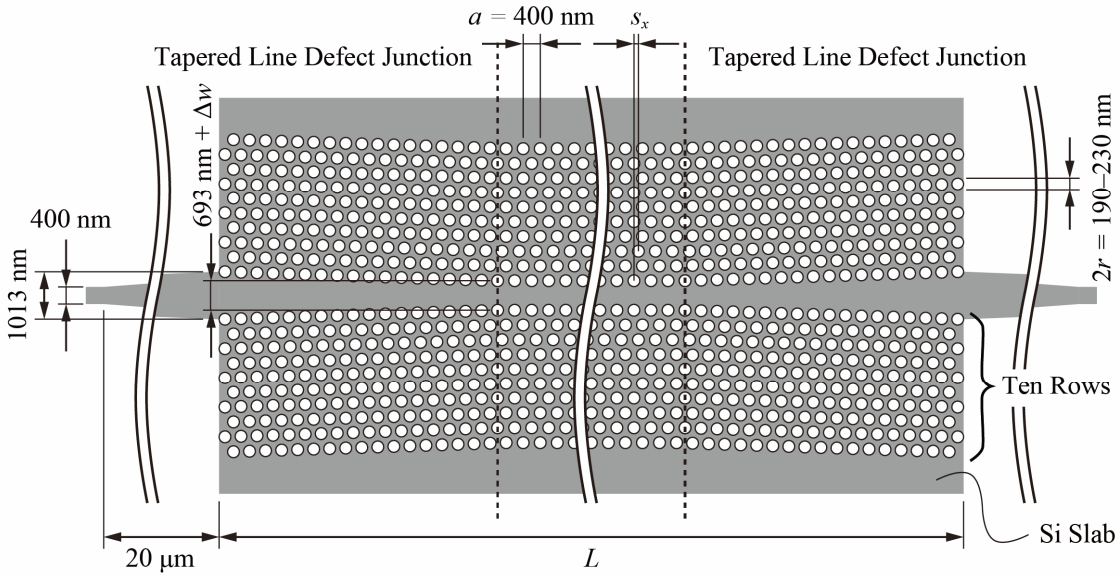

Figure 2.8 Entire structure of the LSPCW.

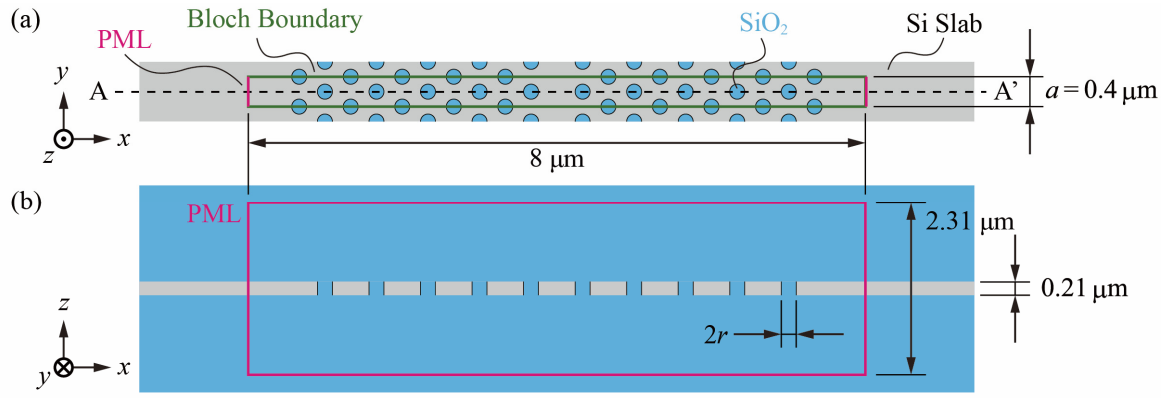

Figure 2.9 FDTD simulation model of LSPCW.

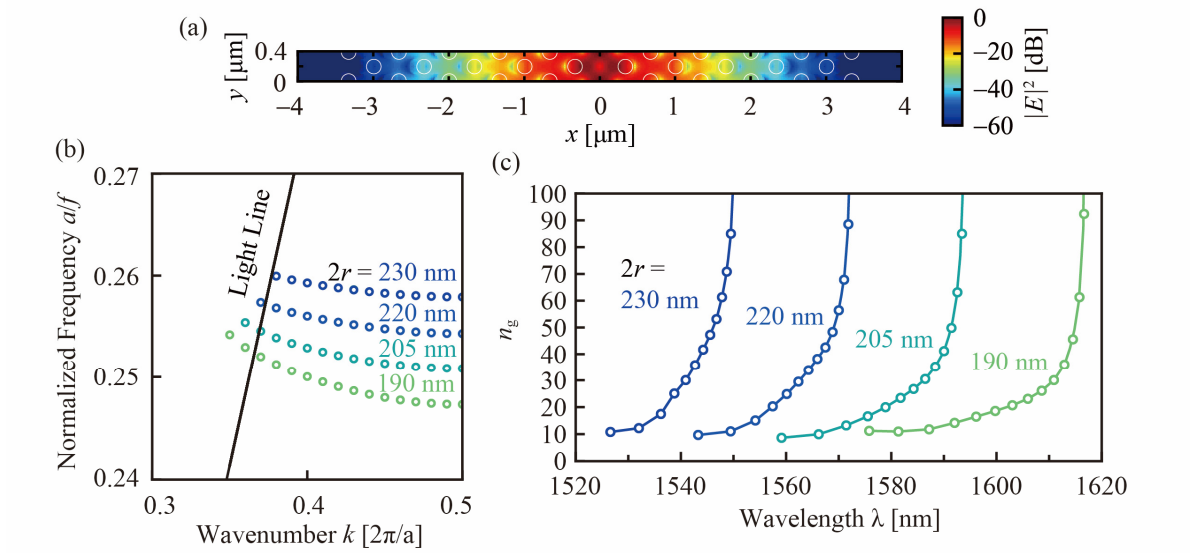

Figure 2.10 (a) Simulated distribution of the slow-light guided mode for $2r = 220$nm, $s_x = 0$, and $k = 0.38$ ($2\pi/a$). (b) Photonic bands calculated for different $2r$. (c) n_g spectra calculated for different $2r$.

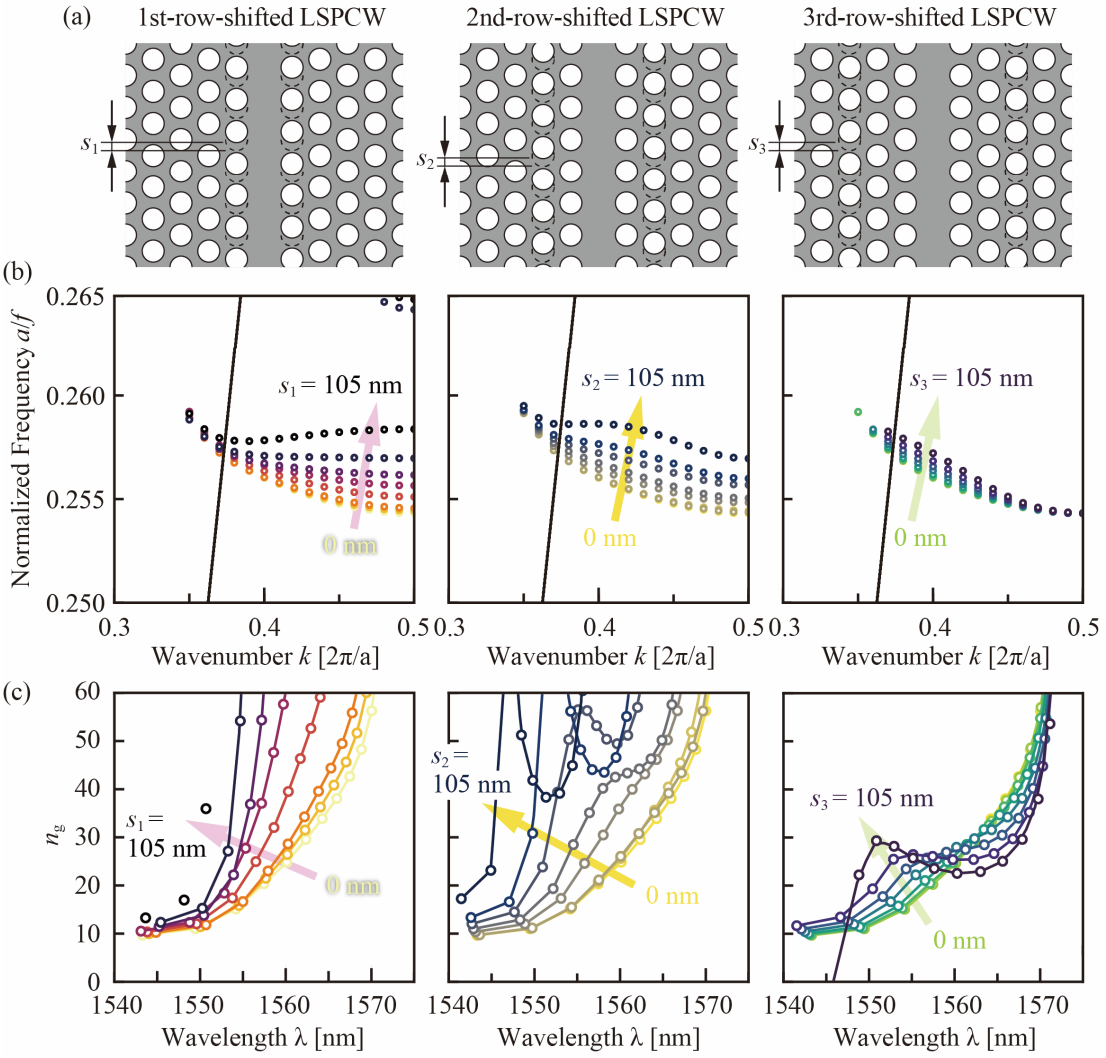

Figure 2.11 (a) Structures of the first-row-shifted, second-row-shifted, and third-row-shifted LSPCWs. (b) Photonic bands and (c) n_g spectra calculated for $s_x = 0$–105 nm at 15-nm step.

was set to be a = 400 μm, which is equivalent as one period of the LSPCW. In addition, I applied Bloch boundary conditions to the y-direction boundaries. Therefore, this model equivalently expresses a long LSPCW while consuming less computational resources. I adopted perfectly matched layers for the other boundaries. *FDTD solutions* has a five-level meshing accuracy setting, ranging from meshing accuracy 1 (lowest) to 5 (highest); the model was meshed with meshing accuracy 2. Figure 2.10(a) shows an example of the calculated modal distribution for $2r$ = 220 nm and s = 0 nm at λ = 1550.67 nm. The light was confined to the line defects with evanescent fields in the PhC. Figure 2.10(b) and Figure 2.10(c) show the calculated photonic bands and the n_g spectra for $2r$ at 15-nm steps and s = 0 nm. The band of the guided modes shifted to the higher-frequency side with the increase of $2r$, with the $2r$ step of 15 nm corresponding to a spectrum shift of approximately 20 nm. As $2r$ increases, the band becomes flatter, the silica light line approaches higher k, and the spectrum becomes narrower. Next, I calculated the photonic bands and the n_g spectra for the first-row-, second-row-, and third-row-shifted LSPCWs in the s_x range of 0–105 nm at 15-nm steps. By the first-row shift, the band edge largely shifts to the higher frequency side. As a result, n_g sharply increases while the spectrum becomes narrower. The shift in the second row raises the band near the center, bringing the band edge to the higher frequency side, thereby producing a higher n_g and a few-nm wide low-dispersion (LD) band, in which n_g is almost constant. Although the first-row shift and second-row shifts change the band edge wavelength, this change can be tuned by changing Δw [2-8]. In contrast, the shift in the third row moderately raises the band near the light line and exhibits a wide LD band, although n_g is relatively low compared with the first-row shift and second-row shift. In addition, this shift does not change the band edge wavelength. As indicated by the above simulation, the lattice shifts in the LSPCW allows the engineering of the photonic band with a high degree of freedom. In particular, the LD band produced by the second-row shift and the third-row shift is useful for wide-wavelength range operation. Figure 2.12 shows a scanning electron microscope (SEM) image of a fabricated PCW without lattice shifts. We confirmed that uniformity of the PhC holes is achieved via the enhanced lithography resolution enabled by the phase shift mask.

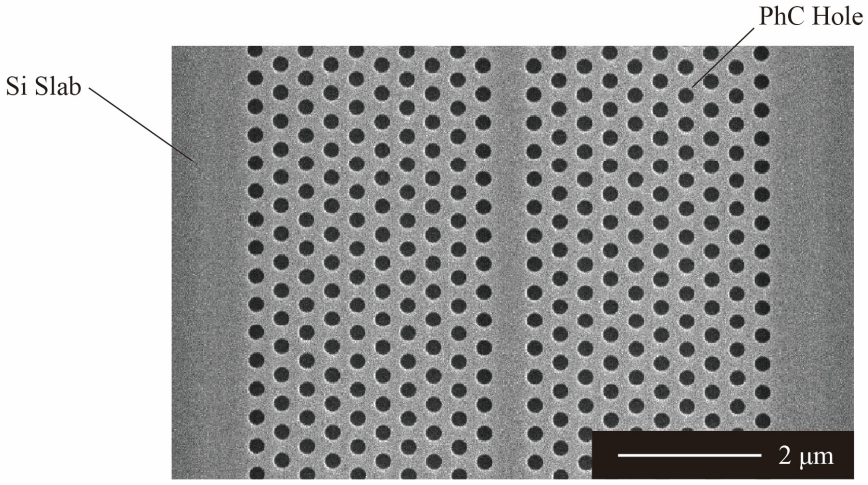

Figure 2.12 SEM image of a PCW without lattice shifts.

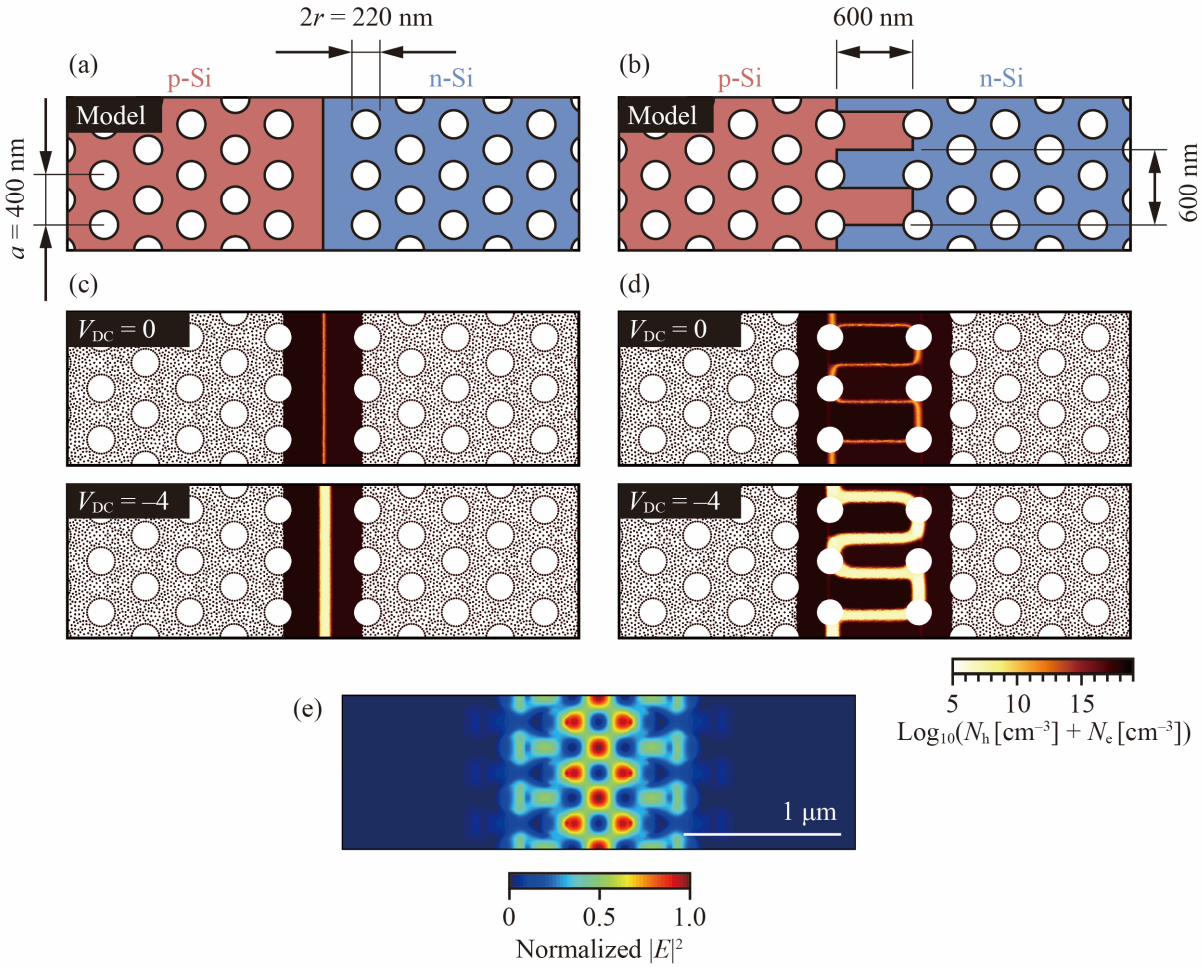

Figure 2.13 Simulation of the carrier distribution and the intensity distribution of the slow-light mode. (a), (b) Simulation models of the linear p-n junction and the interleaved p-n junction with the depth of 600 nm and pitch of 600 nm, respectively. (c), (d) Calculated carrier densities for V_{DC} = 0 and –4. (e) Simulated optical intensity distribution of the slow light mode in the same PCW.

2. 2. 5 P-N Junction

I employed two types of p-n junctions for phase shifters operating in the depletion mode: linear p-n junction and interleaved p-n junction. I calculated the spatial carrier distribution of these junctions using *DEVICE*, which is a commercial carrier transport simulator developed by Lumerical Inc. Figure 2.13(a) and Figure 2.13(b) show the simulation models of the linear p–n junction and the interleaved p–n junction, respectively. The interface of the linear p–n junction was placed at the center of the line defect, and both the width and the depth of the interleaved p-n junction was 600 nm. The doping concentrations were set to be $N_A = 1.05 \times 10^{18}$ cm^{-3} and $N_D = 6.2 \times 10^{17}$ cm^{-3}. These concentrations are the same as those of a lot on which devices were used as described in Chapter5. The models were meshed under the following conditions: Min. edge length of 20 nm, maximum edge length of 200 nm, and max. refine steps of 200000. Moreover, I defined the finer meshing condition near the junctions; the max. edge length was set to be as fine as 8 nm. Figure 2.13(c) and Figure 2.13(d) show the calculated distribution of the carrier density of the linear p-n junction and the interleaved p-n junction, respectively. The outside sparse plots are the result of coarse meshing. The color scale shows the carrier density, which

was calculated as the sum of the densities of the electrons N_e and the holes N_h. Therefore, the low-density regions correspond to the carrier depletion region. Even at $V_{DC} = 0$, the carrier depletion regions appeared because of the built-in potentials. When V_{DC} was increased to –4 V, the carrier depletion regions were broadened to approximately 100 nm. Thus, the carrier density changes at the edges of the carrier depletion regions and the differences from those at $V_{DC} = 0$ (in this case) contribute to Δn_{eff}. Therefore, high junction capacitance C_{pn}, which accumulates large charge Q, is advantageous to obtain a large Δn_{eff}. The interleaved p-n junction has a longer junction length, resulting in higher C_{pn}, than the linear p-n junction. In addition, the overlap between the optical mode and the edge of the depletion region is an important factor to obtain high Δn_{eff}. From this perspective, the interleaved p-n junction is advantageous as well because it covers the wide area in the line defect, as shown in Figure 2.13(d). Figure 2.13(e) shows a simulated intensity distribution of the slow light mode. I confirmed that the interleaved p-n junction overlapped well with the slow light mode. However, high C_{pn} hampers high-speed operation. Therefore, I used a linear p-n junction when high-speed operation is needed or when I want to focus on the EO phase mismatch.

2. 3 Evaluation Methods for Fundamental Optical Characteristics

2. 3. 1 Optical Transmission Measurement System

I used the measurement system shown in Figure 2.14 to evaluate optical transmission spectra of fabricated devices. The linearly polarized light output from the tunable laser (Santec Corp., TSL-210F) was adjusted to be the TE-like polarization by rotating and fixing the polarization-maintaining fiber (PMF). The output power from the tunable laser was set to be 0 dBm. The TE-like polarized light is coupled to a device under test (DUT) via two objective lenses. The first lens collimates the ray of light and the second lens (20 magnification) collect the light and focus on an SSC on the DUT chip. The output light passing through the DUT is was collected the two objective lenses again, brunched to two paths: a path for optical power measurement with the power meter (PM) and a path for the observation of the side wall of the chip with an infrared vidicon camera. The tunable laser and the PM are connected with the computer using these GPIB interfaces. I obtain the optical transmission spectra by sweeping the input wavelength and measuring the optical power simultaneously.

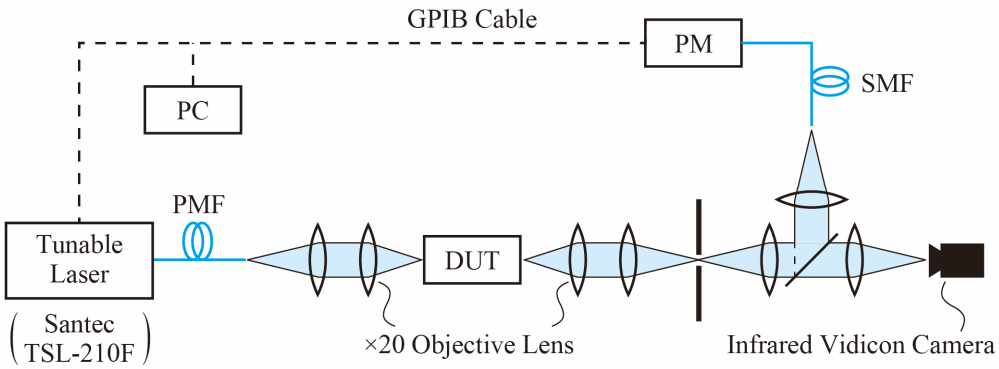

Figure 2.14 Setup for optical transmission measurement.

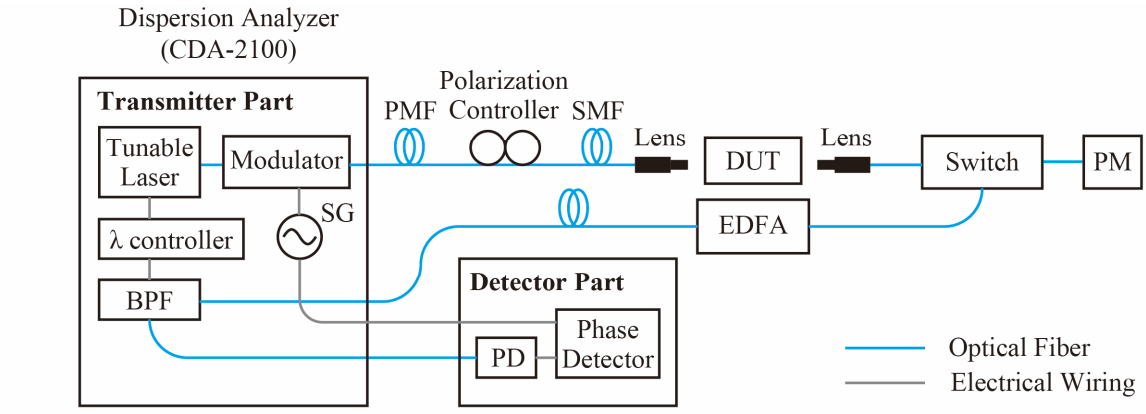

Figure 2.15 Setup for n_g measurement.

2. 3. 2 Group Index Measurement System

I used the measurement system shown in Figure 2.15 to evaluate n_g spectra of fabricated devices. The key equipment is the dispersion analyzer (Alnair labs Corp., CDA-2100). This is consisting of a transmitter part and detector part and measures the group delay time t_g in the travel through a DUT and measurement system. The amplitude of output light from the LD unit of the dispersion analyzer is modulated by the modulator unit of the dispersion analyzer. The modulated light is coupled to the DUT via a SMF with the lens. It is returned to the detector part through the DUT and the fibers after the amplification by the erbium doped fiber amplifier (EDFA) and the filtering by the bandpass filter (BPF) unit to remove amplified spontaneous emission (ASE) noise. I calculated n_g of the device using follows:

$$n_g = \frac{t_{DUT} - t_{ref}}{L_{PCW}} c + n_{g\_ref} \tag{2.1}$$

where t_{DUT} and t_{ref} are the group delay of the device (including the measurement system) and a reference waveguide, respectively, L_{PCW} is length of a PCW of the device, c is the speed of light, and $n_{g\_ref} \approx 4$ is the group index of the reference waveguide.

2. 4 Summary

First, I described fabrication method using MPW service and overview of the CMOS compatible process used in this study. The photomasks used in a photolithography were generated from CAD data of device layouts in GDSII stream format and the devices layout were patterned on an SOI wafer using these photomasks. Phase shift masks were used for the Si layer and PhC layer and they enhanced the resolution to about 100 nm. After that, I described fundamental components: a Si wire waveguide, SSC, MMI coupler, LSPCW, and p-n junction. I adopted the basic designs, which have used in our laboratory, to the Si wire waveguide, SSC, and MMI coupler, and I designed the LSPCW and p-n junction for purpose of this study. The photonic bands and n_g spectra of first-row-shifted, second-row-shifted, third-row-shifted LSPCWs were calculated by the FDTD simulation using *FDTD solutions*. These structures enabled different photonic band engineering. The first-row-shifted and second-row-shifted LSPCWs exhibited high n_g and the second-row-shifted and third-row-shifted LSPCWs exhibited LD slow light. The bandwidth of LD bands of the third-row-shifted LSPCW were as wide as over 10 nm. I calculated

the carrier distribution of the linear p-n junction and interleaved p-n junction using *DEVICE*, too. I confirmed the behavior of the carriers and the well overlap between the carrier depletion regions and slow light mode. Finally, I explained the measurement systems for fundamental optical characteristics: Optical transmission spectra and n_g spectra.

References

[2-1] F. Boeuf *et al.*, "Silicon Photonics R&D and Manufacturing on 300-mm Wafer Platform," *J. Lightwave Technol.*, vol. 34, no. 2, pp. 286–295, Jan. 2016, doi: 10.1109/JLT.2015.2481602.

[2-2] K. Giewont *et al.*, "300-mm Monolithic Silicon Photonics Foundry Technology," *IEEE J. Select. Topics Quantum Electron.*, vol. 25, no. 5, pp. 1–11, Sep. 2019, doi: 10.1109/JSTQE.2019.2908790.

[2-3] "Advanced Micro Foundry" http://www.advmf.com/ (accessed Apr. 24, 2020).

[2-4] "imec.IC-link." https://www.imec-int.com/en/iclink (accessed Apr. 24, 2020).

[2-5] K. Kondo, "Co-propagating slow-light systems in photonic crystal waveguides," Doctral Dissertation, Yokohama National University, 2016.

[2-6] H. Ito, "Wavelength division multiplexing in Si photonics and its applications," Doctral Dissertation, Yokohama National University, 2019.

[2-7] Y. Terada, K. Miyasaka, K. Kondo, N. Ishikura, T. Tamura, and T. Baba, "Optimized optical coupling to silica-clad photonic crystal waveguides," *Opt. Lett.*, vol. 42, no. 22, p. 4695, Nov. 2017, doi: 10.1364/OL.42.004695.

[2-8] T. Tamura, K. Kondo, Y. Terada, Y. Hinakura, N. Ishikura, and T. Baba, "Silica-Clad Silicon Photonic Crystal Waveguides for Wideband Dispersion-Free Slow Light," *J. Light. Technol.*, vol. 33, no. 14, pp. 3034–3040, Jul. 2015, doi: 10.1109/JLT.2015.2420685.

Chapter3
Modulation Efficiency Enhancement via the Slow-Light Effect

3. 1 Overview

In this section, I investigate experimentally a quantitative relation between n_g and $\Delta\phi$ expressed as Equation (1.11). $\Delta\phi$ is proportional to n_g when the other parameters are independent from n_g. However, Δn_{eq} is affected by the overlap between a guided mode and an index-changed region and this overlap potentially depends on n_g. This relation is important issue to design a modulator based on the slow-light effect. For this purpose, I designed and fabricated two different types of Si PCW MZMs: A dispersive PCW MZM and LD LSPCW MZMs. The former easily changes its n_g by merely shifting the operation wavelength, and the latter were designed to have different n_g. I show the effectiveness of the slow-light effect in the development of compact modulators through modulation experiments using these devices.

3. 2 Observation of Modulation Efficiency Enhancement

3. 2. 1 Dispersive Device

I drew the CAD layout of the dispersive Si PCW MZM using the CAD production program. Figure 3.1(a) shows the CAD layout of the device. This device has the 200-μm length p-n incorporated Si PCW without the lattice shift. I expected this device to have the characteristics of gradually increasing n_g toward the band edge, which is useful to investigate the slow light effect, since I can easily change n_g by only shifting the operation wavelength. Figure 3.1(b) shows the p-n incorporated PCW. I set the following structural parameters of the PhC: $t_{Si} = 210$ nm, $a = 400$ nm, and $2r = 200$ nm. The p-n junction was located at the center of the line defect of the PCW, and the p+ and n+ doped Si regions were placed at the distance of 4 μm each other to avoid the strong FCA. The p and n concentrations were set to be $N_A = N_D = 4.8 \times 10^{17}$ cm^{-3}, and the p+ and n+ concentrations were set to be $N_A^+ = N_D^+ = 1.9 \times 10^{19}$ cm^{-3} on this lot. The p and n concentrations are lower than those of other lots in this study. Therefore, a low modulation efficiency was obtained in the fabricated devices; however, I focused on only the relative modulation efficiency change with n_g in this study. Figure 3.1(c) shows the RF electrode. I employed a coplanar waveguide (CPW) structure, which of two ground (G) electrodes and a single signal (S) electrode on the same plane, as the RF electrode structure. I set the width of the S electrode w_S to be 10 μm and the S-G distance d_{SG} to be 13 μm. This CPW was connected with the heavily doped Si via 4-μm width contact holes. Figure 3.1(c) shows the TiN TO phase tuner used to set ϕ_0 of the MZI via

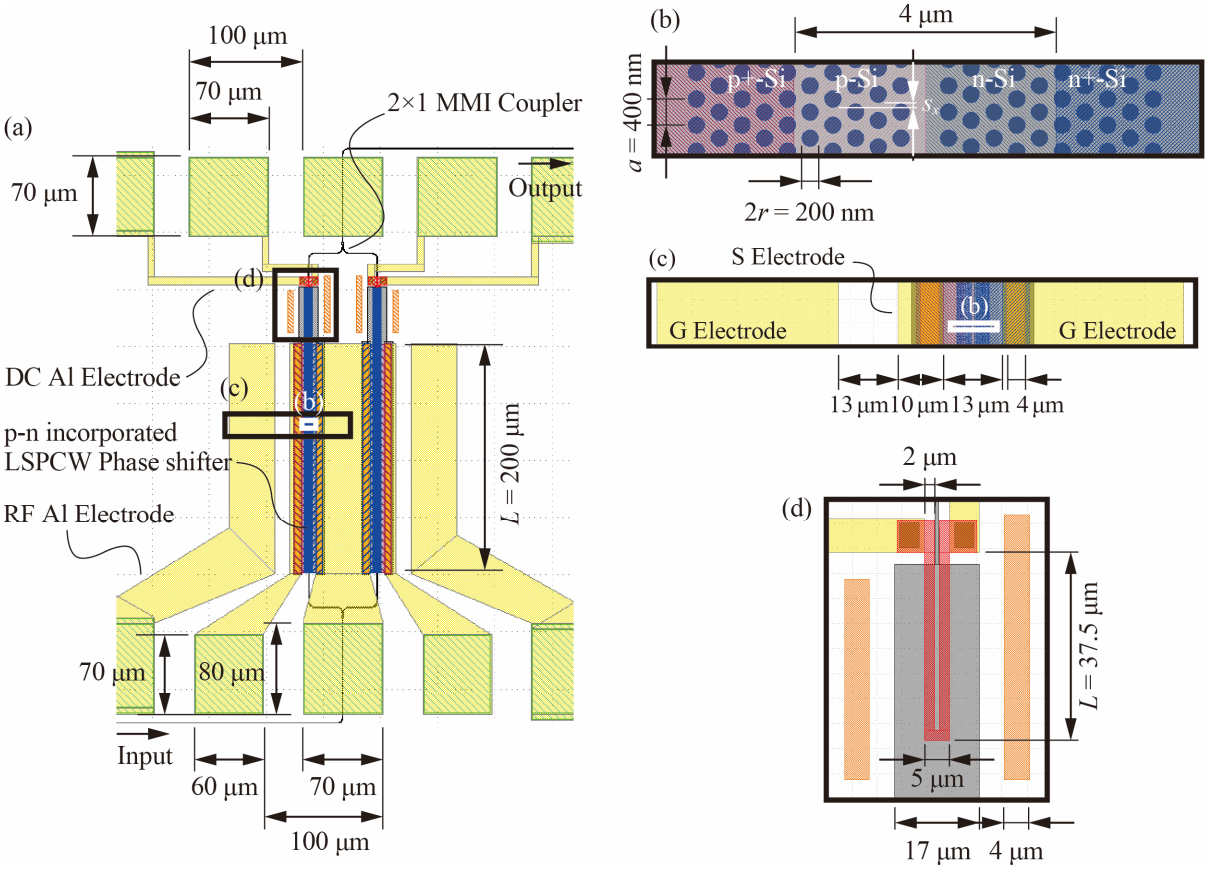

Figure 3.1 CAD layout of a dispersive device without a lattice shift. (a) Overview. (b)–(d) Magnified views of the PCW, CPW, and TO phase tuner.

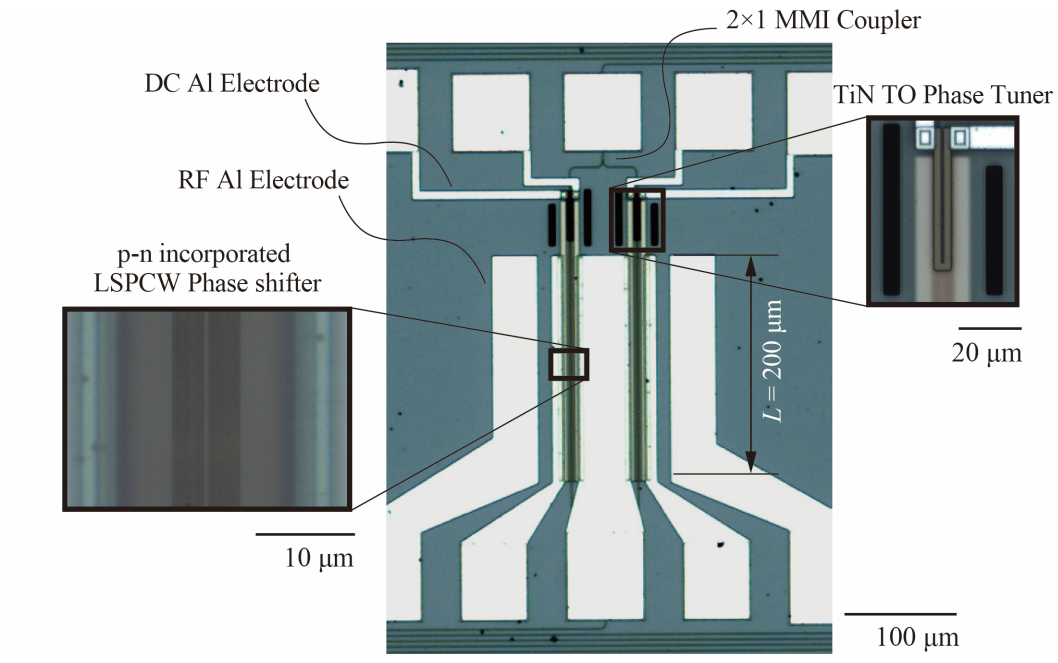

Figure 3.2 Fabricated dispersive device.

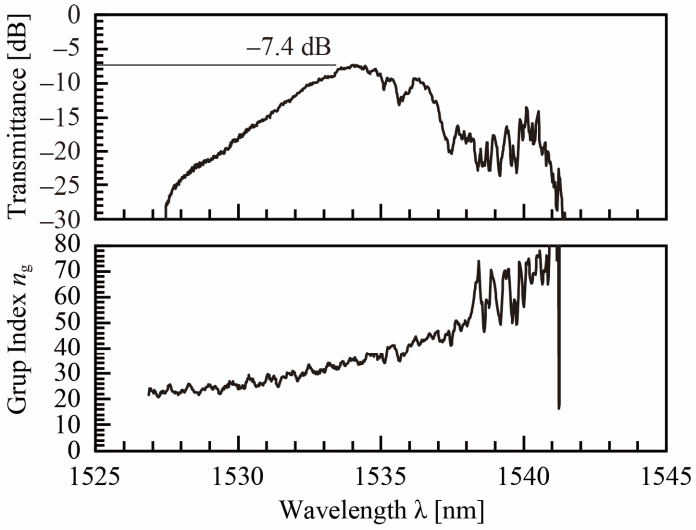

Figure 3.3 Optical transmission spectrum and n_g spectrum of the dispersive device.

heating the PCW. The slow-light effect reduces the length of both the TO phase tuner and the EO phase shifter. These electrodes were connected with a probing pad array with pads spaced at 100-μm pitch. Figure 3.2 shows a micrograph of the fabricated device based on the designed CAD layout. Note that the silica over cladding layer prevents observation using a SEM, which offers high spatial resolution; therefore, I confirmed the structure of the fabricated devices via observations using an optical microscope. The inset on the left shows the magnified view of the PCW. Although the PhC holes are very small, I observed that the PhC and the line defect were patterned and confirmed that all the components were fabricated without apparent fault.

3. 2. 2 Fundamental Characteristics

I measured the transmission and n_g spectra of the device to confirm the fundamental optical characteristics, as shown in Figure 3.3. The PCW exhibited a 14-nm width slow-light propagation band at λ = 1527–1541 nm. A high n_g of 22–80 was observed; the index was observed to gradually change with increase in wavelength toward the band edge. I evaluated the on-chip *IL* to be 7.4 dB at the center of the bowed transmission spectra. This insertion loss includes the losses at each component: the coupling loss between the Si waveguide and the PCW of ~1.5 dB in the total, the loss at the MMI couplers of ~0.5 dB in total, and six bending losses of ~0.5 dB. Hence, the remaining loss of ~5 dB corresponds to the propagation loss in the p-n incorporated PCW, in which n_g equals to 36. This remaining loss includes both the scattering loss and the FCA loss, with over 60% of the propagation loss caused by FCA loss. The insertion loss was found to increase toward both shorter and longer wavelengths. At the shorter wavelength, the slow light mode broadens to the perpendicular direction of light propagation and the FCA loss in the densely doped regions increases. In contrast, the longer wavelength causes both higher scattering loss and higher FCA loss via the higher n_g. Although this wavelength dependence can be flattened by using a photonic band engineered LSPCW, I used this dependence for the investigation of slow-light effects.

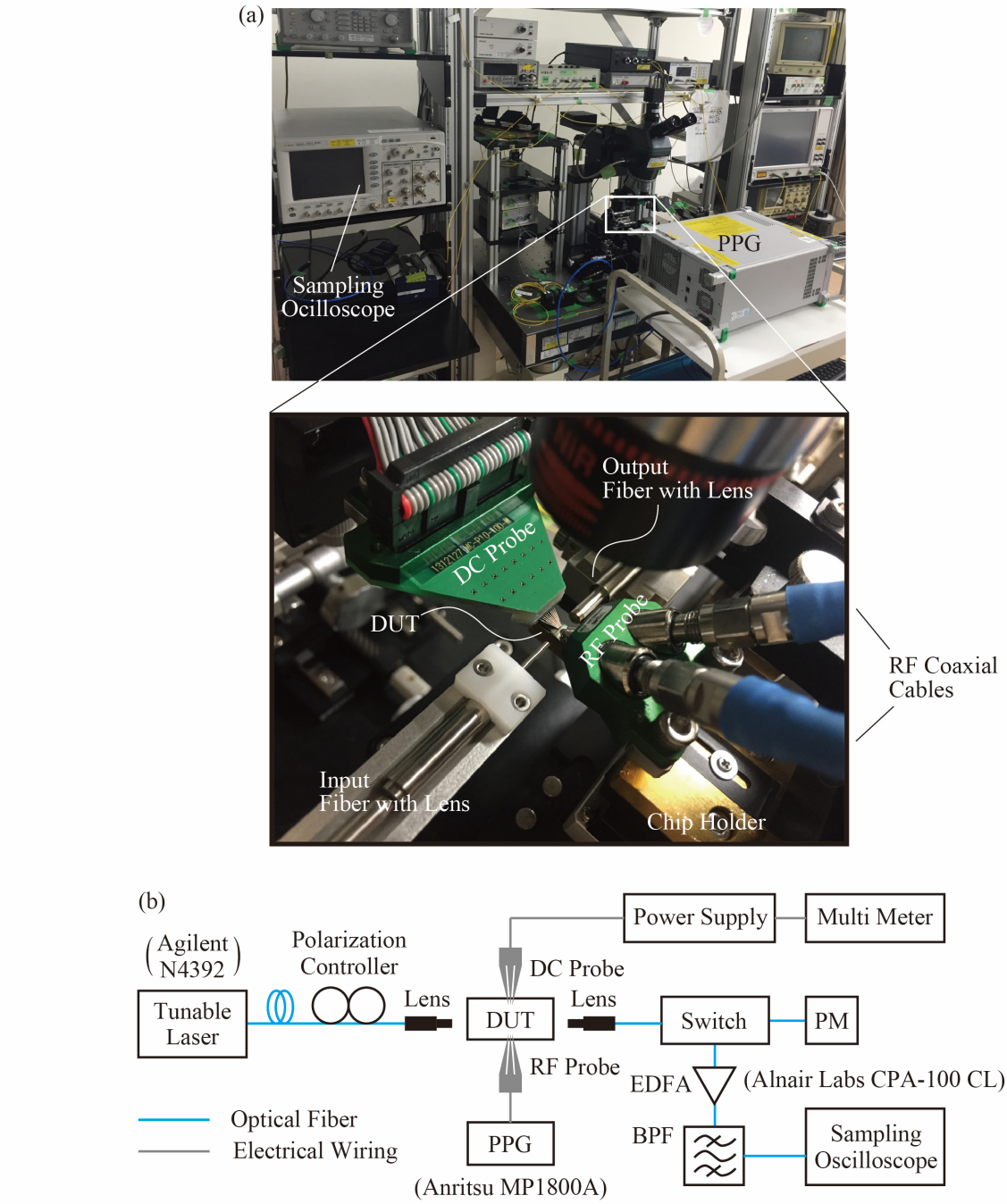

Figure 3.4 Measurement setup of 25-Gbps modulation via a dispersive device. (a) Photograph. (a) Diagram.

3. 2. 3 Modulation Characteristics

(a) Measurement Setup

I constructed the measurement setup shown in Figure 3.4. I input CW light from the tunable laser to the DUT on the chip after adjusting the polarization to be quasi TE mode through an optical fiber using a lens and an SSC. The DUT was placed on a metal holder, as shown in the magnified view of Figure 3.4. I set the laser output power P_{LD} to be 16.5 dBm. Simultaneously, I drove the DUT with a 25-Gbps non-

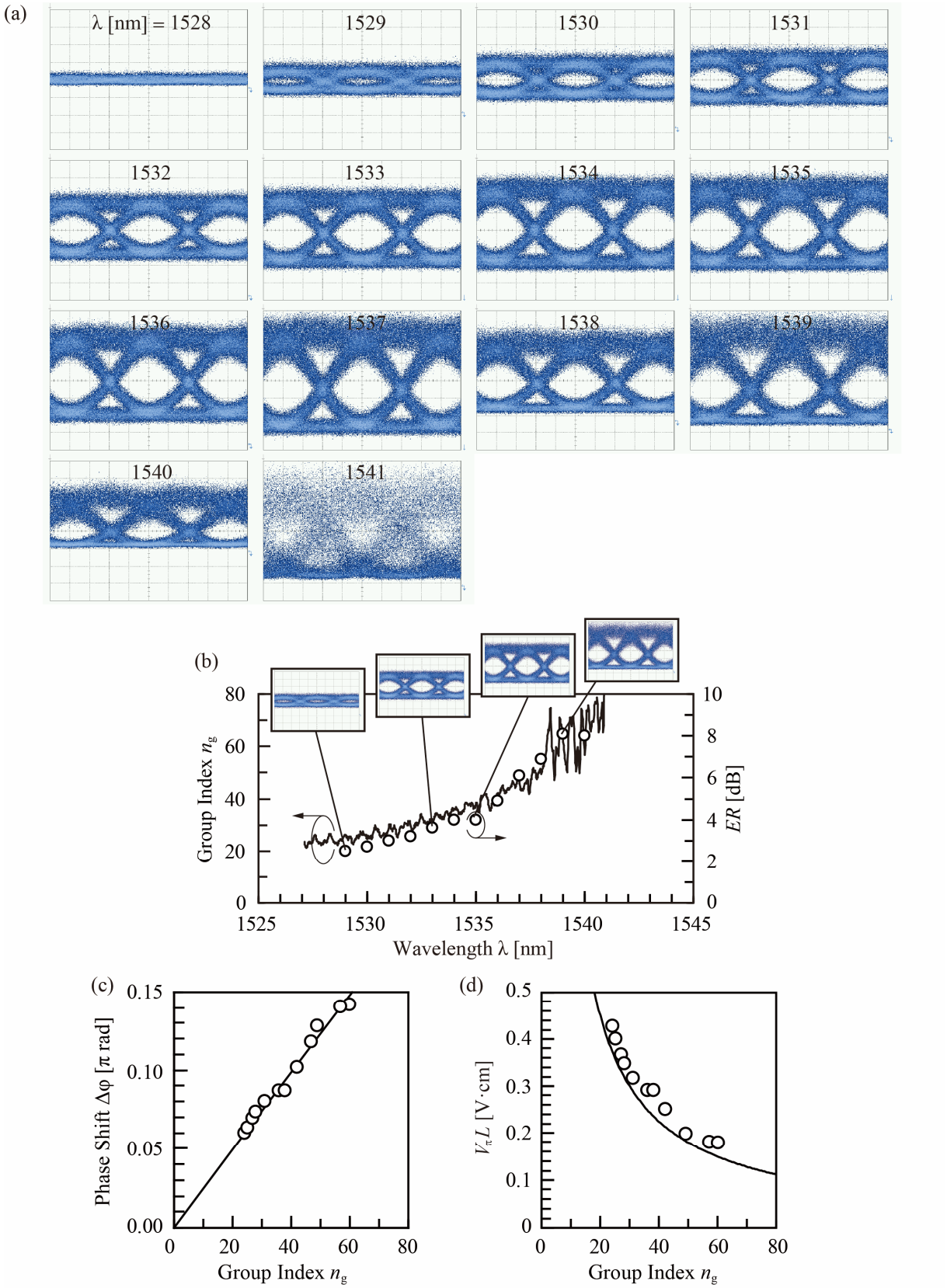

Figure 3.5 25-Gbps modulation using a dispersive device. V_{pp} and V_{DC} were set to be 2.0 V and –1.1 V, respectively. (a) Eye patterns observed at λ = 1528–1541. (b) n_g and measured *ER* spectra. (c) n_g dependence of the measured Δϕ. (d) n_g dependence of $V_\pi L$ calculated from the measured Δϕ.

return-zero (NRZ) pseudo random bit sequence (PRBS) of length of 2^{31}–1 bit generated by a pulse pattern generator (PPG, Anritsu Corp. MP1800A). I set V_{pp} and V_{DC} to be 2.0 V and –1.1 V, respectively, and I set ϕ_0 so that the average output optical power was reduced to 9 dB lower than maximum by heating the PCW with the TO phase tuner. Although this ϕ_0 caused high *ML*, it can compensate for the low modulation efficiency via the low doping concentrations. The modulated output light was amplified by an EDFA to compensate for the optical loss in the system and then was filtered by a BPF to reduce the ASE noise. I set the gain of the EDFA so that the BPF output power P_{BPF} was 0 dBm. Next, I observed the eye pattern of the modulated light using an optical sampling oscilloscope (Keysight Technologies, Inc. 86100C and 86109A).

(b) Results

Figure 3.5(a) and (b) show the measured eye patterns and the *ER* spectra. In the wavelength range of λ = 1528–1540 nm, I observed open eye patterns; however, the eye pattern was closed at λ = 1541 nm because of the large optical loss. These eye amplitudes and *ER* values were found to gradually improved with the increase in n_g. An *ER* of 2.5 dB was observed at n_g = 25, and it was enhanced to 8.1 dB at n_g = 64. I estimated $\Delta\phi$ of the eye patterns from the values of *ER* and ϕ_0. Figure 3.5(c) shows the estimated $\Delta\phi$ versus n_g. As expected from Equation (1.11), $\Delta\phi$ is almost linearly proportional to n_g. Therefore, I confirmed the slow-light enhancement of the modulation efficiency. $\Delta\phi$ was also observed to depend on Δn_{eq}; this dependence is determined by the overlap between the slow light and the region in which the refractive index is changed via the CPD. Conversely, the linear increase of $\Delta\phi$ with n_g indicated that the change of overlap with the increase of n_g was not significant. I also calculated $V_\pi L$ from the estimated $\Delta\phi$ in the single phase shifter based on the measurement conditions and *L* of 200 μm as shown in Figure 3.5(d). The calculated $V_\pi L$ was reduced with the increase in n_g and reached to very small value of 0.18 V·cm at n_g = 57. Moreover, an even smaller $V_\pi L$ of 0.12 V·cm was predicted at n_g = 80 according to a fitted curve. This observation indicates that the large n_g of slow light is advantageous for developing a compact modulator.

3. 3 Sub-100-μm Si LSPCW MZM using a High Group Index

In this section, I investigate the slow-light effect in Si LSPCW MZMs as short as 90 μm designed to have different n_g in the range of 20–40 and demonstrate that the modulation is enhanced by the high n_g.

3. 3. 1 LD Devices

Figure 3.6 shows the designed CAD layout of the 90-μm length LD device, and Figure 3.7 shows the fabricated device. The basic design is the same as that of Figure 3.1; however, the PCW designs were different. Table 3.1 summarizes the structural parameters of the LSPCWs. Device 3.4A has third-low shifted LSPCWs, each of which exhibits a moderate n_g of approximately 20. Alternatively, Devices 3.4B and C have first- and third-row-shifted LSPCWs, and Devices 3.4D and E have second-row-shifted LSPCWs. These structures typically exhibit higher n_g of >25 [3-1]. Therefore, I expected to observe a greater slow-light effect, even in the 90-μm short LSPCW phase shifters. These 2*r* and Δw values were set to be slightly different to tune the operation wavelength. On this lot, N_A and N_D were set to be 9.5 ×

10^{17} cm^{-3} and 5.7 × 10^{17} cm^{-3}, respectively, which are higher than those of the device in Section 3.2 to improve the modulation efficiency.

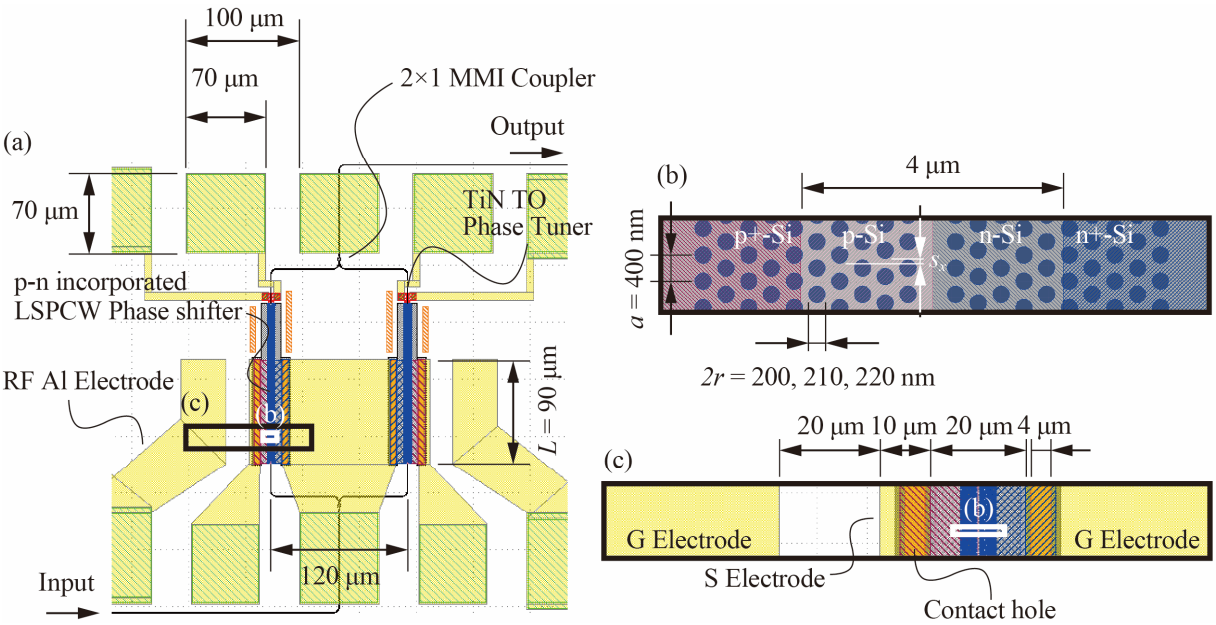

Figure 3.6 CAD layout of a 90-μm length LD device. (a) Overview. (b), (c) Magnified view of the LSPCW and the CPW.

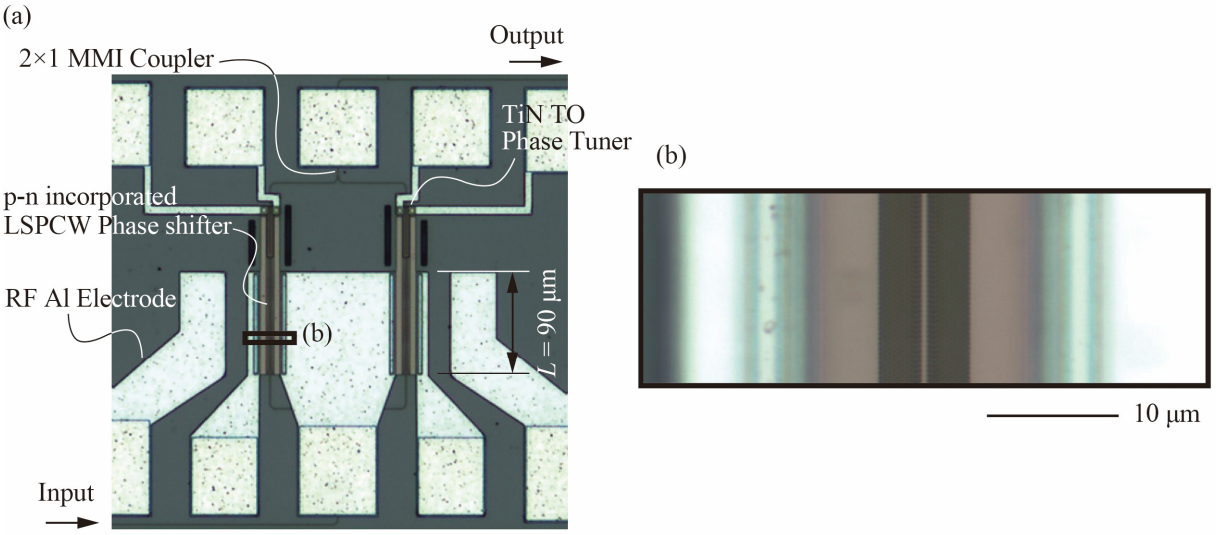

Figure 3.7 Fabricated 90-μm length LD device. (a) Overview. (b) Magnified view of a LSPCW.

Table 3.1 Structural parameters of the 90-μm length LD devices

ID	L	$2r$	s_1	s_2	s_3	Δw
3.4A	90 μm	220 nm	0 nm	0 nm	80 nm	0 nm
3.4B	90 μm	200 nm	110 nm	0 nm	95 nm	30 nm
3.4C	90 μm	200 nm	110 nm	0 nm	95 nm	50 nm
3.4D	90 μm	200 nm	0 nm	90 nm	0 nm	50 nm
3.4E	90 μm	210 nm	0 nm	70 nm	0 nm	40 nm

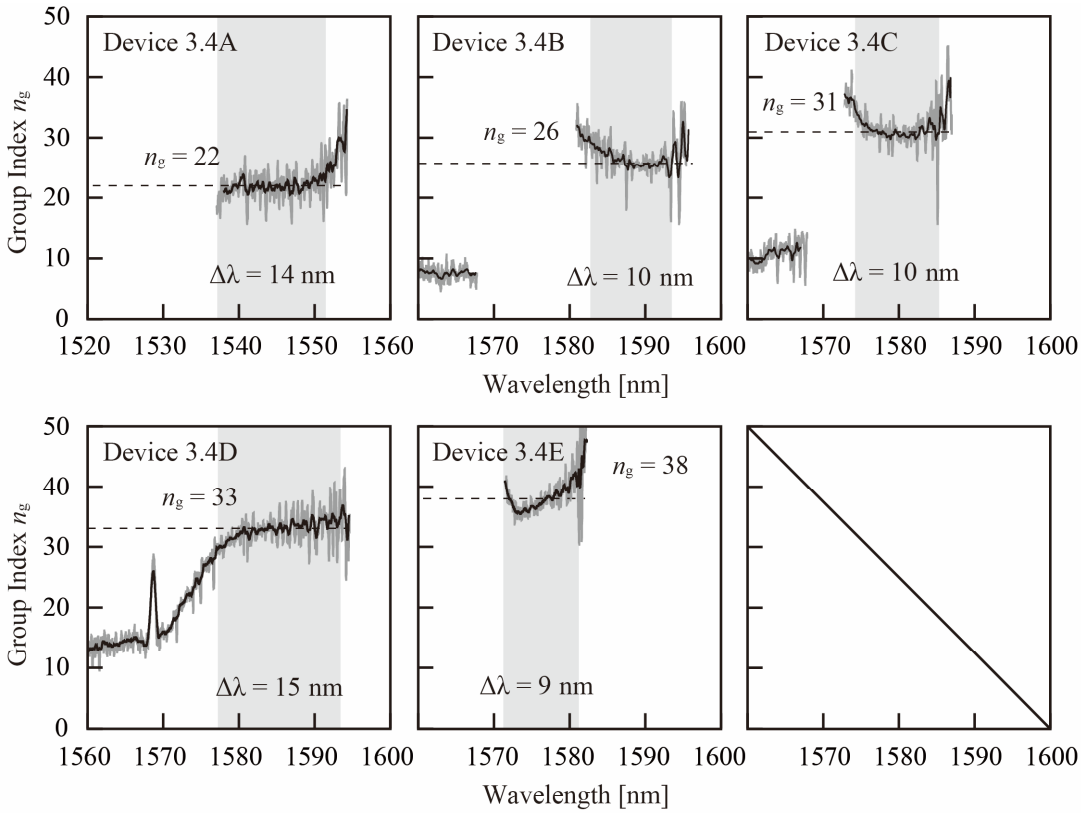

Figure 3.8 Measured n_g spectra of Devices 3.4A–B.

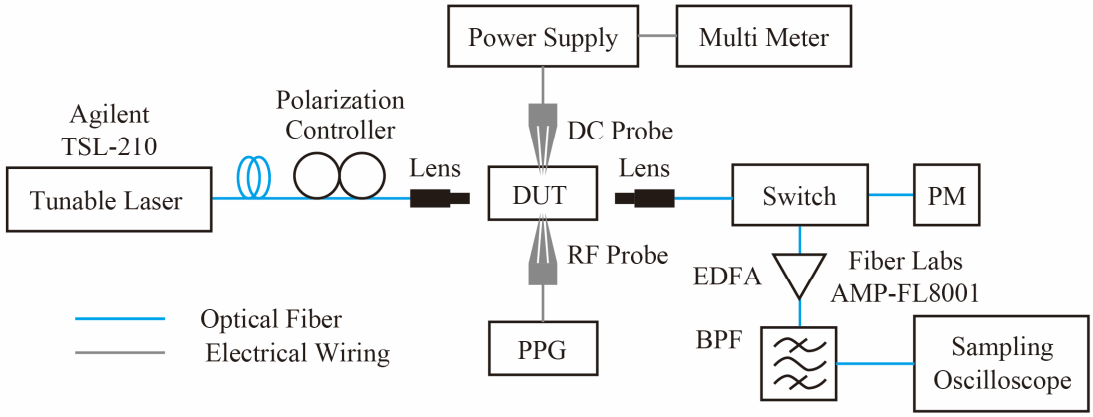

Figure 3.9 Measurement setup of 25-Gbps modulation via a 90-μm long LD device.

3. 3. 2 Fundamental Characteristics

I measured the n_g spectra of Devices 3.4A–E; Figure 3.8 shows the results. The gray curves show the raw data of the measured n_g, and the black curves show the moving average in the wavelength range of ±0.3 nm. Here, I considered the LD slow-light bandwidth as the range that n_g falls within ±10% and colored backgrounds in Figure 3.8. As I expected, Devices B–E exhibited higher n_g of 26–38 than that of Device 3.4A, while they maintained Δλ of ~10 nm. In particular, Device 3.4D exhibited a large n_g of 33 and a wide Δλ of 15 nm. I expected Devices B–E to exhibit 1.2–1.7-fold Δϕ compared with that of Device 3.4A in the following modulation experiment.

3. 3. 3 Modulation Characteristics

(a) Measurement Setup

Figure 3.9 shows the measurement setup. I used a tunable laser (Agilent Technologies, Inc. TSL-210) and EDFA (Fiber labs, Inc. FL8001) that support operation in the L band (λ = 1565–1625 nm). I input 12-dBm power CW light into each device from the tunable laser and adjusted the wavelength so that the received power at the PM became the maximum. Next, I adjusted the gain of the EDFA so that P_{BPF} became 0 dBm. I also set the bit rate, V_{pp}, and V_{DC} of the NRZ PRBS output from the PPG to be 25 Gbps, 1.75 V, and –0.9 V, respectively. I observed the modulated eye patterns after filtering by the BPF using an optical sampling oscilloscope. Here, I tuned the ϕ_0 via the TO phase tuners to set *ER* of the observed eye patterns to be ~3 dB. On this condition, the *ML* decrease with increasing $\Delta\phi$ is enhanced by the slow-light effect.

(b) Results

Figure 3.10(a) shows the observed 25-Gbps eye patterns modulated by Devices 3.4A–E. I obtained open eye patterns with *ER* of ~3 dB from all the devices. *ML* of 6.8, 9.0, 7.1, 4.5, and 5.5 were observed for the n_g of 22, 26, 31, 33, and 38, respectively. I estimated $\Delta\phi$ from the optical transmittance curves as a function of heating powers of the TO phase tuners (the curves correspond to ϕ_0) in addition to the values of *ER* and *ML* as shown in Figure 3.10(b). The set values of ϕ_0 (circle plots in Figure 3.10(b)) and the obtained $\Delta\phi$ could be uniquely determined. Figure 3.10(c) shows $\Delta\phi$ as a function of n_g. Here, $\Delta\phi$ was also found to be linearly proportional to n_g. I obtained a comparable value of $\Delta\phi$ from the 90-μm length LSPCW phase shifter as that of a 200-mm length PCW (Figure 3.5(c)), as shown in Figure 3.10(c), because of the higher doping concentrations: $N_A = 9.5 \times 10^{17}$ cm^{-3} and $N_D = 5.7 \times 10^{17}$ cm^{-3}. The largest $\Delta\phi$ of 0.15π (for the push-pull driving), which corresponds to *ER* of 3.2 and *ML* of 4.5 dB, was obtained by Device 3.4D, which exhibited n_g of 33. I calculated values of $V_\pi L$ based on the estimated $\Delta\phi$ and the measurement conditions of V_{pp} = 1.75 V and V_{DC} = –0.9 V as shown in Figure 3.10(d). The calculated $V_\pi L$ were found to decrease with the increase in n_g and reached to 0.22 V·cm (for the single phase shifter) at n_g = 33. In our previous study, 25-Gbps operation of a 90-μm length single-LSPCW MZM was observed. However, a noisy eye pattern with small *ER* of 2.0 dB was observed for V_{pp} = 3.6 V and V_{DC} = 5 V. This improvement was achieved via the high doping concentrations and the use of push-pull driving. Furthermore, the value of n_g of the previous single LSPCW was not directly measured, although it was estimated to be >40 from the free-spectral range of the transmission spectrum [3-2]. In this experiment, I showed a clear relationship between n_g and $\Delta\phi$ in the studied LSPCW MZMs.

3. 4 **Summary**

I discussed the modulation efficiency enhancement via the slow-light effect observed through the experiments I performed. I designed and fabricated the dispersive device without lattice shifts to have gradually increasing n_g toward the band edge. This design enabled tunable n_g by merely changing the input wavelength. Both the *ER* of the modulated eye patterns and the estimated $\Delta\phi$ increase with increasing n_g. I confirmed that $\Delta\phi$ is linearly proportional to n_g, as theoretically predicted by Equation

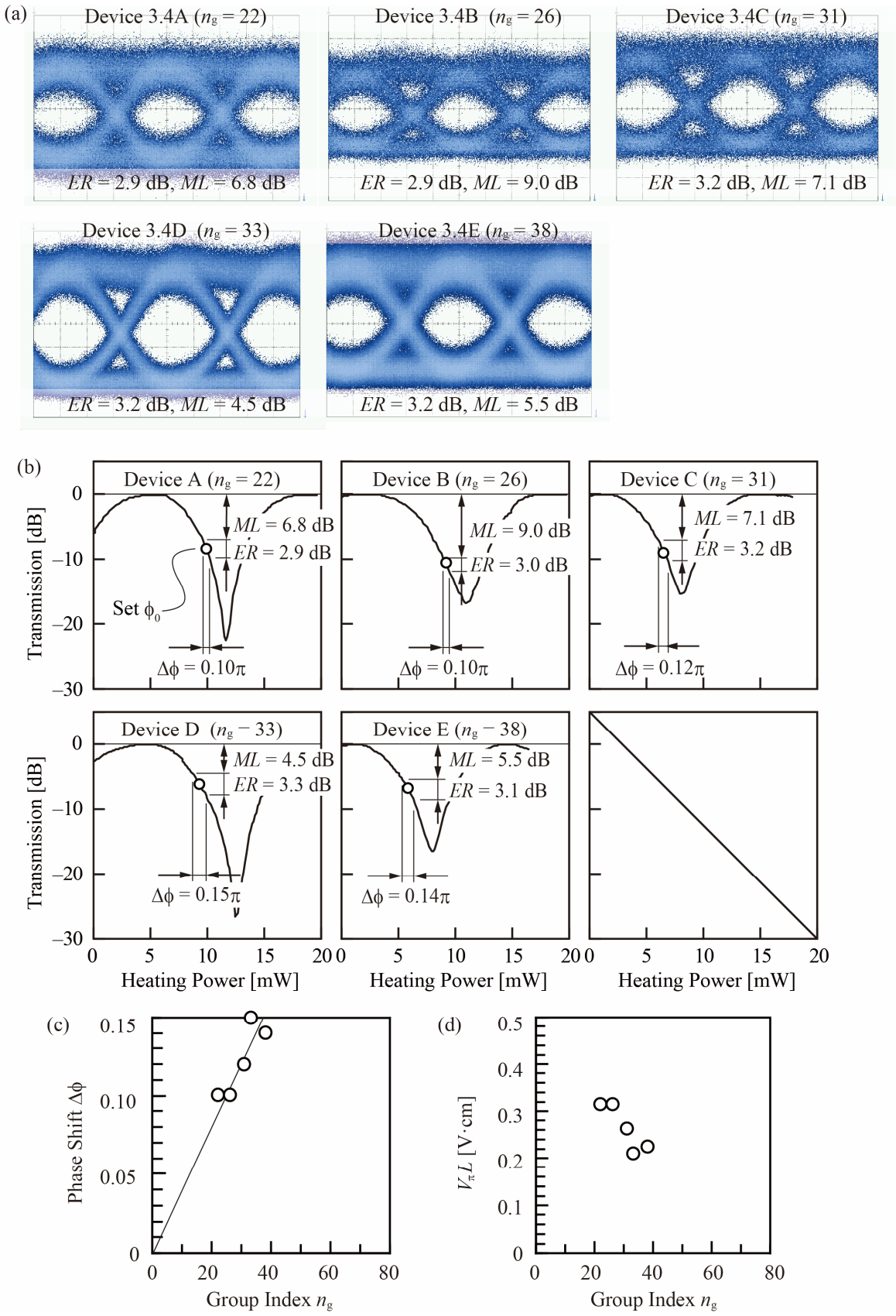

Figure 3.10 Measurement results of the 25-Gbps modulation via the 90-μm long LD device. (a) Observed eye pattens with *ER* of ~ 3 dB. V_{pp} and V_{DC} are equal to 1.75 V and –0.9 V, respectively. (b) Optical transmissions as functions of heating powers. (c) Estimated Δϕ as a function of n_g. (d) Calculated $V_\pi L$ as the function of n_g.

(1.11). The calculated $V_\pi L$ from the estimated $\Delta\phi$ was also reduced with the increase in n_g and it was reached to 0.18π even with the low doping concentration of $N_A = N_D = 4.8 \times 10^{17}$ cm^{-3}. Furthermore, I confirmed the observation of the slow-light effect in five 90-μm length devices (Device 3.4A–E), each of which has a different LSPCW design, and demonstrated 25 Gbps operation, as discussed in Section 3. 3. In this experiment, I obtained a small $V_\pi L$ of 0.22 V·cm for the device that has high n_g of 33 and relatively wide $\Delta\lambda$ of 15 nm. To the best of my knowledge, these observations represents the smallest $V_\pi L$ among the reported CMOS compatible MZMs based on the CPD in Si; this $V_\pi L$ value is 0.07–0.16 times smaller than conventional rib-type MZMs (as shown in Table 1.3) [3-3]–[3-9] and comparable with state-of-the-art hybrid integrated modulators (i. e. III-V modulators [3-10] and SOH modulators [3-11]). Through these experiments, I confirmed the effectiveness of slow-light effects to develop a compact MZM.

References

[3-1] T. Tamura, K. Kondo, Y. Terada, Y. Hinakura, N. Ishikura, and T. Baba, "Silica-Clad Silicon Photonic Crystal Waveguides for Wideband Dispersion-Free Slow Light," *J. Light. Technol.*, vol. 33, no. 14, pp. 3034–3040, Jul. 2015, doi: 10.1109/JLT.2015.2420685.

[3-2] H. C. Nguyen, N. Yazawa, S. Hashimoto, S. Otsuka, and T. Baba, "Sub-100 μm Photonic Crystal Si Optical Modulators: Spectral, Athermal, and High-Speed Performance," *IEEE J. Sel. Top. Quantum Electron.*, vol. 19, no. 6, pp. 127–137, Nov. 2013, doi: 10.1109/JSTQE.2013.2265193.

[3-3] D. J. Thomson *et al.*, "50-Gb/s Silicon Optical Modulator," *IEEE Photonics Technol. Lett.*, vol. 24, no. 4, pp. 234–236, Feb. 2012, doi: 10.1109/LPT.2011.2177081.

[3-4] M. Streshinsky *et al.*, "Low power 50 Gb/s silicon traveling wave Mach-Zehnder modulator near 1300 nm," *Opt. Express*, vol. 21, no. 25, pp. 30350–30357, Dec. 2013, doi: 10.1364/OE.21.030350.

[3-5] Y. Yang, Q. Fang, M. Yu, X. Tu, R. Rusli, and G.-Q. Lo, "High-efficiency Si optical modulator using Cu travelling-wave electrode," *Opt. Express*, vol. 22, no. 24, p. 29978, Dec. 2014, doi: 10.1364/OE.22.029978.

[3-6] H. Xu *et al.*, "High-speed silicon modulator with band equalization," *Opt. Lett.*, vol. 39, no. 16, pp. 4839–4842, Aug. 2014, doi: 10.1364/OL.39.004839.

[3-7] D. Patel *et al.*, "Design, analysis, and transmission system performance of a 41 GHz silicon photonic modulator," *Opt. Express*, vol. 23, no. 11, p. 14263, Jun. 2015, doi: 10.1364/OE.23.014263.

[3-8] M. Pantouvaki *et al.*, "Active Components for 50 Gb/s NRZ-OOK Optical Interconnects in a Silicon Photonics Platform," *J. Light. Technol.*, vol. 35, no. 4, pp. 631–638, Feb. 2017, doi: 10.1109/JLT.2016.2604839.

[3-9] M. Li, L. Wang, X. Li, X. Xiao, and S. Yu, "Silicon intensity Mach–Zehnder modulator for single lane 100 Gb/s applications," *Photonics Res.*, vol. 6, no. 2, p. 109, Feb. 2018, doi: 10.1364/PRJ.6.000109.

[3-10] T. Hiraki *et al.*, "Heterogeneously integrated III-V/Si MOS capacitor Mach-Zehnder modulator," *Nature Photonics*, vol. 11, no. 8, p. 482+, Aug. 2017, doi: 10.1038/NPHOTON.2017.120.

[3-11] S. Wolf *et al.*, "Silicon-Organic Hybrid (SOH) Mach-Zehnder Modulators for 100 Gbit/s on-off Keying," *Sci. Rep.*, vol. 8, no. 1, p. 2598, Dec. 2018, doi: 10.1038/s41598-017-19061-8.

Chapter4
Wide-Wavelength-Range Operation

4. 1 Overview

In this section, I discuss the wide-wavelength-range operation, which corresponds to a temperature stability, of a LSPCW MZM that has a LD bandwidth. The temperature stability is an important characteristic for developing EO modulators used in severe temperature environments in data centers. Previously, our group reported an operation of a LSPCW MZM in a wide wavelength range of 16.9 nm and a wide temperature range of 19–124°C [4-1], but it was characterized only by its eye amplitude. Here, the wide-wavelength-range operation was evaluated by more general characteristics: the frequency response spectrum, *ER* spectrum, and bit-error rate (*BER*) spectrum.

4. 2 Device

4. 2. 1 Design and Fabrication

Figure 4.1 shows the CAD pattern of the designed LSPCW device with the wide LD band, and a CPW.

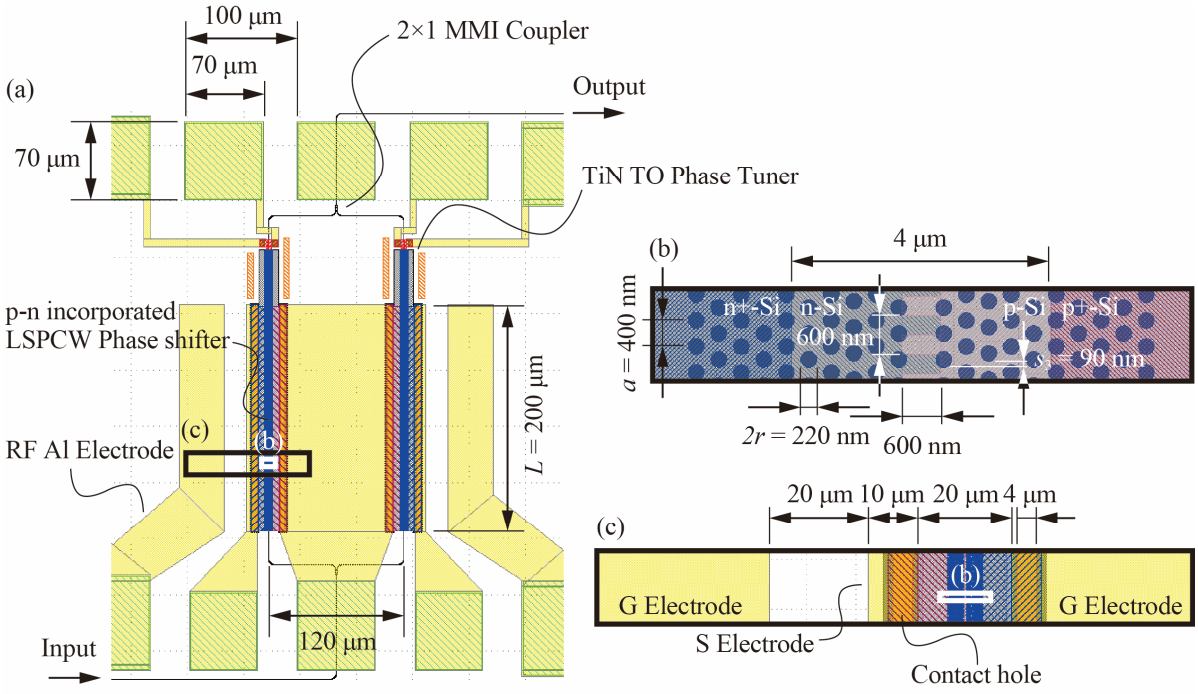

Figure 4.1 CAD layout of a 200-µm long LD device. (a) Overview. (b), (c) Magnified view of a p-n junction and

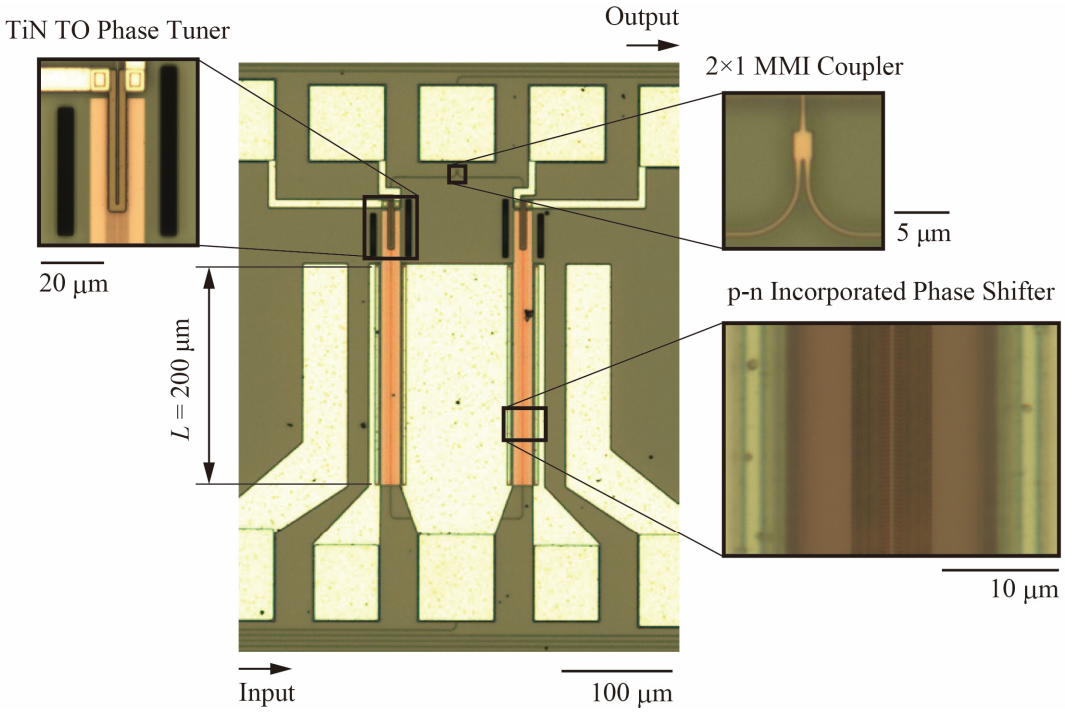

Figure 4.2 Fabricated 200-μm long LD device.

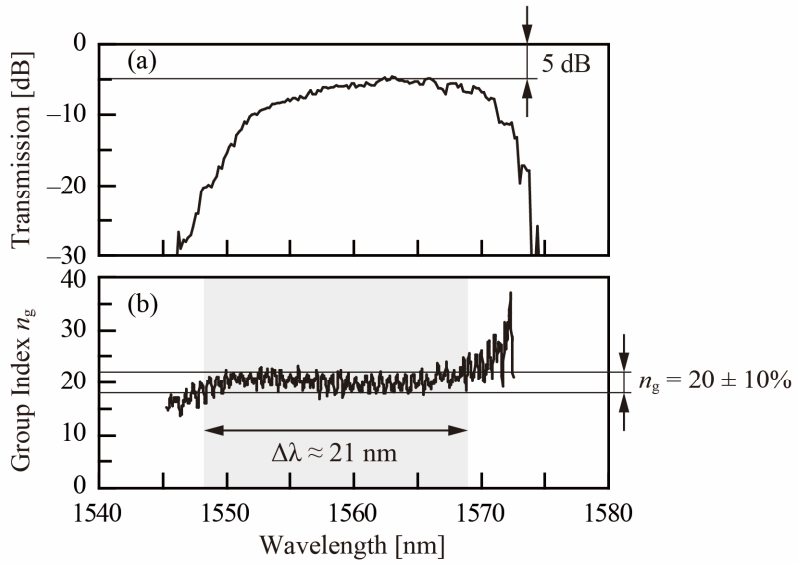

Figure 4.3 Fundamental optical characteristics of the 200-μm long LD device with s_3 = 90 nm. (a) Transmission spectrum. (b) n_g spectrum.

Figure 4.2 shows the fabricated device. The third-low shifted LSPCW of s_3 = 90 nm corresponding to 0.225a was employed as the device with the wide LD band. An interleaved p-n junction, whose interleaved depth and period are both 600 nm, was also employed in this device to obtain large $\Delta\phi$ for relatively low n_g of approximately 20. $\Delta\phi$ was determined by a simulation to increase by roughly 1.8-fold using the interleaved p-n junction with the 600-nm depth [4-2]. However, the frequency response can deteriorate because of the 2.2-fold larger C_{pn} compared with a linear p-n junction. The doping concentrations were $N_A = 9.5 \times 10^{17}$ cm^{-3} and $N_D = 5.7 \times 10^{17}$ cm^{-3} on this lot. The electrode design and

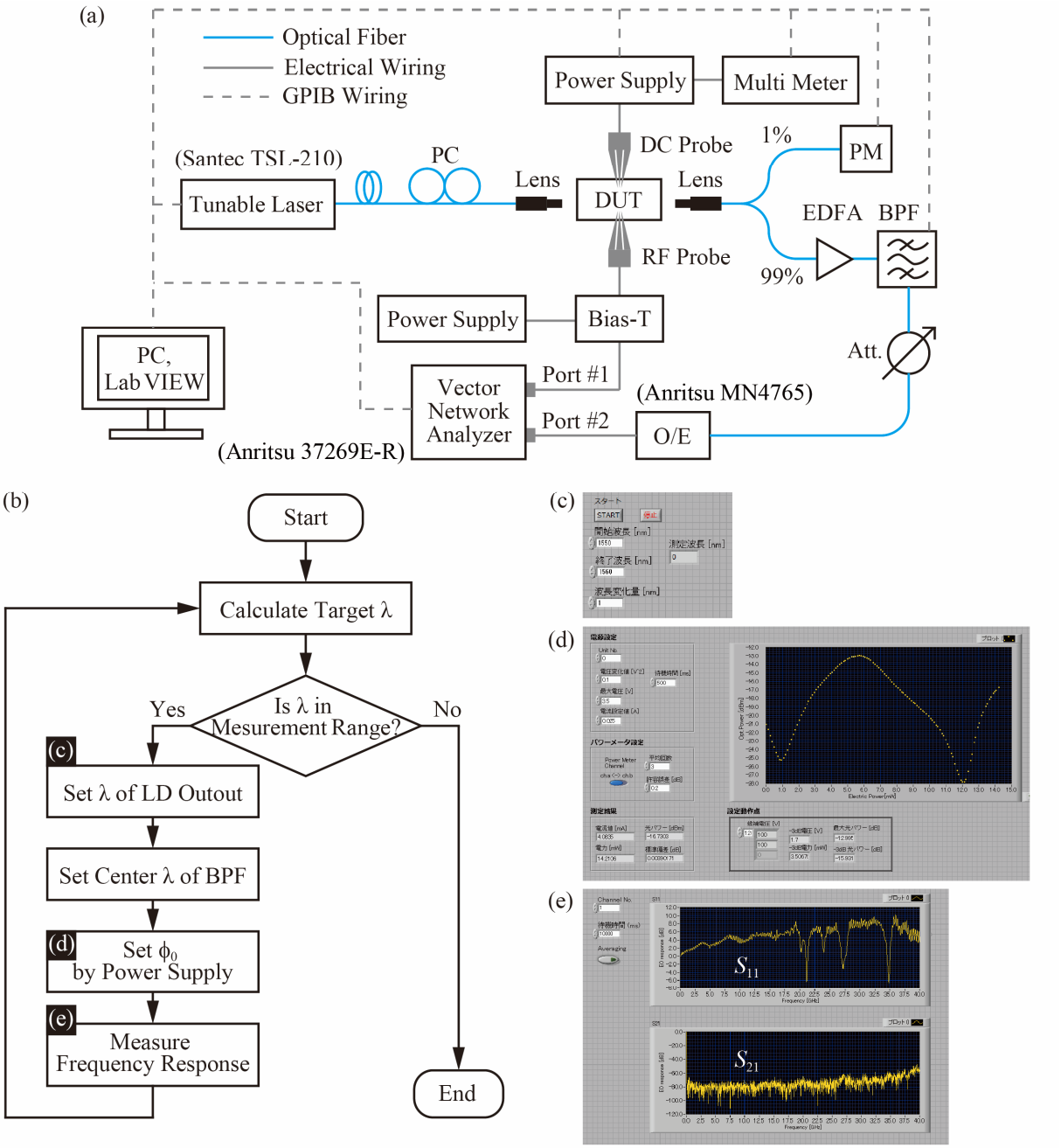

Figure 4.4 System for performing wide-wavelength-range frequency response measurements. (a) Measurement setup. (b) Flowchart of the program. (c)-(e) graphical user interface (GUI) of each part of the program.

the other components are the same as those of the 90-μm LD devices shown in Figure 3.4.

4. 2. 2 Fundamental Characteristics

I measured the transmission spectrum and the n_g spectrum of the LD LSPCW MZM. Figure 4.3(a) shows the measured transmission spectrum. The device exhibited a flat transmission band at λ = 1550-1570 nm with a maximum transmission of −5 dB. Again, this insertion loss includes the following, as explained in Section 3. 2. 2: 1) coupling loss between the Si waveguide and the PCW of ~1.5 dB in total, 2) the loss at the two MMI couplers of ~0.5 dB in total, and 3) six times bending loss of ~0.5 dB. Hence,

the remaining loss of ~2.5 dB corresponds to the propagation loss in the p-n incorporated PCW, in which n_g is approximately equal to 20. Figure 4.3(b) shows the measured n_g spectrum. The device exhibited a low-dispersion band with $n_g \approx 20$ and a bandwidth of $\Delta\lambda = 21$ nm; this value of $\Delta\lambda$ covered approximately 60% of the 35-nm wide C band and the normalized delay-bandwidth product [4-3] was calculated to be 0.27.

4. 3 Frequency Response Measurement

4. 3. 1 Measurement Setup

I constructed a wide-wavelength-range frequency response measurement system, as shown in Figure 4.4(a). The tunable laser (Santec Corp., TSL-210) output was coupled to the DUT via a SMF coupled with a lens and the SSC. Simultaneously, the small-amplitude sinusoidal signal output from Port #1 of the vector network analyzer (VNA, Anritsu Corp. 37269E-R) was applied to the DUT after combination of the output with a DC bias voltage of $V_{DC} = -2.2$ V using a bias tee. ϕ_0 of the MZI was adjusted to be $\pi/2$ by the DC voltage applied to the TO phase tuners. The modulated light was converted to an RF signal using an OE converter (Anritsu Corp. MN4765) with >70 GHz bandwidth after the amplification by the EDFA (Alnair Labs Corp., CPA-100-CL) and the filtering by the BPF (Alnair Labs Corp., CVF-220-CL). The converted RF signal was detected at Port #2 of the VNA to determine the EO response. Simultaneously, the reflected signal was also detected at Port #1 to determine the reflection characteristic S_{11}. The tunable laser, VNA, DC power supply, digital multimeter, PM, and BPF were connected to a computer via GPIB interfaces. These instruments were automatically controlled using a VI program in a LabVIEW development environment. Figure 4.4(b) shows a simple flowchart of the program, and Figure 4.4(c)-(e) shows the graphical user interface (GUI) of each part of the program. First, the program calculates a target λ based on a given initial λ and λ step. If the target λ is in the measurement range, then it is sent to the tunable laser and the BPF; else, the program ends. Next, ϕ_0 is set to be $\pi/2$ based on the measurement of the change in the output optical power with the heating power of the TO phase tuner. Subsequently, the frequency response is measured. The program executes this process until the ending condition is met.

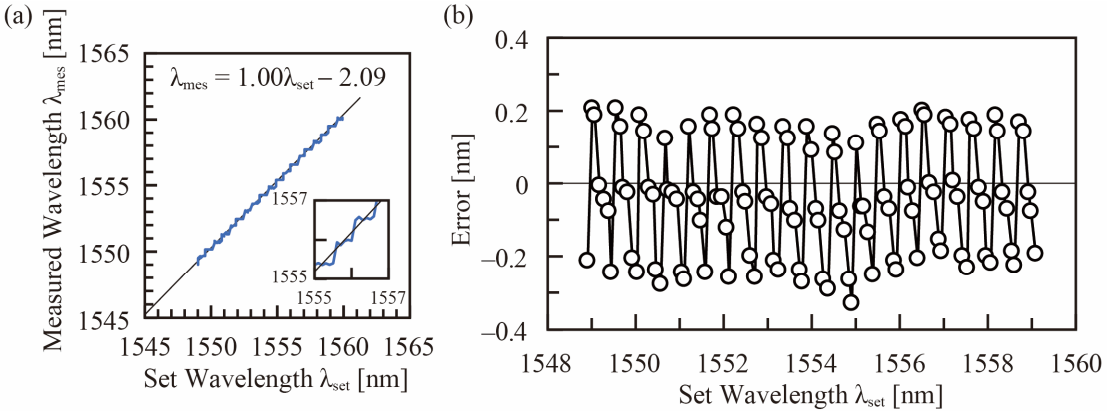

Figure 4.5 Lasing wavelength measurement of a tunable laser (Santec Corp., TSL-210). (a) Relationship between λ_{set} and λ_{mes}. Inset shows an expanded graph of a range from 1555 nm to 1557 nm. (b) Error between λ_{mes} and the regression line shown in (a).

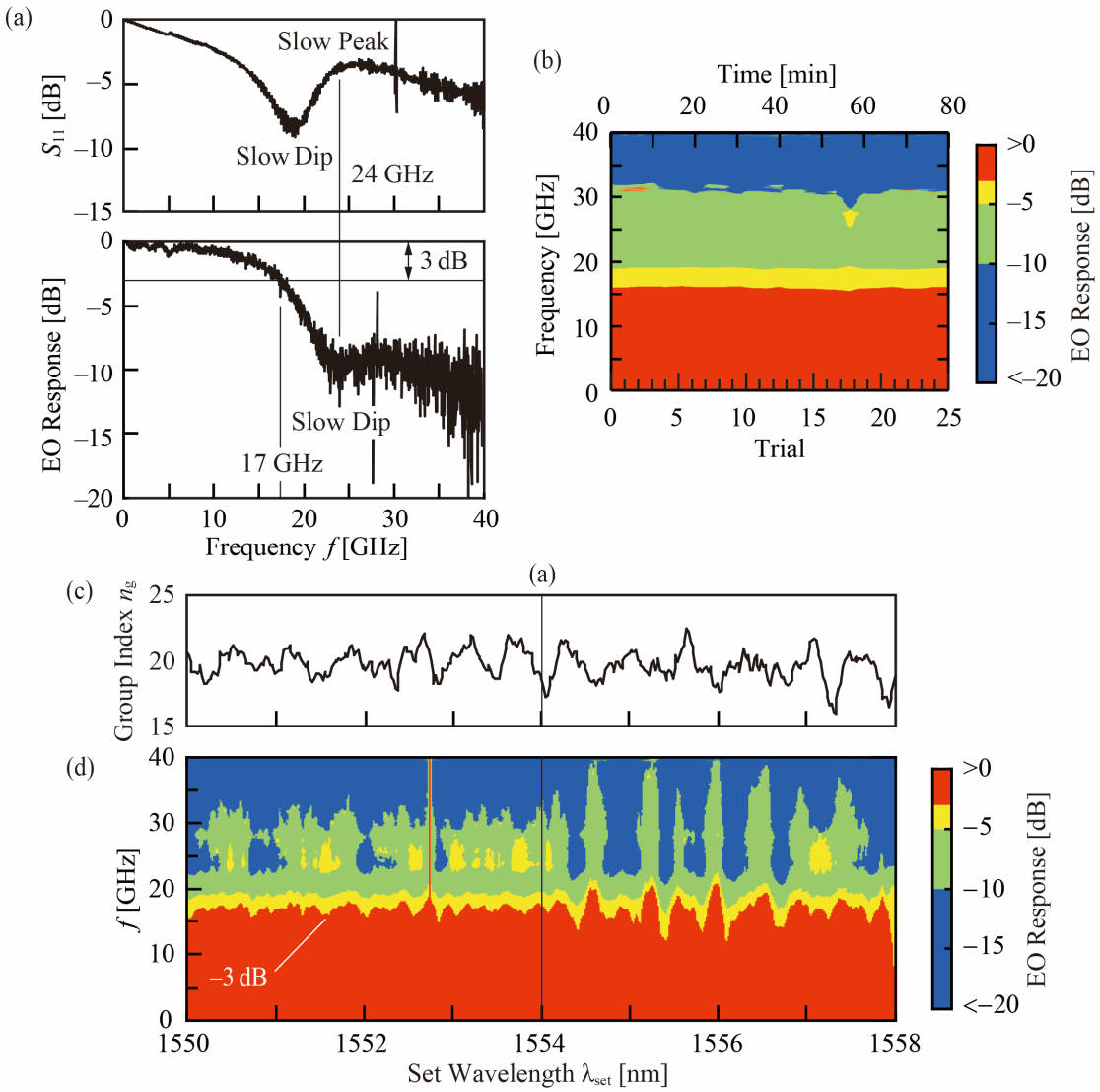

Figure 4.6 Results of a wide-wavelength-range frequency response measurement for V_{DC} = –2.2 V (a) Frequency response at λ = 1554 μm. (b) n_g spectrum. (c) Frequency response spectrum.

Before the frequency response measurement, I confirmed the accuracy of the output wavelength of the tunable laser by directly observing the lasing spectrum using an optical spectrum analyzer (Advantest Corp., Q8384) at the wavelength step of 0.1 nm. Figure 4.5(a) shows the measured wavelength λ_{mes} versus the set wavelength λ_{set}. The λ_{mes} was increased in proportional to λ_{set} according to $\lambda_{mes} = 1.00\ \lambda_{mes} - 2.09$. However, the λ_{mes} was step-wise changed at the microscale. The Figure 4.5(b) shows the error between the λ_{mes} and the regression line and it roughly ranged in the range of –0.2 nm to 0.2 nm. Therefore, I discuss the overall characteristics in the measurement wavelength range of the following measurement results but do not mention the relationship between n_g and the frequency response at a particular wavelength.

4. 3. 2 Results

First, I will describe the frequency response at a single frequency. Figure 4.6(a) shows a frequency response measured at λ = 1554 nm. The EO response and S_{11} exhibited a slow valley and peak at f = 23

GHz, respectively. The high reflectivity at the slow peak is thought to result in the low EO response at the valley. The value of f_{3dB} (determined to be 17 GHz) of the EO response was also affected by the slow valley as well as the RC time constant and the EO phase mismatch. In a finite element simulation using *Lumerical DEVICE*, the obtained resistance R_{pn} and capacitance C_{pn} values of the linear p-n junction were found to be 60 Ω and 50 fF, respectively [4-2]. Therefore, $f_{3dB} = 28.9$ GHz from $1/2\pi(R_{pn} + Z_g)C_{pn}$ was expected for a driver impedance $Z_g = 50$ Ω. The lower value obtained from the experiment indicates the existence of a dominant factor other than the RC time constant. I will discuss this factor in detail in Chapter5. Before moving to the wide-wavelength-range measurement, I confirmed reproducibility at a fixed wavelength. I repeatedly acquired the EO response at $\lambda = 1554$ nm 25 times (the whole acquisition processes took approximately 80 minutes). The fluctuation in the f_{3dB} fell below 1 GHz as shown in Figure 4.6(b). Therefore, if f_{3dB} changes over 1 GHz in the wide-wavelength-range measurement, it can be considered to be due to the wavelength characteristic of the device.

Next, I will discuss the wide-wavelength-range measurement. Figure 4.6(c) and (d) show the low-dispersion n_g spectrum and the frequency response spectrum at the λ step of 0.02 nm in the range of 1550–1558 nm. The interface between the red and yellow areas indicates f_{3dB}. This low-dispersion device exhibited a stable frequency response with f_{3dB} of 18 GHz, although it slowly fluctuated within

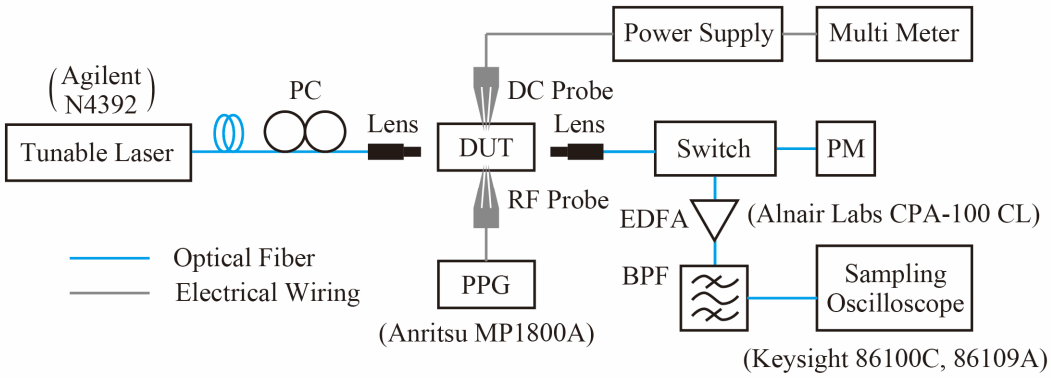

Figure 4.7 Measurement setup for 25-Gbps modulation.

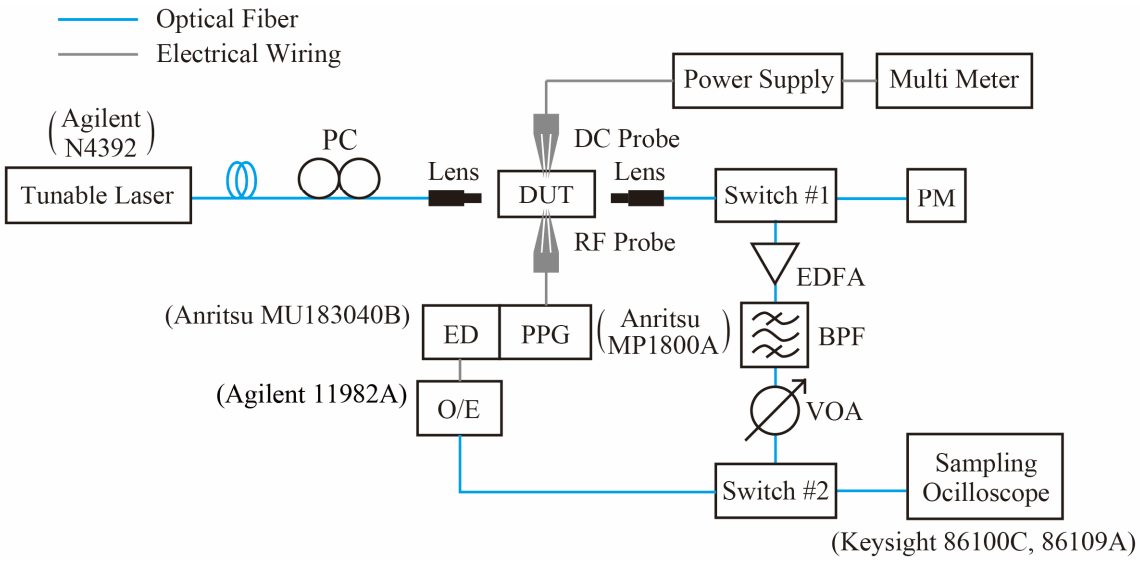

Figure 4.8 Setup for *BER* measurement.

the range of 12–21 GHz. I considered this fluctuation to be caused by the EO phase mismatch and to correspond to the oscillation in n_g. Therefore, I performed the further investigation described in Section 5. 1 used the PCW without the lattice shift that exhibits a larger n_g change.

4. 4 Modulation Characteristics

4. 4. 1 Measurement Setup

(a) Eye Pattern Observation

Figure 4.7 shows the measurement setup used to characterize the wide-wavelength-range modulation. This setup is the same as that in Figure 3.4. The input optical power and the RF signals are the also same: P_{LD} = 16.5 dBm, V_{pp} = 2.0 V, V_{DC} = –1.1 V, bit rate of 25 Gbps, and bit pattern length of 2^{31}-1 bits. Only the DUT and ϕ_0 were changed; ϕ_0 was set so that the average transmission power was decreased by 2 dB from the maximum transmission. Therefore, *ML* in this experiment can be estimated as 2 – *ER*/2.

(b) Bit Error Rate Measurement

The BER is defined as the rate of a number of detected bit errors N_{err} to the number of all transmitted bits N_{bit}. Using the BER, we can evaluate the communication quality of a total system. Figure 4.8 shows the setup used to perform *BER* measurements. The optical and electrical input parts were the same as those in Figure 4.7. The parameters were set as follows: P_{LD} = 16.5 dBm, V_{pp} = 2.0 V, V_{DC} = –1.1 V, and *BR* = 25 Gbps; the bit pattern length was 2^7-1 bits. The modulated signal was amplified and filtered by the EDFA and the BPF, respectively. A variable optical attenuator was also used to control the received optical power P_r at the EO converter (Agilent Technologies 11982A). After the EO conversion, the *BER* was measured using an error detector module (Anritsu Corp. MU183040B) combined with the PPG. We can only measure *BER* probabilistically over a limited measurement time *t*. The confidence level (CL) is given by [4-4]

$$CL = 1 - e^{-N_{bits} \cdot BER} = 1 - e^{-t \cdot BR \cdot BER} \tag{4.1}$$

In this measurement, I set t to be 20 s, which corresponds to a *BER* of 5.99×10^{-12} at a *CL* of 0.95. If I evaluate the *BER* of 1×10^{-12} in *t of* 20 s, the value of *CL* decreases to 0.39. Note that, I evaluated *BER* to be 1×10^{-12} if no error was detected in 20 s, although its *CL* was limited.

4. 4. 2 Results

(a) Eye Pattern Observation

Figure 4.9 shows the *ER* spectrum in the wavelength range of λ = 1549.5–1565.5 and the eye patterns at λ = 1551.5, 1559.5, and 1564.5 nm. This low-dispersion device exhibited nearly uniform eye patterns over the measurement range of Δλ of 16 nm, and the *ER* range was 2–3 dB. In the range of λ = 1549.5 – 1554.5 nm, *ER* was higher than 2.5 dB but gradually decreased with the decrease in n_g. The fluctuation in *ER* was caused by the oscillation in n_g, which ranges from 18 to 22. The n_g ratios to the center n_g of

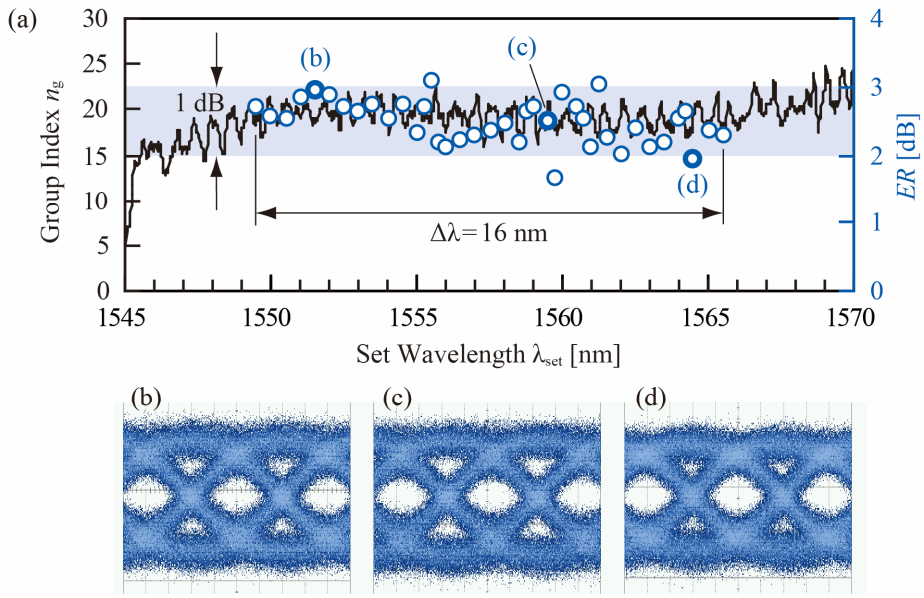

Figure 4.9 Results of the wide-wavelength-range 25-Gbps modulation. (a) n_g and *ER* spectra (b), (c), and (d) Eye patterns observed at λ = 1551.5, 1559.5, and 1564.5 nm.

20 were 0.9 and 1.1. To obtain *ER* of 2.5 dB (the center value of the *ER* range), $\Delta\phi$ of 0.180π is needed at $\phi_0 = \pi/2$. Furthermore, to obtain *ER* values of 2.0 dB and 3.0 dB, $\Delta\phi$ values of 0.145π and 0.216π are needed, and these $\Delta\phi$ values are 0.80-fold and 1.19-fold of the center $\Delta\phi$ of 0.180π, respectively. These $\Delta\phi$ ratios roughly agreed with the n_g ratios. In this experiment, *ER* was below 3 dB, which is one criterion; however, this result can be improved by using a larger *ML*, a larger V_{pp}, or a higher n_g. The eye amplitudes at the center of each eye patterns became smaller than the amplitudes between the '0' level and the '1' level because f_{3dB} is approximately 18 GHz, which is not high relative to the bitrate.

(b) Bit Error Rate Measurement

Figure 4.10(a) shows *BER* at each wavelength, and Figure 4.10(b) shows the *BER* and *ER* spectra measured at wavelength of λ = 1558 – 1560 nm with λ step of 0.2 nm. This spectral range is a part of the wavelength range covered in the previous section. The *BER* was found to linearly decrease with P_r, reaching 1×10^{-12} at almost all of the measurement wavelengths when P_r is equal to –5 dBm; furthermore, it reached 1×10^{-12} at all the measurement wavelengths when P_r increased to –4 dBm. An *ER* spectrum similar to that of Figure 4.9 was measured. The fluctuation of *BER* was found to correspond to the fluctuation of *ER* within 1 dB, as shown in Figure 4.10(b).

4. 4. 3 Discussion

In the above-described experiments, the low-dispersion device exhibited flat *ER* and *BER*, with slow fluctuations in each measurement wavelength range. The 1-dB fluctuation in *ER* also changed the error-free P_r power by 1 dB. Therefore, stable error-free operation can be achieved by adding a 1-dB margin to the *ER*. This additional margin can be accomplished in two ways while maintaining V_{pp} at 2 V: (1) giving additional *ML* (which was currently set to be as small as 0.5-1.0 dB) and (2) using higher n_g. However, because both (1) and (2) also increase the optical loss, the merit of the increase in *ER* must be

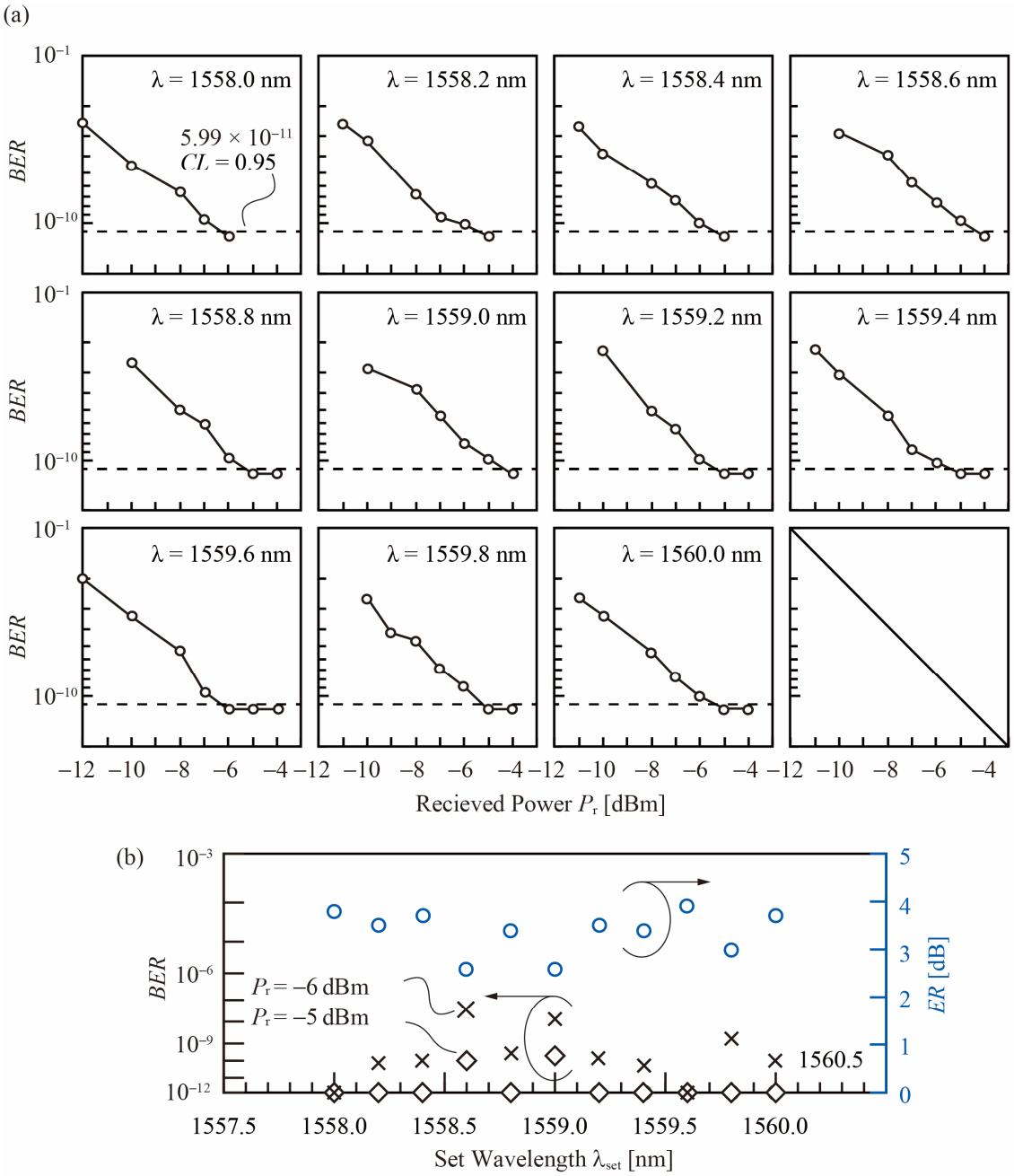

Figure 4.10 Results of the wide-wavelength-range *BER* measurement. (a) *BER* as a function of P_r at λ = 1558–1560 nm. (b) *BER* and *ER* spectra.

reconfirmed. Alternatively, this fluctuation can be reduced by an optimization of the coupling structure between the LSPCW and Si wire waveguides because it was caused by the Fabry-Pérot resonances in the LSPCW [4-5]. In this case, the required *ER* margin for stable error-free operation will also be reduced.

4. 5 Summary

I discussed the wide-band characteristics of a low-dispersion LSPCW MZM based on the evaluation of the frequency response, *ER*, and *BER*. The fabricated device experimentally exhibited a wide low-dispersion slow-light bandwidth of 21-nm. The frequency response measurement of the device revealed

f_{3dB} of ~18 GHz at V_{DC} = –1.1 V over the wavelength range of 1550–1556 nm. This value of f_{3dB} was affected by not only the RC time constant and the EO phase mismatch but also the undesired RF reflection. Nevertheless, the device exhibited stable 25-Gbps modulation over the wide wavelength range of $\Delta\lambda$ = 16 nm; however, *ER* fluctuated within ~1 dB because of the oscillation of n_g. This 1-dB fluctuation in *ER* also changed the error-free P_r by approximately 1 dB. Therefore, an additional 1-dB margin must be added to *ER* or a reduction of the oscillation of n_g must be achieved for stable error-free operation over a wide wavelength range: in this case, the error-free detection over $\Delta\lambda$ = 16 nm was achieved at P_r = –4 dBm.

References

[4-1] H. C. Nguyen, N. Yazawa, S. Hashimoto, S. Otsuka, and T. Baba, "Sub-100 μm Photonic Crystal Si Optical Modulators: Spectral, Athermal, and High-Speed Performance," *IEEE Journal of Selected Topics in Quantum Electronics*, vol. 19, no. 6, pp. 127–137, Nov. 2013, doi: 10.1109/JSTQE.2013.2265193.

[4-2] Y. Terada, T. Tatebe, Y. Hinakura, and T. Baba, "Si Photonic Crystal Slow-Light Modulators with Periodic p–n Junctions," *J. Light. Technol.*, vol. 35, no. 9, pp. 1684–1692, May 2017, doi: 10.1109/JLT.2017.2658668.

[4-3] T. Baba and D. Mori, "Slow light engineering in photonic crystals," *J. Phys. D*, vol. 40, no. 9, pp. 2659–2665, Apr. 2007, doi: 10.1088/0022-3727/40/9/s06.

[4-4] "How Do I Measure the Bit Error Rate (BER) to a Given Confidence Level on the J-BERT M8020A and the M8040A High-Performance BERT? | Keysight Technologies." https://www.Keysight Technologies.com/main/editorial.jspx?ckey=1481106&id=1481106&nid=-11143.0.00&lc=eng&cc=US (accessed Jun. 07, 2020).

[4-5] R. Sarkissian and J. O'Brien, "Group index oscillations in photonic crystal waveguides," *Applied Physics Letters*, vol. 105, no. 12, p. 121102, Sep. 2014, doi: 10.1063/1.4896519.

Chapter5
High-speed Operation by Electrooptic (EO) Phase Matching

5. 1 Experimental Observation of EO Phase Mismatch

I performed an experiment to clearly observe the EO phase mismatch. More specifically, I measured the frequency response of the dispersive PCW MZM, whose n_g is easily tunable by merely changing the operation wavelength; this device was used in Chapter3. The measurement system used is the same as that in Figure 4.4. The measurement conditions were also the same as those used previously: V_{DC} = –2.2 V, $\phi_0 = \pi/2$, and λ step of 0.02 nm. Figure 5.1 shows the n_g spectrum and the frequency response spectrum. This device exhibited n_g of 35‐80 in the wavelength range of λ = 1534‐1540 nm. f_{3dB} around 15 GHz was measured for $n_g \approx 35$; this value was found to decrease with the increase in n_g and was lower than 10 GHz on the average for n_g higher than 50. I confirmed the strong correlation between n_g and the frequency response. When the wavelength is changed, the optical transmission and k in the PCW are also changed; however, these characteristics do not affect the frequency response. Therefore, the observed degradation was apparently caused by the EO phase mismatch.

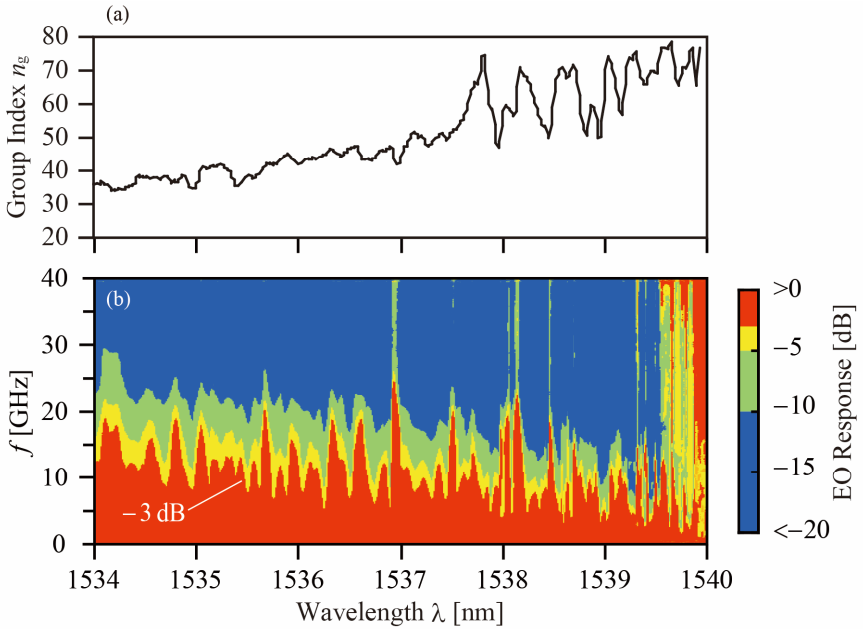

Figure 5.1 (a) n_g spectrum and (b) frequency response spectrum for V_{DC} = –2.2 V of the dispersive device.

5. 2 Meanderline Electrode

Figure 5.2 shows illustrations of how light and RF signals propagate in different devices. In the conventional Si rib waveguide, n_g is typically ~4, and the difference from the RF equivalent refractive index n_{RF} (which typically ranges in 2-4 [1-5]) is small. Therefore, the slow light and the RF signals copropagate over the long distance, and EO phase match is realized by n_{RF} tuning based on the traveling electrode design. In contrast, the large n_g of slow light ($n_g > 20$) is significantly larger than n_{RF}, and the relative position between the slow light and the RF signals becomes greater as the propagation proceeds. Thus, the n_{RF} tuning approach is simply not applicable to this problem. To solve this problem, I employed meanderline electrodes, as shown in Figure 5.3. In the first half section of the phase shifter, the slow light and RF signals copropagate, being displaced, as shown in Figure 5.3(a). In the second half section, the RF signal, which was delayed in the meanderline, copropagates with the slow light, as shown in Figure 5.3(b). A similar EO phase matching scheme in III-V compound modulator using ridge waveguide structure was previously reported in Ref. [5-6]; however, the slow-light device requires a much longer delay.

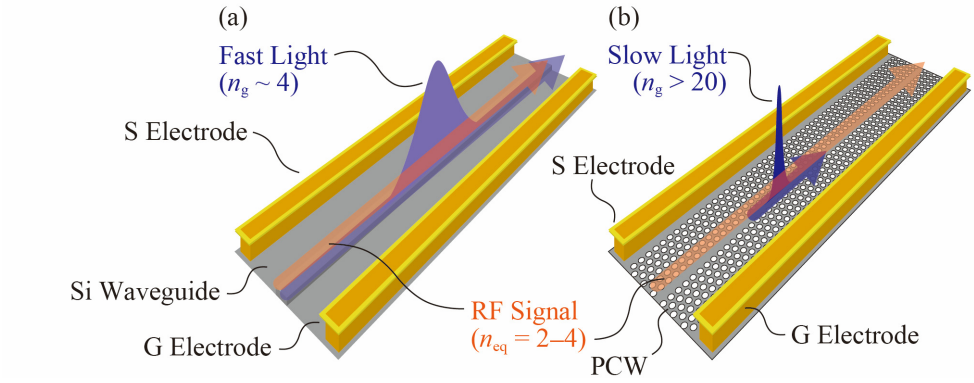

Figure 5.2 Illustrations of EO phase mismatch in (a) a fast-light waveguide and (b) a slow-light waveguide.

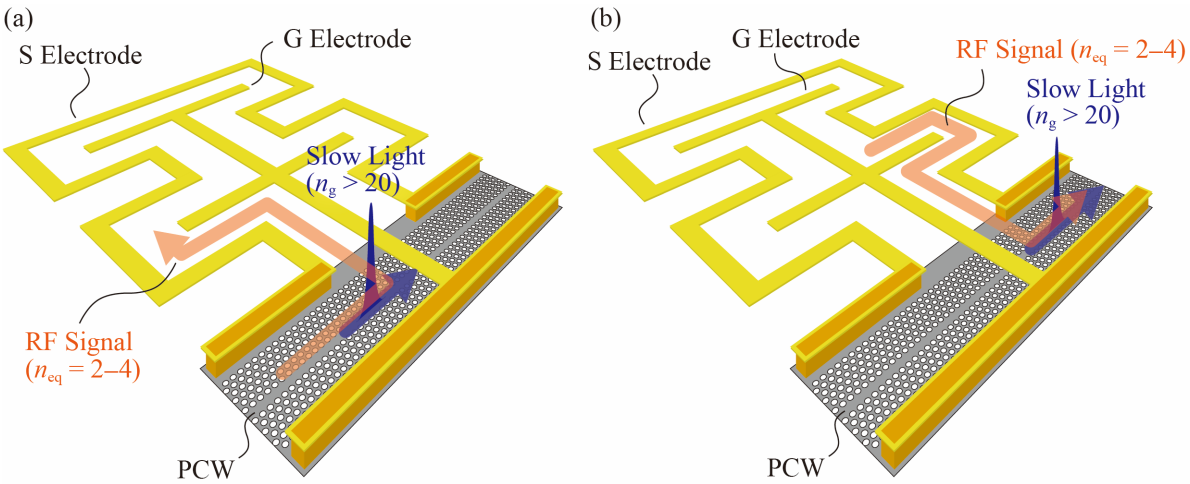

Figure 5.3 Illustrations of EO phase matching via a meanderline electrode. (a) First half section of a phase shifter. (b) Second section of a phase shifter.

5. 3 **Theoretical Analysis**

In this section, I describe the design of the meanderline electrodes and estimate the possible improvement in frequency response based on two equivalent circuits: traveling-wave electrode model [5-7],[5-8] and distributed-element circuit model.

5. 3. 1 Traveling-Wave Electrode Design

I analyzed the theoretical behavior of the slow light and RF signals in traveling-wave electrodes by considering the relevant wavenumbers and propagation velocities for the meanderline electrode. Figure 5.4(a) shows the traveling-wave circuit model of a normal electrode, in which the light and the RF signal propagate along the z axis. The averaged effective voltage V_{ave} that a wave packet of light receives in the phase shifter (length L) is expressed as follows:

$$V_{\mathrm{ave}}(f)=\frac{V_0}{1+\Gamma_{\mathrm{L}}e^{-2\gamma L}}\left(e^{j\varphi_+}\sin c\varphi_+ +\Gamma_{\mathrm{L}}e^{j\varphi_-}e^{-2\gamma L}\sin c\varphi_-\right) \tag{5.1}$$

$$\gamma=\alpha+j\beta_{\mathrm{RF}} \tag{5.2}$$

$$\varphi_{\pm}=\frac{(\beta_{\mathrm{o}}\pm j\gamma)L}{2} \tag{5.3}$$

$$\beta_{\mathrm{o}}=\frac{2\pi f n_{\mathrm{g}}}{c},\quad \beta_{\mathrm{RF}}=\frac{2\pi f n_{\mathrm{RF}}}{c} \tag{5.4}$$

where V_0 is the voltage at $z = 0$, Γ_g is the RF reflectivity at $z = 0$ (as seen from the transmission line side), Γ_L is the RF reflectivity at $z = L$ (as seen from the transmission line side), γ is the RF complex propagation constant whose α and β_{RF} are the attenuation constant and propagation constant, respectively, β_o is the modal propagation constant of light, and c is the speed of light. Here, the relation between V_0 and the output voltage from the signal generator is determined by the internal impedance of the signal generator Z_g and the input impedance Z_{in} and is expressed as follows:

$$V_0=\frac{Z_{\mathrm{in}}}{Z_{\mathrm{g}}+Z_{\mathrm{in}}}V_g \tag{5.5}$$

Here, Z_{in} is defined as follows:

$$Z_{\mathrm{in}}=\frac{V(z=0)}{I(z=0)} \tag{5.6}$$

where $V(z)$ and $I(z)$ are the voltage and current, respectively, at a position z. These are expressed using a forward-propagating voltage V_f, a back-propagating voltage V_b, and the characteristics impedance of the CPW, Z_0:

$$V(z)=V_{\mathrm{f}}e^{-\gamma z}+V_{\mathrm{b}}e^{\gamma z}=V_{\mathrm{f}}\left(e^{-\gamma z}+\Gamma_{\mathrm{L}}e^{\gamma(z-2L)}\right) \tag{5.7}$$

$$I(z)=\frac{V_{\mathrm{f}}}{Z_0}e^{-\gamma L}-\frac{V_{\mathrm{b}}}{Z_0}e^{\gamma L}=\frac{V_{\mathrm{f}}}{Z_0}\left(e^{-\gamma L}-\Gamma_{\mathrm{L}}e^{\gamma(z-2L)}\right) \tag{5.8}$$

Z_{in} is obtained by substituting these equations into Equation (5.6).

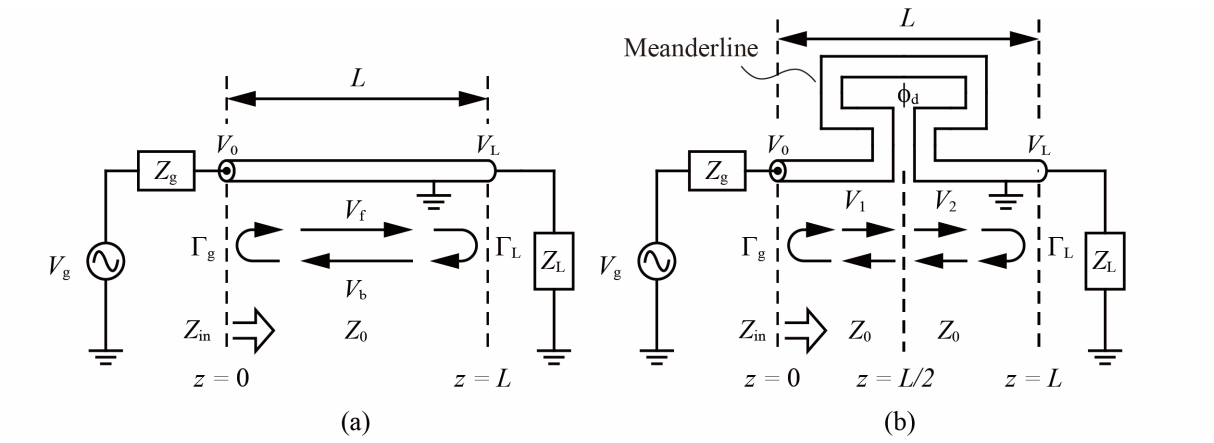

Figure 5.4 Traveling electrode models. (a) Normal electrode model. (b) Meanderline electrode model.

$$Z_{\text{in}} = \frac{V_{\text{f}}\left(1+\Gamma_{\text{L}}e^{-2\gamma L}\right)}{\frac{V_{\text{f}}}{Z_0}\left(1-\Gamma_{\text{L}}e^{-2\gamma L}\right)} = Z_0\frac{1+\Gamma_{\text{L}}e^{-2\gamma L}}{1-\Gamma_{\text{L}}e^{-2\gamma L}} \tag{5.9}$$

Here, Γ_g is expressed as:

$$\Gamma_{\text{g}} = \frac{Z_{\text{g}}-Z_0}{Z_{\text{g}}+Z_0} \tag{5.10}$$

Therefore, we obtain Equations (5.11) and (5.12) by transforming Equation (5.10).

$$1+\Gamma_{\text{g}} = \frac{2Z_{\text{g}}}{Z_{\text{g}}+Z_0} \tag{5.11}$$

$$1-\Gamma_{\text{g}} = \frac{2Z_0}{Z_{\text{g}}+Z_0} \tag{5.12}$$

Substituting Equation (5.9), Equation (5.5) can be written as Equation (5.13):

$$\begin{aligned} V_0 &= \frac{Z_0\dfrac{1+\Gamma_{\text{L}}e^{-2\gamma L}}{1-\Gamma_{\text{L}}e^{-2\gamma L}}}{Z_{\text{g}}+Z_0\dfrac{1+\Gamma_{\text{L}}e^{-2\gamma L}}{1-\Gamma_{\text{L}}e^{-2\gamma L}}}V_g \\ &= \frac{Z_0}{Z_{\text{g}}+Z_0}\frac{1+\Gamma_{\text{L}}e^{-2\gamma L}}{\dfrac{Z_{\text{g}}}{Z_{\text{g}}+Z_0}\left(1-\Gamma_{\text{L}}e^{-2\gamma L}\right)+\dfrac{Z_0}{Z_{\text{g}}+Z_0}\left(1+\Gamma_{\text{L}}e^{-2\gamma L}\right)}V_g \end{aligned} \tag{5.13}$$

Substituting Equation (5.11) and (5.12), this equation can be written as Equation (5.14):

$$\begin{aligned} V_0 &= \frac{Z_0}{Z_{\text{g}}+Z_0}\frac{1+\Gamma_{\text{L}}e^{-2\gamma L}}{\frac{1}{2}\left(1+\Gamma_{\text{g}}\right)\left(1-\Gamma_{\text{L}}e^{-2\gamma L}\right)+\frac{1}{2}\left(1-\Gamma_{\text{g}}\right)\left(1+\Gamma_{\text{L}}e^{-2\gamma L}\right)}V_g \\ &= \frac{Z_0}{Z_{\text{g}}+Z_0}\frac{1+\Gamma_{\text{L}}e^{-2\gamma L}}{1-\Gamma_{\text{g}}\Gamma_{\text{L}}e^{-2\gamma L}}V_g \end{aligned} \tag{5.14}$$

We obtain Equation (5.15) by substituting Equation (5.14) into Equation (5.1).

$$V_{\mathrm{ave}}(f)=\frac{Z_0}{Z_{\mathrm{g}}+Z_0}\frac{V_{\mathrm{g}}}{1-\Gamma_{\mathrm{g}}\Gamma_{\mathrm{L}}e^{-2\gamma L}}\left(e^{j\varphi_+}\,\mathrm{sinc}\,\varphi_+ +\Gamma_{\mathrm{L}}e^{j\varphi_-}e^{-2\gamma L}\,\mathrm{sinc}\,\varphi_-\right) \tag{5.15}$$

The degradation ratio of the EO response η can be obtained as Equation (5.16):

$$\eta=\left|\frac{V_{\mathrm{ave}}(f)}{V_{\mathrm{ave}}(0)}\right|=\left|\frac{1-\Gamma_{\mathrm{g}}\Gamma_{\mathrm{L}}}{\left(1+\Gamma_{\mathrm{L}}\right)\left(1-\Gamma_{\mathrm{g}}\Gamma_{\mathrm{L}}e^{-2\gamma L}\right)}\left(e^{j\varphi_+}\,\mathrm{sinc}\,\varphi_+ +\Gamma_{\mathrm{L}}e^{j\varphi_-}e^{-2\gamma L}\,\mathrm{sinc}\,\varphi_-\right)\right| \tag{5.16}$$

In the same manner, we can obtain V_{ave} and η of the meanderline model, whose meanderline length is L_{d} (shown in Figure 5.4):

$$V_{\mathrm{ave}}(f)=\frac{Z_0V_{\mathrm{g}}\left\{\left(e^{\frac{j\varphi_+}{2}}+e^{\frac{j3\varphi_+}{2}-j\varphi_{\mathrm{d}}}\right)\mathrm{sinc}\frac{\varphi_+}{2}+\Gamma_{\mathrm{L}}e^{-2\gamma L}\left(e^{\frac{j\varphi_-}{2}-j2\varphi_{\mathrm{d}}}+e^{\frac{j3\varphi_+}{2}-j\varphi_{\mathrm{d}}}\right)\mathrm{sinc}\frac{\varphi_-}{2}\right\}}{2(Z_0+Z_{\mathrm{g}})(1-\Gamma_{\mathrm{g}}\Gamma_{\mathrm{L}}e^{-2\gamma L})} \tag{5.17}$$

$$\eta(f)=\left|\frac{1-\Gamma_{\mathrm{g}}\Gamma_{\mathrm{L}}}{\left(1+\Gamma_{\mathrm{L}}\right)\left(1-\Gamma_{\mathrm{g}}\Gamma_{\mathrm{L}}e^{-2\gamma L}\right)}\left(\begin{array}{l}\left(e^{\frac{j\varphi_+}{2}}+e^{\frac{j3\varphi_+}{2}-j\varphi_{\mathrm{d}}}\right)\mathrm{sinc}\dfrac{\varphi_+}{2}\\ +\Gamma_{\mathrm{L}}e^{-2\gamma L}\left(e^{\frac{j\varphi_-}{2}-j2\varphi_{\mathrm{d}}}+e^{\frac{j3\varphi_+}{2}-j\varphi_{\mathrm{d}}}\right)\mathrm{sinc}\dfrac{\varphi_-}{2}\end{array}\right)\right| \tag{5.18}$$

where ϕ_{d} is the delayed RF phase in the meanderline, and is given as follows:

$$\varphi_{\mathrm{d}}=\frac{2\pi f n_{\mathrm{d}}L_{\mathrm{d}}}{c} \tag{5.19}$$

where n_{d} is the equivalent index of the meanderline. Assuming that the phase shifter and the signal generator constitute a simple RC circuit, the transfer function of the voltage applied to the depletion region $G(f)$ is given by

$$G(f)=\frac{1}{\sqrt{1+\left\{2\pi f\left(Z_{\mathrm{g}}+R_{\mathrm{pn}}\right)C_{\mathrm{pn}}\right\}^2}} \tag{5.20}$$

where R_{pn} and C_{pn} are the resistance and capacitance of the p-n junction, respectively. Therefore, the EO response EO S_{21} considering both EO phase mismatch and RC time constant is obtained as Equation (5.21).

$$\mathrm{EO}\ \ S_{21}(f)=20\cdot\log_{10}\left(G(f)\cdot\eta(f)\right) \tag{5.21}$$

5. 3. 2 Distributed Constant Circuit

γ and Z_0 must be determined for practical calculation; these values are obtained using a distributed-constant equivalent circuit. Figure 5.5(a) shows the correspondence between the structure of the phase shifter and the proposed distributed-constant equivalent circuit. the electrical elements are defined as follows: the resistance and capacitance per length of a p-n junction are R_{p} and R_{n}, respectively; the total resistance per length of the p-n junction is $R_{\mathrm{pn}} = R_{\mathrm{p}} + R_{\mathrm{n}}$; and the resistance, capacitance, and inductance per length of the CPW are R_{CPW}, C_{CPW} and L_{CPW}, respectively. Note that I used R_{pn} and C_{pn} as just the resistance and capacitance, respectively, in previous sections, whereas I use R_{pn} and C_{pn} as the resistance

per length and capacitance per length, respectively, in this section.

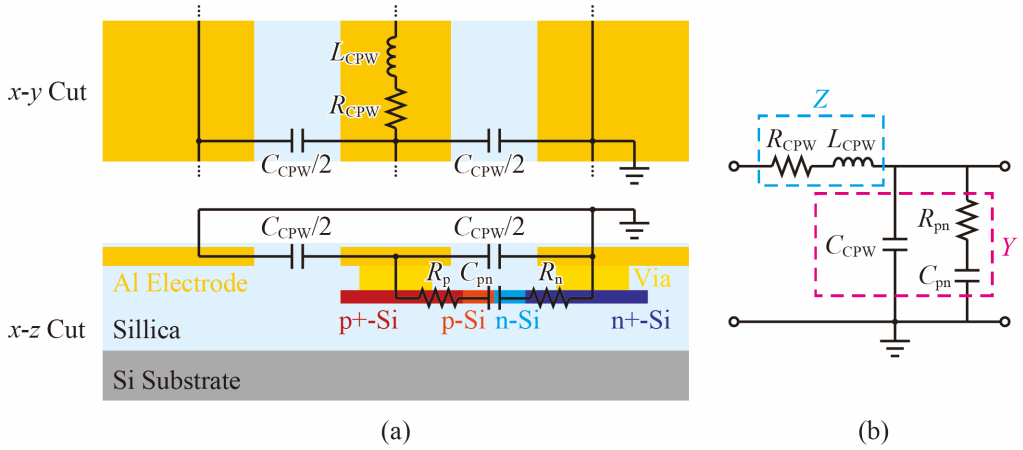

Figure 5.5 Distributed-constant circuit model. (a) Correspondence between the CPW structure and each element. (b) Circuit diagram.

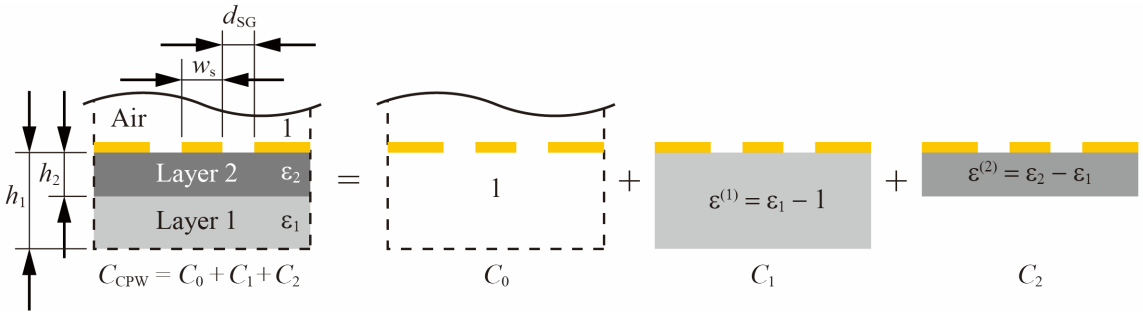

Figure 5.6 Illustration of the layer division of a CPW on SOI.

Figure 5.5(b) shows the proposed distributed-constant equivalent circuit of the phase shifter. The serial impedance Z and parallel admittance Y of this circuit are written as follows:

$$Z = R_{CPW} + j\omega L_{CPW} \tag{5.22}$$

$$Y = j\omega C_{CPW} + \frac{j\omega C_{pn}}{1 + j\omega R_{pn} C_{pn}} \tag{5.23}$$

where the ω is the angular frequency of a signal. In the same manner, Z and Y for a simple CPW without a p-n junction are written as follows:

$$Z = R_{CPW} + j\omega L_{CPW} \tag{5.24}$$

$$Y = j\omega C_{CPW} \tag{5.25}$$

C_{CPW} of a CPW on the multilayer substrate is obtained as the sum of the capacitances calculated based on the permittivity minus that of the background [5-9]. As shown in Figure 5.6, the two-layer substrate can be divided into three layers, including the air above the CPW. In the case of the SOI wafer, Layer 1 and Layer 2 correspond to the Si substrate and the BOX layer, respectively. The layer capacitance per length of the CPW (whose electrode thickness is negligible and whose G electrode width is infinity) surrounded by air C_0 is given by Equation (5.26) [5-9]:

$$C_0 = 4\varepsilon_0 \frac{K(k_0)}{K(k_0')} \tag{5.26}$$

$$k_0 = \frac{w_s/2}{w_s/2 + d_{GS}} \tag{5.27}$$

$$k_0' = \sqrt{1 - k_0^2} \tag{5.28}$$

where $K(k)$ is a complete elliptic integral of the first kind and is given by Equation (5.29):

$$K(k) = \int_0^{\pi/2} \frac{1}{\sqrt{1 - k^2 \sin^2 \theta}} d\theta \tag{5.29}$$

Similarly, the i th layer' capacitance C_i (i = 1, 2) is given by Equation (5.30):

$$C_i = 2\varepsilon_0 \varepsilon^{(i)} \frac{K(k_i)}{K(k_i')} \tag{5.30}$$

$$\varepsilon^{(1)} = \varepsilon_1 - 1 \tag{5.31}$$

$$\varepsilon^{(2)} = \varepsilon_2 - \varepsilon_1 \tag{5.32}$$

$$k_i = \frac{\sinh\left(\frac{\pi w_s / 2}{2h_i}\right)}{\sinh\left(\frac{\pi (w_s / 2 + d_{GS})}{2h_i}\right)} \tag{5.33}$$

where ε_i is the capacitance of the i th layer. In Ref. [5-7], ε_1 less than or equal to ε_2 is assumed; however, ε_1 is larger than ε_2 for the SOI wafer. Therefore, I allow $\varepsilon^{(2)}$ to be a negative value. Thus, we can obtain C_{cpw} as follows:

$$C_{CPW} = C_0 + C_1 + C_2 \tag{5.34}$$

In this condition, we obtain the equivalent permittivity of the CPW ε_{eq} as follows:

$$\varepsilon_{eq} = \frac{C_{CPW}}{4\varepsilon_0 \frac{K(k_0)}{K(k_0')}} \tag{5.35}$$

Furthermore, if the CPW is lossless, L_{cpw} is given as follows:

$$L_{CPW} = \frac{1}{c^2 \cdot C_0} \tag{5.36}$$

γ is written as Equation (5.37) using Z and Y [8]:

$$\gamma = \alpha + j\beta = \sqrt{ZY} \tag{5.37}$$

We obtain Equation (5.38) by substituting Equations (5.22) and (5.23) into Equation (5.37):

$$\gamma = \sqrt{\left(R_{CPW} + j\omega L_{CPW}\right)\left(j\omega C_{CPW} + \frac{j\omega C_{pn}}{1 + j\omega R_{pn} C_{pn}}\right)} \tag{5.38}$$

If we substitute Equations (5.24 (5.24) and (5.25) into the above equation, we obtain the complex propagation constant of the CPW without the p-n junction γ_{CPW} as follows:

$$\gamma_{CPW} = \sqrt{j\omega C_{CPW}\left(R_{CPW} + j\omega L_{CPW}\right)} \tag{5.39}$$

α and β are obtained as the real part and imaginary part, respectively, of γ or γ_{CPW}. Using β, the phase velocity of the RF signal ν_{RF} is written as follows:

$$\nu_{RF} = \frac{\omega}{\beta} \tag{5.40}$$

Therefore, we obtain n_{RF} as follows:

$$n_{RF} = \frac{c}{\nu} = \frac{c\beta}{\omega} \tag{5.41}$$

Furthermore, Z_0 is expressed using Z and Y as follows:

$$Z_0 = \sqrt{\frac{Z}{Y}} \tag{5.42}$$

and is expressed by substituting Equations (5.22) and (5.23) into the above equation as follows:

$$Z_0 = \sqrt{\frac{R_{CPW} + j\omega L_{CPW}}{j\omega C_{CPW} + \dfrac{j\omega C_{pn}}{1 + j\omega R_{pn} C_{pn}}}} \tag{5.43}$$

When we substitute Equations (5.24) and (5.25) into the above equation, we obtain Z_0 of the CPW without the p-n junction:

$$Z_0 = \sqrt{\frac{R_{CPW} + j\omega L_{CPW}}{j\omega C_{CPW}}} \tag{5.44}$$

5. 3. 3 *S* Parameter

Equations of electrical *S* parameters are derived based on the traveling waveguide theory. Here, I describe only the absolute value of the *S* parameters which showing the amplitude of the *S* parameters. Γ_L is expressed using Z_L and Z_0 as follows:

$$\Gamma_L = \frac{Z_L - Z_0}{Z_L + Z_0} \tag{5.45}$$

Using Γ_L, Z_{in} is expressed as follows:

$$Z_{in} = Z_0 \frac{1 + \Gamma_L e^{-2\gamma L}}{1 - \Gamma_L e^{-2\gamma L}} \tag{5.46}$$

The total reflectivity between the device and the input circuit Γ_{in} is obtained using Z_{in} and corresponds to S_{11}.

$$S_{11} = \left|\Gamma_{\text{in}}\right| = \left|\frac{Z_{\text{in}} - Z_{\text{g}}}{Z_{\text{in}} + Z_{\text{g}}}\right| \tag{5.47}$$

I also derive S_{21} below. The transmission coefficient of voltage T_{in} is given as follows:

$$\left|T_{\text{in}}\right| = \left|1 + \Gamma_{\text{in}}\right| = \left|\frac{2Z_{\text{in}}}{Z_{\text{in}} + Z_{\text{g}}}\right| \tag{5.48}$$

Moreover, the propagation loss in the CPW η_{RF} is given as follows:

$$\eta_{\text{RF}} = e^{-\alpha L} \tag{5.49}$$

We can obtain S_{21} as the product of T_{in} and η_{RF}.

$$S_{21} = \left|T_{\text{in}}\right| \cdot \eta_{\text{RF}} = \left|\frac{2Z_{\text{in}}}{Z_{\text{in}} + Z_{\text{g}}}\right| e^{-\alpha L} \tag{5.50}$$

5. 3. 4 Calculation Results

(a) Electrical Properties of the CPW and the *S* Parameters

I estimated the electrical properties of the CPW by substituting the structural parameters and the simulated values of R_{pn} and C_{pn} into the equations described in Section 5. 3. 1, 5. 3. 2, and 5. 3. 3. First, I numerically calculated C_{CPW}, L_{CPW}, and ε_{eq} using the parameters provided in Table 5.1. Figure 5.7 shows the results. C_{CPW} increases with an increase in w_{s} and decreases with an increase in d_{GS}. The typical values of devices used in this chapter are w_{s} = 10 μm and d_{GS} = 7 μm, and C_{CPW} is calculated to be 0.13 pF/mm based on these values. This capacitance per unit length corresponds to 26 fF for L = 200 μm. Furthermore, L_{CPW} decreases with an increase in w_{s} and increases with an increase in d_{GS}. For w_{s} = 10 μm and d_{GS} = 7 μm, L_{CPW} is calculated to be 0.38 nH/mm, which corresponds to 76 pH for L = 200 μm. ε_{eff} increases with increases in both w_{s} and d_{GS}. To ensure $d_{\text{GS}} \geq 1$ μm, ε_{eff} must be from 3.0 to 5.7; ε_{eff} = 4.5 for w_{s} = 10 μm and d_{GS} = 7 μm.

Based on these electrical properties, I calculated α, n_{RF}, and Z_0 for a CPW without a p-n junction and a p-n loaded CPW. Table 5.2 shows the parameters used. Figure 5.8 (a), (b), (c) show the calculated α, n_{RF}, and Z_0. The CPW without a p-n junction exhibited α = 0.4 dB/mm, n_{RF} = 2.1, and $|Z_0|$ = 54 Ω for almost the entire calculated frequency range. Compared with these values, α and n_{RF} increased and Z_0 decreased for the p-n loaded CPW. α strongly depends on the frequency and is 2.2 dB/mm and 5.3 dB/mm at f = 20 GHz and 40 GHz, respectively, and corresponds to 0.44 dB and 1.6 dB, respectively,

Table 5.1 Parameters used in the calculation of the electrical properties.

Parameter	Value
ε_1	4
ε_2	12
h_1	3000 μm
h_2	3 μm
w_{s}	4, 7, 15 μm
d_{SG}	4, 10, 15 μm

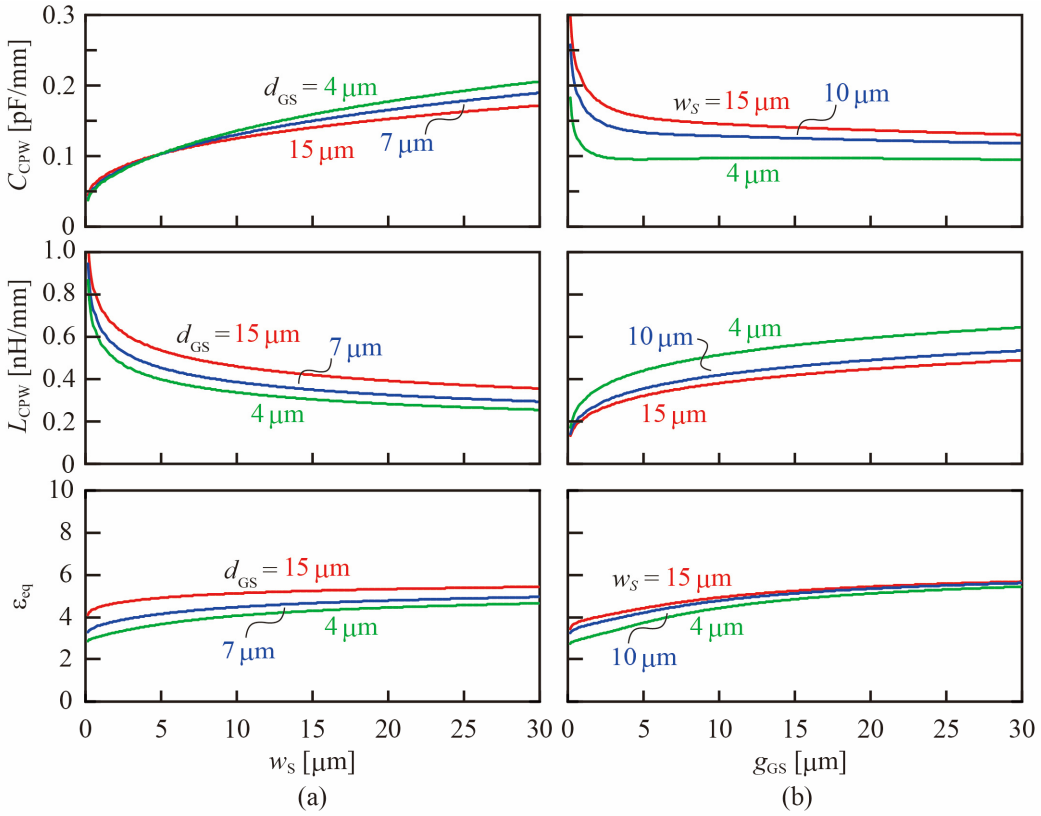

Figure 5.7 Calculated C_{CPW}, L_{CPW}, and ε_{eq} in a CPW. (a) w_S dependence. (b) g_{GS} dependence.

Table 5.2 Paramters used in the calculation of the S parameters.

Parameter	Value
ε_1	4
ε_2	12
ε_{eq}	4.5
h_1	3000 μm
h_2	3 μm
w_s	10 μm
d_{SG}	7 μm
R_{CPW}	5 Ω/mm
C_{CPW}	0.13 pF/mm
L_{CPW}	0.38 nH/mm
R_{pn}	12 Ω·mm (= 60 Ω × 0.2 mm)
C_{pn}	0.25 pF/mm (= 0.05 pF/0.2 mm)
Z_g	50 Ω
Z_L	50 Ω

for L = 0.2 μm. n_{RF} ranges from 3.2 to about 4, which is much smaller than $n_g \sim 20$, although it is approximately double of that of a CPW without a p-n junction. Z_0 was found to be ~35 Ω, which is smaller than $Z_L = Z_g = 50$; this case corresponds to $\Gamma_L = \Gamma_g = 0.18$. Furthermore, I calculated the S parameters, and Figure 5.8 (d) and (e) show the calculated S_{11} and S_{21}. S_{21} is higher than –3 dB, even at f = 40 GHz; this result includes 1.1-dB propagation loss and 1.6-dB reflection loss. f_{3dB} of the EO response due to S_{21} can be estimated to be a 6.4-dB cutoff frequency. The calculated S_{21} exhibited a 6.4-

dB cutoff frequency much higher than 40 GHz. Therefore, this parameter does not strongly limit the total f_{3dB}.

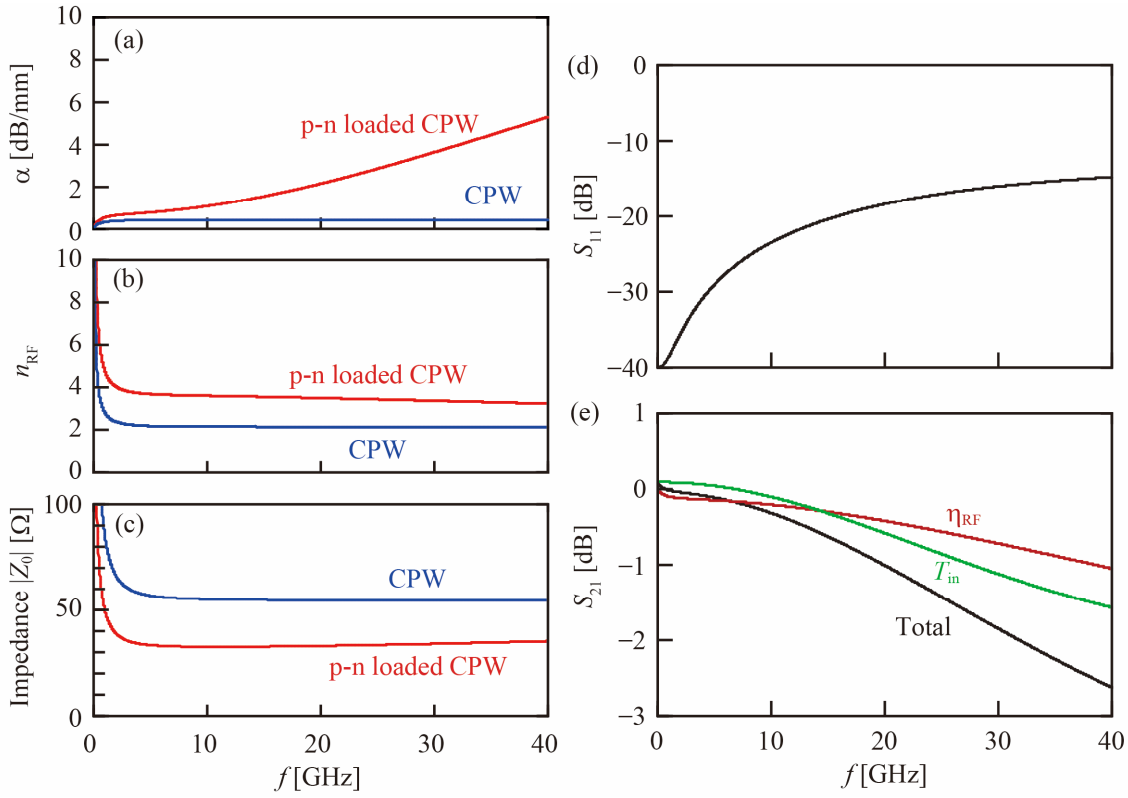

Figure 5.8 Calculated characteristics of the CPW. (a) α. (b) n_{RF}. (c) Z_0. (d) S_{11}. (e) S_{21}.

Table 5.3 Parameters used in the calculation of the frequency response.

Parameter	Value
ε_1	4
ε_2	12
h_1	3000 μm
h_2	3 μm
w_s	4, 7, 15 μm
d_{SG}	4, 10, 15 μm

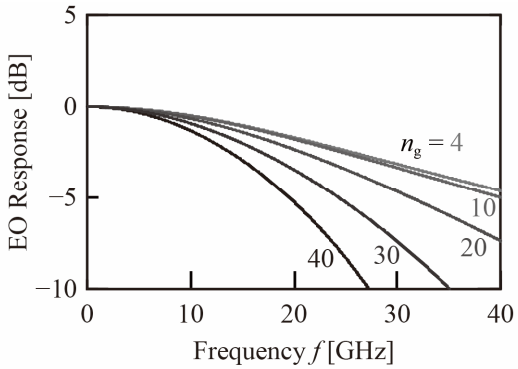

Figure 5.9 Calculated frequency response for n_g = 4, 10, 20, 30, and 40.

(b) EO Response

Figure 5.9 shows the calculated response for different n_g, where $\Gamma_g = \Gamma_L = 0$, $n_{RF} = 4$, $\alpha = 0$, $R_{pn} = 12\ \Omega \cdot$mm, and $C_{pn} = 0.25$ pF/mm. I set $\Gamma_g = \Gamma_L = 0$ and $\alpha = 0$ to focus on the EO phase mismatch. When $n_g = 4$ (phase matching condition), the response is determined only by $G(f)$, and $f_{3dB} = 28.9$ GHz, as previously mentioned; this value decreases to 15.1 GHz when n_g increases to 40. Thus, the frequency response affected by the phase mismatch was theoretically predicted even for a device length of only 200 μm. Figure 5.10(a) shows the calculated frequency response for different L_d. I set n_d to be 2 considering the calculation result in 5. 3. 4(a). For $n_g = 20$, the response is improved as L_d is increased

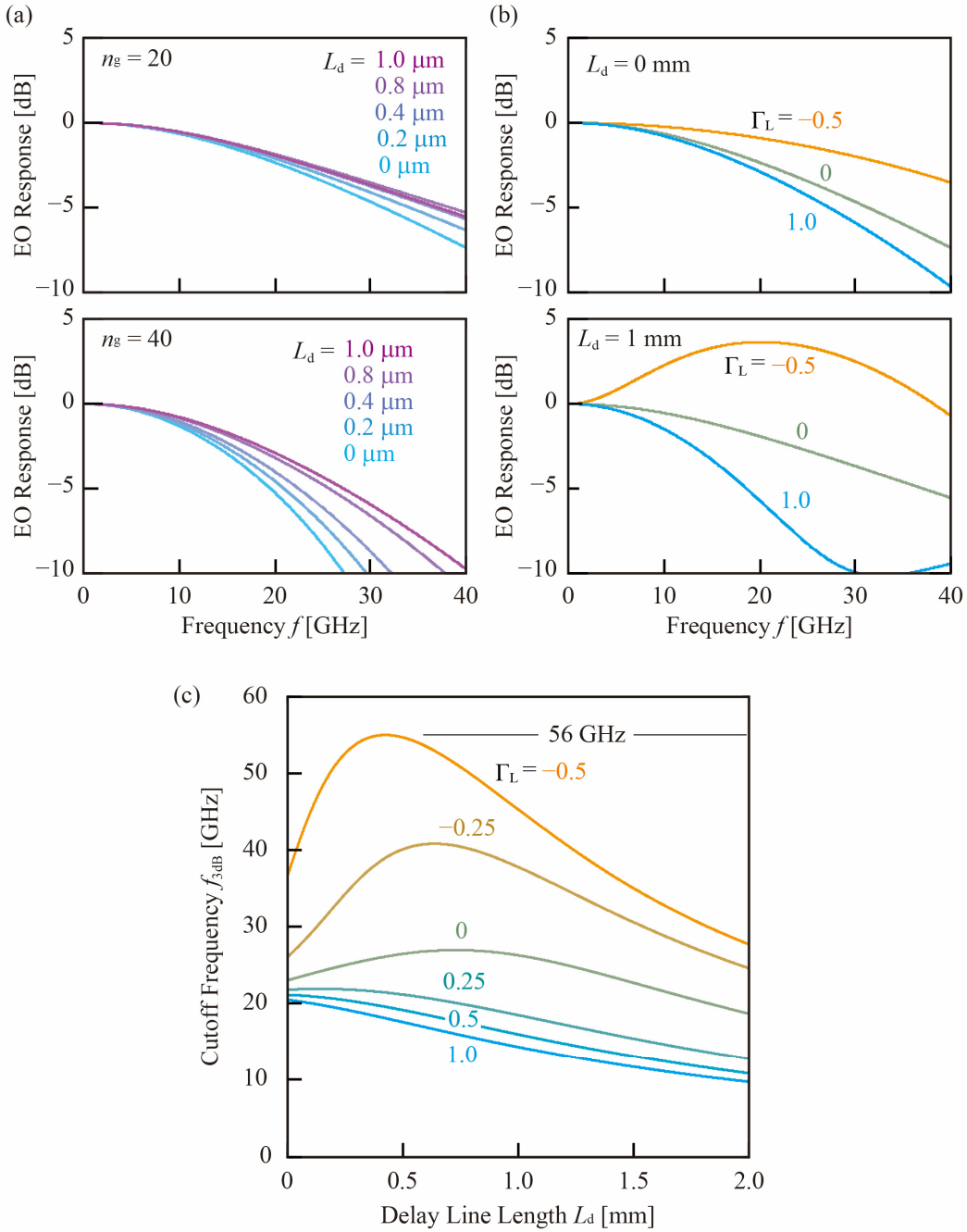

Figure 5.10 (a) Calculated frequency response. (a) L_d dependence. (b) Γ_L dependence. (c) f_{3dB} as a function of L_d.

from 0 mm to 0.8 mm, but it is rather degraded at L_d = 1.0 mm, i.e., the phase mismatch becomes larger again. For n_g = 40, the response is simply improved by a longer L_d. Γ_L also influences the response greatly because slow light in the phase shifter is modulated not only by the forward-propagating RF signals but also by the backward ones. Depending on their phase relationship, the modulation by the forward wave is strengthened or canceled by the backward wave. Even without reactance components, Γ_L can be a negative value that cancels the forward wave. Figure 5.10(b) shows the calculated response for Γ_g = 0 and different Γ_L. When L_d = 0 mm, the response is simply improved by a negative Γ_L because the low-frequency components are particularly small and the high-frequency components are relatively high. When L_d = 1.0 mm, the response around 20 GHz is particularly emphasized for Γ_L = –0.5. Figure 5.10(c) summarizes the L_d dependence of f_{3dB} for different Γ_L. The negative Γ_L improves the f_{3dB} significantly; a high f_{3dB} of 56 GHz and 40 GHz are estimated for Γ_L = –0.5 and –0.25, respectively, at their respective optimum L_d.

5. 4 Suppression of the Coupled Slotline Mode

Before I designed the meanderline electrodes, I investigated the cause of the slow peak and dip in the measured S_{11} and EO response that appeared in Figure 4.6 to improve the EO response via the meanderline electrode. Some research groups have reported a similar peak and dip in the frequency response [5-3],[5-10] and found it to be generated by an excitation of the coupled slotline (CSL) mode [5-11]. This mode can be excited in a CPW whose electrical potential in two G electrodes are unbalanced. This mode originates from the asymmetric structure of the CPW including the p-n diode; this structure is loaded on the one side of the G-S-G structure. The simplest way to solve this problem is the commonization connecting with the two G electrodes because the electrical potential in one conductor is equipotential, assuming the resistance is negligible.

For the simple investigation, I attempted Al wire bonding on CPWs of two fabricated devices as shown in Figure 5.11. I used not only the device with the one set of G-S-G-S-G probing pads used in the aforementioned experiments but also the device with the two sets of probing pads. First, I manually peeled the top-coated SiO_2 on the Al electrodes by scratching with a pair of tweezers. Figure 5.11(a) and (b) show the devices after the peeling process. Subsequently, I bonded the Al wires on the G electrodes using an ultrasonic bonder. Figure 5.11(c) and (d) shows the device after the bonding. I measured the electrical frequency response of the wire-bonded devices using the measurement setup shown in Figure 5.12(a). The devices were simply connected with a VNA via the coaxial cables and the RF probes. Figure 5.12(b) shows the measured frequency response of the device with the one set of probing pads. In this measurement, the upper RF probe in Figure 5.12(a) was detached from the device and opened. The slow valley and dip were eliminated, and a smooth S_{11} was observed. In the same manner, the valleys and peaks in the S_{11} and S_{21} of the device with the two sets of the probing pads were suppressed.

Although the wire bonding approach was effective for the suppression of the CSL mode, it is physically unstable and needs an additional process. Therefore, I designed devices with/without the G commonization and fabricated them on a SOI with t_{Si} = 210, as shown in Figure 5.13. In the device without the commonization (Figure 5.13(a)), the three G electrodes were designed to be separated from each other. In contrast, in the device with the commonization (Figure 5.13(a)), the G electrodes were connected with the commonization lines (each with a width of 20 μm) outside the S electrodes. In addition, these devices have two sets of G-S-G-S-G RF probing pads (ten pads in total), allowing

measurement of the electrical S_{11} and S_{21} of the single phase shifter using the two pairs of G-S-G probing pads (six pads in total) in the G-S-G-S-G configuration. Figure 5.13(c) and (d) show the fabricated devices. Dopants of $N_A = 9.5 \times 10^{17}$ cm^{-3} and $N_D = 5.7 \times 10^{17}$ cm^{-3} were implanted on this lot. Figure 5.14(a) shows the measurement setup. The two ports of the VNA were connected the single phase shifter via the two pairs of G-S-G probing pads and the G-S-G RF probe. Figure 5.14(b) shows the measured *S* parameters. The device without commonization exhibited unsmooth *S* parameters that exhibit a slow peak and valley at *f* of ~20 GHz and ~26 GHz, respectively. These frequencies almost correspond to the peak and dip of S_{11} shown in Figure 4.6(a). In contrast, the peaks and valleys were suppressed for the device with the commonization, with flatter *S* parameters obtained. I also show the calculated line fitted to the device with the commonization in Figure 5.14(b). These curves were calculated using the following parameters: $R_{pn} = 30$ Ω·mm (= 150 Ω · 0.2 mm), $C_{pn} = 0.3$ pF/mm (= 0.06 pF/0.2 mm), and the other parameters identical to those in Table 5.2. As these values are greater than the simulated values, a concern was that these larger values degrade the EO response in the following measurements. However, the predicted f_{3dB} of

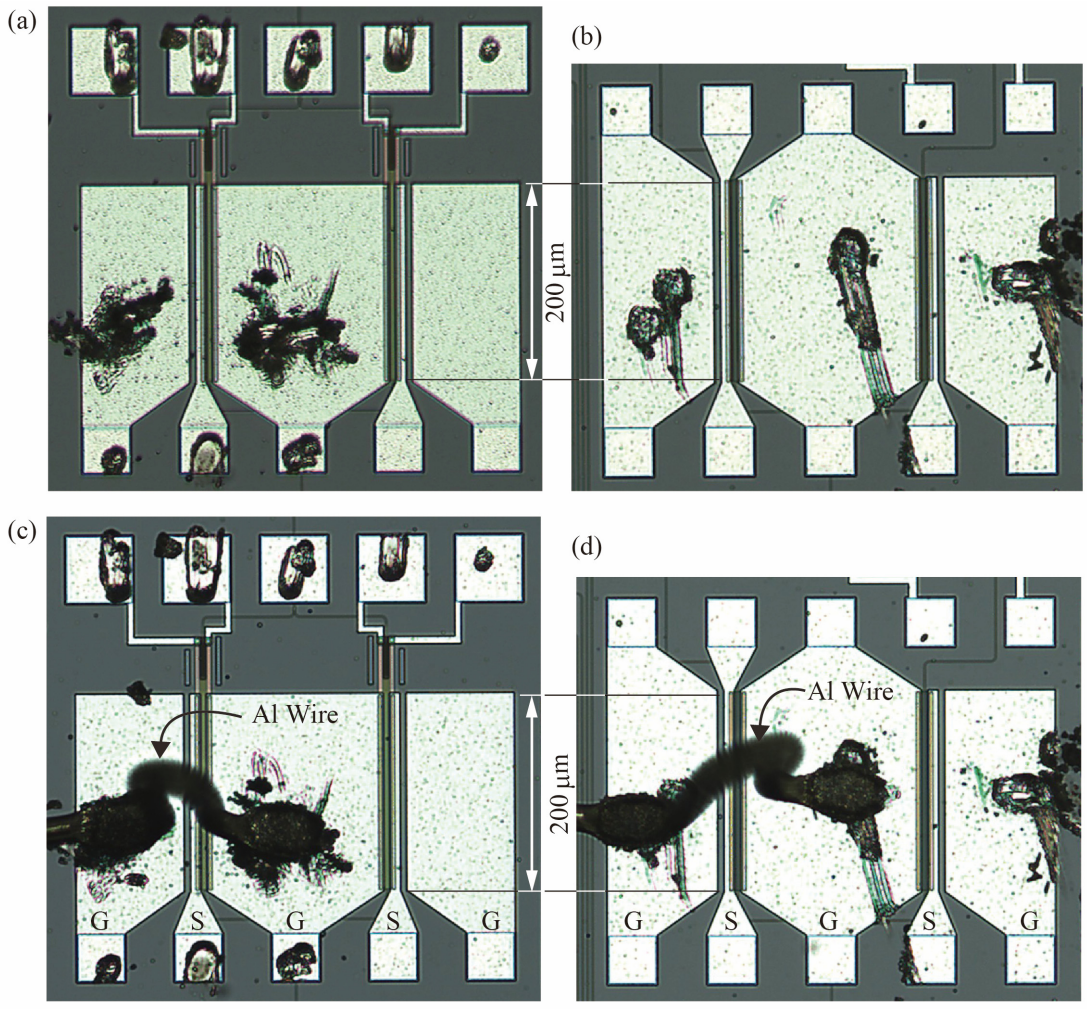

Figure 5.11 Devices for Al wire bonding. (a) Device with a set of G-S-G-S-G pads after top-coat peeling. (b) Device with two sets of the G-S-G-S-G pads after top-coat peeling. (c) Device with the set of G-S-G-S-G pads after Al wire bonding. (b) Device with two sets of the G-S-G-S-G pads after Al wire bonding.

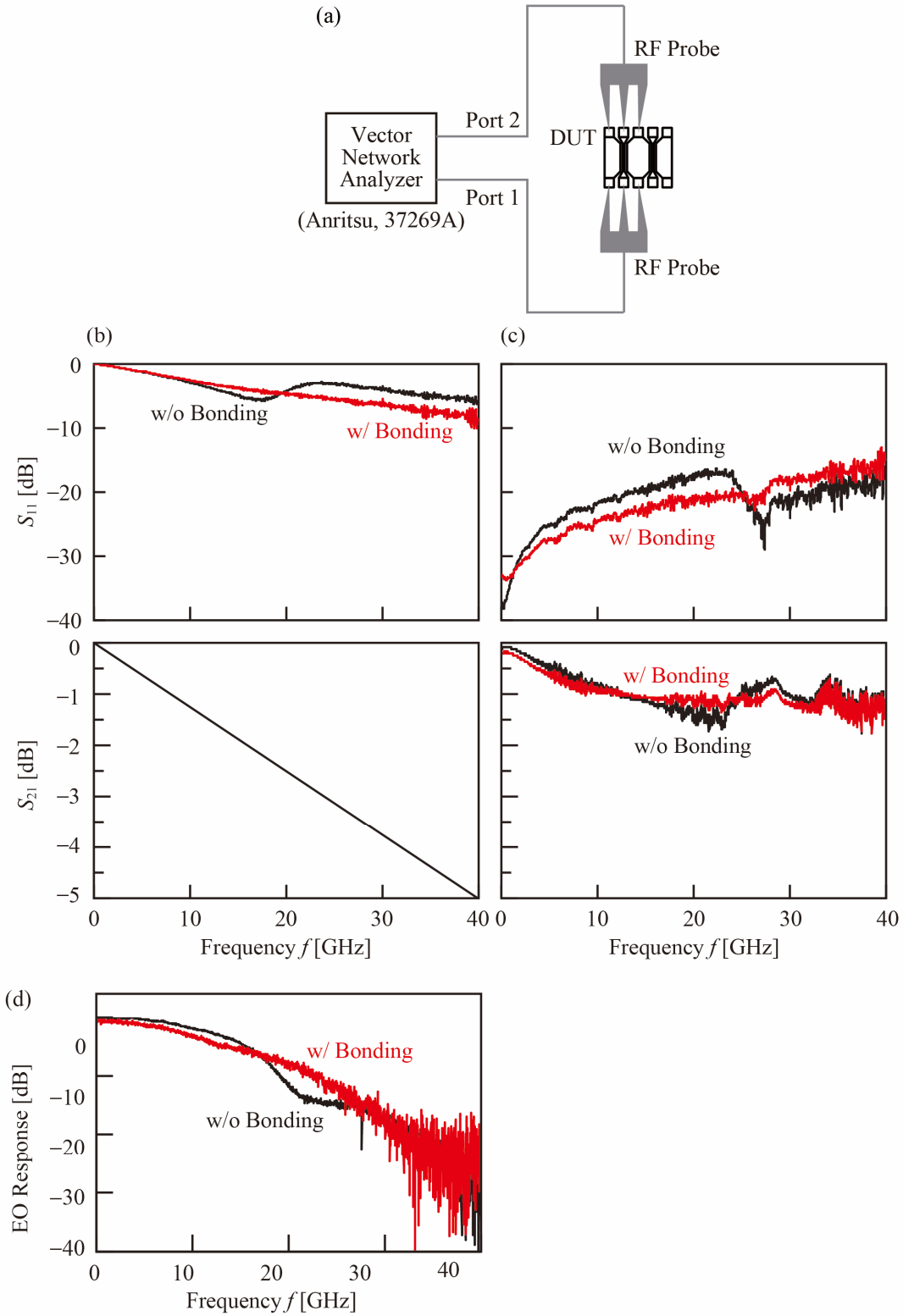

Figure 5.12 *S* parameter measurements of the wire-bonded devices. (a) Setup, (b) Measured *S* parameters of the device with the set of G-S-G-S-G pads. (c) Measured *S* parameters of the device with the two set of G-S-G-S-G pads. (d) Measured EO response of the device with the set of G-S-G-S-G pads.

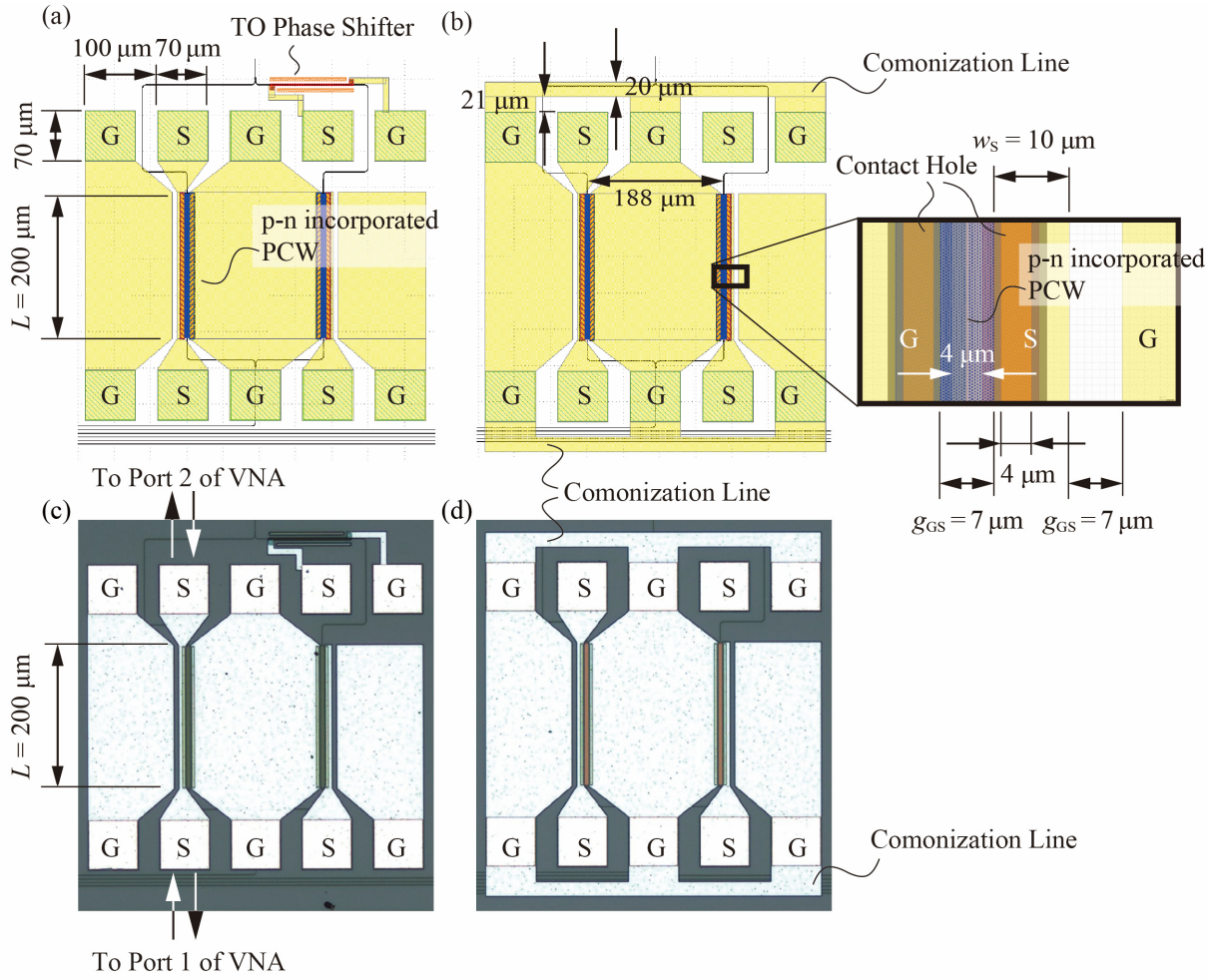

Figure 5.13 Devices with two sets of G-S-G-S-G probing pads for electrical *S* parameter measurements. (a), (b) CAD patterns. (c), (d) Fabricated devices. (a), (c) Device without G commonization. (b), (d) Device with G commonization.

56 GHz at maximum was very high for the target bit rates. Therefore, the designed device had an enough margin in f_{3dB} relative to the imperfect prediction.

5. 4. 1 Design and Fabrication of Meanderline Electrode Device

I designed and fabricated meanderline electrode devices and normal electrode devices for reference in two lots. Figure 5.15(a) shows the meanderline electrode device, and Figure 5.15(b) shows the normal electrode device fabricated on the first lot, for which t_{Si} is 210 nm. The G electrodes of the devices were commonized at the probing pads and at the end of the phase shifters; however, these devices have no load resistors for the simplicity of the layout. I employed the structural dimensions of L = 200 mm and $2r$ = 190 nm for the PCW without the lattice shift, and w_s = 10 µm and d_{SG} = 7 µm for the CPW, as shown in Figure 5.15(c). The p-n junction was of linear shape to focus on the EO phase mismatch. Figure 5.15(d) shows a magnified view of the meanderline whose L_d is 1186 µm. This meanderline has the same CPW structure as that of the phase shifters and were folded using twenty-four 90-degree bends. To minimize the bending loss, the bending angles were slanted at a 45-degree angle. For these devices, Si slabs were placed below the meanderlines and were connected with the meanderlines. However, as

this contact potentially induces excess propagation loss, I removed the Si slabs and the contact holes in the second lot. Figure 5.15(e) and (f) show the fabricated devices. I employed t_{Si} of 210 nm and doping concentrations of $N_A = 9.5 \times 10^{17}$ cm^{-3} and $N_D = 5.7 \times 10^{17}$ cm^{-3} on this lot. I also designed the devices with load resistors as the termination for the high-speed operations and fabricated them in the second lot.

Figure 5.16(a) and (b) show the CAD layout of the devices. I implemented the load resistors of R_L = 20, 30, and 50 Ω using the TiN layer, as shown in Figure 5.16(c). I determined these dimensions based on the sheet resistance value of 18 Ω/□ evaluated in a previous lot. I also designed the open-terminated device. I expected that Γ_L becomes negative for R_L = 20 and 30 Ω because Z_0 was estimated to be 35 Ω in the calculation in Section 5. 3. 4. L_d values of the meanderlines were designed to be 422, 804, 1186, and 1568 μm, as shown in Figure 5.16(d). The Si slabs below the meanderlines were removed, as mentioned above. The doping concentrations were set to be $N_A = 1.05 \times 10^{18}$ cm^{-3} and $N_D = 6.2 \times 10^{17}$ cm^{-3} on this lot. The other parameters were set to be the same as those of the device shown in Figure 5.15, except for 2r of 220 nm. Figure 5.16(e) shows the fabricated device with the load resistors based on the CAD layout.

I also fabricated test element groups (TEGs) for evaluations of RF losses at the bends in the meanderlines as shown in Figure 5.17(a), and the resistance of the fabricated devices R_{fab} as shown in Figure 5.18(a). TEG for the RF bending loss evaluation includes twenty-four 45° or 90° bends over their 1250-μm length at 50-μm intervals. The CPW structures are the same as those of the above-mentioned devices. I measured the S_{21} of the TEG using the same measurement setup as that shown in Figure 5.12. Figure 5.17(b) shows the results. The 45° bending pattern exhibited a loss below that of the 90° pattern. At f = 10 GHz, the S_{21}s were –0.70 dB and –1.1 dB for the 45° and 90° bending pattern, respectively. Because these values included the propagation losses and the twenty-four bending losses, the 45° and 90° bending losses were evaluated to be <0.03 dB and <0.05 dB, respectively. At f = 40 GHz, the S_{21}s

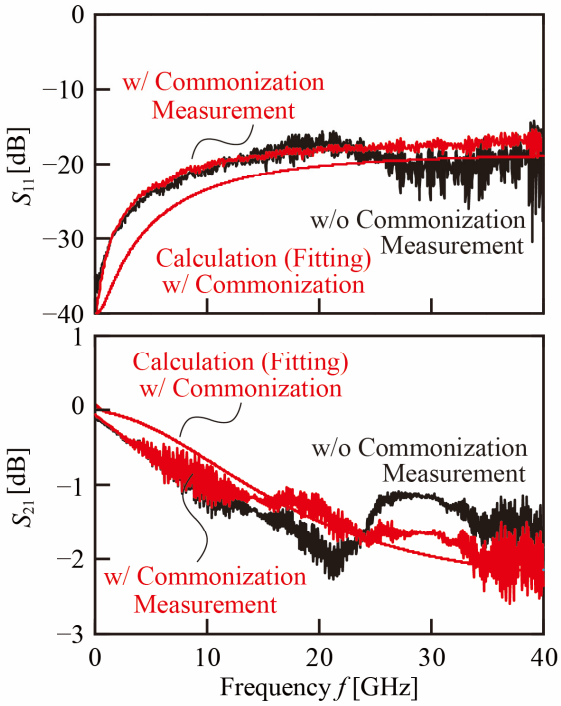

Figure 5.14 Measured electrical S parameters of the devices with/without the G commonization.

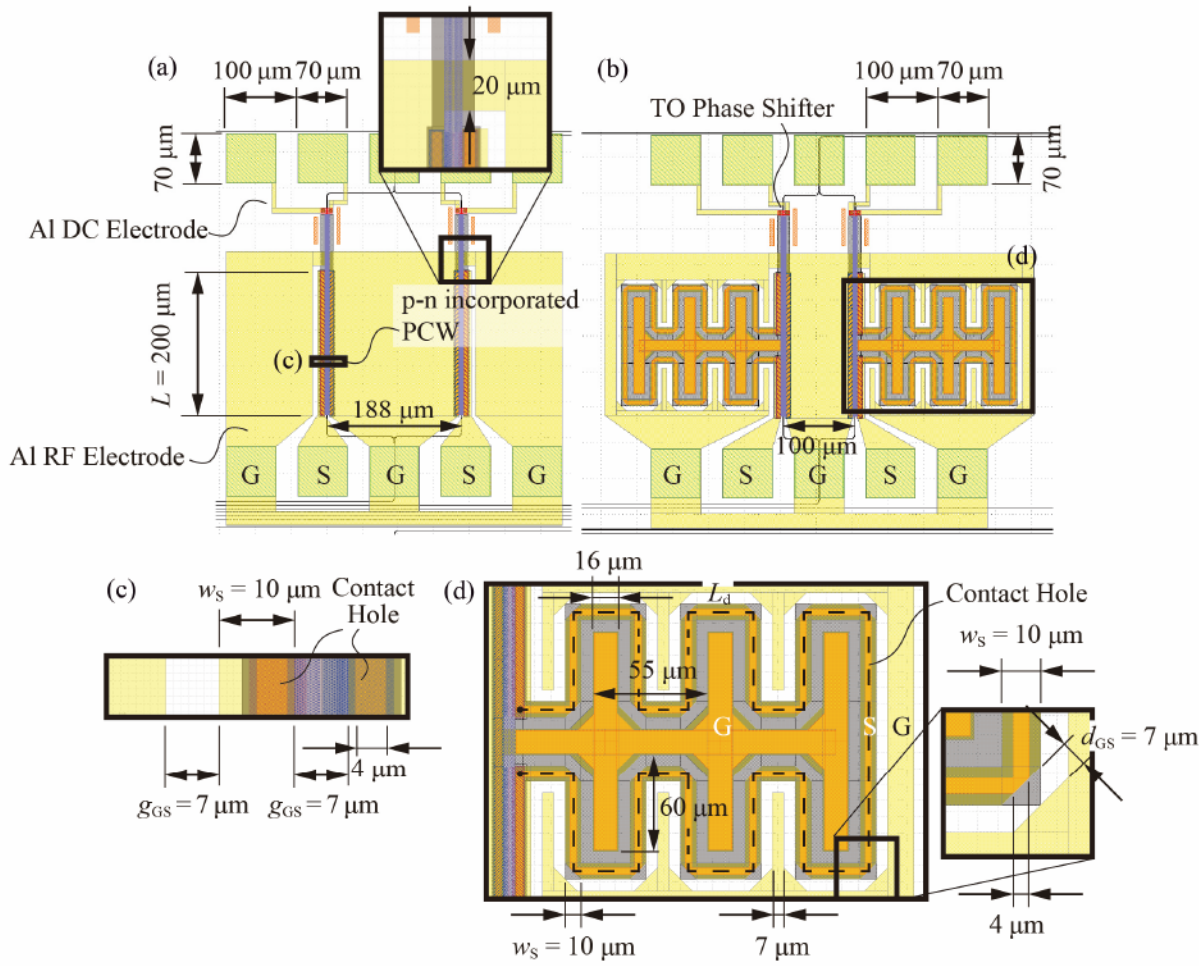

Figure 5.15 Reference normal electrode device and meanderline electrode device without a load resistor. (a), (b) CAD patterns of the normal electrode device and meanderline electrode device with L_d of 1186 μm. (c), (d) Magnified view of the CPW and the meanderline electrode. (e), (f) Fabricated normal electrode device and meanderline electrode device with L_d of 1186 μm.

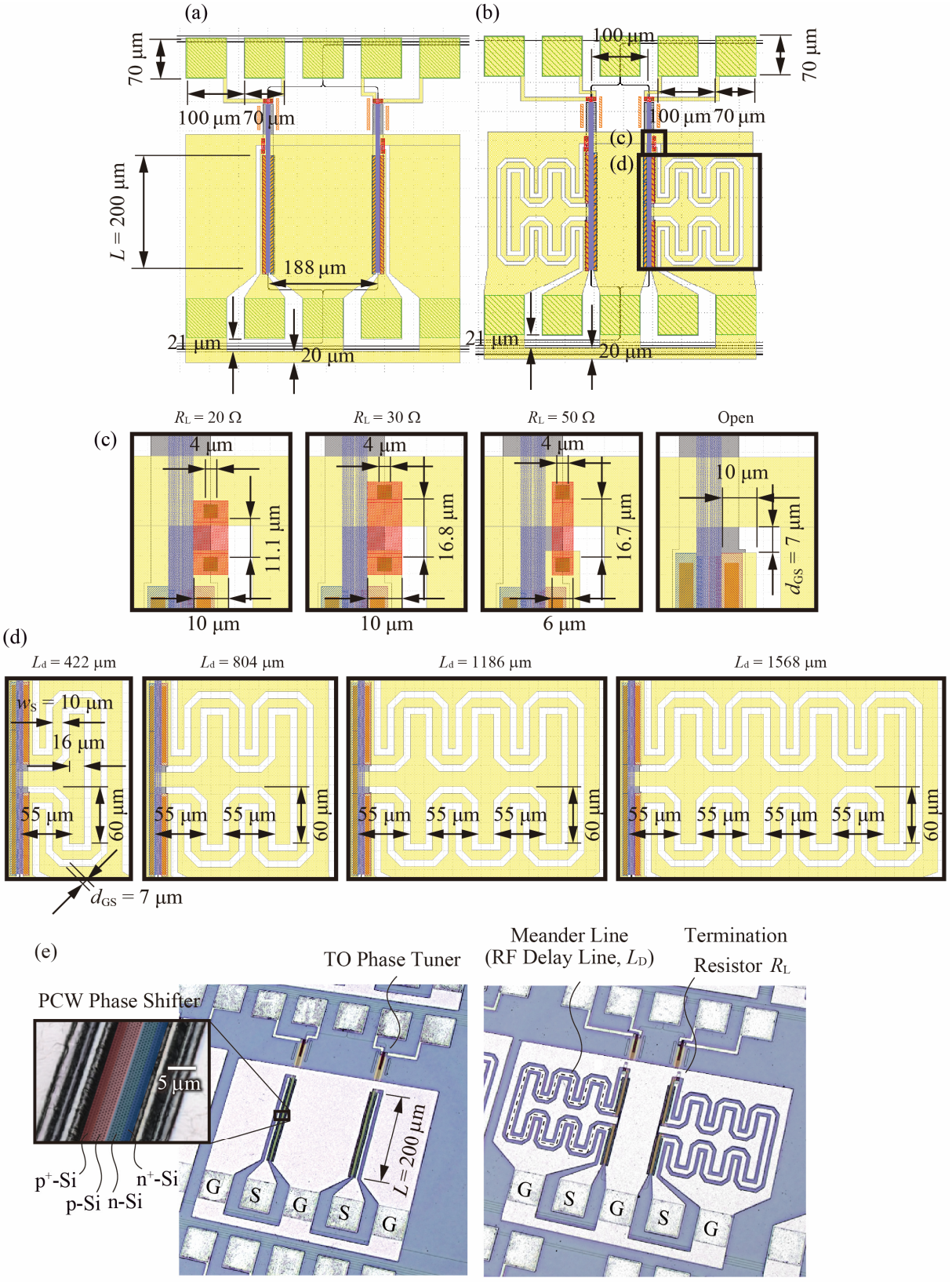

Figure 5.16 Reference normal electrode device and meanderline electrode device with load resistors. (a), (b) CAD patterns of the normal electrode device and the meanderline electrode device with L_d of 804 μm. (c), (d) Magnified view of the load resistors and the meanderline electrodes. (e) Fabricated normal electrode device and meanderline electrode device with L_d of 1186 μm.

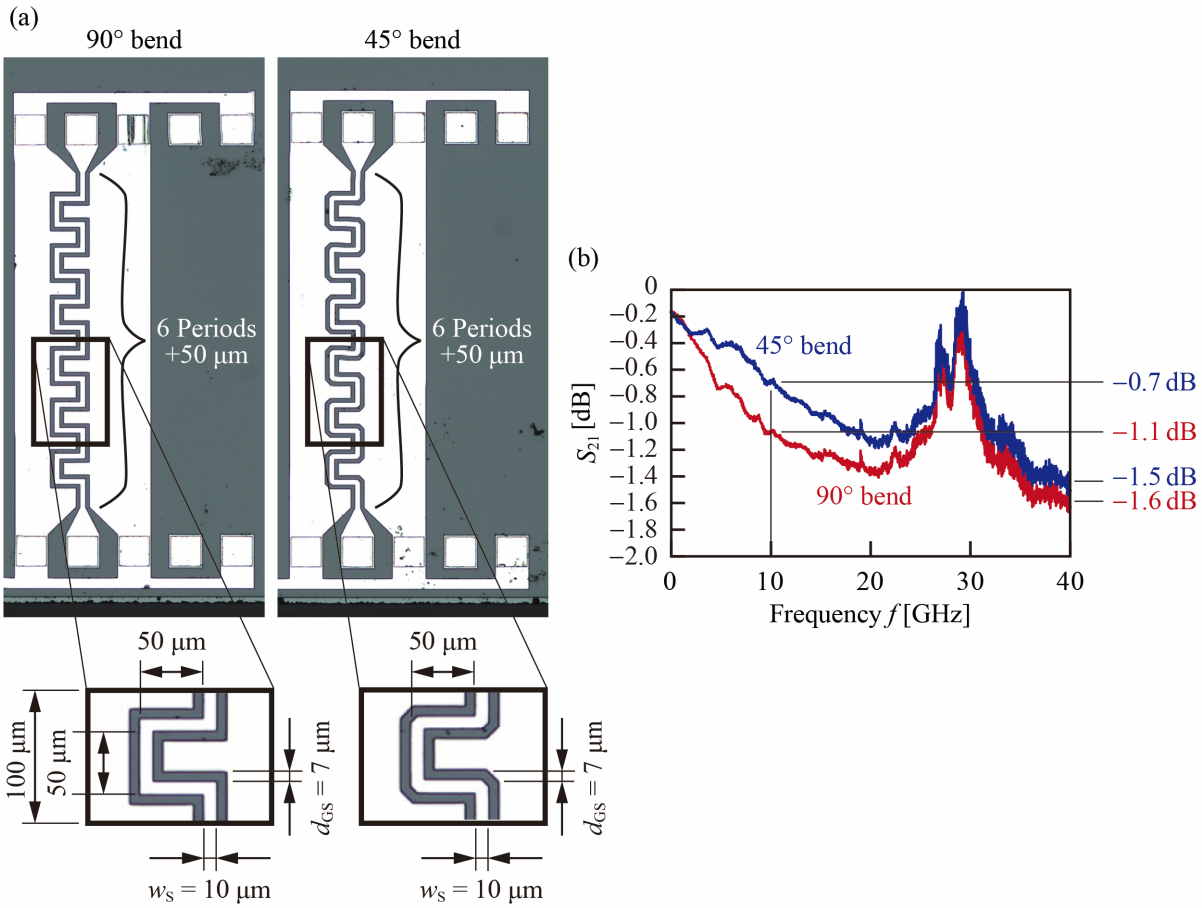

Figure 5.17 (a) TEG for an evaluation of RF bending losses. (b) Measured S_{21} of the TEG.

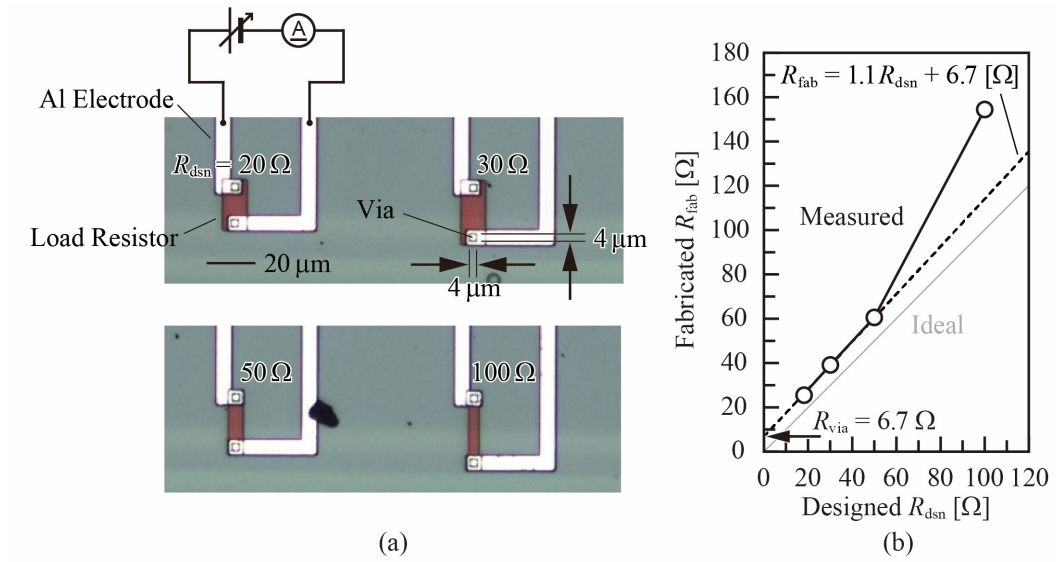

Figure 5.18 TEG for an evaluation of load resistors. (a) Micrographs. (b) R_{fab} as a function of R_{dsn}.

increased to –1.5 dB and –1.6 dB for the 45° and 90° bending pattern, respectively. In this case, the 45° and 90° bending losses were evaluated to be <0.06 dB and <0.07 dB, respectively. Furthermore, R_{fab} was evaluated via *IV* measurements and to be 28, 39, 60, and 154 Ω for the designed load resistance R_{dsn} of 20, 30, 50, and 100 Ω, respectively; R_{fab} was expressed as $R_{fab} = 1.1R_{dsn} + 6.7$ [Ω]. The intercept of 6.7

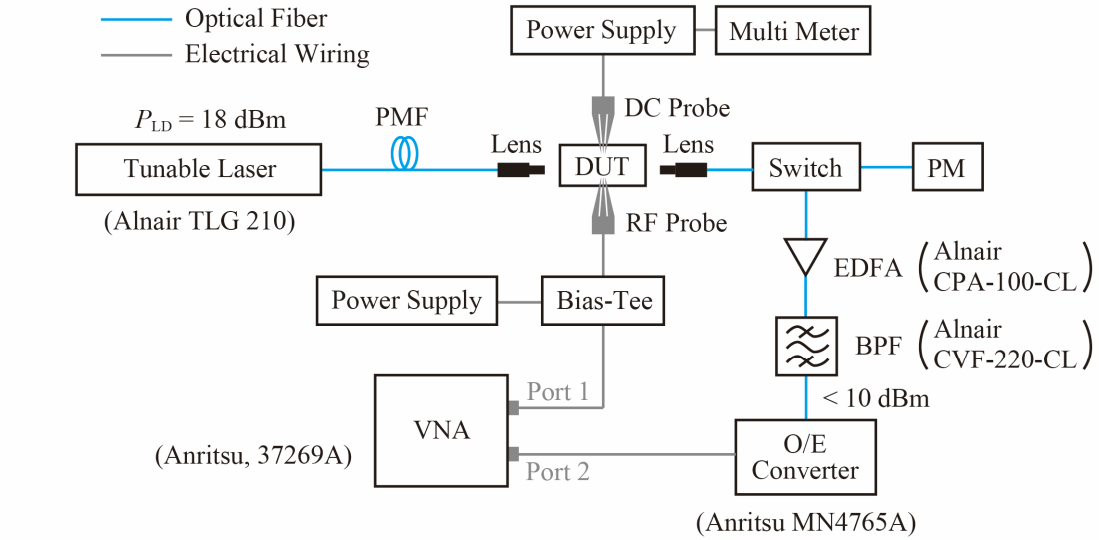

Figure 5.19 Setup for measuring the EO frequency response.

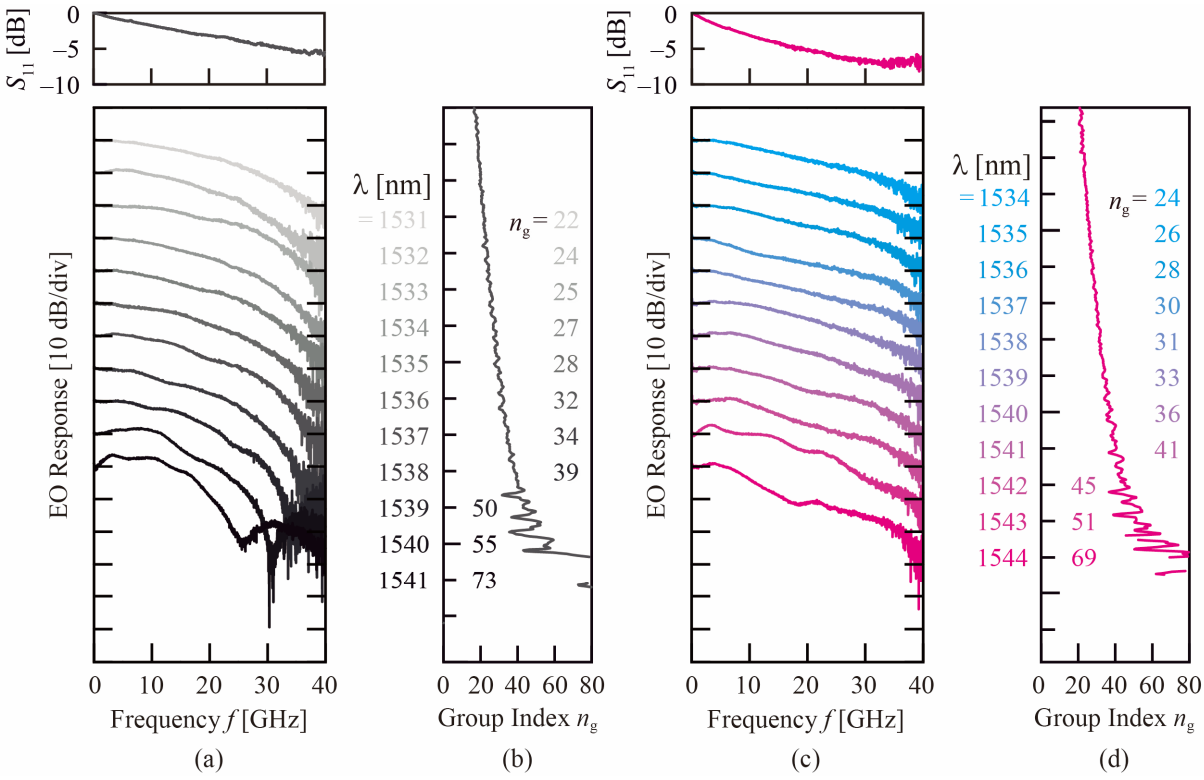

Figure 5.20 Measured frequency response for V_{DC} = –2 V and n_g spectra of open-terminated devices (a), (b) Normal electrode device. (c), (d) Meanderline device with L_d of 1186 μm.

Ω corresponds to resistance of metal vias in the contact holes R_{via}. Because of the relatively narrow width of 5 μm, the large fabrication error occurred at R_{dsn} = 100 Ω. This error will be reduced by employing a larger size resistor in addition to utilizing the above equation.

5. 5 Frequency Response Measurement

5. 5. 1 Measurement Setup

I used the measurement setup shown in Figure 5.19 to perform the frequency response measurements of the meanderline devices. TE-like polarized light was input into the DUT via a PMF with a lens. The P_{LD} was set to be 18 dBm. The incident light was modulated by the DUT driven by small amplitude signals from the VNA. The modulated light was converted into RF signals after the amplification by the EDFA and filtering by the BPF. The converted RF signals returns to Port 2 of the VNA. I appropriately changed the λ of the tunable laser to tune n_g of the PCW.

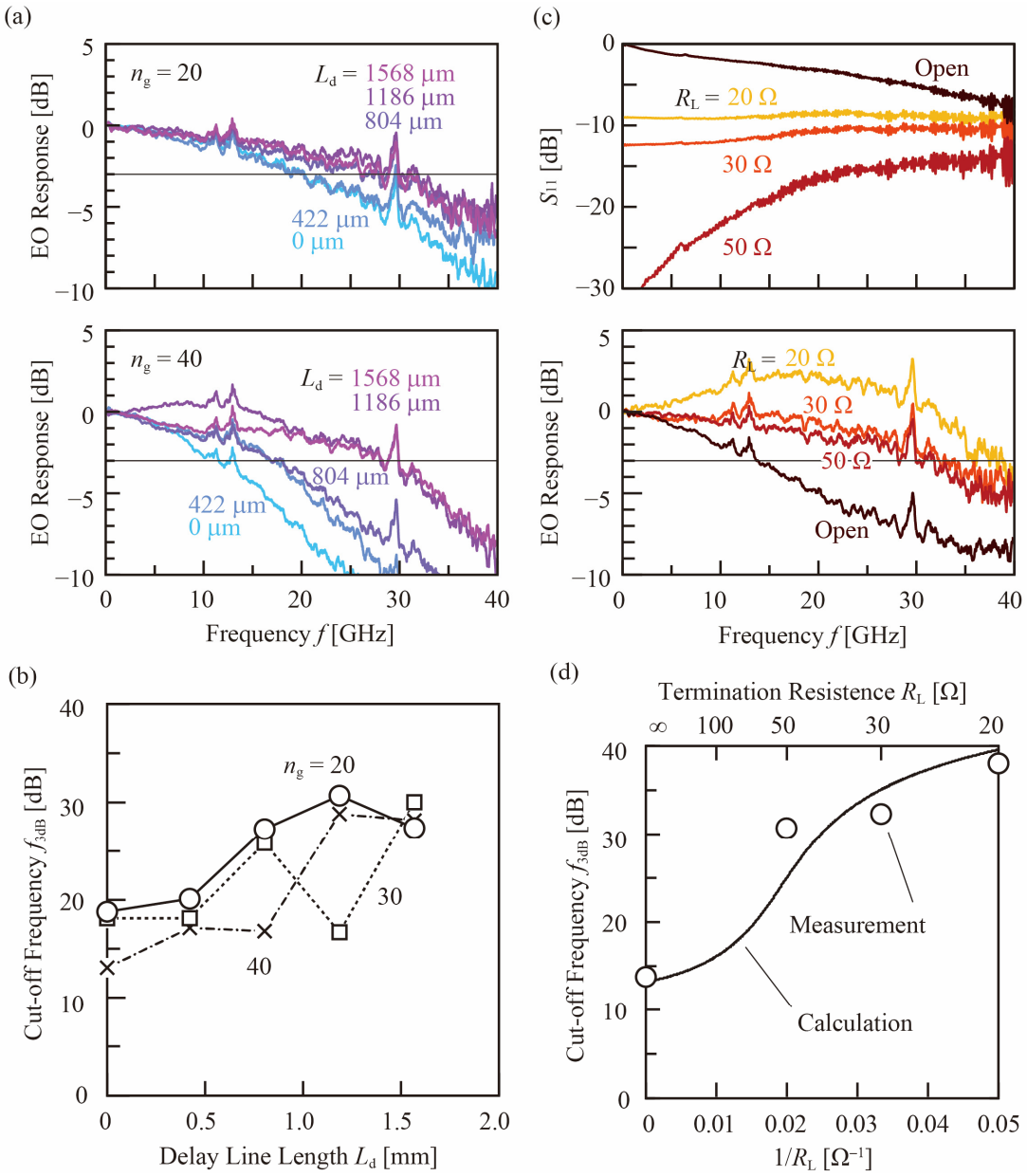

Figure 5.21 Measured frequency response of terminated devices for V_{DC} = –2 V. (a) EO response of 50-Ω terminated devices with different L_d. (b) f_{3dB} of the 50-Ω terminated devices as a function of L_d. (c) S_{11} and EO response of device with L_d of 1186 µm for n_g = 20. (d) f_{3dB} of the devices with L_d of 1186 µm as a function of $1/R_L$.

5. 5. 2 Results

First, I measured the devices without the load resistors by changing λ to observe the phase matching via the meanderline electrode. Simultaneously, I observed S_{11} to confirm the reduction of the slow dips and valleys. Figure 5.20 shows the EO response, S_{11}, and n_g spectra of the meanderline electrode device and normal electrode device. These devices exhibited a smooth S_{11} without dips and peaks; smooth EO responses were also observed. The EO response of the normal electrode device was degraded with the increase in n_g, as shown in Figure 5.20(a). In particular, when n_g is greater than 39, sharp dips appeared in the EO responses because of the large EO phase mismatch. In contrast, the degradation in the EO response of the meanderline device was suppressed compared with those of the normal device, as shown in Figure 5.20(c). Furthermore, no sharp dip was observed, even for very high n_g of 69 because of the improved EO phase matching. Next, I measured the devices with the load resistors for high-speed operation. Figure 5.21(a) shows the measured EO response of the device terminated with R_L = 50 Ω for different L_d. A longer L_d improved the frequency response at n_g of 20 (upper) and 40 (lower), with pronounced improvement observed for the higher n_g of 40. Figure 5.21(b) summarizes the evaluated f_{3dB}. For n_g = 20, f_{3dB} was evaluated to be 19 GHz and improved to ~30 GHz for L_d = 1186 μm and 1568 μm. Even for higher n_g of 30 and 40, f_{3dB} was improved to ~30 GHz. Furthermore, I measured the EO response for L_d = 1186 μm and different R_L; Figure 5.21(c) shows the measured S_{11} and EO response. The open-terminated device, device, which has no load resistor, exhibited a high S_{11} of >–10 dB over the measured frequency range. When the device was terminated by R_L = 50 Ω, S_{11} was reduced to approximately –14 dB at f = 40 GHz, and <–30 dB at the lowest frequency. In contrast, S_{11} increased again for R_L = 20 Ω and 30 Ω. I expected that R_L was less than Z_0 of the phase shifters and that Γ_L are negative values. The EO response of the device terminated with the load resistors was very much improved compared with the open-terminated device. In particular, for R_L = 20 Ω, the improvement was remarkable. Figure 5.21(d) summarizes f_{3dB} as a function of $1/R_L$. The measured f_{3dB} were in agreement with the calculated curve. Therefore, the calculation modeled the meanderline device well. f_{3dB} was improved to as high as 38 GHz for R_L = 20 Ω. This was considered to be adequate for 50 Gbps operation.

5. 6 **High-speed Modulation Experiments**

5. 6. 1 OOK Modulation

I performed eye pattern measurements via modulation of the meanderline devices at several different bit rates to determine their large signal response. I describe the measurement setup, conditions, and results at each bit rate in the sections below.

(a) 25 and 32 Gbps Modulation

Figure 5.22 shows the measurement setup for 25 and 32 Gbps modulation. The setup is nearly the same as that of Figure 4.7, except the tunable laser was exchanged to TLG-200 (Alnair Labs Corp.), which can output light in TE-like polarization. As a result, I removed the polarization controller and directly connected the laser to the PMF with a lens. This allowed the high-power input of approximately 16 dBm to the DUT. However, I still used EDFA to adjust the received power at 0 dBm. I set V_{pp} = 1, 2 V, V_{DC} =

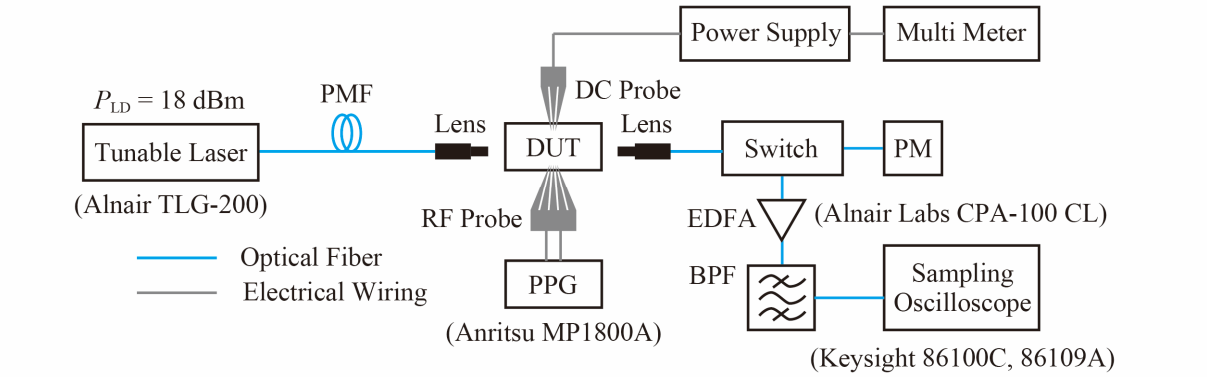

Figure 5.22 Setup for 25 and 32 Gbps modulation.

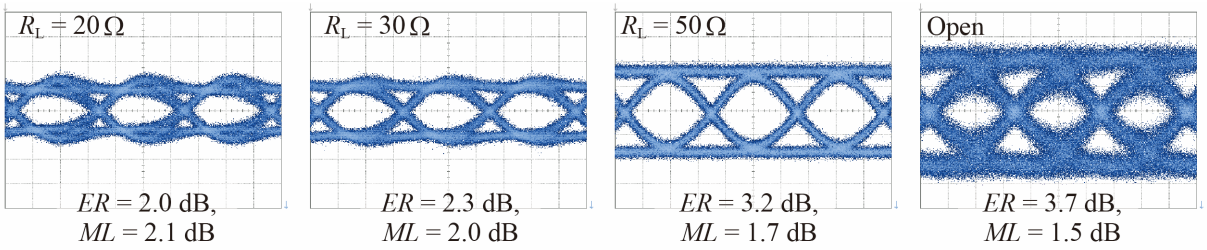

Figure 5.23 32-Gbps eye patterns for V_{pp} = 2 V, V_{DC} = –1 V, R_L = 20, 30, 50 Ω, and open termination.

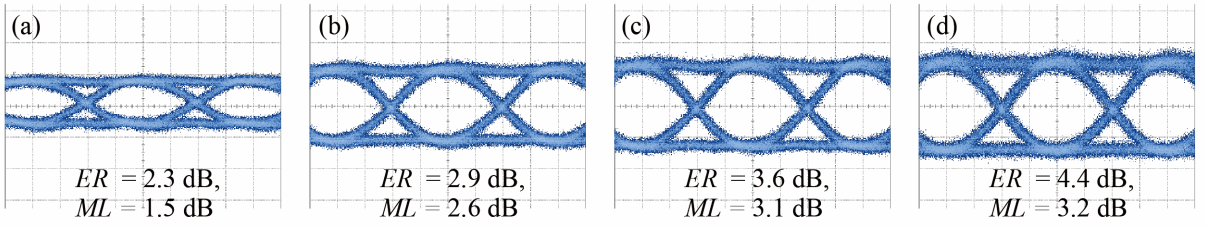

Figure 5.24 25-Gbps eye patterns for small voltage of V_{pp} = 2 V, V_{DC} = –1 V. ϕ_0 was set so that the average optical loss was reduced by (a) 3 dB, (b) 4 dB, (c) 5 dB, and (d) 6 dB.

–0.5, –1 V, and n_g = 40, 30 while changing the wavelength for the modulation at both 25 Gbps and 32 Gbps.

First, I checked the effect of the load resistor on the modulation characteristics at 32 Gbps. I set V_{pp} = 2 V, V_{DC} = –1 V, $\phi_0 = \pi/2$, and λ = 1552 nm to have n_g = 30. Figure 5.23 shows the observed 32-Gbps eye patterns for devices with L_d = 1186 μm, R_L = 20, 30, 50, and ∞ Ω (∞ Ω corresponds to open termination). Although the open-terminated device exhibited a noisy eye pattern, it also exhibited the largest *ER* of 3.7 dB among the evaluated four devices. This result was caused by the large positive Γ_L of almost unity; the large positive RF reflection caused constructive interference at low RF frequency and enhanced the RF amplitude to roughly twice the original voltage. Simultaneously, the rising and falling times increased because of the moderate frequency response. In addition, a ripple was observed in the modulated waveform that broadened the linewidth of the eye pattern. In contrast, the low R_L of 20 and 30 Ω reduced the eye amplitude and *ER*, but remarkably improved the linewidth and SNR of the eye patterns because of the small negative Γ_L, which emphasizes the response at high frequency. For moderate R_L of 50 Ω, a clear and orderly eye pattern with relatively large *ER* of 3.2 dB was observed at this bit rate.

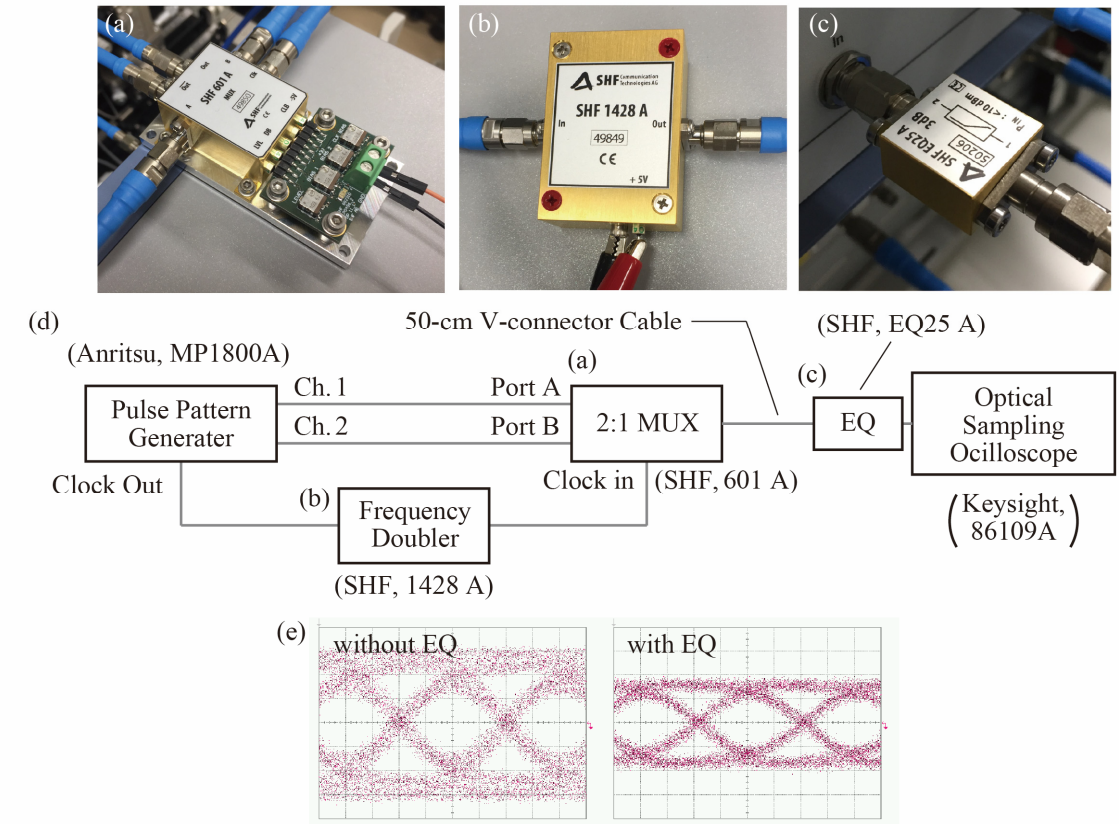

Figure 5.25 (a) 2:1 MUX (SHF, Inc., 601 A), (b) Frequency doubler (SHF, Inc., 1428 A), (c) EQ (SHF, Inc., EQ25 A), (d) Setup for 50-Gbps signal generation. (e) Electrical 50-Gbps eye pattern with/without EQ.

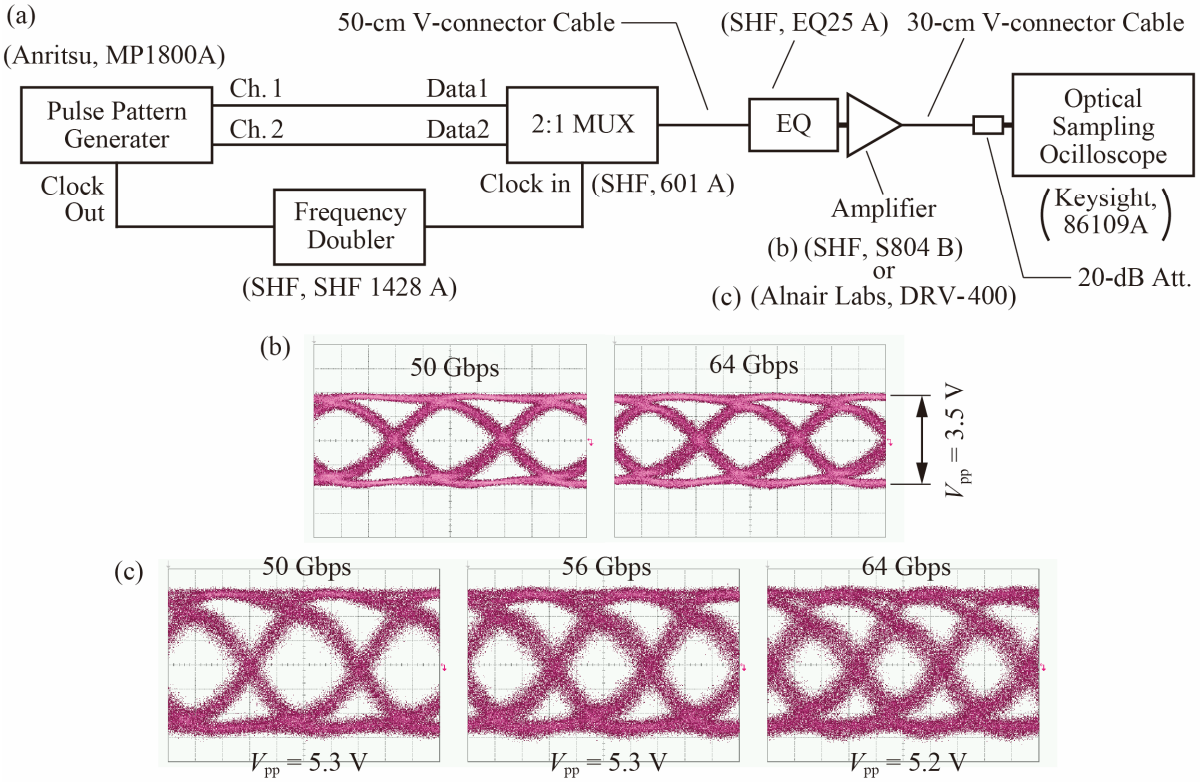

Figure 5.26 (a) Setup for amplifier measurement. (b) 50- and 64-Gbps electrical eye patterns amplified by S804 B. (c) 50-, 56-, and 64-Gbps electrical eye patterns amplified by DRV-400.

Next, I performed 25-Gbps modulation with low V_{pp} of 1 V and V_{DC} of –0.5 V. I shifted λ to 1556 nm so that n_g increased to 40, and I exchanged the DUT to the device with R_L of 50 Ω and long L_D of 1568 mm. Figure 5.24 shows the observed eye patterns at different ϕ_0 set so that the average transmission power was reduced by 3, 4, 5, and 6 dB from the maximum. I observed clear eye patterns, even at $\phi_0 = \pi/2$, which corresponds to an average optical loss of 3 dB; however, *ER* was as small as 2.3 dB. *ER* was improved to 2.9, 3.6, and 4.4 dB with the increase in the average optical loss to 4, 5, and 6 dB, respectively. *ML* was even as small as 3.2 dB when the large *ER* of 4.4 dB was obtained.

(b) 50, 56, 64 Gbps Modulation

I tried to demonstrate the operation at further high bitrates of 50, 56, and 64 Gbps. The NRZ PRBS signals at these bit rates was generated using a 2:1 MUX (SHF, Inc., 601 A), a frequency doubler (SHF, Inc., 1428 A), and an equalizer (EQ, SHF, Inc., EQ25A) added to the PPG (Anritsu Corp., MP1800A). Figure 5.25(a)–(b) shows their photographs, and Figure 5.25(d) shows the setup for the signal generation and a confirmation of the necessity for the equalization. Two-channel 25-Gbps signals from the PPG

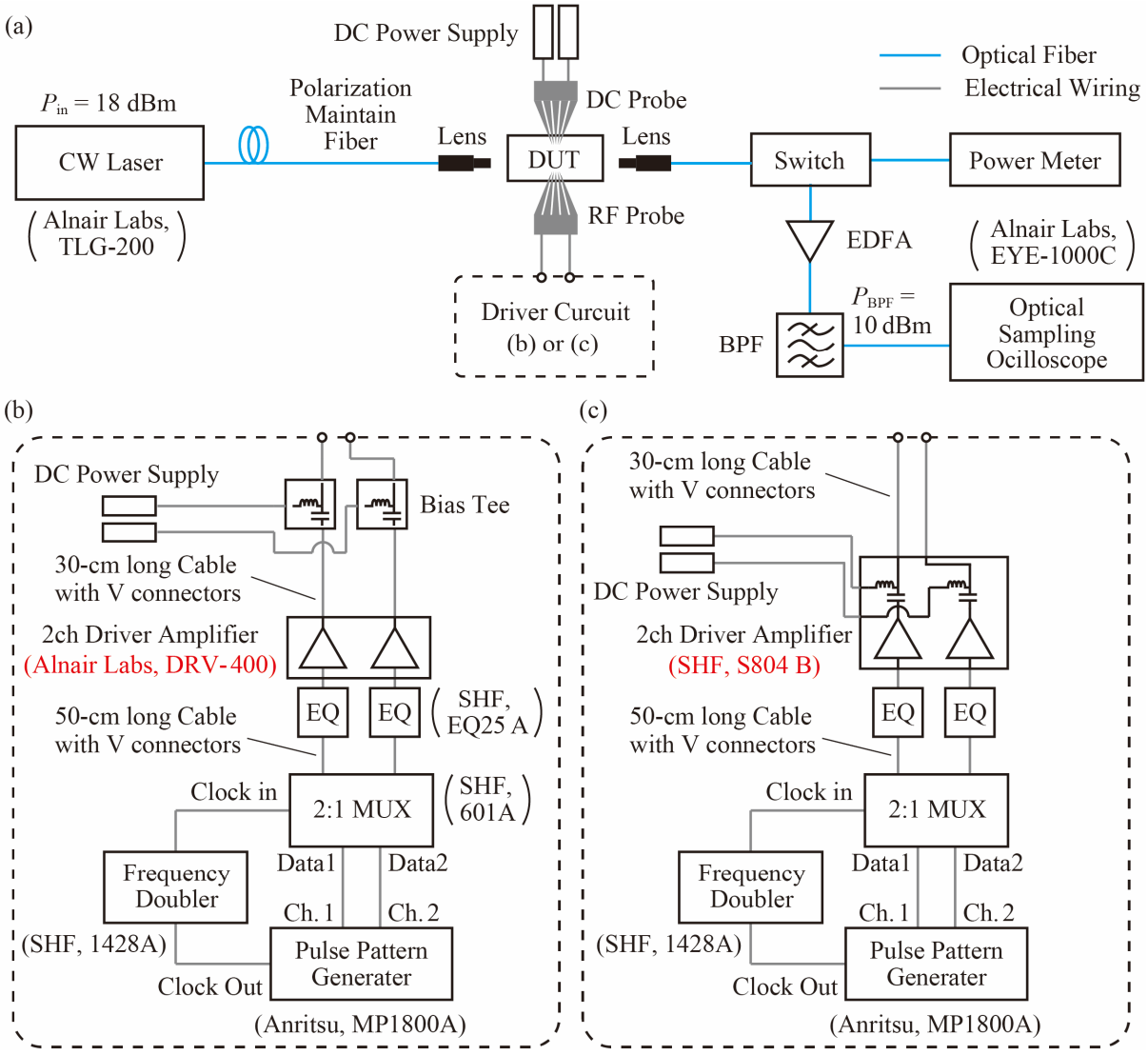

Figure 5.27 (a) Measurement setup. (b) Driver circuit using DRV-400. (c) Driver circuit using S804 B.

were input to Ports A and B of the 2:1 MUX. The two-channel signals were set to have different bit lengths. Simultaneously, the clock signal (clock frequency f_{clk} = 12.5 GHz) of the PPG was sent to the 2:1 MUX after the clock frequency was doubled by the frequency doubler. The 2:1 MUX generated 50-Gbps NRZ PRBS signal from the two different 25-Gbps NRZ PRBS signals and the 25-GHz clock signal. I observed the electrical eye pattern of the generated 50-Gbps signal using a sampling oscilloscope (f < 50 GHz) with or without the EQ. Figure 5.25(e) shows the observed eye patterns. The 0-level and 1-level lines in the eye pattern without the EQ were broadened by the signal degradation inthe 50-cm long coaxial cable. On the contrary, the eye pattern with the EQ was much clearer than that without the EQ. Although the eye amplitude was reduced to approximately 2/3, the SNR was still much better. This experiment showed that the EQ is needed for a high-quality signal generation. I also checked the signal quality after amplifications by two different amplifiers: S804 B (SHF, Inc., f < 60 GHz) and DRV-400 (Alnair Labs Corp., f < 40 GHz). Figure 5.26(a) shows the measurement setup. I added to the amplifiers a 30-cm coaxial cable and a 20-dB attenuator for protection of the oscilloscope in the setup shown in Figure 5.25(d). Figure 5.26(b) shows the 50- and 64-Gbps signals amplified by S804 B at its maximum gain. V_{pp} was increased to 3.5 V while maintaining the narrow linewidth and the low rising and falling times. Figure 5.26(c) shows the signal amplified by DRV-400 with its maximum gain. The

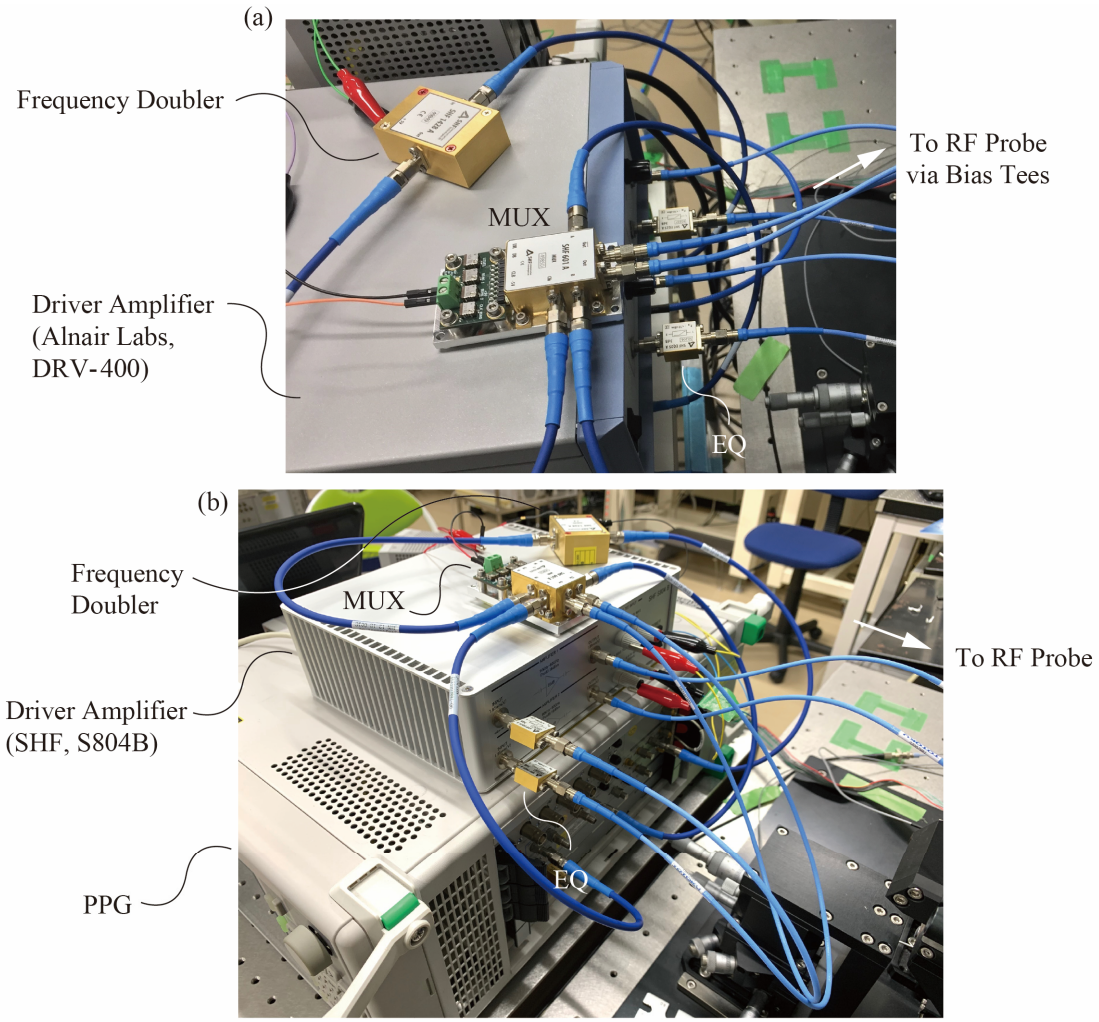

Figure 5.28 (d) Photograph of driver circuit using DRV-400. (e) Photograph of driver circuit using S804 B.

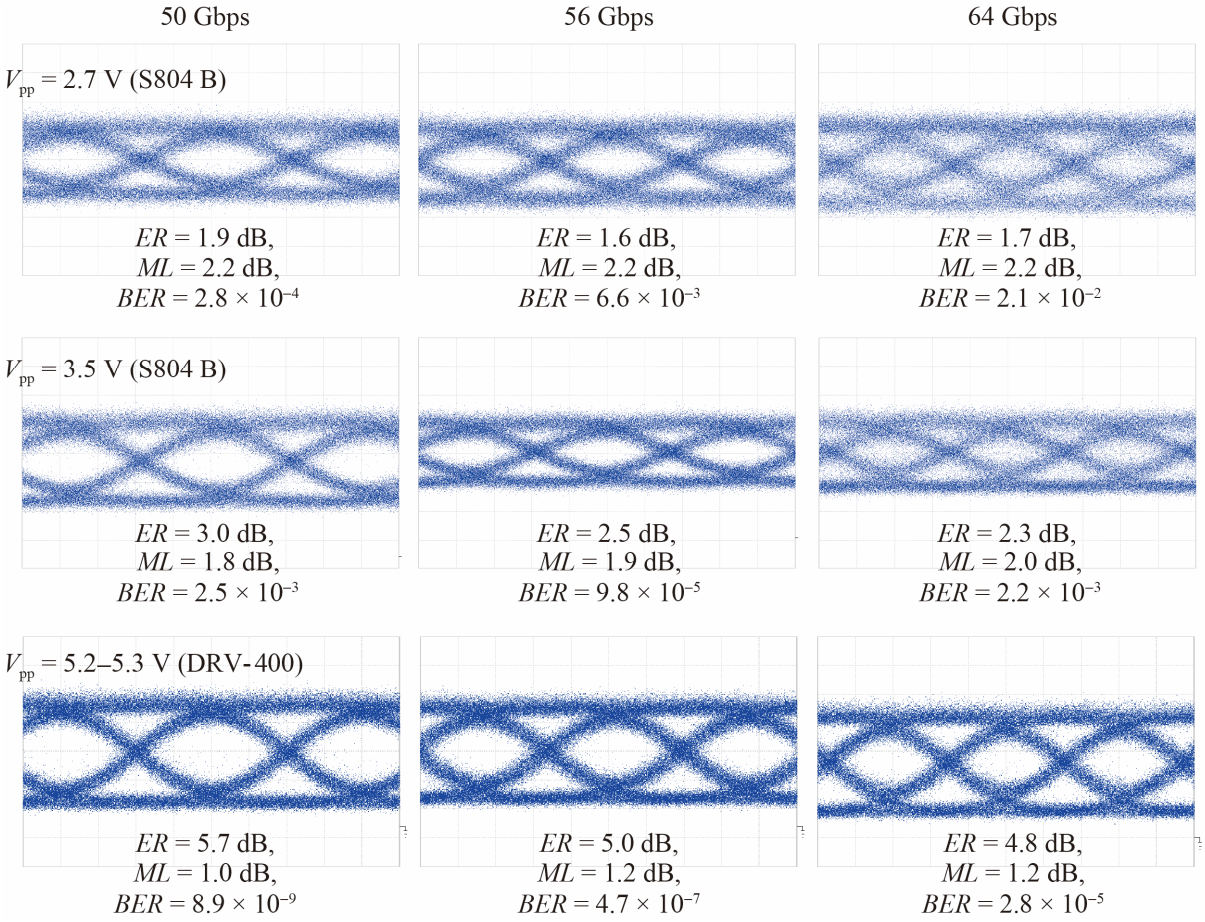

Figure 5.29 50-, 56-, 64-Gbps eye patterns modulated by 20-Ω terminated meanderline device for n_g = 20, V_{pp} = 2.7, 3.5, 5.2–5.3 V and V_{DC} = –3 V.

system exhibited a higher V_{pp} of 5.2–5.3 V, although the rising and falling times were lengthened. When the gain of S804 B was reduced to the minimum, it exhibited V_{pp} of 2.7 V. Thus, I was able to apply V_{pp} of 2.7–5.3 V to a DUT using the two amplifiers.

Figure 5.27 shows the measurement setup. I switched two different driver circuits to achieve the required V_{pp}: circuits using DRV-400 and S804 B shown in Figure 5.27(b) and (c), respectively. The photographs of DRV-400 and S804 B are also shown in Figure 5.27(d) and (e), respectively. In the optical circuit, I employed a high-speed asynchronous optical sampling oscilloscope (Alnair Labs Corp., EYE-1000C) with a bandwidth of over 500 GHz. I input amplified modulated light with 10-dBm power to the sampling oscilloscope and observed the eye patterns. Figure 5.29 shows the observed eye patterns when I input applied voltages of V_{pp} = 2.7, 3.5, 5.2–5.3 V and V_{DC} = –3 V to the 20-Ω terminated meander line device with L_d = 1186 mm. At V_{pp} equal to 2.7 V, I observed clear eye patterns with ER of 1.9 and 1.6 dB at 50 and 56 Gbps, respectively, while their eye amplitudes were small. However, the eye pattern became noisy at 64 Gbps because of the instable self-trigging. For V_{pp} equal to 3.5 V, *ER* was increased to 3.0, 2.5, and 2.3 dB at 50, 56, and 64 Gbps, respectively. The clear open eye was observed at 50 and 64 Gbps; however, the eye pattern at 64 Gbps was still unclear. When V_{pp} was increased to 5.2–5.3 V, I observed a clear open eye with a high *ER* of 5.7, 5.0, and 4.8 dB at 50, 56, and 64 Gbps, respectively. From these eye patterns at 50, 56, and 64 Gbps, low *BER*s of 8.9 × 10^{-9}, 4.7 × 10^{-7}, and 2.8 × 10^{-5}, respectively, were estimated.

5. 6. 2 PAM4 Modulation

(a) Signal Generation and Measurement Setup

I attempted to demonstrate 20–50-Gbaud PAM4 modulation. Figure 5.30 shows the measurement setup used. The PAM4 signals were generated by a 3-bit digital-to-analog convertor (DAC), 128-Gbps PPG (SHF, Inc., 12103A, 56 Gbps per channel), and synthesized clock generator (SHF, Inc., 78122B); their photographs are shown in Figure 5.30(b)–(d). The 3-bit DAC generated 20–50-Gbaud PAM4 signals

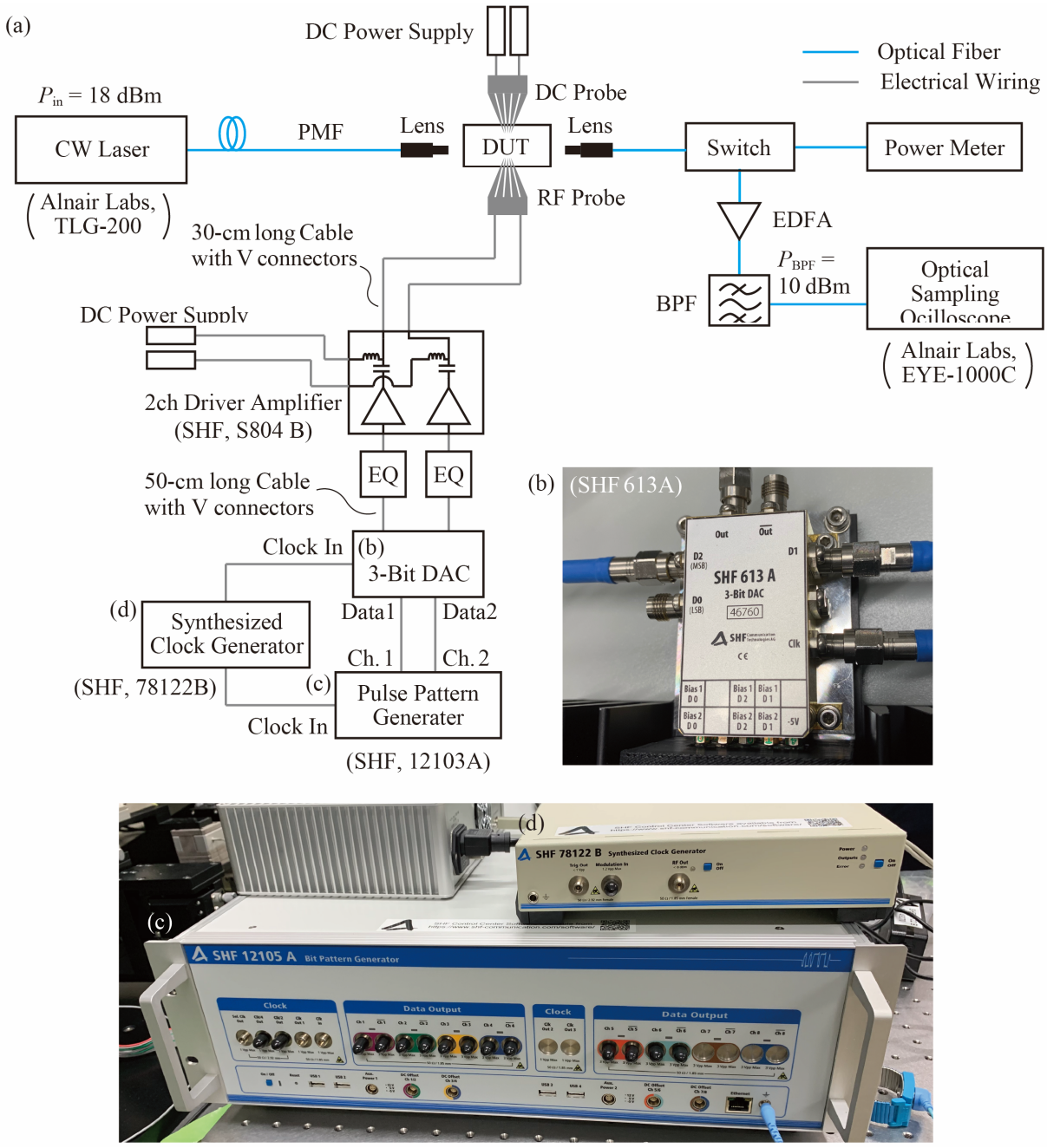

Figure 5.30 (a) Measurement setup for PAM4 modulation. (b) 3-bit DAC (SHF, Inc., 613A). (c) PPG (SHF, Inc., 12103A). (d) Synthesized clock generator (SHF, Inc., 78122B).

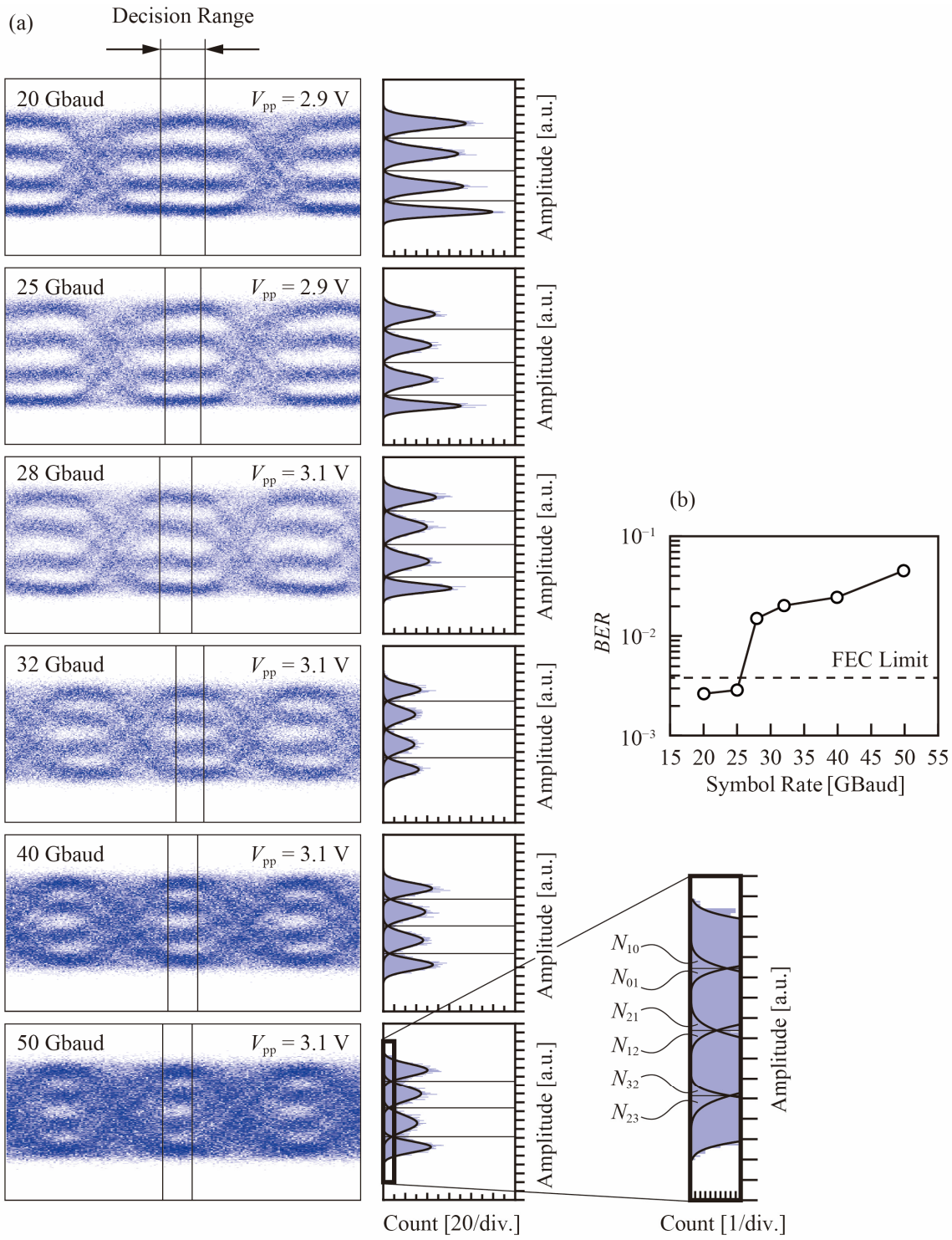

Figure 5.31 (a) Observed PAM4 eye patterns and their amplitude histograms at 20–50 Gbaud (40–100 Gbps) for V_{pp} = 2.9–3.1 V. (b) PAM4 *BER* estimated from the eye patterns. The decision ranges are shown in (a).

according to the two-channel 20–50-Gbps PRBS signals from the PPG; the signals were synchronized with the clock generator. The PAM4 signals were applied to a DUT after the amplification to V_{pp} = 2.9 or 3.1 V (depending on the symbol rate) via S804 B with a high linearity, which is important to generate evenly-spaced PAM4 signals. I used the same DUT with Section 5. 6. 1; R_L is equal to 20 Ω and L_d is equal to 1186 μm.

(b) Results

Figure 5.31 (a) shows the PAM-4 eye patterns and their amplitude histograms in the decision ranges for V_{DC} = –3 V and $n_g \approx 20$. I defined the width of the decision range as the one fourth of a symbol. The open eye patterns were observed for data rates of up to 28 Gbaud. The pitch of the four-level amplitudes was slightly unequal because of the nonlinearity of the device. Although the eye pattern became noisier with the increase in the symbol rate, I observed barely opened eye even at the high symbol rate of 50 Gbaud corresponding to 100 Gbps. I also estimated the *BER* from the amplitude histograms. The histograms were fitted with four Gaussian curves, from which I obtained the number of symbols in the Gaussian curves and each overlapped area. In the case of the PAM4 format, the *BER* can be estimated as

$$BER = \frac{N_{\text{error}}}{N_{\text{all}}} = \frac{N_{10} + N_{01} + N_{21} + N_{12} + N_{32} + N_{23}}{N_0 + N_1 + N_2 + N_3 - \left(N_{10} + N_{01} + N_{21} + N_{12} + N_{32} + N_{23}\right)} \tag{5.51}$$

where N_a is the number of the symbols involved in ath-level curves and N_{ab} is the number of ath-level symbols judged as bth-level symbols. Figure 5.31 (b) shows the estimated *BER* versus the symbol rate. The *BER* is below the forward error correction limit of 3.8×10^{-3} [5-12] up to 25 Gbaud, but exceeds 10^{-2} at higher baud rates. It is known that 1.5-fold f_{3dB} is required against the baud rate in the PAM-4 operation. In this study, frequency equalization was only applied to the measurement system. Further improvement can be expected by the equalization of the device.

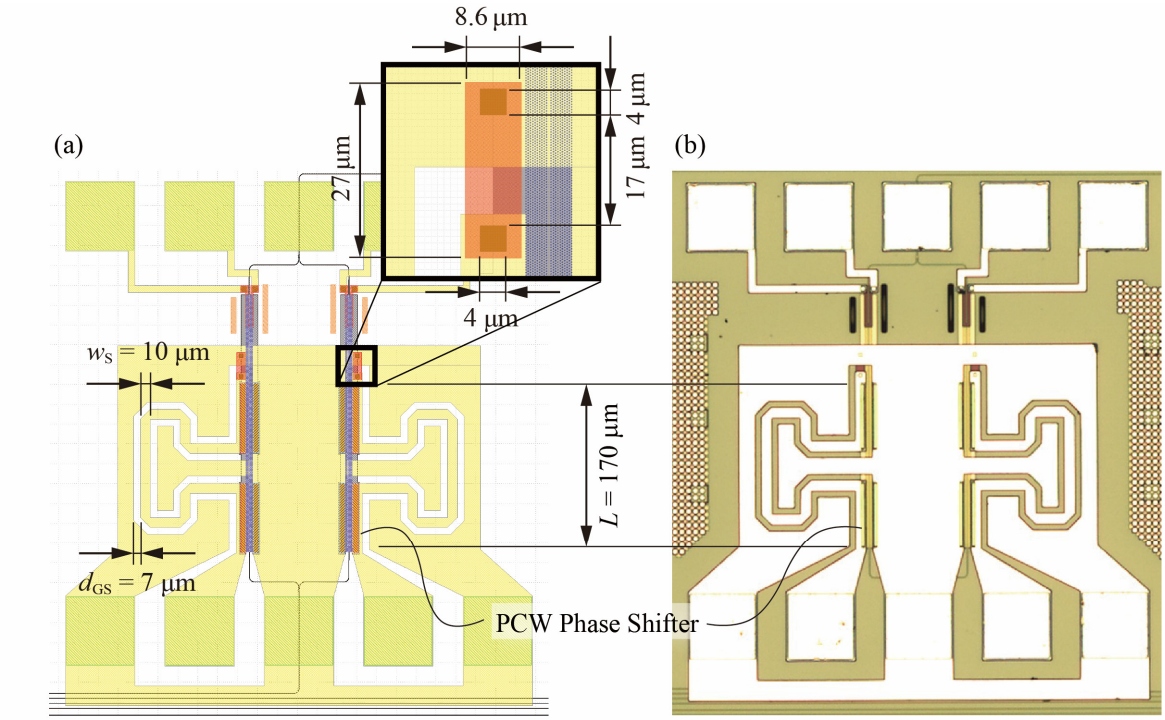

Figure 5.32 45-Ω terminated Meanderline device for the WDM transmission experiment. The structural parameters are L = 170 μm, a = 404, 407 nm, $2r$ = 224 nm, and L_d = 370 μm.

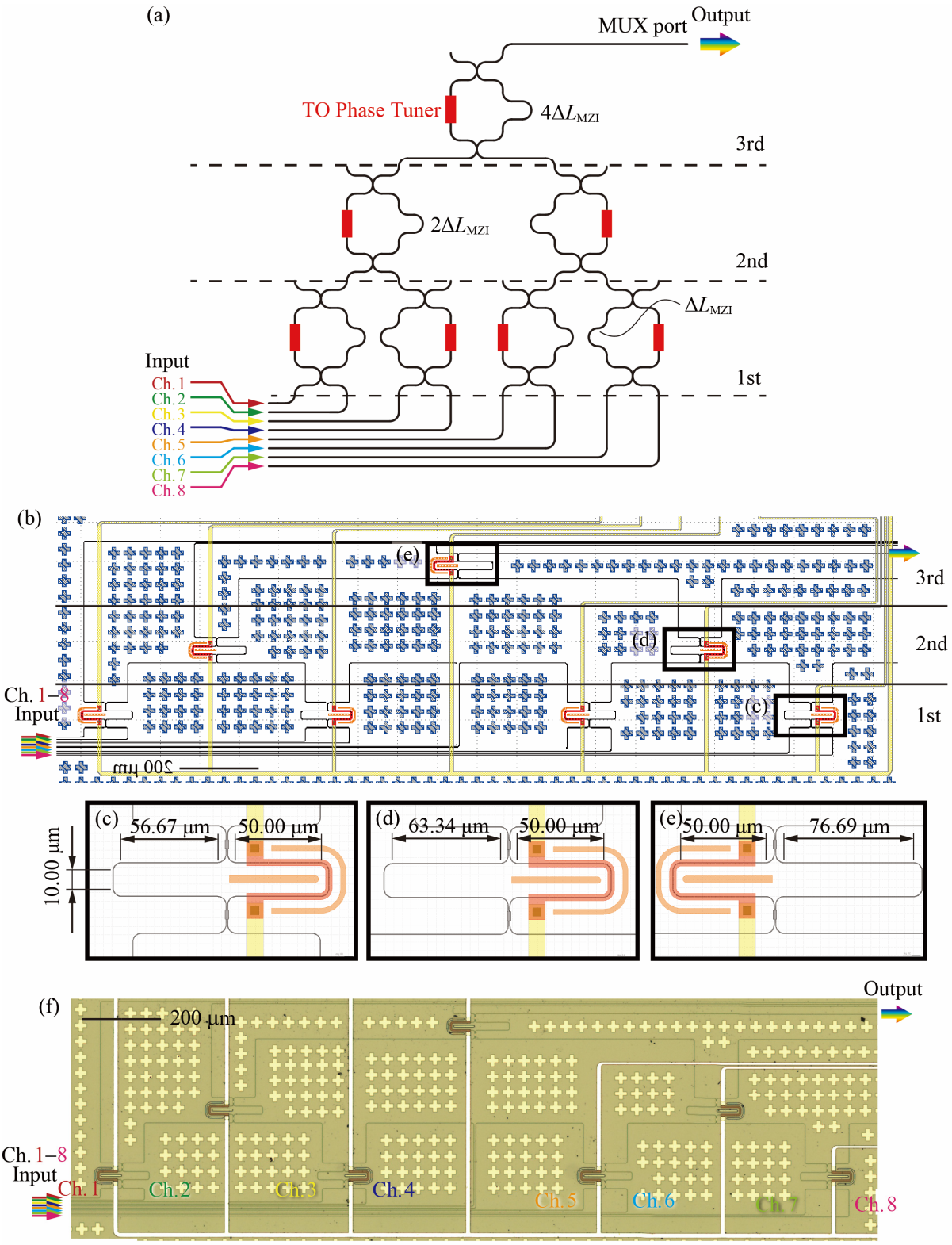

Figure 5.33 8-ch optical MUX based on 2 × 2 asymmetric MZIs. (a) Schematic. (b) Overall CAD pattern. (c), (d), and (e) Magnified CAD patterns of the 2 × 2 asymmetric MZIs at 1st, 2nd, and 3rd stages, respectively. ΔL_{MZI} at 1st 2nd 3rd stages are 13.97, 27.94, and 55.87 μm, and their *FSR* are 40, 20, and 10 nm, respectively. (f) Micrograph of the fabricated device.

5. 6. 3　50 Gbps/ch WDM Transmission

(a)　Devices and Measurement Setup

I performed a WDM transmission experiment on a 45-Ω terminated meanderline devices fabricated on a SOI with t_{Si} of 205 nm and an additional 8ch optical MUX chip. Figure 5.32(a) shows the designed CAD pattern and the fabricated device. The structural parameters of the meanderline devices were L = 170 μm, a = 404, 407 nm, $2r$ = 224 nm, s = 0 nm, w_S = 10 μm, g_{GS} = 7 μm, and L_d = 370 μm, and the doping concentrations were set to be $N_A = 1.05 \times 10^{18}$ cm^{-3} and $N_D = 6.2 \times 10^{17}$ cm^{-3} on this lot. The different designs in a were employed to give them the different operation wavelengths. The PCWs with the lattice shifts were originally designed to change n_g, but their high n_g dispersion hampered the homogeneous modulation in this experiment. This problem can be easily solved by employing dedicated LSPCWs for WDM transmissions. In general, a shorter L offers a higher f_{3dB} at the same R_L. As shown in Fig. 5.17, the 200-μm device exhibited f_{3dB} of 32 GHz at R_L = 50 Ω. Therefore, the device used in this experiment, which has the shorter L and smaller R_L, should exhibit f_{3dB} exceeding 32 GHz.

Figure 5.33(a), (b) and (c) show a schematic, a CAD pattern, and a micrograph of the 8ch optical MUX, respectively. This MUX consists of a three-stage tournament tree based on 2 × 2 asymmetric MZIs. A single MZI at each stage gives the simple sinusoidal response with respect to the incident wavelength. The structures of the MZIs at the 1st, 2nd, and 3rd stage (the 1st stage is the nearest to the 8ch inputs) are shown in Figure 5.33(c), Figure 5.33(d), and Figure 5.33(e), respectively. In the

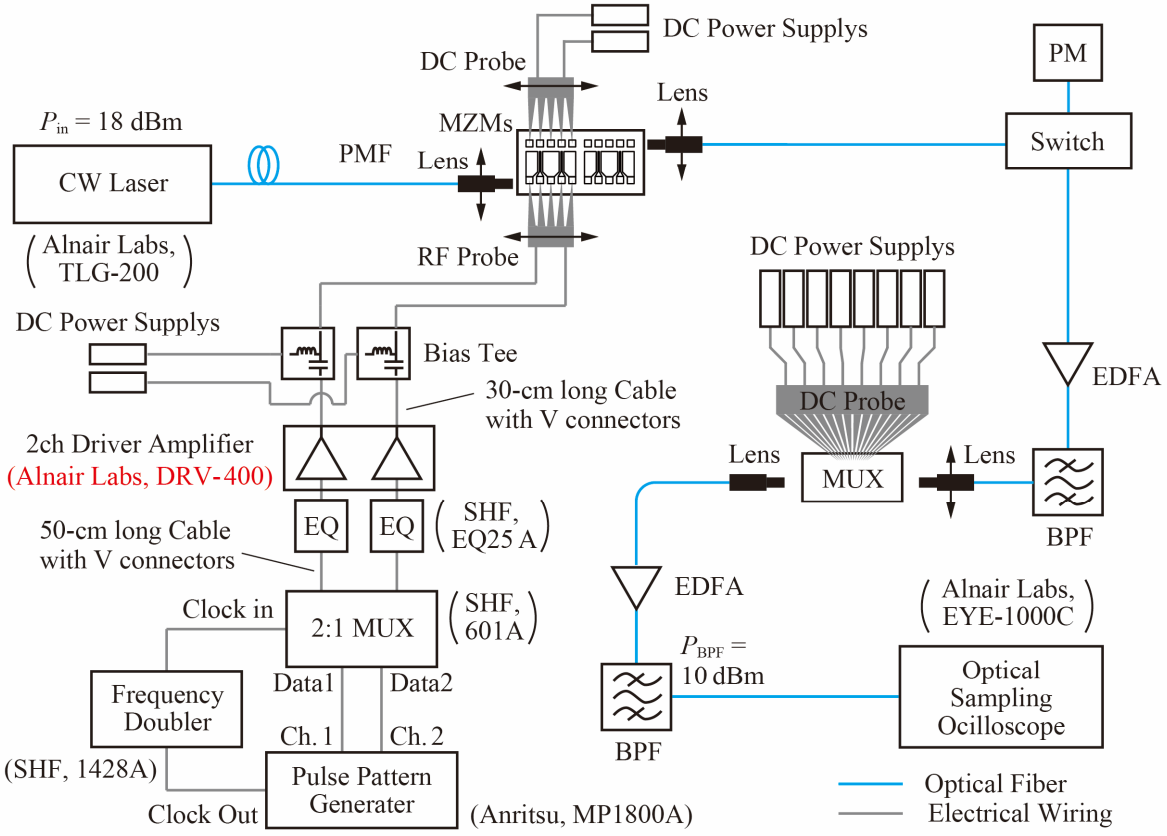

Figure 5.34　Setup for the WDM transmission experiment.

asymmetric MZMs, the horizontal length of the reference arms was 100 μm in total, and the vertical length was 10 μm. Hence the total length in the reference arms L_{ref} was 225.7 μm including two 90-degree bends at a radius of 5 μm. TO phase tuners above the waveguides were used to compensate fabrication errors. The lengths of the other arms, which determine the arm length difference ΔL_{MZI} from the reference length, were set so that a free spectral range (*FSR*s) at each level equals an integer multiple of channel spacing *s* of the MUX. The relationship between ΔL_{MZI} and *FSR* is given by [5-13]

$$\Delta L_{MZI} = \frac{\lambda^2}{n_g \times FSR} \tag{5.52}$$

Assuming λ = 1.55 mm and n_g = 4.5, ΔL_{MZI} at the 3rd stage was determined to be 55.87 μm, which corresponds to *FSR* of 10 nm. At the 1st and 2nd stage, the *FSR* must be 4 × 10 = 40 nm and 2 × 10 = 20 nm, respectively. To obtain these values, ΔL_{MZI} at the 1st and 2nd stage was set to 13.97 μm and 27.94 μm, respectively.

Figure 5.34 shows the measurement setup, which is based on that of the 50-, 56-, and 64-Gbps modulation experiments, for the WDM transmission experiment. In this experiment, I used four channels in the 8-ch MUX. Therefore, I used the two meanderline devices with the different values of *a*, switching between them to cover the four-channel wavelength range of approximately 5 × 3 = 15 nm by their PCWs without the lattice shifts. These devices were driven by 50-Gbps NRZ PRBS signals with V_{pp} = 5.3 V and V_{DC} = –3 V. The values of ϕ_0 was set so that the eye patterns became apparently clearest. The modulated light by these devices were guided to the MUX chip after an amplification and a filtering stage via an EDFA and an BPF, respectively, to compensate for the coupling loss. The light was coupled to an SSC of each channel of the MUX chip and passed through the MUX circuit. The output from the MUX port was amplified to 10 dBm and then filtered again. Subsequently, I observed the eye patterns using the same optical sampling oscilloscope as that shown in the Figure 5.27 and Figure 5.30.

(b) Results

Figure 5.35(a) shows the normalized transmission spectrum of each channel of the 8-ch MUX without the TO phase tuning. Although the channel spacing of approximately 5 nm was observed, the crosstalk between the channels was large. After the TO phase tuning, the transmission spectra were evenly aligned and the crosstalk was suppressed to approximately –20 dB, as shown in Figure 5.35(b). Figure 5.35(c) shows the normalized transmission spectra of the meanderline PCW modulators. These devices originally had the transmission band at λ = 1528–1539 nm and λ = 1539–1549 nm; however, these bands were redshifted by roughly 5 nm via heating due to the relatively high RF power and the TO phase tuners above the PCWs. The former effect was not intended, whereas the latter effect was intended to adjust the wavelength to the four transmission wavelengths of λ_1 = 1537.5 nm, λ_2 = 1543.0 nm, λ_3 = 1548.0 nm, and λ_4 = 1553.5 nm of the 8-ch MUX. Figure 5.35(d) shows the observed 50-Gbps eye patterns at these four wavelengths before and after the multiplexing. I observed 4-ch clear eye patterns even after the multiplexing in the additional MUX chip. Although I showed the measured *ER* at each measurement condition, these *ER* values were affected by the two nonlinear amplification stages via the EDFAs. Therefore, the observation does not directly represent the performance of the PCW modulators. In this experiment, the MUX channels were constricted to four channels because of the relatively narrow transmission band and the highly dispersive n_g spectra in the PCW modulators without the lattice shifts.

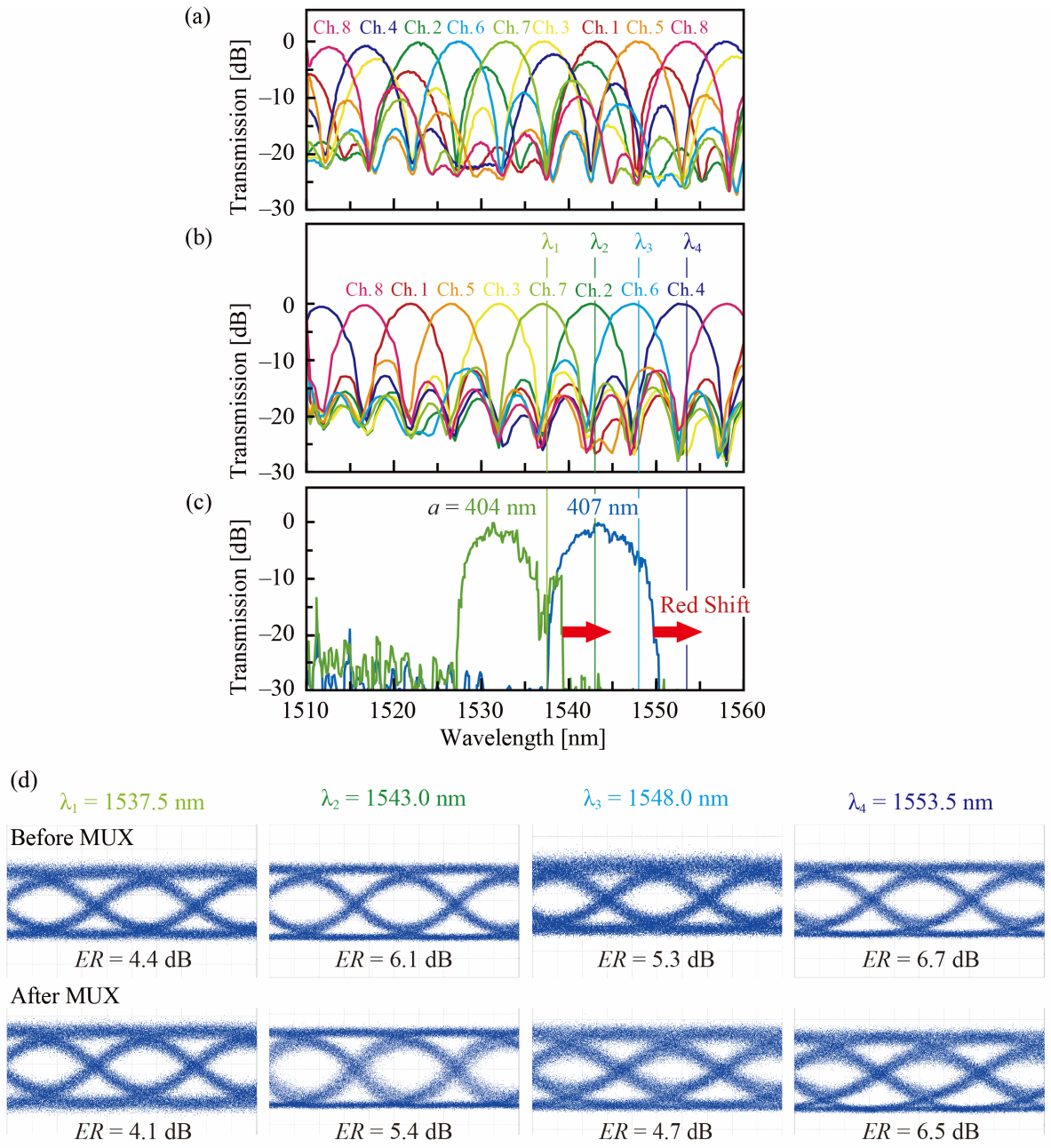

Figure 5.35 Measurement results of the WDM transmission experiment. (a) Normalized transmission spectrum of the 8-ch MUX before the TO phase tuning. (b) Normalized transmission spectrum of the 8-ch MUX after the TO phase tuning. (c) Normalized transmission spectrum of the 45-Ω terminated meanderline PCW modulators. (d) Observed 50 Gbps eye patterns for V_{pp} = 5.3 V and V_{DC} = –3 V.

The inhomogeneous eye patterns were also caused by the high dispersion. These problems will be solved by employing dedicated LSPCWs for the WDM transmissions. Simultaneously, 1.5-fold higher n_g of 30 will be available using this approach. In that case, the transmission bandwidth of the slow light will be narrowed to approximately 10 nm; however, this will not become a drawback in the WDM transmission in which the operation wavelengths are strictly managed.

5. 7 Summary

I experimentally observed the EO phase mismatch that constrains the frequency response of slow-light modulators in a dispersive PCW MZM. This EO phase mismatch is caused by the large velocity difference between the slow light and the RF signals for the modulation, even for the very short L. To address this mismatch, I introduced a meanderline electrode, which simply delays the RF signals with its meandering RF CPW, thereby reducing the EO phase mismatch. I theoretically analyzed the EO phase mismatch to design the meanderline electrode based on the traveling-wave electrode models and the distributed-constant circuit models. The theoretical analysis revealed that meanderline electrodes are effective in improving the frequency response and Γ_L, which is another important factor that controls the phase of the RF reflection. By setting L_d = 425 μm and Γ_L = –0.5 V, a very high f_{3dB} of 56 GHz was theoretically estimated.

Before demonstrating the phase matching achieved using fabricated meanderline devices, I attempted to remove the slow valley and dip in the measured frequency response. These undesired valley and dip originated from the TSL mode that is excited via an electrical potential imbalance between two G electrodes in a CPW. Therefore, I introduced the G-commonized structure to eliminate the slow valley and dip.

I fabricated the designed meanderline devices with load resistors (which determines Γ_L) and then measured the frequency response. The meanderline electrode device with 50-Ω termination exhibited f_{3dB} of ~30 GHz, whereas the normal electrode device exhibited f_{3dB} of 19 GHz. Furthermore, a 20-Ω terminated meanderline electrode device exhibited high f_{3dB} of 38 GHz. In the OOK modulation experiments, very clear 25- and 32-Gbps eye patterns were observed for the 50-Ω terminated meanderline device at small V_{pp} of 1 and 2 V, respectively. I obtained the 50- and 56-Gbps open eye patterns using the 20-Ω terminated meanderline device at V_{pp} = 3.5 V and achieved an even higher rate (64-Gbps) open eye pattern by increasing V_{pp} to 5.2 V. I also observed PAM4 open eye patterns at 20, 25, and 28 Gbaud. At higher symbol rate of 32, 40, 50 Gbaud, the eye patterns became noisy but remained opened. Furthermore, the 50-Gbps/ch WDM transmission was demonstrated with the additional WDM chip. In this experiment, the number of the cannels were constricted to four channels by the non-dedicated PCW design. This will be easily solved by employing dedicated LSPCWs. This approach will enable the 8-ch multiplexing; total bitrate will reach to 400 Gbps.

References

[5-1] R. Ding *et al.*, “Design and characterization of a 30-GHz bandwidth low-power silicon traveling-wave modulator,” *Optics Communications*, vol. 321, pp. 124–133, Jun. 2014, doi: 10.1016/j.optcom.2014.01.071.

[5-2] R. Ding *et al.*, “High-Speed Silicon Modulator With Slow-Wave Electrodes and Fully Independent Differential Drive,” *J. Lightwave Technol.*, vol. 32, no. 12, pp. 2240–2247, Jun. 2014, doi: 10.1109/JLT.2014.2323954.

[1-3] H. Xu *et al.*, “High-speed silicon modulator with band equalization,” *Optics Letters*, vol. 39, no. 16, pp. 4839–4842, Aug. 2014, doi: 10.1364/OL.39.004839.

[5-4] D. Patel *et al.*, “Design, analysis, and transmission system performance of a 41 GHz silicon photonic modulator,” *Opt. Express*, vol. 23, no. 11, p. 14263, Jun. 2015, doi:

10.1364/OE.23.014263.

[5-5] A. Samani *et al.*, "A Low-Voltage 35-GHz Silicon Photonic Modulator-Enabled 112-Gb/s Transmission System," *IEEE Photonics Journal*, vol. 7, no. 3, pp. 1–13, Jun. 2015, doi: 10.1109/JPHOT.2015.2426875.

[5-6] Y. Tang, Y. Yu, Y. Ye, U. Westergren, and S. He, "Design and optimization of an arbitrarily segmented traveling wave electrode for an ultrahigh speed electroabsorption modulator," *Optics Communications*, vol. 281, no. 20, pp. 5177–5182, Oct. 2008, doi: 10.1016/j.optcom.2008.07.014.

[5-7] R. E. Collin, *Foundations for microwave engineering*. John Wiley & Sons, 2007.

[5-8] D. M. Pozar, *Microwave Engineering*, 4th Edition. Wiley, 2011.

[5-9] E. Carlsson and S. Gevorgian, "Conformal mapping of the field and charge distributions in multilayered substrate CPWs," *IEEE Transactions on Microwave Theory and Techniques*, vol. 47, no. 8, pp. 1544–1552, 1999.

[5-10] X. Tu *et al.*, "Silicon optical modulator with shield coplanar waveguide electrodes," *Optics Express*, vol. 22, no. 19, p. 23724, Sep. 2014, doi: 10.1364/OE.22.023724.

[5-11] G. E. Ponchak, J. Papapolymerou, and M. M. Tentzeris, "Excitation of coupled slotline mode in finite-ground CPW with unequal ground-plane widths," *IEEE Transactions on Microwave Theory and Techniques*, vol. 53, no. 2, pp. 713–717, Feb. 2005, doi: 10.1109/TMTT.2004.840571.

[5-12] A. Leven, F. Vacondio, L. Schmalen, S. ten Brink, and W. Idler, "Estimation of Soft FEC Performance in Optical Transmission Experiments," *IEEE Photon. Technol. Lett.*, vol. 23, no. 20, pp. 1547–1549, Oct. 2011, doi: 10.1109/LPT.2011.2162725.

[5-13] F. Horst, W. M. J. Green, S. Assefa, S. M. Shank, Y. A. Vlasov, and B. J. Offrein, "Cascaded Mach-Zehnder wavelength filters in silicon photonics for low loss and flat pass-band WDM (de-)multiplexing," *Opt. Express*, vol. 21, no. 10, p. 11652, May 2013, doi: 10.1364/OE.21.011652.

Chapter6
Frequency-Swept Modulation for a FMCW LiDAR System

6. 1 Overview

As a new application of the Si LSPCW MZM, I investigated a frequency-swept modulation scheme used in an FMCW LiDAR system that needs frequency-swept light source [6-1]–[6-4]. A direct frequency sweep via a tunable laser is the simplest method to generate frequency-swept light. However, it needs a complex frequency stabilizer based on an optical feedback circuit [6-5]–[6-7], represented by an optical phase locked loop, to obtain a high linearity of the temporal frequency sweep. On the contrary, the frequency sweep method using an EO modulator and a frequency-swept RF source can generate linearly frequency-swept light without such a complex optical compensation circuit, because the mature RF signal source undertakes the linear frequency sweep. Here, it is necessary to confirm that δf of a single-tone optical modulation is below 100 kHz to ensure 300-m distant ranging with an adequate margin. δf is usually constricted by a linewidth of a laser source, but the effect of modulation characteristics of a modulator to linewidth δf must be also paid an attention; I observed single-tone modulation spectra via the Si LSPCW MZM after an OE conversion. The next step is the initial demonstration of the periodical frequency-swept modulation scheme. Sawtooth-shaped and triangular frequency-swept modulations are used for the FMCW system, with the frequency span B and the temporal linearity of the frequency sweep being important factors. B determines the ranging resolution ΔR and is given by

$$\Delta R = \frac{cR_{\max}}{2B(R_{\max} - R)} \approx \frac{c}{2B} \tag{6.1}$$

for the sawtooth-shaped frequency sweep and

$$\Delta R = \frac{cR_{\max}}{B(R_{\max} - R)} \approx \frac{c}{B} \tag{6.2}$$

for the triangular frequency sweep, where c is the speed of light and $R_{\max}$ is the maximum ranging distance. For example, ΔR of approximately 5 cm is obtainable for the sawtooth-shaped frequency sweep with B = 3 GHz.

6. 2 Evaluation of Single-Tone Modulation

Figure 6.1 shows a measurement setup for the evaluation of single-tone modulation. The DUT has the

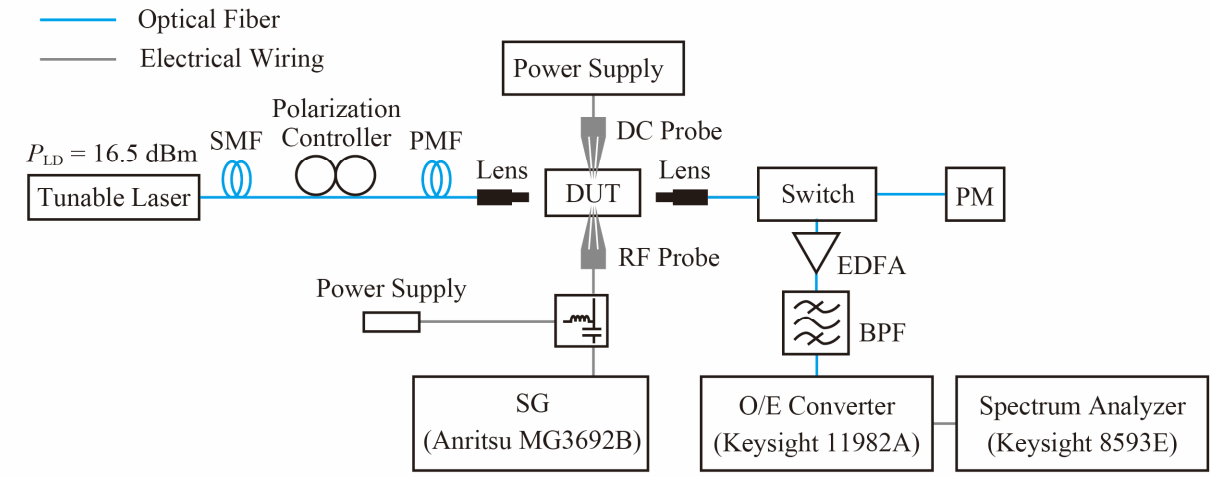

Figure 6.1 Setup for single-tone modulation.

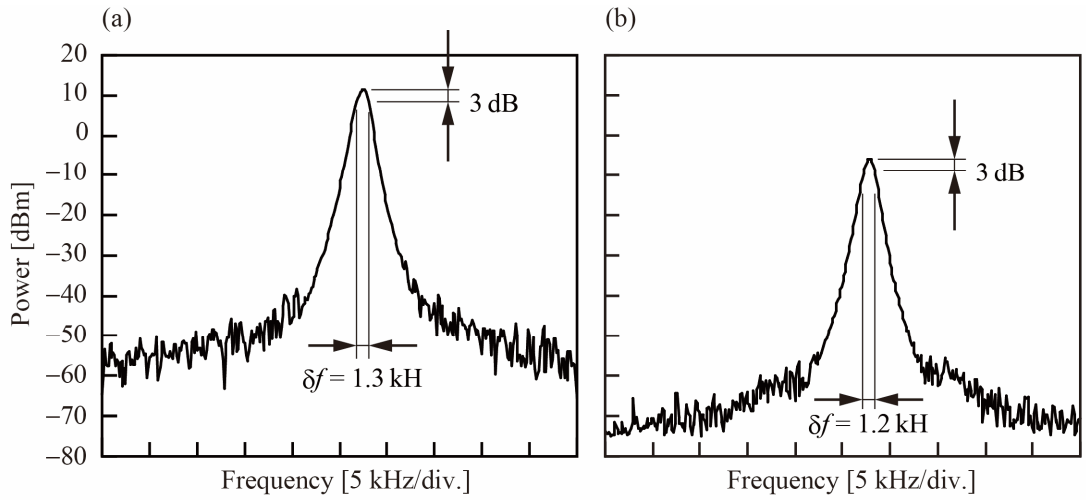

Figure 6.2 Single-tone frequency spectra. (a) Input RF signal. (b) Modulated signal.

same design as that of Section 4. 2: L = 200 μm, a = 400 nm, $2r$ = 220 nm, s_3 = 95 nm, $N_A = 9.5 \times 10^{17}$ cm^{-3}, and $N_D = 5.7 \times 10^{17}$ cm^{-3}. The load resistors were omitted to obtain high modulation efficiency. The light from the tunable laser was modulated by the DUT using the RF single-tone signal generated by a signal generator (Anritsu Corp., MG3692B). I set their parameters as follows: P_{LD} = 16.5 dBm, V_{DC} = –2 V, RF power P_{RF} of 13 dBm, and RF frequency f_{RF} of 2 GHz. I observed the frequency spectrum after the OE conversion with the span set to 50 kHz and the resolution bandwidth (*RBW*) set to 1 kHz. The average received power P_r was adjusted to 9 dBm by tuning the gain of the EDFA. Figure 6.2 shows the RF spectra of the input single-tone signal generated by the SG and the output single-tone signal after the modulation and OE conversion stages. The value of δf of the input single-tone signal was found to be 1.3 kHz, which is near the *RBW*; the value may be restricted by the *RBW*. After the modulation and the OE conversion stages, the value of δf was still maintained. It was found from this result that the modulation by the Si LSPCW MZM does not affect the δf and that a sufficiently narrow δf can be obtained, if a lasing linewidth of a laser source is narrow enough.

6. 3 Beat Signal Generation between Two Single-Tone Signals

I performed a beat signal generation experiment between two single-tone signals modulated by LSPCW MZMs; this experiment is an initial and fundamental experiment to verify coherent ranging operation. Figure 6.3(a) shows the measurement setup. TE-like polarized light with λ = 1540 nm was split into two optical paths denoted Path1 and Path2 that were coupled into DUT1 and DUT2, respectively. Path1 included a variable optical attenuator to simulate an optical loss during generation and detection in an actual LiDAR system. Here I define the average optical power in Path1 and Path2 just before the mixing step in the fiber coupler as P_1 and P_2, respectively. DUT1 and DUT2 are LSPCW MZMs of identical design; both devices have L = 500 μm, $2r$ = 220 nm, and s_3 = 80 nm. These devices were driven by two different SGs, denoted SG1 (Anritsu Corp., MG3642A) and SG2 (Anritsu Corp., MG3692B), with the ϕ_0 of the devices set to $\pi/2$. Figure 6.3(b) and (c) show the temporal waveforms of the sinusoidal signals output from SG1 and SG2, respectively, detected using a sampling oscilloscope. In this measurement, I

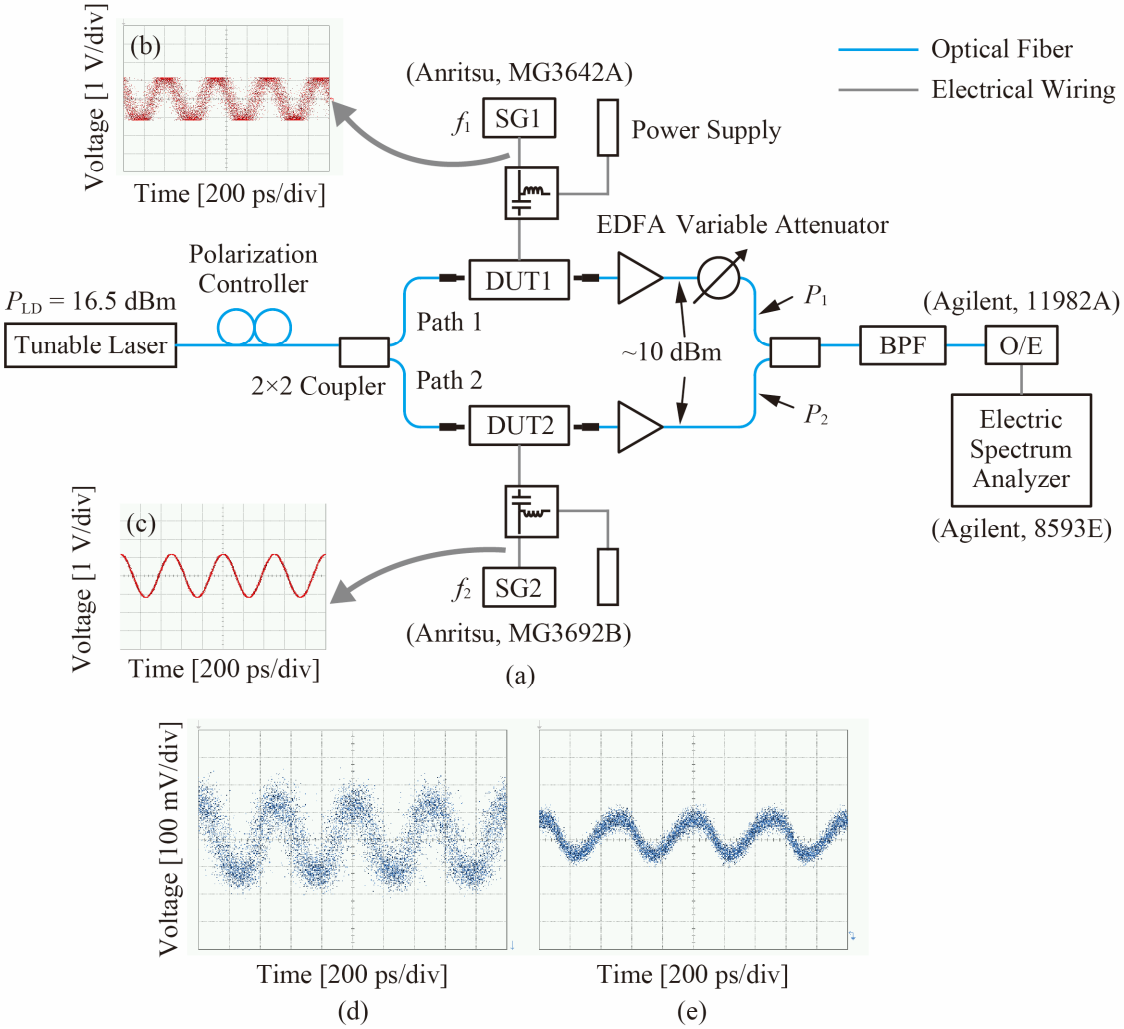

Figure 6.3 (a) Measurement setup for beat signal generation using two single-tone signals. (b) Observed temporal waveform of a 1.8-GHz frequency output signal from SG1. (c) Observed temporal waveform of a 2.0-GHz frequency output signal from SG2.

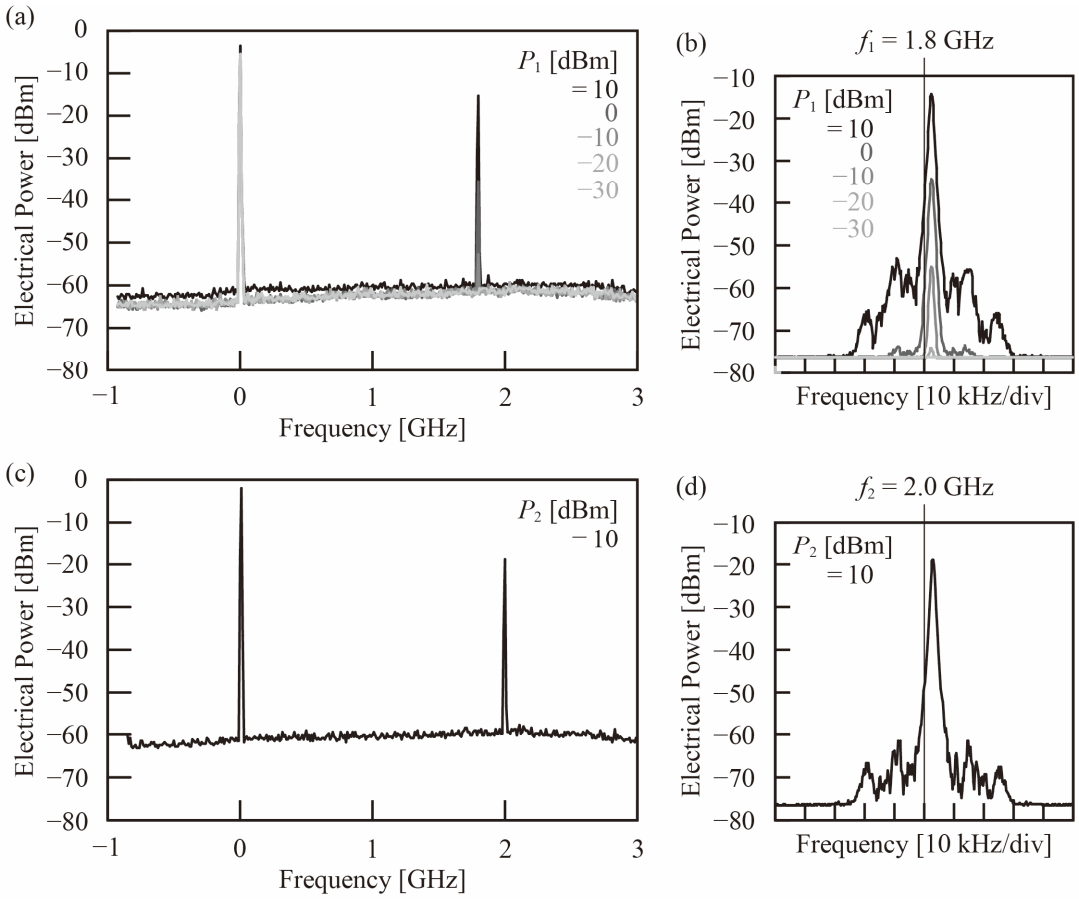

Figure 6.4 Observed frequency spectra in Path1 in the frequency range of (a) 4 GHz and (b) 1 GHz. Observed frequency spectra in Path2 in the frequency range of (c) 4 GHz and (d) 1 GHz.

set the following parameters: frequency of SG1 f_1 = 1.8 GHz; frequency of SG2 f_2 = 2.0 GHz; and V_{pp} = 2.4 and 2.3 V for SG1 and SG2, respectively. Although, the signal output from SG2 exhibited sufficiently high quality, the signal output from SG1 exhibited a large amount of jitter. I observed the waveform modulated by these signals with a coupled DC voltage of V_{DC} = –2 V after the amplification and the bandpass filtering stages. Figure 6.3(d) and (e) show the observed waveforms that reflect the input waveform qualities. However, the observed waveform qualities at the sampling oscilloscope could be also affected by the trigger signal quality. Therefore, I confirmed the signal qualities using a spectrum analyzer, which requires only the signal inputs. Figure 6.4(a) and (b) show the observed spectra in Path1 at P_1 = –30, –20, –10, 0, and 10 dBm for the frequency spans of 4 GHz and 100 kHz, respectively. I observed the spectral peaks at 0 Hz and f_1 = 1.8 GHz. The DC component included a residual optical carrier that corresponds to an unmodulated component. As shown in Figure 6.4(b), the spectral peak reached to –14 dBm at maximum, but it was 24 dB lower than P_1 = 10 dBm. This low modulation efficiency (which was caused by the small V_{pp} of 2.4 V) can be improved by using a deeper modulation process via a higher V_{pp}. The spectral peak power was changed in proportional to the square of P_1. Although the spectrum had a sidelobe of ~30-kHz width, the linewidth was as narrow as approximately 1 kHz. Figure 6.4(c) and (d) show the observed spectra in Path2 at P_2 = 10 dBm at the frequency spans of 4 GHz and 100 kHz, respectively. Similar spectral power and the linewidth as those of Path1 were observed. Therefore, the adequate signal quality of SG2 was confirmed by this measurement. Figure 6.5(a) shows the beat spectrum after the mixing of the light beams in Path1 and Path2 in the frequency

range of 4 GHz. I observed several frequency components, including the target frequency $f_A = f_2 - f_1 =$ 0.2 GHz. Figure 6.5(b) shows the spectrum around f_A in the frequency span of 1 GHz. The detected beat power was –27 dBm for $P_1 = P_2 = 10$ dBm and was observed to reduce in proportional to P_1, whereas the power of the f_1 component was reduced in proportional to square of P_1; this characteristic is one of the most attractive behaviors of the coherent detection approach. Figure 6.5(c) shows the further

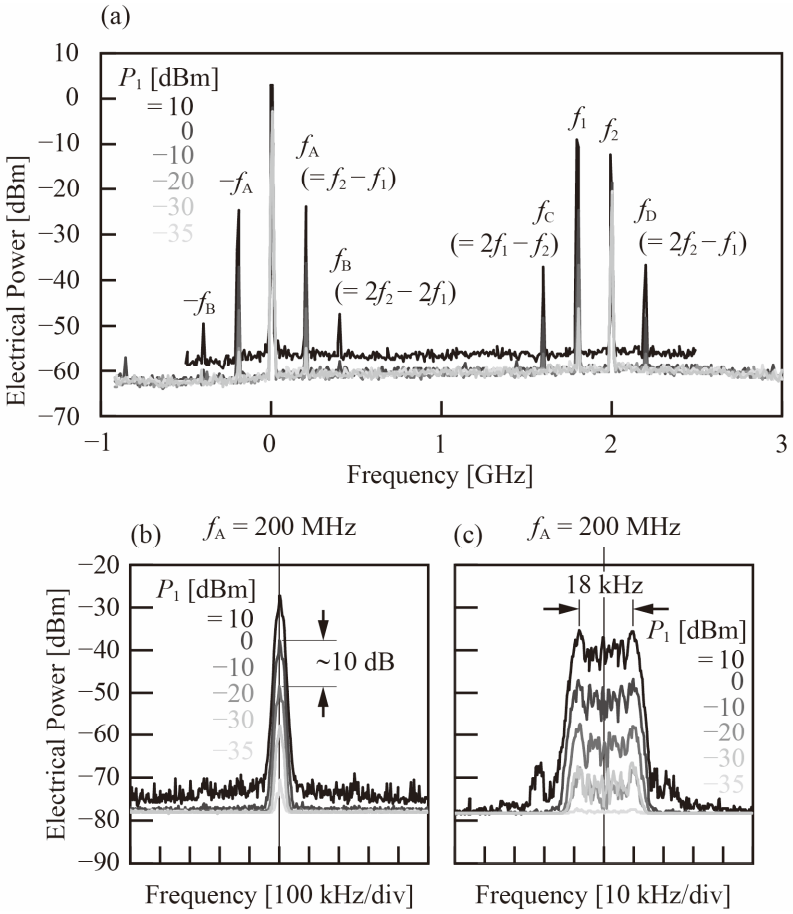

Figure 6.5 Observed beat spectra between the two single-tone signals for $f_1 = 1.8$ GHz and $f_2 = 2.0$ GHz. The frequency span was set to (a) 4 GHz, (b) 1 GHz, and (c) 100 kHz.

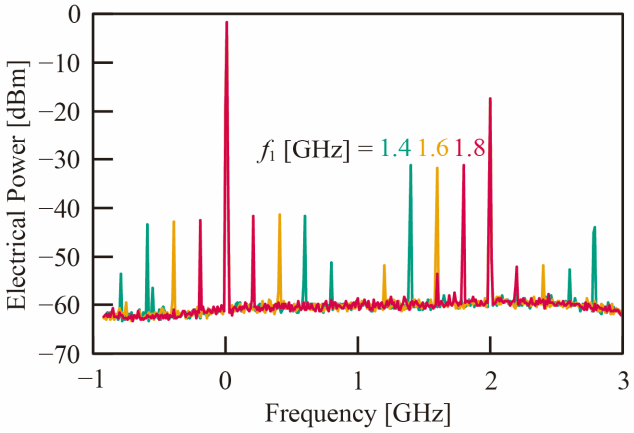

Figure 6.6 Observed beat spectra between the two single-tone signals for $f_1 = 1.4$, 1.6, and 1.8 GHz and $f_2 = 2.0$ GHz.

magnified beat spectrum in the frequency span of 100 kHz. The spectral peak was broadened to 18 kHz. This broadening originated from the sidelobes in the spectra in each path. Subsequently, I observed the beat spectrum by manually changing the f_{I} from 1.8 GHz to 1.6 GHz and 1.4 GHz as shown in Figure 6.6. I verified that f_{A} was shifted 0.2 GHz, 0.4 GHz, and 0.6 GHz, respectively. Although f_{I} was shifted manually in this experiment because this is an early trial, this shift of f_{A} corresponds to a change in a ranging distance in an FMCW LiDAR.

6. 4 Frequency-Swept Modulation

6. 4. 1 Frequency-Swept Signal Generation

I generated frequency-swept signals using an arbitrary waveform generator (AWG, Agilent Technologies, Inc., M8195A, sample rate: 65 GSa/s) and *IQ Tools*, which is a signal generation software package.

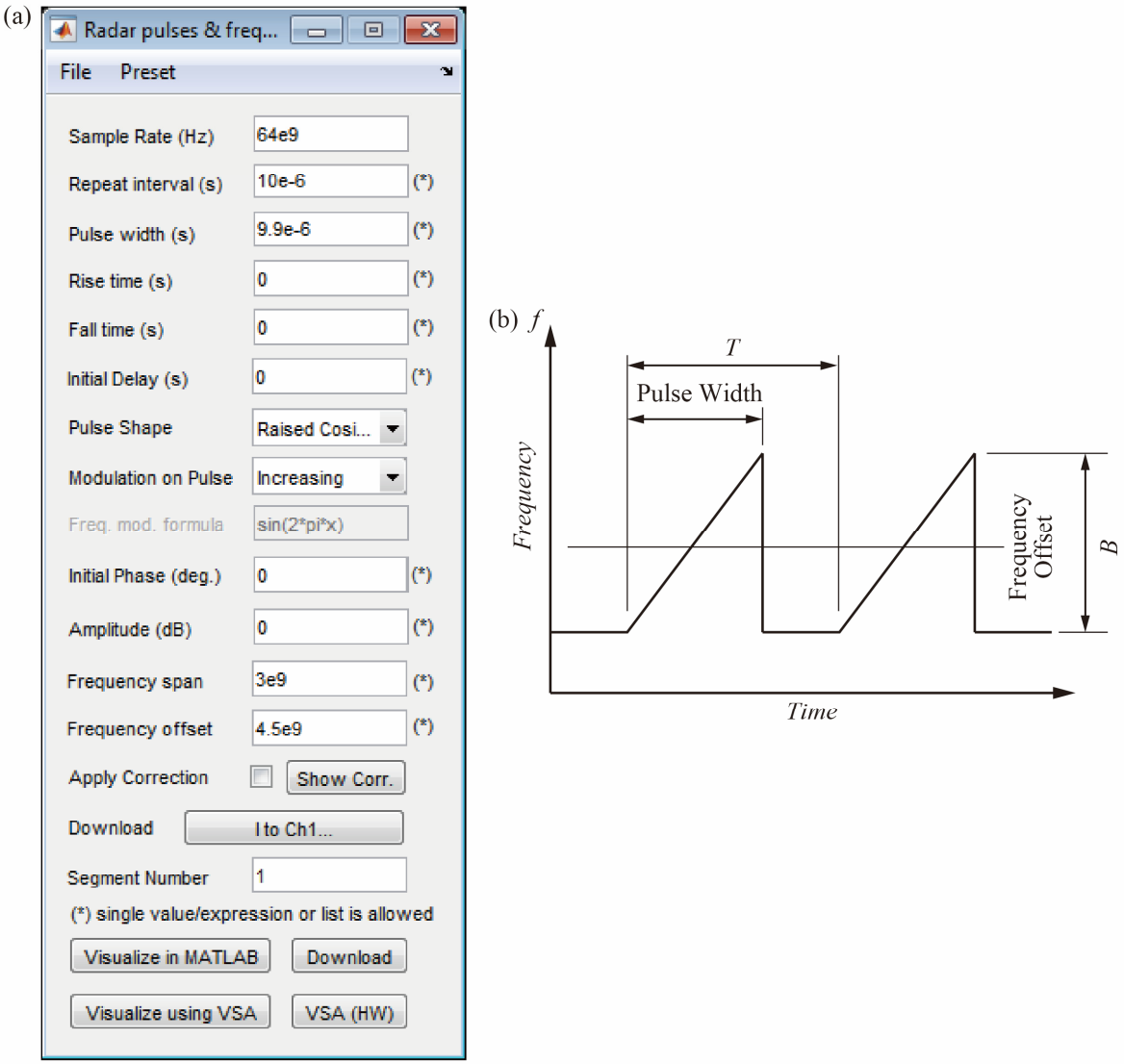

Figure 6.7 (a) GUI of *Radar pulses & frequency chirps* in *IQ tools*. (b) Illustration of a generated sawtooth-shaped frequency-swept signal.

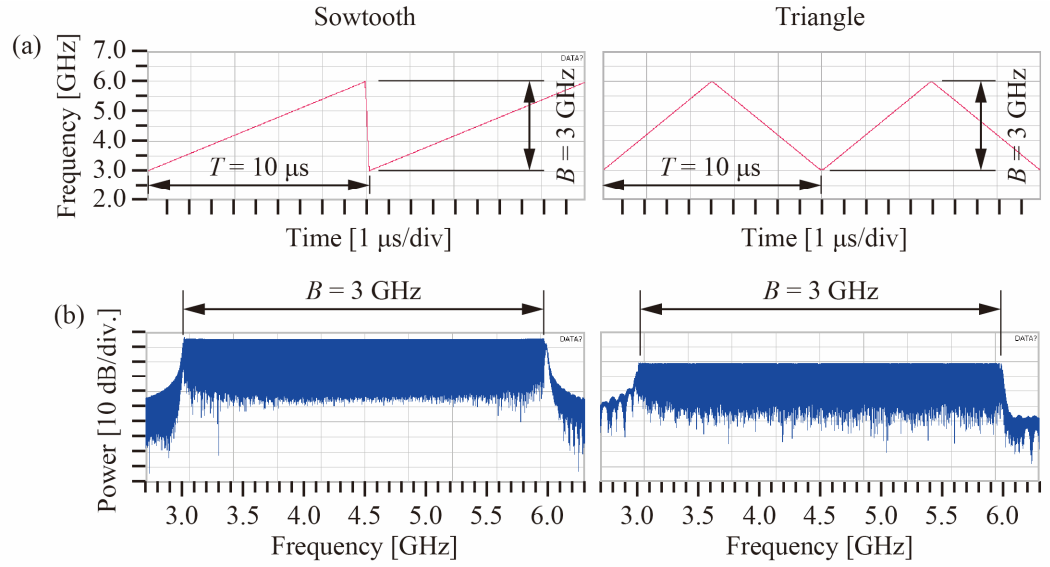

Figure 6.8 Sawtooth-shaped frequency-swept signal data internally generated in the AWG with B = 3 GHz, f_{center} = 4.5 GHz, and T = 10 μs. (a) Frequency spectrum. (b) Frequency as a function of time.

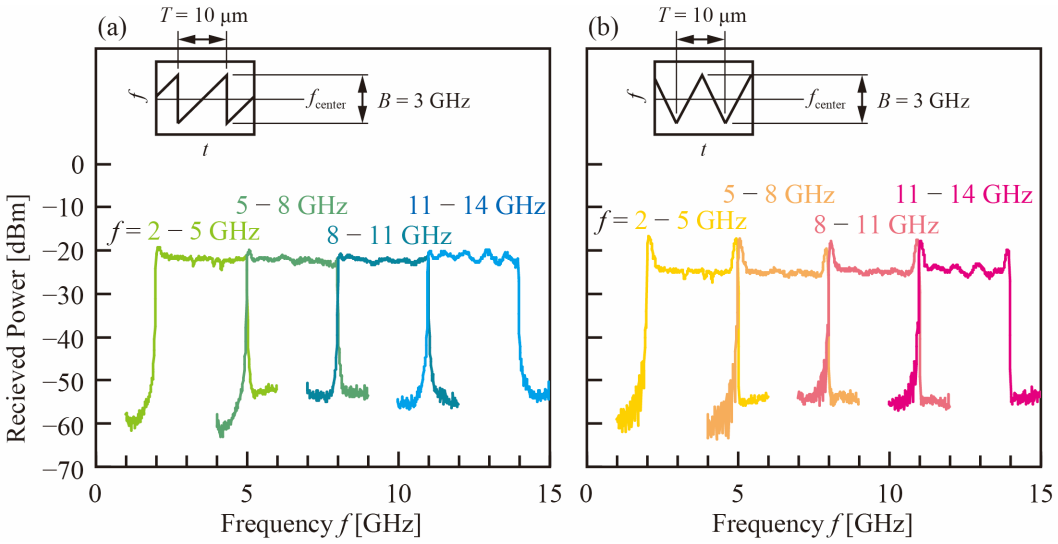

Figure 6.9 Observed spectra of the frequency-swept signals. (a) Sawtooth-shaped frequency-swept signals and (b) triangular frequency-swept signals for V_{pp} = 1 V, B = 3 GHz, T = 10 μs at f_{center} = 3.5, 6.5, 9.5, and 12.5 GHz. Insets show the outlines of each frequency as a function of time.

Figure 6.7(a) shows a GUI of *Rader pulses & frequency chirps* of *IQ Tools*. This tool helps generate frequency-swept signals with the AWG. The fundamental shape of the frequency-swept signals is set by *Modulation on Pulse*. The sawtooth-shaped and triangular frequency sweeps used were realized by choosing *Increasing* and *Inversed V*, respectively. Here, other important parameters are the repeat interval T, the pulse width, the frequency offset, and B. Figure 6.7(b) shows the correspondence between these parameters and a generated sawtooth-shaped frequency-swept signal. The pulse width is the time width of the frequency modulation pulse in the repeat interval. I set the pulse width to be T – 0.1 μs and T – 0.025 μs for the sawtooth-shaped signals and the triangular signals, respectively. The frequency offset corresponds to the center frequency f_{center} in the frequency sweep.

Figure 6.8 shows the temporal frequency changes and frequency spectra of the sawtooth-shaped and

triangular frequency-swept signals with B of 3 GHz, f_{center} of 4.5 GHz, and T of 10 μs that were internally generated in the AWG. As shown in Figure 6.8(a), the frequency of the sawtooth-shaped frequency-swept signal increased linearly over the period T = 10 μs, and the frequency of the triangular frequency-swept signal increased and decreased linearly over the period T = 10 μs. Figure 6.8(b) shows the frequency spectra taht had the 3-GHz wide flat top corresponding to the setting, although many combs appeared overall because of the 64-GSa/s sample rate. I also measured the spectrum of the output signals from the AWG. Figure 6.9(a) and Figure 6.9(b) show the measured spectra of the sawtooth-shaped frequency-swept signal and the triangular frequency-swept signal, respectively, for V_{pp} = 1 V, B = 3 GHz, T = 10 μs at f_{center} = 3.5, 6.5, 9.5, and 12.5 GHz. I observed the following: 1) a flat top with 1.5-dB fluctuation at f_{center} = 3.5, 6.5, and 9.5 GHz and 2) increased fluctuation of approximately 3 dB at f_{center} = 12.5 GHz. The spectra of the triangular frequency-swept signal exhibited sharp peaks at the edges of the flat spectra; these peaks may be caused by discontinuous waveform and will be suppressed by applying a window function. The higher f_{center} is advantageous for separation between the fundamental frequency $f_{1st} = f_{center} \pm B/2$ and the second-order harmonics $f_{2nd} = 2(f_{center} \pm B/2)$. To avoid overlap between these frequency components, f_c must be higher than $3/2 \times B$ at minimum. Therefore, large B requires high f_c , which imposes a burden to RF circuits and results in small ΔR.

6. 4. 2 Modulation Experiment

Figure 6.10 shows the measurement setup for the frequency-swept modulation experiment. The DUT is an interleaved p-n incorporated LSPCW MZM with L = 500 μm, $2r$ = 220 nm, and s_3 = 80 nm fabricated using the same lot as the device used in Section 6. 2. The load resistors were also omitted to obtain large modulation efficiency. The device was driven by the frequency-swept signals output from the AWG with V_{pp} = 0.1, 0.5, and 1 V and V_{DC} = –0.5 V. I set P_{LD} = 16.5 dBm, B = 3 GHz, T = 10 μs, f_{center} = 3.5, 6.5, 9.5, and 12.5 GHz, and $\phi_0 = \pi/2$. With modulation, sidebands appear at frequencies shifted by f_{1st} from a carrier frequency f_c ($>> f_{1st}$). The modulated light was amplified so that the observed spectra have the almost same power as the input signal shown in Figure 6.9. Next, I observed the frequency spectra with the spectrum analyzer after filtering by the BPF and OE conversion. Only the beat frequencies between the carrier (frequency f_c) and the sidebands (frequency $f_c \pm f_{1st}$) are detectable because f_c is much higher than the bandwidth of the OE converter.

Figure 6.11(a) and Figure 6.11(b) show the observed modulated spectra of the sawtooth-shaped and triangular frequency-swept signals, respectively, for V_{pp} = 1 V. These spectra appeared corresponding to Figure 6.9, although the spectral power decreased with the increase in the modulation frequency because of the insufficient frequency response of the open-terminated 500-μm long DUT. Despite this reduced power, the spectrum at f_{center} = 3.5 GHz was almost flat. It is necessary to design appropriate L to obtain a flat spectrum at the higher modulation frequency. In any case, I confirmed the frequency-swept modulation through the spectral observation. Subsequently, I measured the frequency spectra while changing V_{pp} at f_{center} = 3.5 GHz, as shown in Figure 6.11(a). The flattop power was roughly proportional to the input power calculated from the V_{pp}. Simultaneously, the spectral power in the frequency range of 5 – 10 GHz increased because of the second-order harmonics generated by nonlinearity of the modulation. As mentioned above, this harmonic power can be separated with the fundamental frequency by optimizing f_{center} and B.

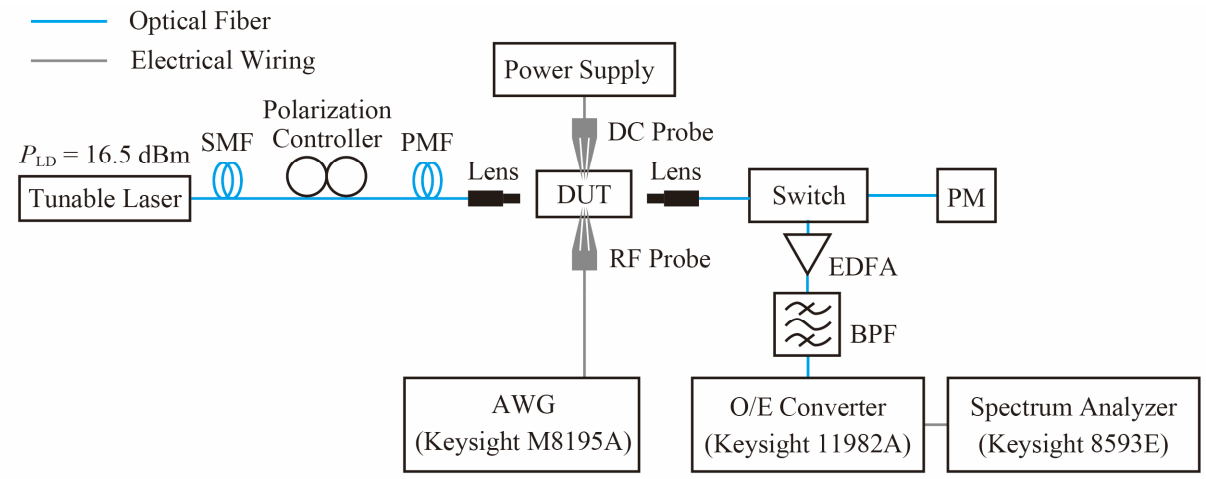

Figure 6.10 Measurement setup for frequency-swept modulation.

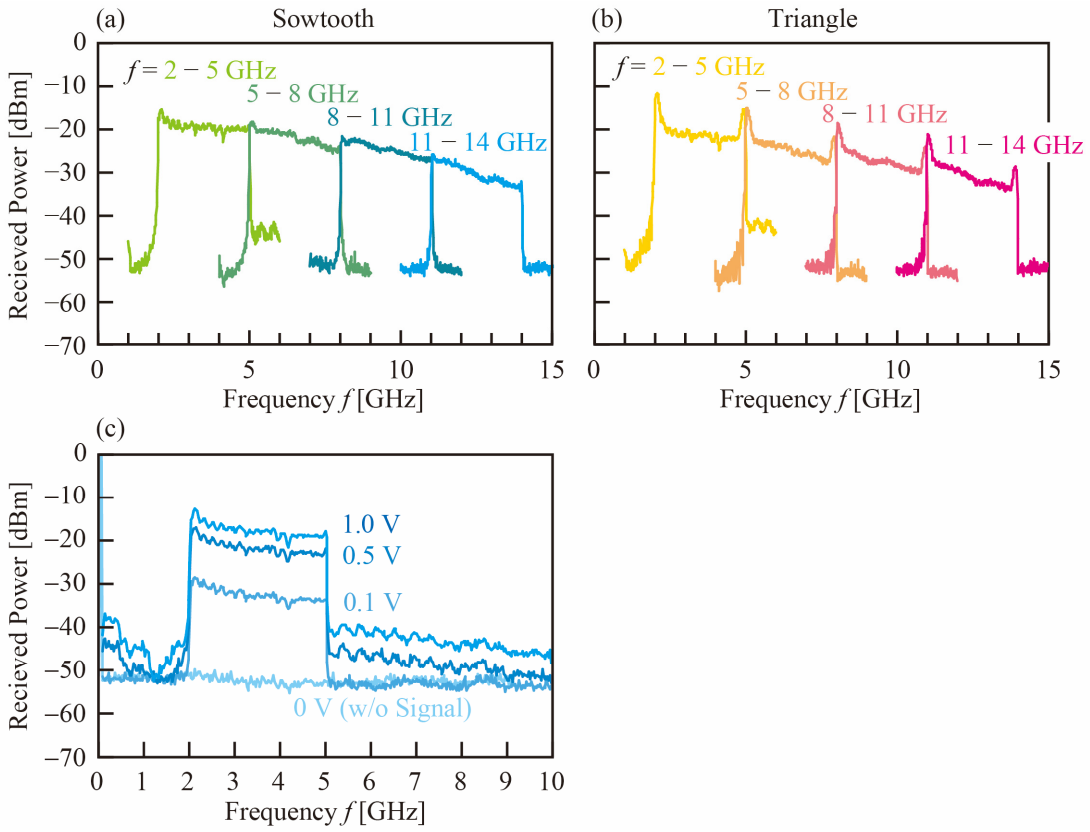

Figure 6.11 Frequency-swept modulation spectra for B = 3 GHz and T = 10 μs. (a) Sawtooth-shaped frequency sweep for different frequencies. (b) Triangular frequency sweep for different frequencies. (c) Sawtooth-shaped frequency sweep for different values of V_{pp}.

6. 5 Ranging Experiment in Optical Fiber System

6. 5. 1 Measurement Setup

Figure 6.12(a) shows the measurement setup for the ranging experiment. This system has an additional fiber optic interferometer compared to the system shown in Figure 6.10. After the amplification to 10

dBm and the bandpass filtering, the modulated light was split into two paths: a reference path whose length is L_{ref} = 153.5 cm and a delay line whose length is L_{delay}. The delay line was used to simulate the distance to a target object. The light in the two paths was mixed by a 2 × 2 fiber coupler and input into a balanced InGaAs photodetector (Discovery semiconductors, Inc., DSC-710). The signal converted into the RF signal was detected using the spectrum analyzer. Figure 6.12(b) and (c) shows the frequency as a function of the time after the propagation through the reference path and the delay line, respectively. These different propagation lengths of L_{delay} and L_{ref} result in the delay time difference Δt between the light beams. Therefore, a constant beat frequency f_{beat} is generated by the mixing and is detected using the spectrum analyzer, as shown in Figure 6.12(d). f_{beat} is given by

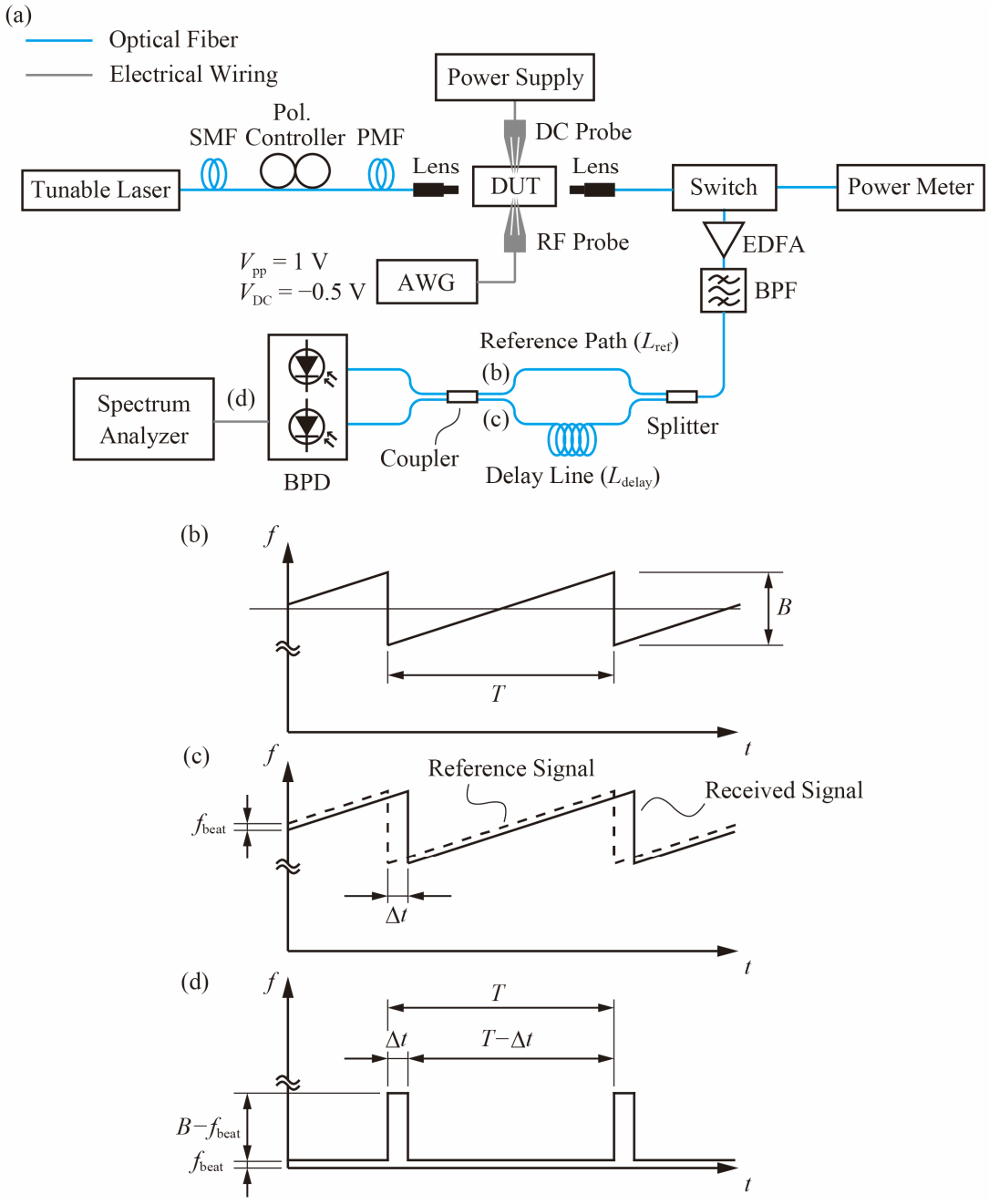

Figure 6.12 (a) Measurement setup for the fiberoptic ranging experiment with L_{ref} = 153.5 cm. (b)–(c) Frequency as a function of time at each location shown in (a).

$$f_{\text{beat}} = \frac{n_{\text{SMF}}\left(L_{\text{delay}} - L_{\text{ref}}\right)}{c} \times \frac{B}{T} \tag{6.3}$$

for the sawtooth-shaped frequency-swept modulation, and

$$f_{\text{beat}} = \frac{n_{\text{SMF}}\left(L_{\text{delay}} - L_{\text{ref}}\right)}{c} \times \frac{2B}{T} \tag{6.4}$$

for the triangular frequency-swept modulation, where n_{SMF} (= 1.45) is the refractive index of a SMF.

6. 5. 2 Results

First, I attempted to range a delay line of L_{delay} = 1002 ± 10 cm using a sawtooth-shaped frequency-swept modulation with B = 3 GHz, f_{center} = 3.5 GHz, T = 5 μs. Under this condition, f_{beat} of 24.5–25.0 MHz was expected. Figure 6.13 shows the observed spectrum for frequency spans of 100, 10, 1, and 0.1 MHz. As shown in Figure 6.13(a), f_{beat} was measured to be 25.0 MHz, which corresponds to the expected range. For the narrower span of 10 MHz (Figure 6.13(b)) and 1 MHz (Figure 6.13(c)), I observed combs with the regular intervals of $1/T$ = 0.2 MHz. If the next comb is detected as the f_{beat} because of amplitude noise, the result is a 6.9-cm error corresponding to the 0.2-MHz interval. For an even narrower span of 1 MHz, the width of the single comb was evaluated to be 17.3 kHz, which corresponds to 6-mm ranging precision, i.e., reduced ranging precision. Figure 6.14 shows observed

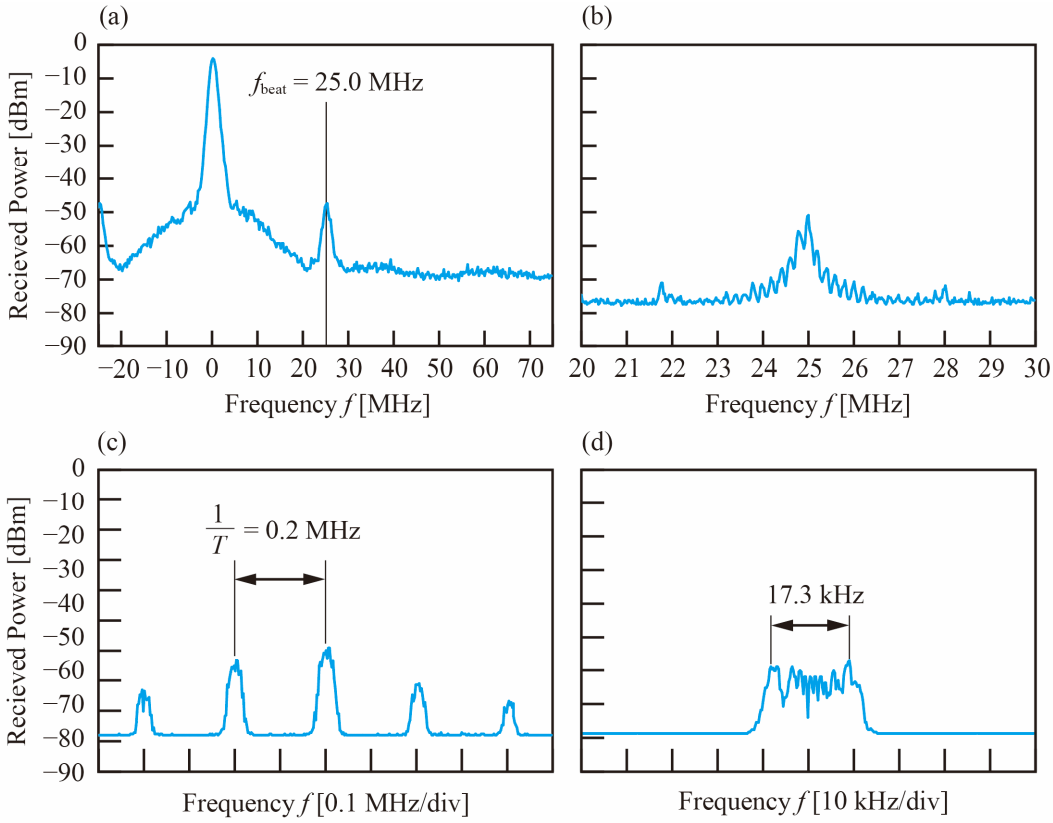

Figure 6.13 Measured ranging spectra for the sawtooth-shaped frequency-swept modulation with B = 3 GHz, T = 5 μm and delay line of L_{delay} = 1002 ± 10 cm. The center frequency of spectrum was set to be 25 MHz, and the span of the spectrum analyzer was set to be (a) 100 MHz, (b) 10 MHz, (c) 1 MHz, and (d) 0.1 MHz.

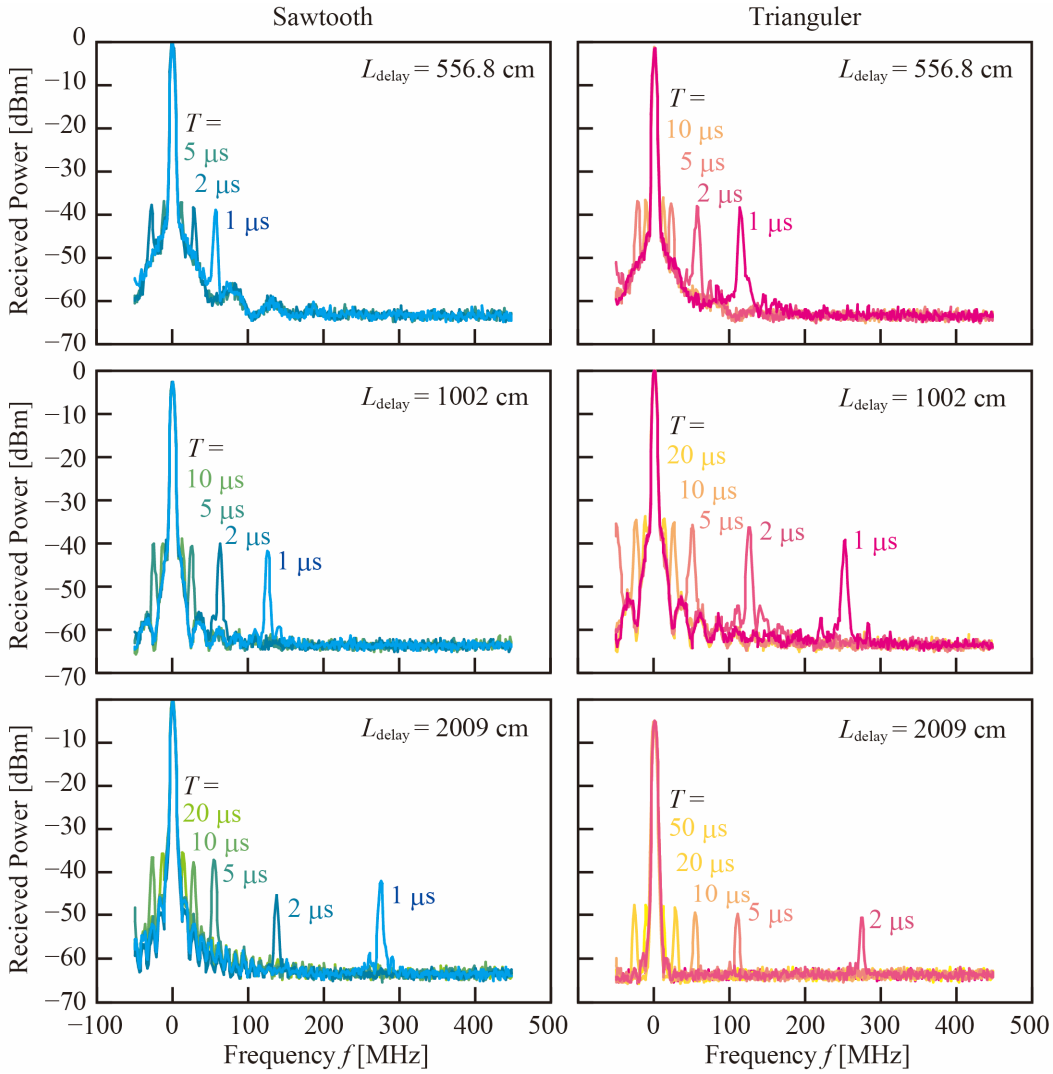

Figure 6.14 Measured ranging spectra for the sawtooth-shaped and triangular frequency-swept modulations with B = 3 GHz, T = 1, 2, 5, 10, and 20 μm, and delay line values of L_{delay} = 556.8, 1002, and 2009 cm.

ranging spectra using the sawtooth-shaped and triangular frequency-swept modulations for different L_{delay} and T. The observed f_{beat} values are nearly in agreement with the expected values for the all conditions. The detected spectral peak power differed by the span, with an estimated –40 dBm for the span of 500 MHz. When the total incident power of 10 dBm (10 mW) is input into the balanced photodetector with 0.75-A/W sensitivity, the photocurrent of 7.5 mA is produced, corresponding to 4.5 dBm (2.8 mW) in a 50-Ω impedance circuit. Therefore, it is considered that most optical power did not contribute to the generation of the beat signal because of the low V_{pp} of the frequency-swept signal that determines the sideband power. In this experiment, I used no RF amplifier, which is required to obtain a high beat power.

6. 6 Summary

I investigated frequency-swept modulation using the LSPCW MZM and the AWG. First, I confirmed the quality of the single-tone modulation after the OE conversion and obtained δf of 1.2 kHz, which was constricted by the *RBW* of the RF spectrum analyzer. Using such single-tone modulated signals, I

attempted beat signal generation. When I drove the two LSPCW MZMs at two signals of different frequency of f_1 = 1.8 GHz and f_2 = 2.0 GHz, I observed several frequency components, including f_A = 0.2 GHz (which is required in a FMCW LiDAR system), and observed a shift with the shift in f_1. Subsequently, I generated sawtooth-shaped and triangular frequency-swept signals with B= 3 GHz using the AWG and applied these signals to the LSPCW MZM. The modulated signals exhibited frequency-swept spectra corresponding to the generated signal. I also performed an initial ranging experiment in the fiberoptic system and obtained f_{beat} = 25.0 MHz, which agrees with the theoretical value estimated for L_{delay} = 1002 ± 10 cm. Values of f_{beat} corresponding to the theoretical values for L_{delay} = 556.8 and 2009 cm and T = 1, 2, 5, 10, and 20 μs were also observed.

References

[6-1] S. W. Henderson, C. P. Hale, J. R. Magee, M. J. Kavaya, and A. V. Huffaker, "Eye-safe coherent laser radar system at 2.1 μm using Tm,Ho:YAG lasers," *Opt. Lett.*, vol. 16, no. 10, pp. 773–775, May 1991, doi: 10.1364/OL.16.000773.

[6-2] C. V. Poulton *et al.*, "Coherent solid-state LIDAR with silicon photonic optical phased arrays," *Optics Letters*, vol. 42, no. 20, p. 4091, Oct. 2017, doi: 10.1364/OL.42.004091.

[6-3] A. Martin *et al.*, "Photonic Integrated Circuit-Based FMCW Coherent LiDAR," *J. Lightwave Technol.*, vol. 36, no. 19, pp. 4640–4645, Oct. 2018, doi: 10.1109/JLT.2018.2840223.

[6-4] Z. Xu *et al.*, "Frequency-Modulated Continuous-Wave Coherent Lidar With Downlink Communications Capability," *IEEE Photon. Technol. Lett.*, vol. 32, no. 11, pp. 655–658, Jun. 2020, doi: 10.1109/LPT.2020.2990942.

[6-5] K. Iiyama, Lu-Tang Wang, and Ken-Ichi Hayashi, "Linearizing optical frequency-sweep of a laser diode for FMCW reflectometry," *J. Lightwave Technol.*, vol. 14, no. 2, pp. 173–178, Feb. 1996, doi: 10.1109/50.482260.

[6-6] L. N. Langley *et al.*, "Packaged semiconductor laser optical phase-locked loop (OPLL) for photonic generation, processing and transmission of microwave signals," *IEEE Trans. Microwave Theory Techn.*, vol. 47, no. 7, pp. 1257–1264, Jul. 1999, doi: 10.1109/22.775465.

[6-7] C. M. Eigenwillig, B. R. Biedermann, G. Palte, and R. Huber, "K-space linear Fourier domain mode locked laser and applications for optical coherence tomography," *Opt. Express*, vol. 16, no. 12, p. 8916, Jun. 2008, doi: 10.1364/OE.16.008916.

Chapter7 **Conclusion**

In this study, I aimed to develop compact Si LSPCW MZMs with well-balanced performance, including broad-wavelength operation and the high-speed operation required in the 400G Ethernet standard and the next-era standards. Toward this target, I investigated modulation enhancement via the slow-light effect, broad-wavelength operation in the LD slow-light band, and the limiting factor of the frequency response in such devices. Based on these results, I improved of the frequency response and demonstrated high-speed modulation by employing meanderline electrodes that compensate the EO phase mismatch in such devices. In addition, I performed frequency-swept modulation using the AWG as a step toward the FMCW LiDAR application and for initial verification of the ranging action in the fiber optic system. In the below subsections, I present summaries of these studies.

7. 1 **Modulation Efficiency Enhancement via Slow Light Effect**

Through the modulation experiments using PCW/LSPCW devices that have small L of 90 or 200 μm, I clearly confirmed the proportional relationship between $\Delta\phi$ and n_g, and the reduction of $V_\pi L$ via the slow-light effect. This result indicates that slow light with a large n_g of 30–70 is advantageous for size reduction of modulators. In this experiment, I also obtained a small $V_\pi L$ of 0.18 V·cm and 0.22 V·cm for the high-dispersion PCW device with very large n_g of 57 and the LD LSPCW device with large n_g of 33 and wide $\Delta\lambda$ of 15 nm, respectively. To the best of my knowledge, these results represent the smallest $V_\pi L$ among the reported CMOS-compatible MZMs based on the CPD in Si. Even smaller $V_\pi L$ can be achievable in a LD device by employing a larger n_g. In that case, however, $\Delta\lambda$ will be narrowed, and the propagation loss will be increased. Therefore, an appropriate design according to the system requirement is necessary.

7. 2 **Wide-Wavelength-Range Operation**

I evaluated the fundamental optical characteristics, the frequency response, the *ER*, and the *BER* of the fabricated device in the LD band. The device exhibited a wide LD band with $n_g = 20 \pm 10\%$ and $\Delta\lambda =$ 21 nm, allowing for operation over a wide temperature range. The on-chip *IL* of this device was evaluated to be 5 dB from the measured transmission spectrum. In the frequency response measurement, the device exhibited f_{3dB} of ~18 GHz at $V_{DC} = -1.1$ V in the wavelength range of 1550–1556 nm. In the eye pattern measurement, uniform 25-Gbps eye patterns and slowly fluctuating *ER* within 1 dB were observed over the wide wavelength range of $\Delta\lambda = 16$ nm. This 1-dB fluctuation in *ER* also changed the error-free detection power by approximately 1 dB. Therefore, the LD device can offer stable error-free operation without any thermal stabilization if a 1-dB margin in *ER* or detection power is provided.

7. 3 High-Speed Operation via Electrooptic (EO) Phase Matching

I experimentally observed the EO phase mismatch, which constrains the frequency response. The theoretical analysis indicated that the meanderline electrodes and negative Γ_L improves the frequency response, with f_{3dB} reaching 56 GHz for L = 200 μm, L_d = 425 μm, and Γ_L = −0.5. The fabricated meanderline devices with load resistors to control Γ_L also exhibited f_{3dB} of >30 GHz, whereas the normal electrode device exhibited f_{3dB} of 19 GHz. For the 20-Ω terminated meanderline electrode device, a high f_{3dB} of 38 GHz was obtained. Using these devices, I observed the very clear 25- and 32-Gbps eye patterns with small V_{pp} of 1 and 2 V, respectively. Furthermore, the 50- and 56-Gbps open eye patterns were obtained with V_{pp} of 3.5 V, and the even faster 64-Gbps open eye pattern was also obtained by increasing V_{pp} to 5.2 V. V_{pp} can be reduced by employing larger n_g; for example, V_{pp} of 3.5 and 5.2 V will be reduced to 2.3 and 3.5 V for n_g = 30, respectively. I attempted PAM4 modulation and observed open eye patterns at 20, 25, and 28 Gbaud. At higher symbol rates of 32, 40, 50 Gbaud, the eye patterns became noisy and barely remained opened. In the WDM transmission experiment using the additional MUX chip, 50-Gbps/ch transmission in the four channels (the total bitrate: 200 Gbps) was demonstrated. The number of the channels was limited by the non-dedicated modulator design; an appropriate modulator design for 8-ch WDM will allow for 400 Gbps transmission.

7. 4 Frequency-Swept Modulation for a FMCW LiDAR System

I attempted frequency-swept modulation, which is needed in a FMCW LiDAR system, using the LSPCW MZM and the AWG. Before performing the frequency-swept modulation, I confirmed the single-tone modulation quality and obtained a narrow δf of 1.2 kHz after OE conversion. Moreover, in the experiment to observe the beat signal between two single-tone modulated signals, I verified the generation of the desired beat frequency and the adequate beat signal quality. The frequency-swept signals were generated by the AWG. I drove the device with the generated signals and observed the frequency-swept modulation spectra. Based on this frequency-swept modulation, Based on this frequency-swept modulation, I also attempted the ranging operation in the fiberoptic system, and I obtained f_{beat} corresponding to the L_{delay} = 1002 ± 10 cm which simulates a distance to a target object.

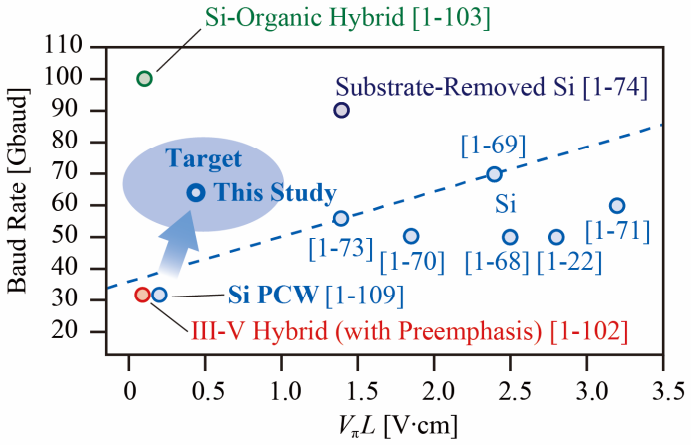

Figure 7.1 Benchmarking of MZMs on SOI and the device in this study.

Table 7.1 Comparison of reported MZMs on SOI and the device in this study.

Ref.	Group	Year	Material	Structure	L [mm]	f_{3dB} [GHz]	Baud Rate [Gbaud]	V_{pp} [V]	V_{DC} [V]	ER [dB]	On-chip IL (under Operation) [dB]	$V_\pi L$ [V·cm]	E_{bit} [pJ/bit]
[7-1]	Univ. Surrey	2012	Si	Rib MZM	1	>40 @–4V	50	6.5	–6	2.22	4.2 (7.4)	2.8 @–4 V	4.2
[7-2]	A*STAR	2013	Si	Rib MZM	3	30 @0 V	50	1.5	0	3.4	5.5 (7.1)	~2.5 @0 V	0.45
[7-3]	A*STAR	2014	Si	Rib MZM	3	37 @–5 V	50.5	3.5	–5	7.08	~9 (NA)	1.85 @–6 V	NA
[7-4]	CAS	2014	Si	Rib MZM	0.75	55 @–3 V	70	5.3	–1.5	6.1	3.3 (NA)	2.4 @–3 V	NA
[7-5]	McGill Univ.	2015	Si	Rib MZM	4.25	41 @–4 V	60	4.8	–4	3.8	3.8 (NA)	3.2 @–4 V	NA
[7-6]	IMEC	2017	Si	Rib MZM	1.5	27 @–1 V	56	2.5	–0.75	2.3	2.2 (NA)	1.39 @ NA	0.75
[7-7]	HUST	2018	Substrate-Removed Si	Rib MZM	2	>60 @-8 V	90	5	–6	3.3	5.4 (NA)	1.4 @–4 V	NA
[7-8]	KIT	2018	SOH	MZM	1.1	25	100	1.4	NA	NA	~11 (NA)	0.1 @–2 V	0.098
[7-9]	NTT	2017	III-V/Si Hybrid	MOS MZM	0.25	2.2	32	0.9	0.9	3.1	~1 (NA)	0.09	NA
[7-10]	YNU	2012	Si	LSPCW MZM	0.09	NA	40	5.3	–0.5	NA	6.2 (NA)	NA	NA
[7-11]	YNU	2017	Si	LSPCW MZM	0.2	22 (Calc.)	32	1.75	–0.9	3	>2 (>3)	0.2 @0 V	0.17
This Study		2020	Si	LSPCW MZM	0.2	38 @–2V	64	3.5–5.2	–3	2.3–4.8	5 (6.2–7.0)	0.44 @0 V	0.3–0.7

7. 5 Comprehensive Conclusion

Table 7.1 summarizes the specifications of the Si PCW/LSPCW MZMs obtained in this study and provides a comparison with MZMs on SOI reported in other studies. The Si modulators reported elsewhere have a long L of several centimeters. In contrast, the Si PCW/LSPCW modulator reported in this study has the very short L of 200 μm, but still exhibited competitively highperformance characteristics, including 64-bps operation capability. Simultaneously, this device will have 16-nm broad operation wavelength by employing the third-row LSPCW. The IL of the LSPCW device was evaluated to be 5 dB; however, it can be reduced by 1 dB by optimization of the passive optical components. The $V_\pi L$ of the phase shifter was evaluated to be 0.44 V· cm. Therefore, the benchmark of this device lies in the target region on Figure 7.1, and it exhibits the highest performance based on the indicated evaluation criteria among the CMOS-compatible Si MZMs. The above results demonstrated the feasibility of the Si LSPCW MZM as a compact, low-cost, high-speed modulator with a wide operating wavelength range for use in 400G Ethernet and networks based on the next generation of

standards. In addition, the feasibility for a frequency-swept source used in a FMCW LiDAR was demonstrated as a new application of the Si LSPCW MZM.

References

[7-1] D. J. Thomson *et al.*, "50-Gb/s Silicon Optical Modulator," *IEEE Photonics Technol. Lett.*, vol. 24, no. 4, pp. 234–236, Feb. 2012, doi: 10.1109/LPT.2011.2177081.

[7-2] M. Streshinsky *et al.*, "Low power 50 Gb/s silicon traveling wave Mach-Zehnder modulator near 1300 nm," *Opt. Express*, vol. 21, no. 25, pp. 30350–30357, Dec. 2013, doi: 10.1364/OE.21.030350.

[7-3] Y. Yang, Q. Fang, M. Yu, X. Tu, R. Rusli, and G.-Q. Lo, "High-efficiency Si optical modulator using Cu travelling-wave electrode," *Opt. Express*, vol. 22, no. 24, p. 29978, Dec. 2014, doi: 10.1364/OE.22.029978.

[7-4] H. Xu *et al.*, "High-speed silicon modulator with band equalization," *Opt. Lett.*, vol. 39, no. 16, pp. 4839–4842, Aug. 2014, doi: 10.1364/OL.39.004839.

[7-5] D. Patel *et al.*, "Design, analysis, and transmission system performance of a 41 GHz silicon photonic modulator," *Opt. Express*, vol. 23, no. 11, p. 14263, Jun. 2015, doi: 10.1364/OE.23.014263.

[7-6] M. Pantouvaki *et al.*, "Active Components for 50 Gb/s NRZ-OOK Optical Interconnects in a Silicon Photonics Platform," *J. Light. Technol.*, vol. 35, no. 4, pp. 631–638, Feb. 2017, doi: 10.1109/JLT.2016.2604839.

[7-7] M. Li, L. Wang, X. Li, X. Xiao, and S. Yu, "Silicon intensity Mach–Zehnder modulator for single lane 100 Gb/s applications," *Photonics Res.*, vol. 6, no. 2, p. 109, Feb. 2018, doi: 10.1364/PRJ.6.000109.

[7-8] S. Wolf *et al.*, "Silicon-Organic Hybrid (SOH) Mach-Zehnder Modulators for 100 Gbit/s on-off Keying," *Sci. Rep.*, vol. 8, no. 1, p. 2598, Dec. 2018, doi: 10.1038/s41598-017-19061-8.

[7-9] T. Hiraki *et al.*, "Heterogeneously integrated III-V/Si MOS capacitor Mach-Zehnder modulator," *Nature Photonics*, vol. 11, no. 8, p. 482+, Aug. 2017, doi: 10.1038/NPHOTON.2017.120.

[7-10] H. C. Nguyen, N. Yazawa, S. Hashimoto, S. Otsuka, and T. Baba, "Sub-100 μm Photonic Crystal Si Optical Modulators: Spectral, Athermal, and High-Speed Performance," *IEEE J. Sel. Top. Quantum Electron.*, vol. 19, no. 6, pp. 127–137, Nov. 2013, doi: 10.1109/JSTQE.2013.2265193.

[7-11] Y. Terada, K. Miyasaka, K. Kondo, N. Ishikura, T. Tamura, and T. Baba, "Optimized optical coupling to silica-clad photonic crystal waveguides," *Opt. Lett.*, vol. 42, no. 22, p. 4695, Nov. 2017, doi: 10.1364/OL.42.004695.

Acknowledgements

First, I would like to thank Prof. Toshihiko Baba (Yokohama Nat'l Univ.) for his enthusiastic guidance and for the many pieces of advice he gave me not only on my study but also on my life. I would like to thank Prof. Yasuo Kokubun (now of Chuo Univ.) for helpful discussions in periodical meetings. I would like to thank associate Prof. Yoshiaki Nishijima (Yokohama Nat'l Univ.) for helpful discussions in the periodical meetings and for friendly dairy conversations. I would like to appreciate Prof. Hiroyuki Arai (Yokohama Nat'l Univ.), Prof. Nobuyuki Yoshikawa (Yokohama Nat'l Univ.), and associate Prof. Taro Arakawa (Yokohama Nat'l Univ.) for discussion in periodical meetings and a doctoral dissertation public defense of this study.

I would like to show my respect to Dr. Hong C. Nguyen (now of Sumitomo Electric Industries, Ltd.), who is a pioneer of Si PCW modulators, and Dr. Yosuke Terada (now of Furukawa Electric Co., Ltd.), who engaged himself in development of the Si PCW modulators and improved the performance before my study. I would like to thank Dr. Shota Kita (now of NTT Basic Research Laboratory) for helpful discussions and comments he gave me in many conferences and the doctoral dissertation public defense. I would like to thank assistant Prof. Keisuke Kondo (now of Utsunomiya Univ.) for many pieces of advice on my study and on my life as a doctoral student.

I would like to thank old members of Baba Laboratory: Dr. Keisuke Watanabe (now of Univ. Exeter), Dr. Takumi Watanabe (now of ELIONIX, Inc.), Mr. Yoji Kishi (now of Tokyo Seimitsu Co., Ltd.), Mr. Yoshiaki Kanemura (now of Fujitsu Frontech, Ltd.), Mr. Daichi Takahashi (now of Olympus Corp.), Shun Kinugasa (Hitachi Automotive Systems, Ltd.), Mr. Takuya Tamura (now of Omron Corp.), Mr. Yuki Furuta (now of Terumo Corp.), Mrs. Keiko Hojo (now of KDDI Corp.), Mr. Kenji Miyasaka (now of Fujikura Ltd.), Mrs. Mai Sakemoto (now of Yoshida Dental MFG. Co., Ltd), Ms. Moe Takeuchi (now of Nippon Television Network Corp.), Mr. Tomoki Tanaka (now of Canon, Inc.), Mr. Yu Hasegawa (now of SHARP Corp.), Mr. Akihiro Sakata (now of V Technology Co., Ltd.), Mr. Atsuhiro Tanaka (now of Musashi Engineering, Inc.), Mr. Kensuke Itagaki (now of Future Architect, Inc.), Mr. Ryota Hirano (now of Step, Inc.), Mr. Tomoki Tatebe (now of Mitsubishi Heavy Industries, Ltd.), Mr. Goro Takeuchi (now of KDDI Corp.), Mr. Tomoki Yokokawa (now of NTT Docomo, Inc.), Mr. Yoshito Saijo (now of Furukawa Electric Co., Ltd.), Mr. Yuya Furukado (now of Yomiuri Telecasting Corp.), Mr. Daichi Akiyama (now of Fujitsu Frontech, Ltd.), Mr. Ryotaro Abe (now of NTT Docomo, Inc.), Mr. Taichi Takeda, Mr. Yuma Kusunoki, Mr. Kosuke Hayashi, Mr. Shuntaro Isoda, Mr. Yu Terada.

I would like to thank current members of Baba Laboratory: Dr Hiroshi Abe, Dr. Shoji Hachuda, Dr. Hiroyuki Ito, Dr Armandas Balcytis, Dr. Takemasa Tamanuki, Mr. Ryo Tetsuya, Mr. Mikiya Kamata, Mr. Ryo Shiratori, Mr. Jun Maeda, Mr. Ryo Kurahashi, Mr. Li Liucun, Naoya Kodama, Mr. Jun Gondo, Mr. Kouhei Takahashi, Mr. Kazuki Miyauchi, Ms. Miki Omishi, Mr. Takashi Kubota, Mr. Saneyuki Suyama, Mr. Keisuke Hirotani.

I would like to thank members of Kokubun Laboratory, Nishijima Laboratory, and Arakawa Laboratory for discussions in the periodical meeting.

I would like to thank secretaries of Baba Laboratory: Ms. Toshiyo Takahashi, Ms. Tomoko Mando, Ms. Yukie Iguchi, Ms. Satomi Isono, Ms. Masako Akaishi, and Makiko Koyanagi for their clerical

support.

I appreciate Mr. Okitsu of SHF Japan Co., Ltd. and Mr. Takezawa of i-wave Co., Ltd. for help with the experiment.

Finally, I would like to appreciate my parents, my sister, and my fiancée for their mental and financial support.

This paper is based on results obtained from a project commissioned by the New Energy and Industrial Technology Development Organization (NEDO).

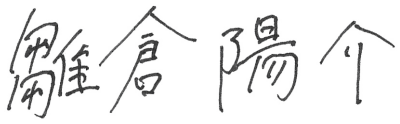

Publications

Journal Papers

[1] T. Tamura, K. Kondo, Y. Terada, Y. Hinakura, N. Ishikura, and T. Baba, "Silica-Clad Silicon Photonic Crystal Waveguides for Wideband Dispersion-Free Slow Light," *Journal of Lightwave Technology*, vol. 33, no. 14, pp. 3034–3040, Jul. 2015, doi: 10.1109/JLT.2015.2420685.

[2] Y. Hinakura, Y. Terada, T. Tamura, and T. Baba, "Wide Spectral Characteristics of Si Photonic Crystal Mach-Zehnder Modulator Fabricated by Complementary Metal-Oxide-Semiconductor Process," *Photonics*, vol. 3, no. 2, p. 17, Apr. 2016, doi: 10.3390/photonics3020017.

[3] Y. Terada, T. Tatebe, Y. Hinakura, and T. Baba, "Si Photonic Crystal Slow-Light Modulators with Periodic p–n Junctions," *Journal of Lightwave Technology*, vol. 35, no. 9, pp. 1684–1692, May 2017, doi: 10.1109/JLT.2017.2658668.

[4] Y. Furukado, H. Abe, Y. Hinakura, and T. Baba, "Experimental simulation of ranging action using Si photonic crystal modulator and optical antenna," *Opt. Express*, vol. 26, no. 14, pp. 18222–18229, Jul. 2018, doi: 10.1364/OE.26.018222.

[5] Y. Hinakura, Y. Terada, H. Arai, and T. Baba, "Electro-optic phase matching in a Si photonic crystal slow light modulator using meander-line electrodes," *Optics Express*, vol. 26, no. 9, pp. 11538–11545, Apr. 2018, doi: 10.1364/OE.26.011538.

[6] Y. Hinakura, H. Arai, and T. Baba, "64 Gbps Si photonic crystal slow light modulator by electro-optic phase matching," *Opt. Express*, vol. 27, no. 10, pp. 14321–14327, May 2019, doi: 10.1364/OE.27.014321.

[7] M. Kamata, Y. Hinakura, and T. Baba, "Carrier-Suppressed Single Sideband Signal for FMCW LiDAR Using a Si Photonic-Crystal Optical Modulators," *Journal of Lightwave Technology*, vol. 38, no. 8, pp. 2315–2321, 2020.

[8] Y. Hinakura, H. Arai and T. Baba, "Development of 64 Gbps Si photonic crystal modulator", *IEICE Trans. Electron.*, 2020 (Invited Paper).

[9] Y. Hinakura, D. Akiyama, H. ITO, H. Arai and T. Baba, *IEEE J. Sel. Top. Quantum Electron.*, 2020, submitted.

International Conferences

[1] Y. Hinakura, Y. Terada, H. Arai and T. Baba, "Electro-optic phase matching in Si slow-light modulators", Int. Sympo. Photon. Electron. Convergence, Tokyo, 2016.

[2] Y. Terada, T. Tatebe, Y. Hinakura and T. Baba, "32 Gbps operation in Si photonic crystal slow light modulator," Opt.&Photon. Int. Conf. (Int. Conf. Nanoscience & Nanotechnology), Yokohama, no. ICNN8-1, 2017.

[3] T. Baba, Y. Terada, Y. Hinakura, K. Hojo and H. Ito, "Recent progress in slow light modulators," Advanced Electromagnetics Sympo., Seoul, no. 1A2-1, 2017 (Invited Paper).

[4] Y. Furukado, Y. Hinakura, H. Abe and T. Baba, "Ranging using Si photonic crystal modulator and fiber delay interferometer," Int. Commission for Opt., Tokyo, no. F1G-05, 2017.

[5] Y. Furukado, H. Abe, Y. Hinakura and T. Baba, "Experimental simulation of FMCW LiDAR using Si photonic crystal modulator, optical antenna and fiber delay line", Int. Sympo. Photon. Electron. Convergence, Tokyo, 2017.

[6] Y. Hinakura, Y. Terada, H. Arai and T. Baba, “Improvement of frequency response by electro-optic phase matching in Si photonic crystal slow-light modulator”, Int. Sympo. Photon. Electron. Convergence, Tokyo, 2017.

[7] Y. Furukado, H. Abe, Y. Hinakura and T. Baba, “Experimental simulation of ranging action using Si photonic crystal modulator and optical antenna,” SPIE Photonics West, San Francisco, no. 10539-4, 2018.

[8] Y. Hinakura, Y Terada, H. Arai, and T. Baba, "Electro-optic phase matching in Si photonic crystal slow light modulator", OSA Integrated Photon. Res. Nanophoton. Si Photon., Zurich, no. IW3B.6, 2018.

[9] Y. Hinakura, H. Arai and T. Baba, “High-speed operation of meander line electrode photonic crystal optical modulator”, Int. Sympo. Photon. Electron. Convergence, Tokyo, 2018.

[10] M. Kamata, Y. Hinakura and T. Baba, “Single sideband modulation using Si photonic crystal optical modulator”, Int. Sympo. Photon. Electron. Convergence, Tokyo, 2018.

[11] Y. Hinakura, H. Arai and T. Baba, “40-Gbps Si photonic crystal slow light modulator in the electro-optic phase matching”, SPIE Photonics West, San Francisco, no. 10923-43, 2019.

[12] M. Kamata, Y. Hinakura and T. Baba, "Carrier-suppressed single sideband signal for FMCW LiDAR using Si photonic crystal I-Q optical modulator", Optelectronic and Commun. Conf., Fukuoka, no. MD1-2, 2019.

[13] Y. Hinakura, H. Arai and T. Baba, "64 Gbps Si photonic crystal slow light modulator by electro-optic phase matching", Optelectronic and Commun. Conf., Fukuoka, no. MD2-3, 2019.

[14] M. Kamata, H. Abe, Y. Hinakura, R. Kurahashi and T. Baba, “FMCW ranging action using free-space optical beam with carrier-suppressed single sideband signal generated by Si photonic crystal I-Q optical modulator”, Int. Sympo. Photon. Electron. Convergence, Tokyo, 2019.

[15] Y. Hinakura, H. Arai and T. Baba, “64-Gbps operation of meander line electrode photonic crystal optical modulator”, Int. Sympo. Photon. Electron. Convergence, Tokyo, 2019.

[16] T. Baba, H. Ito, H. Abe, T. Tamanuki, Y. Hinakura, R. Tetsuya, J. Maeda, M. Kamata, R. Kurahashi and R. Shiratori, “Si PIC based on photonic crystal for LiDAR application”, Opt. Fiber Commun. Conf., San Diego, no. M4H.1, 2020 (Invited Paper).

Domestic Conferences

[1] 寺田陽祐, 雛倉陽介, 北條恵子, 建部知紀, 馬場俊彦, “広い動作スペクトルを有する小型 OOK・QPSK フォトニック結晶変調器”, 電子情報通信学会総合大会, no. C-4-19, 2016 (招待講演).

[2] 雛倉陽介, 寺田陽祐, 馬場俊彦, "Si フォトニック結晶マッハツェンダー変調器における広い波長範囲での周波数応答調査", 応用物理学会春季講演会, no. 21p-S611-5, 2016.

[3] 北條恵子, 寺田陽祐, 雛倉陽介, 馬場俊彦, "Si フォトニック結晶 QPSK 変調器 の零バイアス低電圧動作", 応用物理学会春季講演会, no. 21p-S611-6, 2016.

[4] 雛倉陽介, 寺田陽祐, 新井宏之, 馬場俊彦, “Si フォトニック結晶スローライト変調器の光-電気位相整合”, 応用物理学会秋季講演会, no. 14a-B4-5, 2016.

[5] 雛倉陽介, 古門優弥, 阿部紘士, 馬場俊彦, “Si フォトニック結晶変調器による二つの変調信号間のビート周波数の観測”, 応用物理学会秋季講演会, no. 14p-B4-15, 2016.

[6] 寺田陽祐, 雛倉陽介, 北條恵子, 建部知紀, 馬場俊彦, “スローライトを利用した小型 Si フォトニック結晶変調器”, レーザー学会, 2017 (招待講演).

[7] 古門優弥, 阿部紘士, 雛倉陽介, 馬場俊彦, “Si フォトニック結晶光偏向器で受信した信号による FMCW ビート周波数観測”, 電子情報通信学会集積光デバイスと応用技術研究会, no. 11, 2017.

[8] 雛倉陽介, 寺田陽祐, 新井宏之, 馬場俊彦, “電気-光位相整合による Si フォトニック結晶スローライト変調器の周波数応答の改善”, 電子情報通信学会集積光デバイスと応用技術研究会, no. 19, 2017.

[9] 雛倉陽介, 寺田陽祐, 新井宏之, 馬場俊彦, “G 電極共通化 Si フォトニック結晶スローライト変調器の光-電気位相整合”, 応用物理学会春季講演会, no. 15p-P2-3, 2017.

[10] 古門優弥, 雛倉陽介, 阿部 紘士, 馬場 俊彦, “Si フォトニクス FMCW 光レーダーを模したビート周波数観測― 長い遅延に対する依存性 ―”, 応用物理学会春季講演会, no. 17p-F204-7, 2017.

[11] 雛倉陽介, 寺田陽祐, 新井宏之, 馬場俊彦, " Si フォトニック結晶スローライト変調器の光-電気位相整合による周波数応答の改善", 応用物理学会秋季講演会, no. 7p-PA2-3, 2017.

[12] 古門優弥, 阿部紘士, 雛倉陽介, 馬場俊彦, “Si フォトニック結晶光偏向器の受信アンテナ特性”, 応用物理学会春季講演会, no. 18a-B201-6, 2018.

[13] 雛倉陽介, 寺田陽祐, 新井宏之, 馬場俊彦, “Si フォトニック結晶スローライト変調器の周波数応答の計算”, 応用物理学会春季講演会, no. 20a-P4-8, 2018.

[14] 鉄矢諒, 雛倉陽介, 阿部紘士, “馬場俊彦, Si フォトニック結晶光偏向器による送信での変調信号強度”, 応用物理学会秋季講演会, no. 18a-212A-7, 2018.

[15] 雛倉陽介, 鎌田幹也, 馬場俊彦, “Si フォトニック結晶光変調器による搬送波抑制片側波変調”, 応用物理学会秋季講演会, no. 18a-212A-8, 2018.

[16] 雛倉陽介, 新井宏之, 馬場俊彦, “メアンダライン電極フォトニック結晶光変調器の高速変調動作”, 応用物理学会秋季講演会, no. 18p-212A-8, 2018.

[17] 雛倉陽介, 新井宏之, 馬場俊彦, “小型 Si フォトニック結晶スローライト変調器の 64 Gbps 動作”, 電子情報通信学会レーザ・量子エレクトロニクス研究会, 2019.

[18] 板垣健佑, 伊藤寛之, 雛倉陽介, 馬場俊彦, “O バンド Si フォトニック結晶変調器の初期的動作”, 応用物理学会春季講演会, no. 9a-PB2-3, 2019.

[19] 雛倉陽介, 新井宏之, 馬場俊彦, “メアンダライン電極フォトニック結晶光変調器の 64 Gbps 動作”, 応用物理学会春季講演会, no. 11p-W331-8, 2019.

[20] 鎌田幹也, 雛倉陽介, 馬場俊彦, “Si フォトニック結晶 I-Q 光変調器を用いた搬送波抑制片側波信号による FMCW LiDAR のビートスペクトル生成”, 応用物理学会春季講演会, no. no. 12p-W631-72019.

[21] 雛倉陽介, 新井宏之, 馬場 俊彦, 50～64 Gbps Si フォトニック結晶光変調器の開発, 応用物理学会秋季講演会, no. 19p-E206-2, 2019.

[22] 鎌田幹也, 阿部紘士, 雛倉陽介, 倉橋諒, 馬場俊彦, Si フォトニック結晶 I-Q 光変調器を用いて搬送波抑制片側波信号を重畳した空間ビームによる FMCW 測距動作, 応用物理学会秋季講演会, no. 19p-E206-3, 2019.

[23] 鎌田幹也, 雛倉陽介, 馬場俊彦, “Si フォトニック結晶光変調器を用いた搬送波抑制片側波信号による FMCW LiDAR のビートスペクトルと強度振動抑制”, 応用物理学会春季講演会, no. 15a-B415-4, 2020.

[24] 雛倉陽介, 秋山大地, 伊藤寛之, 馬場俊彦, “Si フォトニック結晶変調器を用いた 50 Gbps/ch 波長分割多重”, 応用物理学会春季講演会, no. 15p-B508-11, 2020.